Trinity College Dublin
Coláiste na Tríonóide, Baile Átha Cliath
The University of Dublin

New solid forms of itraconazole and their pharmaceutical applications

A dissertation submitted for the degree of

Doctor of Philosophy

at the School of Pharmacy & Pharmaceutical Sciences, Trinity College Dublin,

the University of Dublin, Ireland

by Ricardo Machado Cruz

Under the supervision of Dr. Lidia Tajber

And the co-supervision of Dr. Maria Jose Santos-Martinez

May 2020

Declaration

I declare that this thesis has not been submitted as an exercise for a degree at this or any other university. A small proportion of the work described in this thesis was carried out by others, and this is duly acknowledged in the text wherever relevant. I declare that all other work is entirely my own.

I agree to deposit this thesis in the University's open access institutional repository or allow the Library to do so on my behalf, subject to Irish Copyright Legislation and Trinity College Library conditions of use and acknowledgement

_____

Ricardo Machado Cruz

In memoriam of

José Carlos Cruz

*"An idea that is not dangerous is unworthy of being called an **idea** at all."*

Oscar Wilde

Table of Contents

Chapter V: Development ITR-TER nano-cocrystals and their use as dry powders for pulmonary administration 129

Summary

Itraconazole (ITR) is an active pharmaceutical ingredient (API) with a broad-spectrum antifungal activity. This API has a very low solubility, which can hinder its bioavailability after oral administration. In this work, approaches such as bottom-up nanonisation, PEGylation of nanoparticles (NPs), cocrystallisation and nano-cocrystallisation were produced and assessed regarding their potential to improve the pharmaceutical properties of ITR.

As regards nanonisation, evaluation of the variables involved in the heat induced evaporative nanoprecipitation (HIEAN) of ITR revealed that the antisolvent:solvent (AS:S) ratio was a critical parameter affecting the particle size of the dispersions. Since changes in this parameter involved altering both solvent volume and the final concentration of ITR, thus affecting the supersaturation degree. The antisolvent temperature was only critical when used at values higher than the boiling point of acetone (>56 °C), affecting the supersaturation due to an increased rate of acetone evaporation. The inclusion of a residual solvent (acetone) evaporation step had no impact on the particle size of the ITR dispersions, however, when used for a prolonged time, it resulted in crystallisation of the particles. The ITR dispersions evaporated for 40 min at 50 mbar showed an enhanced colloidal stability when stored at 4 and 25 °C. The ITR NPs produced with the optimised HIEAN conditions, i.e. the antisolvent phase at 80 °C and the AS:S ratio of 10:1, yielded a monodispersed dispersion with the particle size of 253 ± 16 nm, which had solid-state characteristic of a liquid crystal smectic mesophase.

The following polymers: poly(ethylene glycol) (PEG) and 4-arms PEG (4 ARM) with a molecular weight of 10 kDa were the most suitable candidates for PEGylation of ITR NPs. The modified NPs had sizes below 500 nm. The evaluation of the mucoadhesive properties of PEG, poly(ethylene glycol) methyl ether (MPEG) and 4 ARM PEG (all with a molecular weight of 10 kDa) showed that these polymers interacted weakly and reversibly with mucin, despite being used at high concentrations of 10, 50 and 100 mg/mL. The non-PEGylated and PEGylated ITR NPs produced using the optimised HIEAN method had similar average particle sizes and polydispersity indices, although the PEGylated NPs had their zeta potential partially neutralised, reducing their stability in dispersion. The non-PEGylated ITR NPs were isolated as a smectic mesophase, while the PEGylated NPs were more crystalline. As evidenced by scanning electron microscopy, the morphology of a number of the PEGylated samples was affected by the polymer presence and the systems were composed by a mix of spherical and flake-like particles, instead of the spherical particles as in the non-PEGylated ITR NPs. The non-PEGylated ITR NPs were considered as having a mucopenetrative potential, as the investigation of the mucoadhesive properties revealed no evidence that these particles could strongly interact with mucin. On the other hand, the

PEGylated NPs exhibited mucoadhesive potential in stationary conditions, but when flow conditions were applied the particles had mucopenetrative properties.

The screening for multicomponent forms of ITR identified one new cocrystal produced using terephthalic acid (TER) and eutectic phases with dihydrocaffeic acid, 4-nitrobenzoic acid and the 4-aminosalicylic acid. The single crystal X-ray analysis revealed that the crystalline structure of the new cocrystal (ITR-TER) had a 2:1 stoichiometry. The ITR molecules are in an anti-parallel arrangement with the coformer "trapped" in the space formed between the two ITR molecules. This supramolecular arrangement was stabilised by H-bonds formed between the hydroxyl moiety of the carboxyl acid group and the N4 of the azole ring of ITR while the C3 of the azole group and the carbonyl group of the coformer formed an additional H-bond. The dissolution behaviour of the freeze dried ITR (FD ITR) showed a remarkable improvement considering its intrinsic dissolution rate (IDR) and powder dissolution in comparison to crystalline ITR. Considering the ITR cocrystals with oxalic acid (ITR-OXA), succinic acid (ITR-SUC) and TER, the IDR values and powder dissolution profiles correlated with the aqueous solubility of the coformers. The presence of polymers in the dissolution media prevented the conversion of FD ITR, ITR-OXA and ITR-SUC to crystalline ITR.

The conditions to produce the nano-cocrystals (NCCs) of ITR-TER using the method of antisolvent precipitation were investigated. A mixture of acetone and methanol in a volume ratio of 70:30 (v/v) enabled ITR and TER solubilisation at the highest concentration respecting the cocrystal stoichiometry. Lecithin was used as a stabiliser at 5% (w/w) of the total solid content in the ITR-TER dispersions resulting in monodispersed particles with smaller sizes and lower zeta potential values in comparison to the batch made without lecithin. The ultrasound application to the ITR-TER dispersions reduced the particle sizes when sonication was applied continuously for at least 15 min. Modifications of the method setup was successful to increase the batch size by a 5-fold without affecting the characteristics of the ITR-TER dispersions.

Trojan particles, nano-in-microparticles, produced by spray-drying of ITR-TER NCC with mannitol (MAN), raffinose and trehalose were composed of spherical particles and could be instantaneously redispersed in water releasing the NCCs. The released NCCS has particle sizes smaller than 250 nm as measured by nanoparticle tracking analysis. The median particle size of ITR-TER-MAN was 4.85±0.06 μm, in agreement with the results obtained from the next generation impactor, as the mass median aerodynamic diameter and geometric standard deviation of this sample was 4.02±0.13 μm and 1.74±0.03, respectively. This enabled ITR-TER-MAN to have the largest respirable fraction, of 36.11 ± 0.17%. This indicated that a larger fraction of ITR-TER-MAN could be deposited in deeper regions of the lungs.

Acknowledgements

Publications and Presentations

Publications Associated with the Thesis:

- Machado Cruz, R., Santos-Martinez, M.J., Tajber, L., 2019. Impact of polyethylene glycol polymers on the physicochemical properties and mucoadhesivity of itraconazole nanoparticles. Eur. J. Pharm. Biopharm. 144, 57–67. https://doi.org/10.1016/j.ejpb.2019.09.004

- Machado Cruz, R., Tieger, E., Boleslavská, T, Beranek, J., Calta, P., Tajber, L. Identification of a new itraconazolel cocrystal. In preparation.

Poster Presentations:

- Cruz R M; McComiskey K; Tajber L. Multivariate Analysis of Heat Induced Evaporative Antisolvent Nanoprecipitation of Itraconazole. 38th All Ireland Schools of Pharmacy Conference, RCSI, Dublin, Ireland. 2016 Mar 21-22.

- Cruz, R. M., Santos-Martinez, M.J., Tajber, L. Investigation of adhesive properties of pegylated and non-pegylated itraconazole nanoparticles using quartz crystal microbalance with dissipation. 39th All Ireland Schools of Pharmacy Conference, UCC, Cork, Ireland. 2017 Apr 24-25

- Cruz, R. M.; Bowe, R., Santos-Martinez, M. J.; Tajber, L. Investigation of interactions of Pegylated and Non-Pegylated Itraconazole Nanoparticles with Mucin Using Quartz Crystal Microbalance with Dissipation and Dynamic Light Scattering, 2017 AAPS Annual Meeting and Exposition, San Diego, CA, USA, 2017 Nov 13-15.

- Cruz, R. M.; Umerska, A.; Tajber, L. Development of nanococrystals of itraconazole with terephthalic acid, The 41st All Ireland Schools of Pharmacy Conference, Trinity College Dublin, Dublin, Ireland. 2019 Apr 17-18.

- Cruz, R.M., Tieger, E., Boleslavská, T, Štěpánek, F., Beranek, J., Calta, P., Tajber, L. Cocrystals of itraconazole. 1st ORBIS Summer School and Workshop, Trinity College Dublin, Dublin, Ireland. 2019 Jun 12-14.

Abbreviations and Symbols

$\%_{max}$	Maximum percent of dissolved drug
^exo	Exothermic direction
2θ	2 theta (diffraction angle)
4 ARM PEG	4 Arm-poly(ethylene glycol)
ANOVA	Analysis of variance
API	Active pharmaceutical ingredient
AS	Antisolvent
ASA	4-aminosalicylic acid
BCS	Biopharmaceutics Classification System
BM	Ball milling
cps	Counts per second
DCM	Dichloromethane
DHC	Dihydrocaffeic acid
DLS	Dynamic light scattering
DMPEG	Poly(ethylene glycol) dimethyl
DSC	Differential Scanning Calorimetry
FD ITR	Freeze-dried itraconazole
FT-IR	Fourier transform infrared spectroscopy
HIEAN	Heat induced antisolvent precipitation
HPLC	High Performance Liquid Chromatography
IDR	Intrinsic dissolution rate
ITR	Itraconazole
MAN	Mannitol
MeOH	Methanol
MPEG	Poly(ethylene glycol) methyl ether
NBA	4-nitrobenzoic acid

NCC(s)	Nano-cocrystal(s)
NG	Neat grinding
NGI	Next Generation Impactor
NP(s)	Nanoparticle(s)
NTA	Nanoparticle Tracking analysis
OXA	Oxalic acid
PdI	Polydispersity index
PEG	Poly(ethylene glycol)
PXRD	Powder X-ray diffraction
QCM-D	Quartz crystal microbalance with dissipation
RAF	Raffinose
S	Solvent
SEM	Scanning electron microscopy
SUC	Succinic acid
TER	Terephthalic acid
T_g	Glass transition temperature
TGA	Thermogravimetric analysis
T_{max}	Time to reach the maximum percent of dissolved drug
TRE	Trehalose
WG	Wet grinding
δ_t	total solubility parameter

Chapter I: General Introduction

1.1. Epidemiology of invasive fungal infections

Fungal infections are of a great concern for immunocompromised patients, including transplant receptors and HIV-infected individuals, due to their higher susceptibility to infections in comparison to healthy population (Richardson and Lass-Flörl, 2008). The former individuals are immunosuppressed to avoid rejection of the transplanted solid organs (Sanchez and Larsen, 2007), while HIV-positive individuals can develop the acquired immune-deficient syndrome (AIDS), which means, when the CD4$^+$ T cells count, a marker used to assess the immune system debility, becomes very low in later stages, that their organisms are unable to defend themselves against pathogens normally safe for healthy individuals (Armstrong-James et al., 2014; Mellors et al., 1996).

The consequences of systemic fungal infections in immunocompromised individuals are very severe, including a high mortality risk (Janbon et al., 2019). Indeed, the mortality rate of candidiasis, one of the most common nosocomial infections, has a prevalence ranging from 11 to 81% in liver transplant recipients and from 20 to 27% in pancreas recipients. (Bassetti et al., 2006; De Rosa et al., 2013). The second most common fungal infection is aspergillosis, which along with candidiasis, is responsible for 80% of fungal infection in post-transplanted patients (Abbott et al., 2001). The mortality of aspergillosis is also very high, from 20% in lung-transplanted patients up to 66.7% with kidney and heart transplantation (Sanchez and Larsen, 2007). Among HIV patients, opportunistic fungal infections are a major cause of death, for instance, the pneumocystis pneumonia is responsible for approximately 30% of the deaths of those individuals (Armstrong-James et al., 2014; Limper et al., 2017). Another opportunistic fungal infection is the cryptococcal disease, which was estimated to have 6% of prevalence in these individuals with a CD4$^+$ T cells count lower than 100 cells/μL, and being the cause of 15% of the cause of death in HIV-infected people (Rajasingham et al., 2017).

The concern about invasive fungal infections is aggravated by an increase in the population of immunocompromised individuals in the recent years. For instance, the reported number of global solid organs transplantation increased from 100,900 in 2008 to 135,860 procedures performed in 2016 (GODT, 2019). However, although the global number of new HIV infections and the AIDS-related death had reduced from 2.8 million and 1.5 million in 2007 to 1.8 million and 940,000 in 2017, respectively, the number of people living with the virus increased from 27.4 million to 36.9 million for the same period (Unaids, 2018). The life expectancy in those individuals had improved due to early diagnosis and the increase of people accessing antiretroviral therapy, however, in sub-Saharan Africa and Asia this situation is still tragic, as these places concentrate around 83.7% of people living with HIV and 88.3% of the global HIV-related deaths (Armstrong-James et al., 2014; Unaids, 2018).

Therefore, as the number of the immunocompromised population increases, the number of death caused by opportunistic fungal infections is also likely to increase due to the high mortality rate associated with such diseases (Abbott et al., 2001; De La Rosa et al., 2002; Venkatesan et al., 2005). In order to overcome this growing problem, massive efforts have been put in place in the last decades proposing new drugs and presentations to achieve more effective treatments (Campoy and Adrio, 2017; Scorzoni et al., 2017).

1.2. Itraconazole

Itraconazole (ITR) is an antifungal agent belonging to the azole class, which are molecules characterised by a five-membered attached to other aromatic rings (Saag and Dismukes, 1988). This group is divided into two sub-groups, the imidazoles that have two nitrogen atoms in the azole ring e.g. miconazole and ketoconazole; and the triazoles, which have three nitrogen atoms in their azole ring, e.g. ITR (Fig. 1.1) and fluconazole (Bodey, 1992; Saag and Dismukes, 1988).
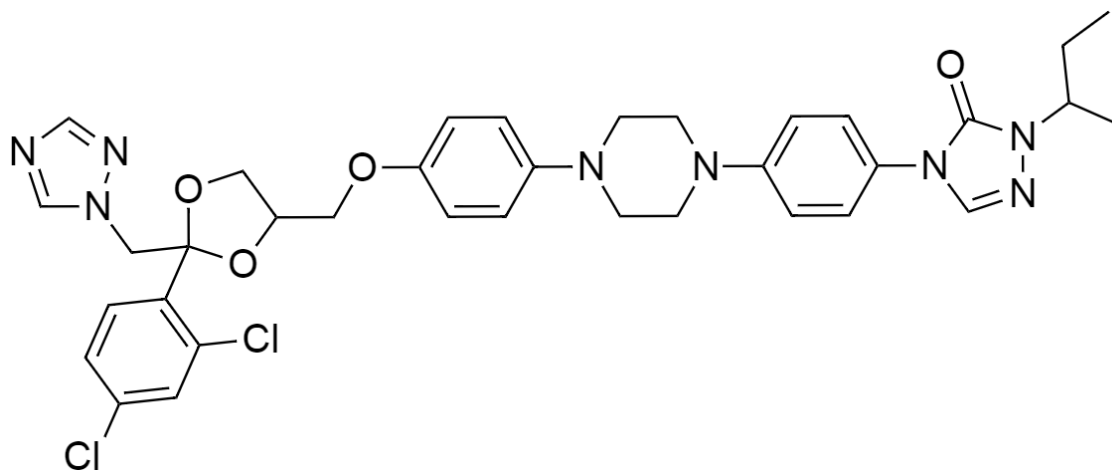
Fig. 1.1: Molecular structure of ITR.

The mechanism of action of azole antifungals is the inhibition of the cytochrome P-450 dependent fungal enzyme, lanosterol demethylase, also known as lanosterol 14α-demethylase or P-450$_{DM}$, to convert lanosterol to ergosterol, a component of the fungal cellular wall. The ergosterol depletion compromises the cellular membrane composition and, consequently, its permeability is also modified (Elewski, 1993; Ghannoum and Rice, 1999). The enzymatic inhibition is possible due to the ability of triazole antifungals to bind to the heme iron of the cytochrome by N4 of azole ring (Fig. 1.1). Additionally, hydrophobic groups of these agents intensify the interactions with the substrate binding site of the enzyme (Yoshida and Aoyama, 1991, 1990).

ITR is an active pharmaceutical ingredient (API) with a broad-spectrum antifungal activity and it is one of the few azole agents used for the treatment of topical and systemic mycoses as well as in the prophylaxis in immune-suppressed patients (Campoy and Adrio, 2017; Denning and Hope, 2010). ITR has been reported to be effective against *Candida*

spp. in oral, oesophageal and vulvovaginal infections, in cases of resistance with first-line treatment azoles (Denning and Hope, 2010). It was also the first azole used in the oral treatment in cases of pulmonary aspergillosis able to reduce corticosteroids needs in cases of allergic bronchopulmonary aspergillosis (Ashbee et al., 2014). Others fungal diseases can also be treated using ITR, such as *Cryptococcal meningitis*, *Blastomyces* and *Mucorales* infections (Berenguer et al., 1994; Denning and Hope, 2010; Slain et al., 2001; Venkatesan et al., 2005). The prophylactic usage of ITR is also effective in some other situations, for instance, its use in neutropenic patients with hematologic malignancies reduced by 40% the incidence of invasive fungal infection caused by *Aspergillus* (Glasmacher et al., 2003). It also showed a protective effect on lung and heart transplanted patients, reducing the incidence of invasive aspergillosis when ITR was used for the prophylaxis for at least one year (Kato et al., 2014; Munoz et al., 2004). In HIV patients, 200 mg daily ITR showed to be effective in the prophylaxis of histoplasmosis and cryptococcosis and its usage is advised especially for patients with CD4 count lower than 100 cell/ µL (McKinsey et al., 1999).

In general, treatment with ITR is safe for most patients as the upper limit of therapeutic concentration (17.1 mg/L) is considerably higher than ITR plasmatic concentration required to treat against most of the fungal diseases (Table 1.1) (Lestner and Hope, 2013; Lestner et al., 2009). However, the inter-individual ITR pharmacokinetic variance aggravated by the association of immunosuppressed patients fragility and the severity of the fungal infections requires monitoring of ITR plasmatic concentration to assure the treatment efficiency and reduced side effects (Andes et al., 2009; Ashbee et al., 2014).

Table 1.1: Examples of relevant systemic concentrations of ITR**.**

Concentration of ITR (µg/mL)	Relevance:
0.306	Maximum concentration of Sporanox® oral solution in healthy patients [*] (Barone et al., 1998)
0.5	Therapeutic concentration to treat against *Candida* in oral mucosal infections (Rex et al., 1997)
0.5 – 1.5	Average concentration reached after 7-15 days of oral treatment[**] in neutropenic cancer patients (Boogaerts et al., 2001)
6.5	Lowest therapeutic concentration to treat against *Aspergillus* and *Coccidioides* (Berenguer et al., 1994; Tucker et al., 1990)
17.1	Maximum therapeutic concentration (Lestner et al., 2009)

(*) a single 200 mg dose of ITR in solution; (**) 250 mg/day intravenous for 7 days, followed by 7 days with 400 mg/day with an oral solution.

The side effects of ITR used for prophylaxis are normally very mild and reversible, with gastrointestinal symptoms, such as abnormal pain, nausea, vomiting diarrhoea and constipation and abnormal liver function the most common. Another reported but rarer side effects are hypokalaemia, cutaneous rash/pruritus and headache (Lestner and Hope, 2013). Despite these side effects being usually not severe, ITR is usually replaced by another antifungal drug for long-term administration (Marr et al., 2004).

According to the Biopharmaceutics Classification System (BCS), which divides APIs based on their solubility and their gastrointestinal permeability (Fig. 1.2), ITR belongs to class II, indicating that it has poor aqueous solubility and high permeability (Amidon et al., 1995; Papadopoulou et al., 2008).
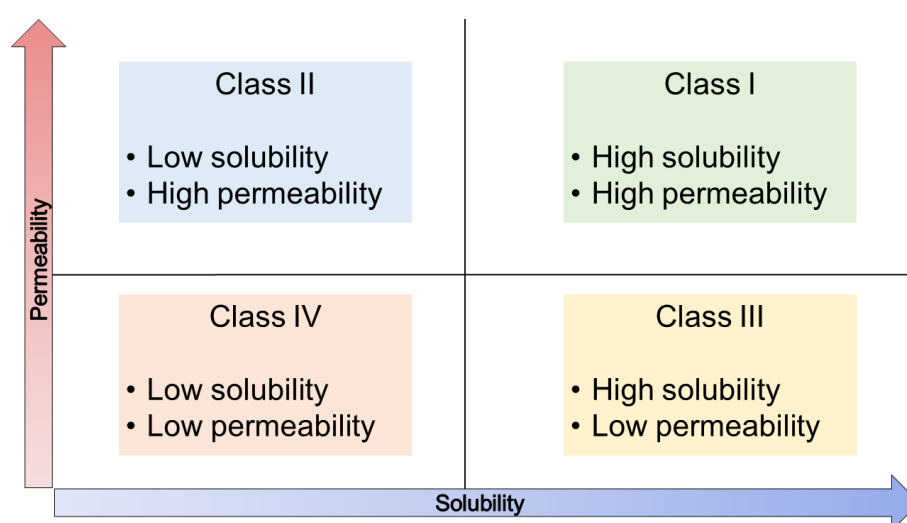
Fig. 1.2: Key characteristics of APIs according to the BCS.

According to the Food and Drug Administration agency (FDA), an API is considered as a high solubility molecule when its highest dose is soluble in 250 mL or less of aqueous media at 37±1 °C and in pH 1-6.8 and as a highly permeable when its oral bioavailability is no less than 85% of the intravenous reference dose (Food and Drug Administration, 2017). Indeed, ITR has a low solubility in pure water (1 ng/mL), which is slightly increased in acidic medium (4 µg/mL), as the drug is a weak base (pKa = 3.7) (Hardin et al., 1988; McComiskey et al., 2018; Stevens, 1999). This poor solubility is due to its long structure and its considerably high molecular weight, 705.65 Da. Furthermore, ITR is composed of multiple aromatic rings and has no H-bond donors, which results in a predominantly hydrophobic character of the molecule, despite the presence of polar regions, which are two chlorine atoms and twelve H-bond receptors (Fig. 1.1). In theory, these characteristics, in addition to a log P value of ITR of 5.53, makes this API unlikely to have desirable absorption or permeation, however, experimental results suggest that antifungal agents are absorbed by active transporters, hence ITR has high permeability (Lipinski et al., 2012).

The commercial form of ITR, Sporanox®, is available as pellets in oral capsules or complexed with hydroxypropyl β-cyclodextrin in the intravenous and oral solution

formulations (Kalepu and Nekkanti, 2015). The pellets in the oral capsules are manufactured by spray-layering a solution of ITR and hydroxypropyl methylcellulose (HPMC) on sucrose beads. Then, the drug-coated beads are treated with a seal coating polymer layer (PEG 20,000 Da) to prevent sticking of the beads (Gilis et al., 1997). The API in these pellets is in the amorphous state, therefore, has an increased apparent solubility. In addition, the HPMC acts as a stabiliser, preventing the crystallisation of ITR into its crystalline form that has a lower aqueous solubility (Kalepu and Nekkanti, 2015).

1.3.Nanoparticles (NPs)

The improvement of pharmacological and/or pharmacokinetic properties of drugs, especially of APIs belonging to BCS class II and IV (Fig. 1.2), can be achieved by the developing drug delivery systems with particles with sizes lower than 1 µm (Parveen et al., 2012). A range of NPs are currently available, including those produced by nanonisation of the micron-sized APIs and manufactured to increase their dissolution rate and, consequently, bioavailability of poorly soluble APIs (Merisko-Liversidge and Liversidge, 2011). This type of NPs are composed by the drug only and are commonly known as "nanocrystals" (Müller et al., 2011). Alternatively, when the nanonisation process results in NPs with less ordered crystal lattice, they are designated as "nanoamorphous", when they are completely disordered, or as "liquid crystal mesophases", when they have an intermediary disordered state (Jog and Burgess, 2018). The APIs can also be incorporated in nanostructured carriers resulting in different characteristics in relation to the pure drug, as in these cases, substances with more suitable properties are used in the carriers to achieve the required objective (Ferrari, 2005; Pinto Reis et al., 2006). Variety of nanocarriers are currently used in drug delivery systems, for instance, the API can be conjugated with another material, usually a polymer or encapsulated in vesicular carriers, such as liposomes, polymeric NPs and nanoemulsions (Onoue et al., 2014; Parveen et al., 2012; Teli et al., 2010).

The improved dissolution rate of nanonised drugs results from the increased surface area in relation to larger particles (Shah et al., 2016). The relation of surface area and dissolution rate is explained by the Noyes-Whitney equation (Noyes and Whitney, 1897):

$$\frac{d_m}{d_t} = \frac{AD(C_S - C)}{h}$$
(Eqn.1.1)

where *dm/dt* is the dissolution rate, *A* is the surface area of the solid, *D* is the diffusion coefficient, C_s is the saturation solubility, *C* is the drug concentration and *h* is the thickness of diffusion layer. According to this equation, a determined quantity of a pharmaceutical substance will have a higher dissolution rate if it is available in a higher surface area form, which is achieved by reducing its particle size dimensions. The explanation for this is, in a

hypothetical suspension, the molecules of a particle are in a constant equilibrium with the solubilised molecules in its surrounding. Consequently, reducing the size of this particle increases the concentration of the solubilised molecules in its vicinity. The Oswald-Freundlich equation (Freundlich, 1926) explains this size-solubility relation and it can be written as:

$$\hat{C}_s = \frac{C_s}{C_s^\infty} = exp\left(\frac{2\gamma_{sl}V_c}{rRT}\right) \qquad \text{(Eqn. 1.2)}$$

where $\hat{C}_s$ is the normalised solubility limit, C_s is the solubility of a spherical particle, C_s^∞ is the solubility of a flat surface, i.e. a particle much larger than the spherical particle, γ_{sl} is the interfacial tension between the solid particle and the surrounding liquid, V_c is the volume of the spherical particle, *r* is the radius of this particle, *R* is the gas constant and *T* is the temperature.

In the case of the disordered nanonised particles, their apparent solubility is also enhanced because these are metastable forms in a higher energy state in relation to the crystalline form. Therefore, the higher solubility of amorphised particles is a consequence of the higher mobility of their molecules resulting in a higher saturation concentration (Grohganz et al., 2013; Hancock and Parks, 2000).

Another interesting feature of NPs is the possibility to modify their surface for different purposes. For instance, proteins or drugs with specific action site can be attached on the particle surface to target these NPs and to improve their distribution by increasing the drug concentration in that site, while at same time the API concentration in other organs and tissues are reduced (Lehto et al., 2016). As a result, side effects of drugs are reduced, improving the life quality of the patients and the effectiveness of the treatment (Loira-Pastoriza et al., 2014). The surface modification can also be used to significantly increase of systemic half-life of NPs by the inclusion of polyethylene glycol (PEG) chains. This is possible because this polymer prevents the opsonisation of NPs in the bloodstream, consequently, reducing their uptake by mononuclear phagocyte system, which plays a great role in the clearance kinetics of such particles (Moghimi et al., 2001; Rabanel et al., 2014).

1.3.1. Nanoparticulate drug delivery systems of ITR

The development of ITR nanocrystals has been already explored using different techniques resulting in formulations with enhanced characteristics. An example was published by Van Eerdenbrugh et al (Van Eerdenbrugh et al., 2008a), where ITR NPs were produced by media milling. There NPs had sizes of 220±4 nm and were stabilised by D-α-tocopherol polyethylene glycol 1000 succinate that conserved the dispersion size for up to 3 months. In addition, these NPs had a 20% higher drug release in comparison to those non-milled.

In another work, ITR nanocrystals were produced with a range of stabilisers by an antisolvent sonoprecipitation technique (Badawi et al., 2011). These NPs were manufactured to have sizes between 170±45 and 380±219 nm and the dissolution studies revealed an improvement by a 3.8 – 8.6-fold of the drug dissolved in relation to ITR used as received.

The nanonised API can exhibit different *in vivo* performances depending on its solid-state properties. A study on *in vivo* bioavailability comparing crystalline or amorphous nano- and microparticles of ITR, which were orally administered to rats, showed different pharmacokinetics of the API (Kumar et al., 2014). In this study, the maximum API concentration in the plasma (C_{max}) of subjects administered with the nano-amorphous powder was 366.6 ng/mL, furthermore, the time when the maximum concentration was detected (T_{max}) was 4 hours, while the crystalline NPs had a C_{max} of 244.8 ng/mL and a T_{max} of 8 hours. The difference was attributed to the faster dissolution rate of the amorphous form, as it is the less thermodynamically stable form. In relation to the microcrystalline form, the nano-amorphous NPs had a remarkable, 18-fold higher bioavailability, highlighting the benefits nanonised drugs can achieve.

Nanonised APIs can also be used to achieve objectives other than the dissolution improvement. Indeed, studies on the application of intravenous ITR nanocrystals in healthy subjects showed that the NPs had similar pharmacokinetic profiles to the Sporanox® parenteral formulation (Mouton et al., 2006). Considering that the commercial formulation contains 40% (w/v) hydroxypropyl-beta-cyclodextrin solution, therefore, the nanonisation of APIs could reduce the needs of excipients and their potential side effects. Furthermore, another application of nanonisation is the reduction of ITR side effects. This was demonstrated comparing the negative inotropic effect of the API, as a nanosuspension and Sporanox®, injected in dogs (McKee et al., 2010). The results showed that, while the commercial form had a significant reduction of the myocardial contractility, no alterations were observed for the subjects treated with the NPs.

Several other examples of nanoparticulate delivery systems using ITR can be found in literature, including polymeric NPs, dendrimers, nanolipidic carriers and others (De Smet et al., 2014; Elkin et al., 2015; Ling et al., 2016; Pardeike et al., 2016). Among them, the development of an oral nanoemulsion containing ITR was demonstrated as showing enhanced *in vivo* pharmacokinetics properties in relation to Sporanox® when orally administered to rats (Thakkar et al., 2015). In this work, the nanoemulsion had a 20% higher drug release over 8 hours in comparison to the commercial form. Moreover, *in vitro* analysis of the antifungal activity showed that the nanoemulsion formulation had a higher inhibitory activity than the plain drug suspension.

In another study, polymeric nanocapsules of monomethoxypoly(ethylene glycol)-b-poly(lactic acid) containing ITR were injected in mice and the *in vivo* performance was

compared to the commercial ITR form that is complexed with hydroxypropyl-beta-cyclodextrin (Ling et al., 2016). The antifungal activity was analogous in both formulations however, Sporanox® had a faster initial release achieving a C_{max} after 8 hours, while the NPs had a more constant release during the experiment, achieving a C_{max} after 16 hours. Furthermore, the haemolysis and the vascular stimulation of these formulations indicated that the polymeric nanocapsule was more biocompatible than the commercial form.

Furthermore, an innovative ITR formulation, wherein albumin micro- and nano-particles containing the API and liposomes, a structure named "albusomes", was lyophilised for the production of vaginal tablets (de Jesús Valle et al., 2017). The dissolution studies of this preparation showed that the formulations containing albumin in concentrations lower than 1% (w/v) could completely release the drug in approximately 10 min, therefore, had a great potential for the local treatment of fungal infections locally.

1.3.2. Top-down nanonisation methods

Nanonised drugs are produced by top-down, bottom-up methods or a combination of both approaches. Methods based on the first approach use physical processes to reduce particle size, whereas the second group of techniques is based on precipitation of solubilised molecules (Pawar et al., 2014). The principle of top-down methods is to use mechanical sources, such as mills and high-pressure homogenisation, to apply a force on the particle surface (stress) generating imperfections (cracks) that propagate through the particle causing its fragmentation (Douroumis and Fahr, 2013; Loh et al., 2015). As the milling takes place, the particles can achieve a critical size, wherein instead of causing fragmentation, the energy from shear stress defects the drug crystal by disordering the position of the molecules in its structure. The accumulation of these defects all over the material results in the amorphisation of the substance (Descamps and Willart, 2016). In certain cases, this can be considered advantageous and intentional, because amorphised materials normally have higher apparent solubilities compared to their crystalline form (Hancock and Parks, 2000). On the other hand, amorphous materials are thermodynamically unstable and they crystallise back into a more stable form, consequently, from the pharmaceutical point of view, amorphous materials must be properly stabilised to assure the conservation of their quality from production to its administration to patients (Laitinen et al., 2013).

Furthermore, conventional dry milling exposes the API to potentially degradation conditions due to the heat conversion of the high energy input during this process (Verma et al., 2009). Therefore, for fragmentation of thermolabile drugs, top-down methods, such as cryogenic milling or high-pressure homogenisation, are more suitable (Loh et al., 2015).

The main advantage of top-down approaches is that no solvent addition is required for the process and no residual solvents are left in the processed powder therefore, the

process is considered to be a more environmental-friendly process (Rabinow, 2004; Shah et al., 2016).

The probable main drawback of top-down methods is their limitation to reduce the particle size, although they are able to produce submicron particles (<1 µm) (Van Eerdenbrugh et al., 2008b). Considering the available methods, high-pressure homogenisation has a better potential for size reduction, as it is able reduce the dimensions of mechanically softer crystals down to approximately 200-300 nm (Loh et al., 2015).

1.3.3. Bottom-up nanonisation methods

Methods based on the bottom-up approach use crystallisation from solutions to produce nanocrystals (Müller et al., 2011). For this purpose, the solutions must be supersaturated to induce the crystallisation (Cogoni et al., 2013). Supersaturation is a state wherein the solute concentration (C) in a solution is higher than its solubility (C*) in a determined condition, thus, expressed as (Eqn. 1.3):

$$S \equiv \frac{C}{C^*} \qquad \text{(Eqn. 1.3)}$$

In fact, the crystallisation mechanism occurs in two stages: nucleation, where the crystal nuclei are formed and a posterior growth (Mullin, 2001).

Nucleation can be classified as primary or secondary, and the former takes place when a supersaturated solution forms a nucleus spontaneously (homogeneous) or by external particles, such as a trace of contaminant (heterogeneous), while the latter nucleation type is induced by crystal seeds (Mullin, 2001). Homogeneous nucleation is the primordial concept that nucleation occurs when a group of solutes interact with each other, forming a cluster. The classical theory of nucleation explains that this agglomeration causes changes of free energy (G), which is calculated considering free energy difference on the surface (ΔG_s) and in the volume (ΔG_v), therefore $\Delta G = \Delta G_s + \Delta G_v$ (Mullin, 2001). Considering this formed cluster as a perfect sphere, the first term can be understood as a positive increase of the interfacial tension (γ) on the surface ($4\pi r^2 \gamma$) and the second is negative and calculated as $4/3\pi r^3 \Delta G_v$, therefore, the generation of a cluster of size "r" represents positive free energy. As a stable system requires a free energy difference (ΔG) ≤ 0, the cluster fate is defined by the most energetically favourable path to reduce the ΔG. According to the free energy diagram (Fig. 1.3), a critical particle size (r_c) must be achieved for the nuclei continue to grow, otherwise, it is energetically favourable if the particle segregates back to independent solutes (Mullin, 2001).
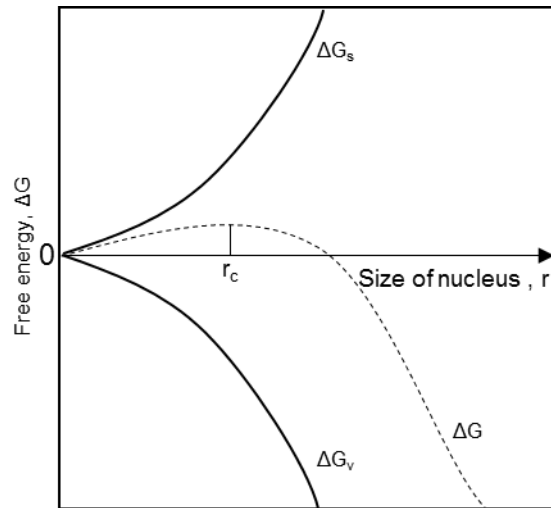
Fig. 1.3: Free energy diagram for nucleation (Mullin, 2001)

A more recent explanation argues that nucleation is a two-steps process, wherein a supersaturated solution present regions with higher solute concentration forming a dense droplet or a dense liquid cluster, which must overcome a non-favourable energetic state, *i.e.* a region with positive ΔG. Immediately after, the conditions are more favourable to the crystal nucleus formation inside this dense liquid (Vekilov, 2010).

The nucleation rate (J) is the number of formed nuclei by a unit of time, which is estimated based on the Arrhenius reaction velocity equation expressed as (Eqn. 1.4):

$$J = A exp[-\frac{16\pi\gamma^3 v^2}{3K^3 T^3 (lnS)^2}]$$ (Eqn. 1.4)

where A is the constant that defines the rate due to frequency of collisions in a correct orientation, γ is the interfacial tension, v is the molecular volume, K is the Boltzmann constant, T is the temperature and S is the degree of supersaturation. Thus, nucleation is driven by the interfacial tension, the temperature and the degree of supersaturation (Mullin, 2001). Thus, a high nucleation rate is induced when a high supersaturation degree is generated, resulting in smaller and monodispersed crystals (D'Addio and Prud'homme, 2011; Mersmann, 1999).

The supersaturation degree can be modified by altering the solute concentration and/or its solubility (Mersmann, 1999). However, several non-linear and inter-dependent factors contribute to the supersaturation (Sinha et al., 2013). A schematic representation of these factors is displayed below (Fig. 1.4).
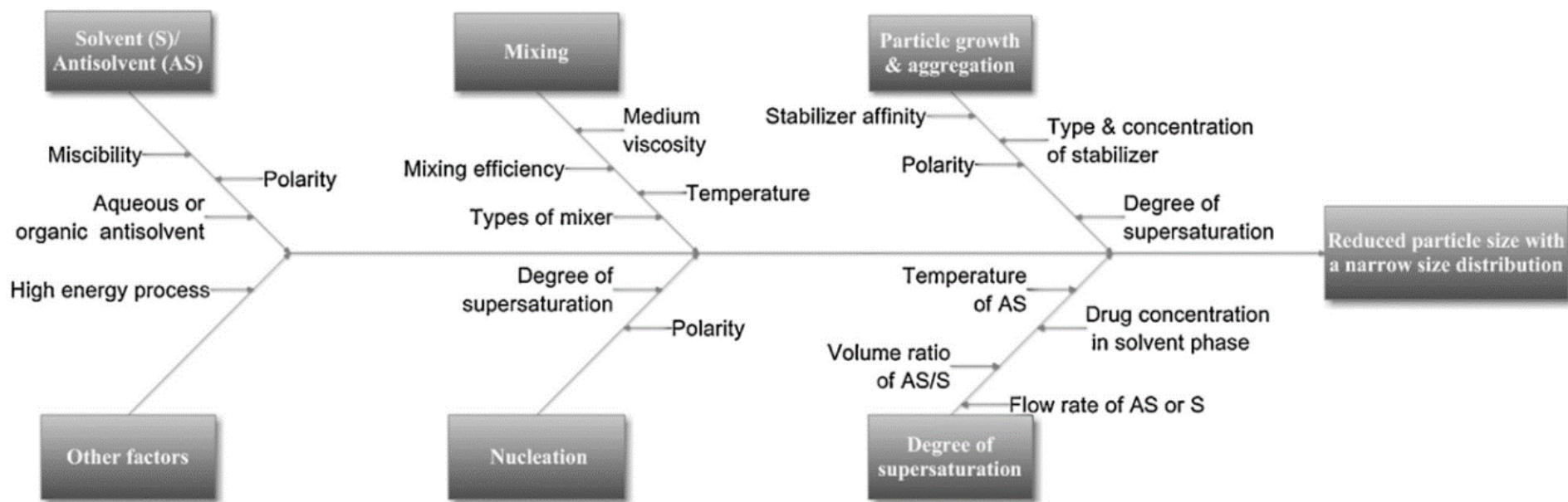
Fig. 1.4: Interdependency of factors impacting on the particle size of API. AS: antisolvent; S: solvent (Sinha et al., 2013).

1.3.3.1. Antisolvent nanoprecipitation

One type of the bottom-up methods to produce nanonised materials is by antisolvent precipitation, which is based, as its fundamental concept, on the abrupt supersaturation increase when a solution containing solute is mixed with a second solvent in which the solute has a lower solubility (antisolvent) (Thorat and Dalvi, 2012). As a result, a high supersaturation degree is generated, inducing a high nucleation rate and, consequently, producing smaller particles (Sinha et al., 2013).

Several factors are involved in this process and their modification can alter the quality of the produced particles (Sinha et al., 2013). Among them, the antisolvent-solvent composition is of a critical importance, as the API solubility in those directly affects the supersaturation, as shown by Eqn. 1.3. Furthermore, the antisolvent-solvent pair must be miscible as when mixed, one solvent can diffuse into the other, spreading the nuclei apart and promoting the formation of monodispersed particles (Matteucci et al., 2006).

Another key factor is the antisolvent-solvent ratio, as their volumes also affect the generated supersaturation degree in the system (Eqn. 1.3). An increase in the antisolvent volume in relation to the solvent phase is expected to increase the supersaturation, resulting in smaller particles. However, this effect is limited to a critical point where the increase in antisolvent volume is unable to change further the particle size (Zhao *et al.*, 2009; Mugheirbi, Paluch and Tajber, 2014).

The process temperature is a factor able to act in a multiple way. At lower temperatures, the solubility of solutes is decreased, and the viscosity is increased resulting in a higher nucleation rate associated with lower particle mobility, which, consequently, reduces potential agglomerations (Sinha et al., 2013). On the other hand, when the solvent and the antisolvent are mixed, high temperatures can be used to rapidly remove a solvent that has a relatively lower boiling point from the system, consequently, increasing the supersaturation degree (D'Addio and Prud'homme, 2011; Mugheirbi et al., 2014).

Drug concentration in the solvent phase is an obvious and important parameter, as its contribution is expressed in the supersaturation equation (Eqn. 1.3). Thus, higher concentrations lead to a higher supersaturation degree. However, this factor also presents an optimum value wherein higher concentrations do not lead to smaller particle sizes (Zhang et al., 2009). This observation was suggested to have two possible reasons: firstly, the elevated number of formed nuclei that increase the system viscosity and consequently reduce the solvent and antisolvent diffusion between them and secondly, the increased viscosity that facilitates collisions of the nuclei, promoting particle aggregation.

Mixing is a determinant parameter to assure homogeneous supersaturation through the system, as such, the successful mixing is achieved when the system is mixed for enough time and intensity, allowing the added phase to be uniformly dispersed, consequently,

obtaining crystals with a monodisperse size (Tung, 2013). At the bench scale, mixing has two levels of interest: the micromixing and mesomixing. The former is the fluid liquid diffusion promoting nucleation at micrometres scale, while the second is related to the millimetric dispersion of feed stream promoting higher supersaturated zones on turbulent eddies, reducing homogeneity of nucleation (Murnane et al., 2008).

Nanocrystal dispersions are often referred to as "nanosuspensions". As such, they are also subject to similar instability issues, mainly caused by Oswald ripening and aggregation (Wang et al., 2013). Ostwald ripening refers to the crystal growth caused by mass displacement from small to bigger particles (Wu et al., 2011). This phenomenon occurs because smaller particles are more soluble (Eqn. 1.2) and have a surrounding layer with higher solute concentration in relation to bigger particles, inducing a diffusion gradient to equilibrate both concentrations. Nevertheless, this causes a local supersaturation around the bigger particles, which are stabilised by the crystal growth (Wu et al., 2011). Therefore, Oswald ripening is a continuous cycle that ends with the complete solubilisation of the smaller particles. Particle aggregation is the association of particles that can result in their coalescence, which is commonly prevented by adsorbing polymeric stabilisers on particle surface in order to increase the electrostatic and/or steric repulsive forces (Wang et al., 2013).

1.3.4. Polyethylene glycol (PEG)

Several stabiliser compounds are available, including polyethylene glycol (PEG) polymers (Fig. 1.5), which are commonly used in drug delivery systems as safe pharmaceutical excipients approved by the FDA (Kolate et al., 2014). Those polymers have ethylene oxide as monomers and the number of these forming units in their polymeric chain will determine the molecular weight. Apart from the chain length, further alterations often are implemented to the PEG molecule leading to different properties. For instance, PEGs can be synthesised as linear or branched (Fig. 1.5), presenting Y shape or being multi-arm (4, 6 or 8 arms). Another example is the functionalisation of the polymer by the addition of groups in the terminal region that could be used in conjugation reactions (Knop et al., 2010).

Pegylation is the term used to designate the covalent conjugation or the adsorption of PEG in a single molecule, such as proteins or low molecular weight drugs, or onto the surface of a larger particle, such as a nanocarrier (Kolate et al., 2014; Rabanel et al., 2014). This alteration of a drug delivery system leads to some interesting advantages, including the prevention of particles aggregation. This effect is possible as the polymeric layer on their surface provides steric hindrance that is responsible for preventing the particles aggregation (Mueller et al., 2011).

Poly(ethylene glycol) (PEG)   Poly(ethylene glycol) methyl ether (MPEG)

Poly(ethylene glycol) dimethyl ether (DMPEG)

4-Arm-poly(ethylene glycol) (4 ARM PEG)
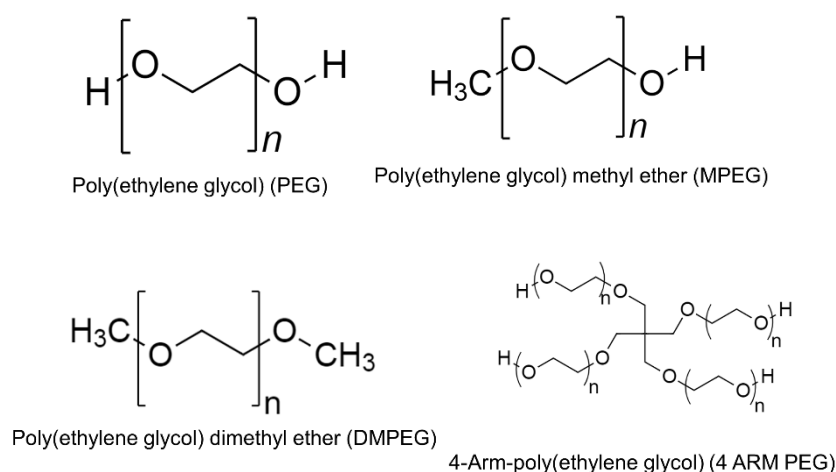
Fig. 1.5: Molecular structures of PEG, MPEG, DMPEG and 4 ARM PEG polymers.

1.4. Cocrystals

A pharmaceutical cocrystal can be defined as a multi-component solid crystal wherein at least one is the active pharmaceutical ingredient (API) and the other(s), the coformer(s) are in a well-defined stoichiometric and bonded by non-covalent interactions (Schultheiss and Newman, 2009; Thakuria et al., 2013). In comparison to a salt, the components of a cocrystal do not become ionised upon the multicomponent system formation, which in some cases is very difficult (Shaikh et al., 2018). Nevertheless, the interactions that form a stable cocrystal are mainly intermolecular hydrogen bonds between functional groups of the API and coformer forming a "supramolecular synthon" (Fig. 1.6). These synthons are classified as homo- or hetero-synthons, depending on the composition of the functional groups involved in the interaction. A homosynthon is composed by an identical group in both molecules (Fig. 1.6a and b), while a heterosynthon is formed by complementary different groups (Fig. 1.6c and d) (Desiraju, 1995). The most frequent H-bond donors in cocrystal synthons are -COOH, -NH and –OH, while the receptors are often carbonyl oxygens and aromatic nitrogens (Gavezzotti et al., 2016). In addition to the H-bond synthons, further weaker interactions including van der Waals forces, π-stacking or halogen bonds can also stabilise the cocrystal (Berry and Steed, 2017).
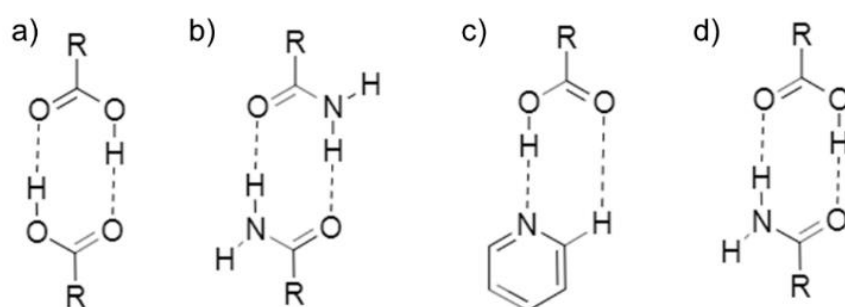
Fig. 1.6: Examples of homosynthons composed by carboxylic acids (a) and amides (b) and heterosynthons formed by a carboxylic acid and an aromatic amine (c) and a carboxylic acid and an amide (d). Adapted from (Desiraju, 1995)

The cocrystallisation of an API normally seeks the improvement of characteristics that influence the bioavailability or the manufacturing of the drug, which will, in turn, be translated to an enhanced formulation (Karimi-Jafari et al., 2018). The improvement in solubility is certainly one of the most common objectives in the development of cocrystals, as it is the limiting factor of absorption of poorly soluble drugs, especially of those of BCS II and IV (Kawabata et al., 2011). The solubilisation of a molecule occurs by its detachment from a solid particle and subsequent solvation in the solvent, therefore, the factors involved in the solubility are the cohesive energy of the molecules in the crystal lattice and the solvation energy, and both factors can be modified by cocrystallisation (Florence and Attwood, 2006). As the presence of coformers in the crystal lattice normally result in the alteration of melting point in relation to the pure API crystalline form, some impact of different interaction forces is present in the crystalline packing of the molecules. However, thermal analysis of multiple cocrystals of an API with different coformers showed that no linear correlation between melting points and their solubility exists (Schultheiss and Newman, 2009). The H-bonds responsible for stabilising the crystalline packing are easily disrupted in aqueous media in relation to hydrophobic interactions, facilitating the interactions between the solvent and the solute (Thakuria et al., 2013). Therefore, solvation of the API and the coformer is more critical for the cocrystal solubilisation in comparison to the cohesive energy of the molecules in the crystal lattice (Babu and Nangia, 2011; Maheshwari et al., 2012).

An example of a molecule, where higher solubility than the API on its own can be achieved by crystallisation is hydrochlorothiazide, a diuretic antihypertensive BCS class IV drug. A 4-fold increase in solubility was achieved when this API was cocrystallised with dimethylaminopyridine (Ranjan et al., 2017). In another case, solubility and the bioavailability of apixaban, an inhibitor of blood coagulation factor Xa, was increased by 2.2 and 2.7 times, respectively, by cocrystallisation with oxalic acid (Chen et al., 2016).

The solubility profile of a cocrystal normally features a peak arising from the quick dissolution of the API followed by a decrease in API concentration to the API crystalline solubility, a behaviour known as "spring" effect (Fig 1.7) (Guzmán et al., 2007). This is due to disruption of the H-bonds in the cocrystal by water and both API and coformer molecules are released from the crystal lattice into the solvent bulk. As coformers are often selected based on their higher solubility in relation to the API, they remain dissolved in the solvent bulk, on the other hand the API become supersaturated and, eventually, it crystallises to its lower energy form (Babu and Nangia, 2011; Bavishi and Borkhataria, 2016; Guzmán et al., 2007). However, this crystallisation can be prevented by stabilisers, extending the supersaturation and causing a "parachute effect" (Fig 1.7), which is used to produce a more sustained concentrations of the solubilised drug (Babu and Nangia, 2011; Guzmán et al., 2007).
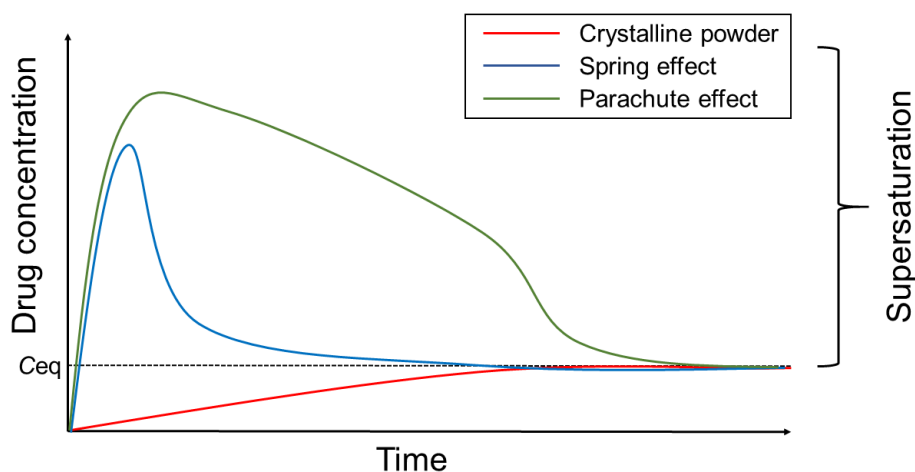
Fig. 1.7: Representation of drug dissolution in a crystalline form, the "spring" and the "parachute" effects. *C*eq is the equilibrium solubility. Adapted from (Bavishi and Borkhataria, 2016).

The development of a cocrystal can also aim at improving the stability of an API. For instance, cocrystallisation of nitrofuran with p-aminobenzoic acid resulted in a form with an improved intrinsic dissolution rate and hydration stability, thus preventing the conversion of the nitrofuran from its stable polymorph into its monohydrated form II, which has a lower dissolution rate (Cherukuvada et al., 2011).

Another example of stability improvement is cocrystallisation of adefovir dipivoxil, a prodrug of the antiviral adefovir, which is very unstable chemically and easily degraded (Gao et al., 2011). In this case, the chemical stability was assessed comparing the API content when the pure form and the cocrystal of adefovir dipivoxil with saccharin were stored at 40 and 60 °C. The results revealed an almost unchanged API content in the cocrystal form at both temperatures, while the pure form was seen to continuously degrade at 40 °C and 71.3% of degradation at 60 °C after 18 days was detected.

Apart from the improvement in the physicochemical properties, another interesting feature of cocrystal development is the possibility of intellectual property protection of the newly identified forms. This is possible because new cocrystals fit in with all the requirements for a patent deposition, i.e. they are new, have non-obvious novelty and have a pharmaceutical application (Trask, 2007). Indeed, this is one reason cocrystallisation has been receiving more attention in the last few years, especially by the pharmaceutical industry, as the number of deposited patent on new cocrystals and cocrystallisation methods has increased around 6-fold in the last decade (Karimi-Jafari et al., 2018).

1.4.1. Cocrystal design

Different approaches are used in the identification of new cocrystals, however, this process should start with a thorough analysis of the API molecular structure to foresee the manners the functional groups could be involved in the cocrystallisation. A valuable source of information at this stage is the Cambridge Structural Database (CSD), a worldwide

database containing a vast number of elucidated crystalline structures, which are used to identify the most common supramolecular synthons of an API (Musumeci et al., 2011). This initial evaluation is important to aid in predicting which coformers have a higher chance to successfully form a stable interaction with the API. Consequently, the experimental work of cocrystal screening could be reduced and focused on those with a higher chance of success (Zhou et al., 2016).

1.4.2. Cocrystallisation Methods

1.4.2.1. Dry grinding

Different cocrystallisation methods are currently used and each one has its own advantages and disadvantages, being more suitable for certain purpose than others. Among them, the cocrystallisation by dry grinding is probably the simplest. This method, also referred as neat grinding, is based on the mechanochemical process, i.e. the application of mechanical energy on the solid API and coformer causing a reduction of their crystal sizes, as in a regular milling process, in addition forcing their intimate contact resulting in the formation of H-bonds (Douroumis et al., 2017). The dry grinding is commonly carried out using a mortar and pestle or ball mills. Besides its simplicity, this method has the main advantage of being free from solvents, consequently, considered as a "green method" (Basavoju et al., 2008).

1.4.2.2. Solvent assisted grinding

The solvent assisted grinding is a slightly more sophisticated cocrystallisation method that employs the addition of small volumes of solvent into the grinding process, which acts as a catalyser improving the synthesis kinetics, consequently reducing the processing time in relation to the dry grinding (Shan et al., 2002). Furthermore, the solvent addition also enables the preparation of cocrystals that cannot be obtained by dry grinding (Childs and Hardcastle, 2007) and to produce different polymorphic forms of the cocrystal depending on the solvent used (Fischer et al., 2014; Trask et al., 2004). Apart from these features, both dry and liquid assisted grindings are similar in relation to their advantages and limitations, for instance, they can produce good purity cocrystals with reduced particle size, however, they are not suitable for a continuous batch production, and not considered the first option for an industrial scale-up (Douroumis et al., 2017).

1.4.2.3. Slurry method

The slurry method is a common procedure for cocrystal screening. In this method, a suspension containing the API and coformer in excess is mixed to induce the cocrystal formation if possible (Zhang et al., 2007). The principle of this method is based on the

balance of solutes and particles in suspension. In a saturated condition, the number of molecules leaving and attaching to a solid particle is in equilibrium (Eqn. 1.5).

$$API_{solid} + Coformer_{solid} \overset{K_{C1}}{\longleftrightarrow} xAPI_{solute} + yCoformer_{solute} \qquad \text{(Eqn. 1.5)}$$
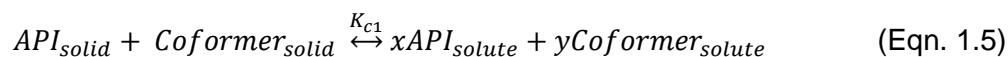
As both solid API and coformers are in excess, a chemical potential is created, which is reduced by the cocrystal nucleation, if the formation of stable synthons is possible. Consequently, a new solid particle is generated, and its formation equilibrium is represented by Eqn. 1.6.

$$nAPI_{solute} + mCoformer_{solute} \overset{K_{C2}}{\longleftrightarrow} Cocrystal_{solide} \qquad \text{(Eqn. 1.6)}$$
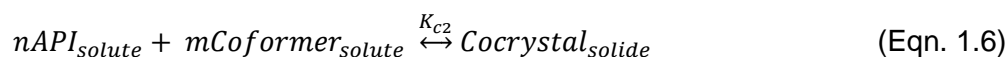
At the initial cocrystallisation, the equilibrium constants, K_{c1} and K_{c2} are shifted to the right, producing more cocrystals, later, the chemical potential is reduced and the equilibrium constants re-established (Zhang et al., 2007).

The slurry method is convenient for screening purposes as no previous knowledge about the API-coformer stoichiometry is required and the procedure has a relatively simple setup with instruments commonly used, therefore, many trial experiments can easily be prepared at once. On the other hand, an extra purification step is normally required after the cocrystallisation by the slurry method, as a mixture of cocrystal and individual components are produced. Another disadvantage is the unpredictable cocrystallisation time, which is dependent on the chemical potential created, therefore, as a higher potential provides a more favourable conditions, then a few hours can be sufficient to produce a significant amount of the cocrystal, while systems with a lower potential can require much longer times (Karimi-Jafari et al., 2018; Malamatari et al., 2017).

1.4.2.4.Slow evaporation

The slow evaporation is a valuable method often used to produce large cocrystal particles, which are preferred for crystalline elucidation by single-crystal analysis (Weyna et al., 2009). In this method, the API and coformer are solubilised in a solvent, which is slowly evaporated, causing supersaturation of the compounds. For a successful cocrystallisation, API and conformer must be in the correct stoichiometry and have similar solubility in the solvent to avoid the crystallisation of isolated compounds. Therefore, phase diagrams (Fig. 1.8) are used to improve the understanding of the cocrystals produced by this method (Miroshnyk et al., 2009). Examples of ternary phase diagrams are shown in Fig. 1.8 when the API and coformer have similar (a) and dissimilar (b) solubilities in the solvent.
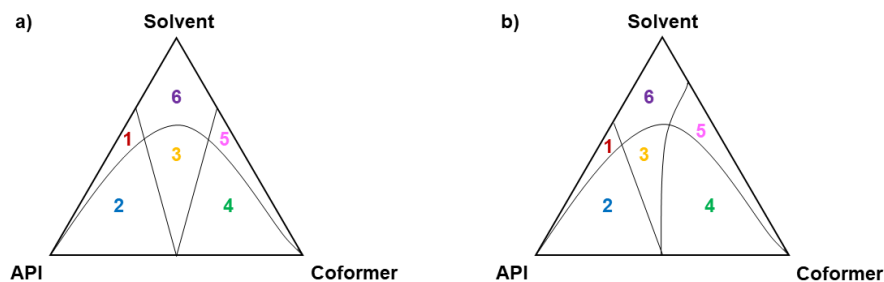
Fig. 1.8: Ternary phase diagram of similar (a) and dissimilar (b) solubilities of API and conformer. The regions are representations of thermodynamic stable species present: (1) API and solvent, (2) API and cocrystal, (3) cocrystal, (4) coformer and cocrystal, (5) coformer and solvent, and (6) solution. Adapted from (Miroshnyk et al., 2009).
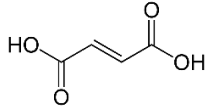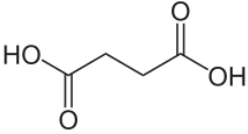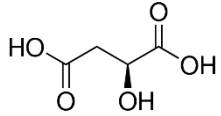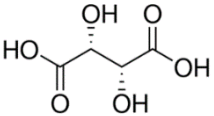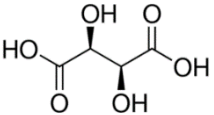
1.4.3. Cocrystallisation of ITR
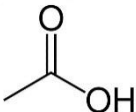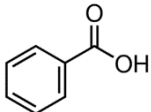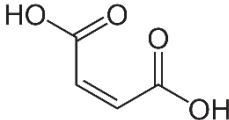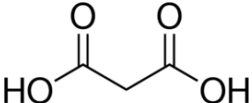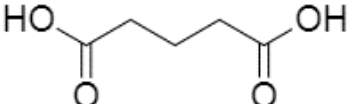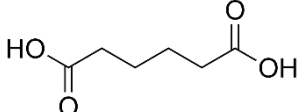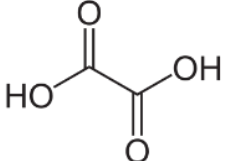
The development of ITR cocrystals was firstly described by Remenar and co-workers (Remenar et al., 2003). In this work, the authors used the API in combination with a number of aliphatic dicarboxylic acids, fumaric acid, succinic acid, L-malic acid, L-tartaric acid, D-tartaric acid and DL-tartaric acid, to form stable cocrystals. Later, others ITR cocrystals were synthesised also using aliphatic dicarboxylic acids (Ober et al., 2013; Ober and Gupta, 2012; Patil et al., 2017; Shevchenko et al., 2013, 2012). A summary of coformers and methods used in attempts to form ITR cocrystals is presented in Table 1.2.
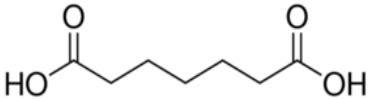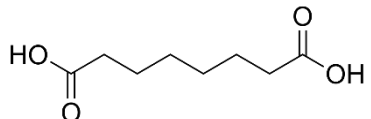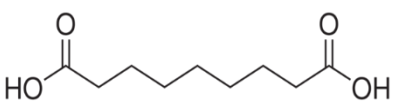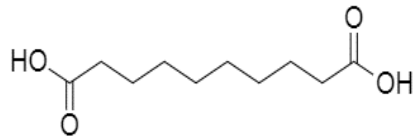
Interestingly, the diversity of the successfully used coformers is limited to linear dicarboxylic acids, with chains made of no longer than 8 carbon atoms (Shevchenko et al., 2013; Weng et al., 2019). These ITR cocrystals have similar structures, where the coformer molecule is fitted in a "pocket" formed by two antiparallel ITR molecules. This arrangement is stabilised mainly by heterosynthons formed by the intermolecular H-bonds on both sides of the acid with the N4 of the 1,2,4-triazole ring of each ITR molecule (Fig. 1.1) (Remenar et al., 2003). In an evaluation of the ITR cocrystal formed with succinic acid, weak halogen bonds C-Cl•••O and C-Cl•••N were also present and able to slightly tilt the 1,2,4-triazole-5-one ring and the *sec*-butyl groups of the ITR molecules (Fig. 1.1) (Nonappa et al., 2013).

As ITR has very poor aqueous solubility, the cocrystallisation has resulted in remarkable improvement in the dissolution profiles of this drug (Remenar et al., 2003). For instance, the dissolution analysis of ITR cocrystals with L-malic and L-tartaric acid in 0.1N HCl revealed profiles comparable to the commercial ITR capsule (Sporanox®, Jassen Pharmaceutica) and a 20-fold higher than the crystalline form. In another example, ITR cocrystal prepared with succinic and malonic acids also had an enhanced intrinsic dissolution rates, around a 11 and 5-fold higher, respectively, than Sporanox® (Shevchenko et al., 2012). In another study, ITR cocrystals were prepared with suberic acid by rapid solvent evaporation and spray drying, resulting in a material able to rapidly dissolve. This cocrystal had a 39-faster intrinsic dissolution rate than the crystalline ITR (Weng et al., 2019).

Table 1.2: Coformers and methods used in attempts to form cocrystals with ITR

Coformer	Molecular structure	Successful	Cocrystallisation method	Stoichiometry	Reference
Fumaric acid		Yes	High throughput crystallisation screen; solvent assisted grinding; solvent evaporation	2-1	(Remenar et al., 2003; Shevchenko et al., 2013)
Succinic acid		Yes	High throughput crystallisation screen; Liquid antisolvent; Solvent assisted grinding; Solvent evaporation	2-1	(Ober and Gupta, 2012; Remenar et al., 2003; Shevchenko et al., 2013)
L-Malic acid		Yes	High throughput crystallisation screen; gas antisolvent crystallization	2-1	(Remenar et al., 2003) (Ober et al., 2013)
L-Tartaric acid		Yes	High throughput crystallisation screen	2-1	(Remenar et al., 2003)
D-Tartaric acid		Yes	High throughput crystallisation screen	2-1	(Remenar et al., 2003)
DL-Tartaric acid		Yes	High throughput crystallisation screen	2-1	(Remenar et al., 2003)

Coformer	Structure	Cocrystal formed	Method	Stoichiometry	Reference
Acetic acid		No	High throughput crystallisation screen	N/A	(Remenar et al., 2003)
Benzoic acid		No	High throughput crystallisation screen	N/A	(Remenar et al., 2003)
Maleic acid		No	High throughput crystallisation screen; Solvent assisted grinding; Solvent evaporation	N/A	(Remenar et al., 2003; Shevchenko et al., 2013)
Malonic acid		No (Remenar et al., 2003)] Yes (Shevchenko et al., 2013, 2012)	High throughput crystallisation screen; Solvent assisted milling; Solvent assisted grinding; Solvent evaporation	2:1	(Remenar et al., 2003; Shevchenko et al., 2013, 2012)
Glutaric acid		No (Remenar et al., 2003)] Yes (Shevchenko et al., 2013)	High throughput crystallisation screen; Solvent assisted grinding; Solvent evaporation	1:2	(Remenar et al., 2003; Shevchenko et al., 2013)
Adipic acid		No (Remenar et al., 2003)] Yes (Shevchenko et al., 2013) (*)	High throughput crystallisation screen; Solvent assisted grinding; Solvent evaporation	1:1:1.3 ([a])	(Remenar et al., 2003; Shevchenko et al., 2013)
Oxalic acid		Yes (**)	Solvent assisted grinding; Solvent evaporation	1:1:0.5 ([b]) 1:1:1 ([c])	(Shevchenko et al., 2013)

Pimelic acid		Yes	Solvent assisted grinding; Solvent evaporation	N/A	(Shevchenko et al., 2013)
Suberic acid		Yes	Solvent evaporation	1:1	(Weng et al., 2019)
Azelaic acid		No	Solvent assisted grinding; Solvent evaporation	N/A	(Shevchenko et al., 2013)
Sebacic acid		No	Solvent assisted grinding; Solvent evaporation	N/A	(Shevchenko et al., 2013)

(*) cocrystal hydrate; (**) cocrystal solvate; ([a]) ITR-adipic acid-H_2O; ([b]) ITR-oxalic acid-acetone; ([c]) ITR-oxalic acid-tetrahydrofuran.

1.5.Pulmonary formulation

The main purpose of the respiratory tract is to provide oxygen to the organism, which is achieved by the constant in- and ex-halation. During the inhalation, the lungs are filled with air rich in oxygen, which is exchanged by carbon dioxide from the blood due to concentration difference of those through the alveolar epithelium, a high vascularisation and extensive surface area of about 160 m^2 (Deli, 2009). As this barrier is also permeable for drugs, especially for lipophilic non-ionised molecules, it has been extensively explored as an alternative administration route, either for systemic or for topical treatments (Loira-Pastoriza et al., 2014).

The use of pulmonary formulations for topical treatment allows the direction of a drug straight to its target, avoiding its distribution to other tissues and organs, consequently reducing undesired side effects. In relation to oral formulations, the pulmonary route also prevents the hepatic first-pass metabolism of drugs, thus, lower doses can be administered to achieve the therapeutic concentration (Newman, 2018). Another advantage of the pulmonary formulation is the possibility to avoid drug injections, like insulin, improving the life quality of patients (Patton, 2005).

The drawbacks of pulmonary formulations are related to their administration, as those formulations require a specialised medical device, such as dry powder or aerosol inhalers and nebulisers, which may be difficult for some patients to handle, resulting in lower doses inhaled and an inefficient treatment (Newman, 2014).

The fate of inhaled particles is dependent on their size (Fig. 1.8). Particles larger than 5 μm are deposited by inertial impaction in upper airways, including mouth and oropharynx, and possibly swallowed. In this case, the particles are very large and unable to pass through the airways without hitting their walls. The probability of this relation is described by Stokes's number, *Stk*, according to equation 1.7:

$$Stk = \frac{\rho_p \, . \, d^2 \, . V}{18 \, . \, \eta \, . \, R} \qquad\qquad \text{Eqn. 1.7}$$

Where ρ_p is the particle density, the d is the particle diameter, V is the air velocity, η is the air viscosity and R is the airway radius. Therefore, the higher the Stoke's number, the more of the particles are subject to inertial impaction (Carvalho et al., 2011).

Particles with a diameter in the range from 1-5 μm can reach the central and distal tracts (Fig. 1.9), as they are subject to gravity force aiding their sedimentation in the deeper regions of the lungs. Particles in the size range from 0.1 – 1 μm are less subject to inertial impaction, consequently, these particles are easily exhaled (Kaur et al., 2012). Nevertheless,

particles smaller than 0.1 µm can reach the alveolar region by concentration diffusion and Brownian motion of these NPs in the lung surfactant (Andrade et al., 2013; Loira-Pastoriza et al., 2014; Paranjpe and Müller-Goymann, 2014).
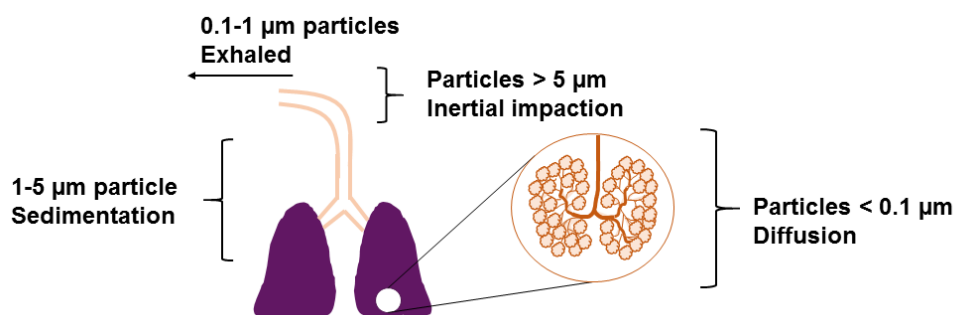
Fig. 1.9: Representation of the deposition places of inhaled particles according to their size.

The pulmonary application of ITR is interesting as the drug has the potential to act locally in invasive fungal infections in the lungs, thus, reducing the exposition of patients to side effects of oral treatments (Hoeben et al., 2006). Currently, no commercial pulmonary formulation of this drug is available on the market nevertheless, some works have already demonstrated the potential for this (Duret et al., 2012; Hoeben et al., 2006; Huang et al., 2018; Merlos et al., 2017; Pardeike et al., 2011). For instance, the development of a nanostructured lipid carrier containing ITR showed a great potential for a fast release formulation, as the NPs could release 80% of the API in 5 min when aerosolised by ultrasonic nebulisation (Pardeike et al., 2011). On the other hand, for a local action of the drug in the lungs, the formulation must be able to increase its residence time in that organ (Loira-Pastoriza et al., 2014). This was observed by Huang and co-workers (Huang et al., 2018) who correlated the *in vitro* dissolution profile of ITR dry powders inhaler formulations and the drug *in vivo* distribution. In this work, the authors found that the formulation with faster dissolution also had higher plasma absorption, which is undesired for local action, therefore, for this purpose, the formulations must have a longer residence time.

1.6. Mucus layer

Mucus is a viscous-elastic complex layer covering the epithelial cells from the mouth to anus, respiratory and female reproductive tracts and eyes. Its composition and physical characteristics are different according to its organ of origin and the presence of any pathological condition. In healthy conditions, the mucus is predominantly composed by water (95% w/w) and a complex mixture of salts, lipids and proteins (Bansil and Turner, 2006; Svensson and Arnebrant, 2010). Regardless of its origin, the mucus layer is responsible for the maintenance of lubrication and moisture, it also acts as a physical barrier against

pathogens and potential noxious particles. This defensive function is assured by the presence of proteins, such as lysozymes and immunoglobulins, in addition to its viscous and elastic nature provided by the mucins, a very polydisperse group of glycoproteins. Their molecular weight range from 0.5 to 20 MDa wherein, approximately 80% are carbohydrates, such as N-acetylgalactosamine, N-acetylglucosamine, fucose, galactose, and sialic acid that provide their anionic nature (Svensson and Arnebrant, 2010). The protein core provides the hydrophobic regions to the mucin due to a high proportion (>10%) of cysteine residues able to form intern disulphide bonds resulting in hydrophobic globules, also described as "cystine knots" (Bansil and Turner, 2006; Khutoryanskiy, 2014). In physiological conditions, the mucus is a porous gel formed by the entanglement and hydration of mucin fibres, allowing it to retain particles larger than its porous mesh size (Cone, 2009). The combination of its morphology and the mucin composition turns the mucus an effective physical barrier able to filter particles by charge and by size exclusion preventing them to reach the epithelium (Lieleg and Ribbeck, 2011).

1.7. Mucoadhesion

The mucoadhesion is the attachment of particles to the mucus layer, which can be used in drug delivery systems to improve the absorption of APIs (Peppas and Huang, 2004). For nanoparticulate drug delivery systems, the explanation of the contact stage of NP can be based on the DLVO theory of colloid stability that was described by Derjaguin and Landau and later by Vervew and Overbeek. This theory advocate that particles in suspension are at the same time under attractive forces and repulsive forces. In this case, the attractive forces between the mucus layer and NPs are van der Waals interactions, surface energy effects and electrostatic attraction if both have opposite charges. The repulsive forces result from the overlapping of electrical double layers and electrostatic repulsion if both have same charges. When the attractive forces are greater than the repulsive forces, the particle moves towards the mucus establishing a contact that is intensified by the strength of their interaction (Khutoryanskiy, 2014; Mansuri et al., 2016).

The exact mechanism of mucoadhesion is a result of the combination of multiple theories, including "wettability", "adsorption", "electronic", "fracture", "diffusion interlocking" and "mechanical" theories (Smart, 2005).

1.7.1. Wettability theory

When a particle is in contact with the mucus (Fig. 1.10), the propensity of the later to spread and eventually cover the particle surface is driven by the resulting interfacial tension (γ). When the surfaces have a low affinity, the γ is high, therefore the formed angle between the mucus layer and the tangent of particle in contact with the mucus, i.e. contact angle (Θ), is high (Florence and Attwood, 2006).
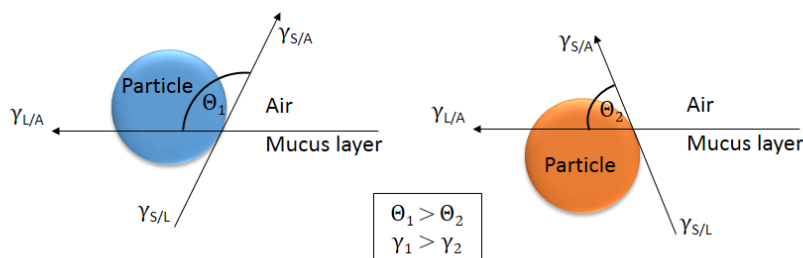
Fig. 1.10: Representation of the wettability of two different particles on the mucus layer. The blue particle has a low affinity with the mucus; therefore, it a higher contact angle is formed (Θ_1). The orange particle has a lower angle (Θ_2), representing the higher affinity of this particle to the mucus layer. Adapted from (Florence and Attwood, 2006)

1.7.2. Adsorption theory

The interaction of surfaces, i.e. drug delivery system and mucus layer, are sustained by intermolecular interactions, such as hydrogen bond, dipole-dipole and van der Waals forces (Peppas and Sahlin, 1996).

1.7.3. Electronic theory

As the mucin presenting negative charges, positively charged particles are trapped in the mucus due to the transfer of electrons that forms a double layer of electrical charges at the interface (Khutoryanskiy, 2014; Peppas and Sahlin, 1996).

1.7.4. Fracture theory

This theory correlates the force required to de-attach a particle from the mucus layer to the multiple forces involved in the adhesion of the same particle and is expressed as:

$$\alpha = \sqrt{E \times {}^{\varepsilon}\!/_{L}} \qquad\qquad \text{(Eqn 1.8)}$$

Where α is the fracture strength, E is the elasticity, ε is the fracture energy and L is the critical crack length (Mansuri et al., 2016).

1.7.5. Diffusion interlocking theory

This approach is valuable for penetrative particles as it is focused on the diffusion of such particles along with the mucin layer that is affected by the concentration gradient (Ponchel et al., 1987).

1.7.6. Mechanical theory

As the mucus has viscoelastic properties, it is able to occupy the irregularities of rough surfaces increasing the interfacial area (Sosnik et al., 2014).

1.7.7. Mucoadhesive properties of drug delivery systems

The concept of "mucoadhesive NPs" has been developed to improve their anchor ability, in order to prolong the contact time of these particles with the mucous layer where higher concentration of the drug could be released and, consequently, absorbed (Sigurdsson et al., 2013). However, this strategy has drawbacks that can lead to the opposite result than the desired. Mucus layers are constantly renewed to assure their protective functions and therefore, anchored NPs could be subject to removal before drug release occurs (Netsomboon and Bernkop-Schnürch, 2016). Therefore, another strategy has been recently considered and instead of attaching NPs to the mucus layer, an effective transport through the layer to the site of absorption is facilitated. Such NPs are referred to as "mucopenetrative NPs" (Wang et al., 2008). An additional advantage of the mucopenetrative NPs is their ability to spread more evenly along the epithelial surface when compared to mucoadhesive NPs (Maisel et al., 2015)

The diffusion of a NP in mucus is mainly defined by its particle size and interactions. The mucus layer has a different arrangement to prevent particles larger than their mesh size to cross this barrier depending on the organ of origin. Additionally, the mucus layer has a negative charge provided by the presence of sialic acid and sulfonic acid, allowing neutral or slightly negative charged particles to diffuse easier than positively or strongly negatively charged particles (Bansil and Turner, 2006; Lieleg and Ribbeck, 2011; Netsomboon and Bernkop-Schnürch, 2016).

PEG polymers have been used to prepare mucoadhesive hydrogels and NPs (Lele and Hoffman, 2000; Partenhauser and Bernkop-Schnürch, 2016; Serra et al., 2009; Wang et al., 2008; Yoncheva et al., 2005). In recent years, the usage of PEGs in nanoparticulate drug delivery systems has focused on turning the formulations to be more penetrative in the mucus layer in order to rapidly reach the epithelium and, consequently, increase absorption (Ensign et al., 2013; Huckaby and Lai, 2018; Lai et al., 2007). For this application, the PEGylation must, firstly, be able to neutralise the particle surface potential to avoid electric attraction to the mucus layer (Bogataj et al., 2003). Secondly, the polymers must have a appropriate molecular weight (Mw). Polymer chains with a high Mw ($\geq$40 kDa) have a greater potential to strongly interact with the mucin fibres and polymers with a low Mw would be unable to neutralise the surface potential effectively (Dünnhaupt et al., 2015; Maisel et al., 2016). Finally, the polymers should be densely grafted on the particle surface to enable mucopenetrative characteristics (Yang et al., 2014). This is important because there is a correlation between the polymer conformation and its density based on the ratio R_F/D, where R_F is the Flory radius and D is the mean distance between the grafted polymer chains. Therefore, a lower the distance D implies that a higher polymer density needs to be used and vice-versa. The Flory radius is the radius of a polymer conformation, which is affected by the polymer density, as

the conformation is dependent of the volume the polymeric chain can occupy on the particle surface (Huckaby and Lai, 2018). Therefore, when the PEG layer coverage has a low density (R_F/D<1) the polymer chains remain in their natural globular form, also referred to as "mushroom" conformation. Increasing the coverage density will stretch their chains into a "brush" (R_F/D>1) or a "dense brush" (R_F/D>2) conformation (Rabanel et al., 2014; Yang et al., 2014).

The investigation of particle behaviour in relation to the mucus is valuable for the development of drug delivery systems in order to predict their pharmacokinetics *in vivo.* This investigation can be carried out using a range of techniques, including *in vivo* and *in vitro* methods, allowing to evaluate the different aspects of interactions with mucus (Bassi da Silva et al., 2017; das Neves et al., 2011; Grießinger et al., 2015). Mucoadhesive properties are the most investigated feature, where interactions of particles with a mucus layer or mucin are identified and quantified. Many methods are available for this, such as quartz crystal microbalance with dissipation (QCM-D), dynamic light scattering (DLS) and microscopy to name a few (Oh et al., 2015; Suk et al., 2016). The analysis of the diffusion and permeability of particles through the mucus layer is also very valuable. These can be assessed by particle tracking analysis, Transwell diffusion system and others (Grießinger et al., 2015; Newby et al., 2018).

1.8. Quartz Crystal Microbalance with Dissipation (QCM-D)

The QCM-D instrument consists of an electronic unit connected to an enclosed chamber platform housing four temperature and flow-controlled modules arranged in a parallel configuration. The principle of analysis is based on the resonance frequency of a quartz crystal induced by applying an alternating electric field across the crystal. The device measures two parameters simultaneously and at real-time: frequency of vibration of the crystal (*f*) and energy dissipation (*D*). An increase in mass bound to the quartz surface decreases the oscillation frequency of the crystal (negative *f* shift). If the layer deposited on the sensor surface is thin and rigid, its mass is proportional to the decrease in f (Sauerbrey, 1959). However, if the layer attached to the sensor is thick and soft, measurements based on changes in *f* may result in underestimation of the deposited mass. In those situations, the analysis of the dissipation factor, related to the viscoelastic properties of the adsorbed layer, is crucial as it plays an important role to accurately calculate the mass (Rodahl and Kasemo, 1995).

1.9. Project Aims

ITR is an API of the BCS class II, therefore, its absorption and bioavailability are limited by its poor aqueous solubility. A modification of the solid-state properties of APIs can result in an improved biopharmaceutical performance of such drugs. Therefore, the overall objective of this research was to develop new forms of ITR, by manipulating the micromeritic and/or solid-state properties, introducing new characteristics that could be more favourable for a pharmaceutical application.

Chapter 2 presents a continuation of the work developed by Mugheirbi and co-workers on the development of the heat induced evaporative antisolvent precipitation (HIEAN) method to produce ITR NPs (Mugheirbi et al., 2014). In summary, this process consists of injecting a solution of ITR in acetone, at 50 °C, into water, at 80 °C. However, the main disadvantage of using the solution of ITR at this temperature is the solvent evaporation and potential seeds formation, which could result in precipitation of large particles (>1 µm). Therefore, these studies aimed to modify the HIEAN method, firstly by investigating the influences of the process parameters on the physical-chemical properties of the produced ITR particles; and secondly, by evaluating further modifications on the method setup to produce the ITR particles in a nanometric size range.

In recent years, mucopenetrative particles have been studied, especially for the oral route of administration, due to their enhanced bioavailability (Chen et al., 2013). To date, investigations of mucoadhesive properties of nanonised ITR were not conducted. Furthermore, as surface modifications of nanonised particles being limited to non-covalent bonding (Laitinen et al., 2013), the initial purpose in Chapter 3 was to identify polymers that could interact with the ITR NPs. It was also aimed to investigate the impact that PEGylation had on the solid-state and nanometric properties of the systems. Ultimately, this investigation also had as objective to determine whether the non-modified and modified ITR NPs had mucopenetrative or mucoadhesive potential.

A few references were available regarding ITR cocrystals presenting that the successful coformers for ITR cocrystallisation were limited to aliphatic dicarboxylic acids (Shevchenko et al., 2013). Furthermore, no information was available in the literature regarding ionic cocrystals of ITR. Therefore, Chapter 4 aimed to identify new cocrystals and ionic cocrystals of ITR combining this API with a wide and diverse range of coformers not limited to dicarboxylic acids. Further investigation had as a purpose to ascertain the relevant molecular elements in coformers that enable the formation of new cocrystal phases of ITR. Ultimately, it was also aimed in this Chapter to evaluate the impact of cocrystallisation in solubility and dissolution profiles.

Chapter 5 focused on the development of NPs of the ITR cocrystal with therephthalic acid (TER) (ITR-TER). The research about nanoparticulate cocrystals (NCC) is scarce, although NCCs have the potential to improve the dissolution rates of poorly soluble drugs due to the coformer presence also due to the reduced particle size. Primarily, in Chapter 5, it was aimed to develop a bottom-up method to prepare ITR-TER NCCs. The second objective was to produce Trojan particles containing the NCC embedded into microparticles by spray drying and to assess the solid-state and aerodynamic properties of the dried powders regarding their potential for pulmonary administration.

Chapter II: Optimisation and modification of the itraconazole nanoprecipitation method

2.1.Introduction

In the pharmaceutical area, nanoparticles (NPs) are a valuable approach to improve characteristics of drugs, including their physicochemical and pharmacokinetic properties, consequently also enhancing their bioavailability. Ultimately, this could represent a significant improvement in the behaviour of patients, increasing their compliance to treatments (Moghimi et al., 2001; Onoue et al., 2014; Parveen et al., 2012).

Diversified nanoparticulate drug delivery systems are currently used for pharmaceutical purpose, among them, nanonised drugs are notably interesting. This form relies on the reduction of the particle size of APIs to modify their properties, therefore, they are composed mostly by the drug itself, reducing the exposition of patients to a large number of excipients and their potential adverse effects (Gao et al., 2012; Rabinow, 2004).

Nanonised drugs are produced normally by top-down or bottom-up approaches, where the first use physical processes, such as mills and high-pressure homogenization to reduce the size of particles, whereas the second is based on the precipitation of solubilised molecules to form solid particles (Pawar et al., 2014). Although top-down approaches have interesting advantages, especially as they do not require solvents (Verma et al., 2009), the particle reduction by milling is limited, even in a prolonged process (Loh et al., 2015). This limitation is associated with the mechanical transfer of energy to the particles, as after reaching a critical size, results in developing defects on particle surfaces as opposed to causing fractures. The accumulation of these defects results in the amorphisation of the material (Loh et al., 2015). Alternatively, the bottom-up approach is potentially able to produce smaller particles than top-down methods (Van Eerdenbrugh et al., 2008).

One bottom-up technique, known as nanoprecipitation, uses rapid precipitation in antisolvent to produce nanoparticles. This method is based on the generation of a supersaturation when a solubilised drug is subject to a fast transition to another solvent, in which it has a lower solubility (Nagy et al., 2008). The supersaturation has a critical role in this process because it affects the nucleation rate (J) as demonstrated by the equation:

$$J = Aexp[-\frac{16\pi\gamma^3 v^2}{3K^3 T^3 (lnS)^2}] \qquad \text{(Eqn. 1.4)}$$

where A is the constant that defines the rate due to the frequency of collisions in a correct orientation, γ is the interfacial tension, v is the molecular volume, K is the Boltzmann constant, T is the temperature and S is the degree of supersaturation (Mullin, 2001). As a higher nucleation rate normally leads to smaller particles, the conditions for nanoprecipitation must generate high supersaturation degree to produce particles with nanometric sizes. Therefore, the supersaturation degree can be increased by increasing the concentration of solute in a solution (*c*) or by decreasing the solubility of substance in

the solvent (c^*), as the supersaturation is a ratio of these parameters (Eqn. 1.3) (D'Addio and Prud'homme, 2011):

$$S \equiv \frac{c}{c^*} \qquad \text{(Eqn. 1.3)}$$

The heat induced evaporative antisolvent precipitation (HIEAN) method was a process developed by Mugheirbi et al. (2014) to produce disordered NPs of itraconazole (ITR) (Mugheirbi et al., 2014). Briefly, this process consists of injecting a solution of ITR in acetone into water at 80 °C. Consequently, the drug supersaturation is generated as ITR has a relatively higher solubility (6.4 mg/mL) in the organic phase, while the aqueous solubility is much lower (1 μg/mL) (Hardin et al., 1988; Mugheirbi et al., 2014). In addition, the process is intensified by the temperature of the antisolvent, as the heat increases the evaporation rate of acetone reducing the solubility of the drug in the system. However, in the original set up of this process (Mugheirbi et al., 2014), the ITR solution was heated to 50 °C, which is close to the evaporation point of acetone (56 °C). Thus, a volume of the solvent might be lost at this temperature prior to the addition to the antisolvent phase, consequently, forming seeds and heterogeneous nucleation might occur with these new nuclei forming upon contact with the particles already present in the solvent phase resulting in large particles, out of the nanometric scope (Vekilov, 2010). Therefore, the aim of this chapter was to modify the HIEAN method in order to improve its success rate, at the same time the characteristics of the ITR particles are conserved in relation to the original set up. For this purpose, the solvent phase was kept at room temperature (25 °C), in place of the heating, in order to minimise the seeds formation. As this modification directly affects the supersaturation degree (Sinha et al., 2013), the parameters potentially able to influence the particle size were evaluated whether they were able to counter-balance the supersaturation degree. Then, an additional solvent evaporation step was investigated if further removal of the residual acetone could improve the stability of particles in the liquid dispersion and to determine its the optimum conditions (Mugheirbi and Tajber, 2015). Finally, the new method set up was optimised to establish the ideal conditions of production of monodispersed particles of ITR with reduced sizes.

2.2.Materials and Methods

2.2.1.Materials

Itraconazole was purchased from Glentham Life Sciences Ltd. (Wiltshire, UK). Acetone Chromasolv® (HPLC grade) was purchased from Sigma-Aldrich (Arklow, Ireland).

2.2.2.Methods

2.2.2.1.Production of ITR NPs

ITR NPs were produced by the modified method of heat induced evaporative antisolvent nanoprecipitation (HIEAN) (Mugheirbi et al., 2014). Initially, a 2 mg/mL ITR solution (solvent phase) was prepared by dissolving 20 mg of the API in 10 mL of acetone. Then, an aliquot of this solution at 25 °C was rapidly injected using a 0.5 mm x 16 mm Sterican® needle into 20 mL of deionised water (Elix®, Merck Millipore, Ireland) (antisolvent phase) kept at different temperatures as described in Tables 2.1 and 2.3 and under a constant magnetic agitation at 1,300 rpm using a hot plate SD-162 (Stuart, UK). Finally, the dispersion was transferred immediately to a jacketed cylinder at 4 °C and then cooled until room temperature under constant mixing at 1,300 rpm.

2.2.2.2.Screening of process variables

The ITR dispersions were prepared as described in Section 2.2.2.1, using the antisolvent temperature and the antisolvent:solvent (AS:S) ratio (v/v) as described in Table 2.1. The following process parameters: antisolvent temperature and the AS:S ratio were selected as factors for a full factorial experimental design in 2 levels. The factorial combination of these conditions resulted in seven experiments, including three repetitions at the central point (Table 2.1). The response measured was the mean particle size and statistical analysis was performed by electronic spreadsheet FATPC 11, provided by Unicamp (Universidade de Campinas, Brazil) (Teófilo and Ferreira, 2006).

Table 2.1: Selected factors and levels used for parameter screening of nanoprecipitation method.

Parameter	Level		
	(-1)	(0)	(+1)
Antisolvent temperature (°C)	40	50	60
AS:S ratio (v/v)	10:1	10:1.5	10:2

The effect (ef) of the factors and their interaction was calculated as the difference between the averages of the individual observation (y_i) in the higher level $(y_{i(+)})$ in relation to the lower level $(y_{i(-)})$, as demonstrated in the Eqn 2.3 (Teófilo and Ferreira, 2006):

$$ef = \frac{\sum_{i=1}^{n/2} y_{i(+)} - \sum_{i=1}^{n/2} y_{i(-)}}{n/2} \qquad \text{(Eqn 2.3)}$$

The effects were statistically evaluated using t-test with 95% of confidence, accordingly, they were considered significant when $|t_{calc}| \geq t_{\alpha}$. The error of the analysis was calculated as the variance observed in the triplicates in the central point, Runs V-VII.

2.2.2.3.Removal of solvent from NP dispersion by evaporation under reduced pressure

For this purpose, ITR dispersions were prepared as described in Section 2.2.2.1, using the antisolvent phase at 80 °C, 2 mL of the solvent phase and the AS:S ratio of 10:1. Then, the samples were transferred to 100 mL round bottom flasks and subjected to evaporation in a Rotavapor R-205 attached to a vacuum pump V-700 (Büchi, Switzerland). The flasks were maintained at 30 °C in a heating bath B-490 (Büchi, Switzerland). Different pressures and times (Table 2.2) were used to evaluate the efficiency of this process. The samples were analysed in triplicate.

Table 2.2: Time and pressure used to evaluate the evaporation step

Time (min)	Pressure (mbar)
20	90
30	90
30	50
40	50

2.2.2.4.Optimisation of the modified HIEAN method

The ITR dispersions were prepared as described in Section 2.2.2.1, using the antisolvent temperature and the AS:S ratio as described in Table 2.3. Then, the samples were evaporated as described in Section 2.2.2.3 for 30 min and under a reduced pressure of 60 mbar. This optimization was carried out in triplicate.

Table 2.3: Conditions used in the optimisation of HIEAN method.

Sample	Antisolvent temperature (°C)	AS:S ratio (v/v)
#1	60	10:0.5
#2	60	10:1
#3	70	10:1
#4	80	10:0.5
#5	80	10:1

AS: antisolvent phase; S: solvent phase

2.2.2.5.Isolation of NPs

ITR dispersions were transferred to 50 mL plastic centrifuge tubes (CellStar®, Greiner Bio-one, Austria) and centrifuged at 12,000 rpm at 4 °C for 30 min using an Eppendorf 5810R centrifuge (Hamburg, Germany). The supernatant was discarded, the pellets dried and kept at 25 °C.

2.2.2.6.Particle size and polydispersity index analysis of NPs

The mean hydrodynamic particle diameter based on intensity distribution and polydispersity index (PdI) were determined by dynamic light scattering (DLS) at 25 °C using a 173° scattering angle in a Zetasizer Nano series Nano-ZS ZEN3600 fitted with a red laser light beam (λ = 633 nm) (Malvern Instruments Ltd., UK). An aliquot of 0.4 mL of the sample was placed into a clear disposable plastic cuvette (ZEN0040). The equilibration time was set to 2 min at 25 °C. Measurements for each sample/batch were taken in triplicate. Results were corrected for dynamic viscosity of the continuous phase measured using a Vibro Viscometer SV-10 (A&D Ltd., Japan). This analysis was done for every preparation of nanoparticles.

2.2.2.7.Differential scanning calorimetry (DSC)

Thermal analysis was performed by carefully weighting dried samples and placing them in 40 µL aluminium pans that were sealed with a lid and pierced with three holes for ventilation. The samples were subjected to DSC runs in the temperature range from 25 to 200 °C with a heating rate of 10 °C/min using a Mettler Toledo DSC 821e (Greifensee, Switzerland) under nitrogen purge (flow rate of 20 mL/min) (Paluch et al., 2010). An empty aluminium pan was used as a reference. The DSC was calibrated with an indium standard.

2.2.2.8.Powder X-ray diffraction (PXRD)

Powder X-ray diffraction was performed using a Rigaku Miniflex II, desktop X-ray diffractometer (Japan) equipped with a Cu Kα radiation X-ray source. Dried samples were mounted on a low-background silicon sample holder and scanned over a 2θ range of 2-40 degrees at a step scan rate of 0.05° per second (Paluch et al., 2010).

2.2.2.9.Stability analysis

The stability analysis was aimed to compare samples prepared with and without an additional evaporation step. For this purpose, ITR dispersions were prepared as described in Section 2.2.2.1, using the antisolvent phase at 70 °C and 2 mL of solvent phase. Then, one group of the samples was evaporated for 40 min at 50 mbar in a Rotavapor R-205 attached to a vacuum pump V-700 and maintaining the flasks at 30 °C in a heating bath B-490. An aliquot of 10 mL of each preparation was transferred to a 50 mL plastic centrifuge

tube that was stored at 25 and 4 °C. The particle size was measured by DLS as described in Section 2.2.2.6 at 0, 24, 48, 72 and 96 hours.

2.2.2.10.Statistical analysis

Statistical analysis of the data was carried out using GraphPad Prism® for Windows, version 5.01, applying Student's t-test or one-way ANOVA with Tukey's post-test with 95 % of confidence when appropriate. Statistical significance was considered when $p < 0.05$.

2.3. Results and Discussion

2.2.3.Screening of process variables

This first step aimed at evaluating how the antisolvent temperature and the AS:S ratio may have impacted the size of the particles produced by HIEAN when the solvent phase is at room temperature. For this purpose, a variable screening was performed by a factorial design in two levels (Table 2.4). The antisolvent temperature factor was selected because it could affect the supersaturation, as at a lower temperature, the API equilibrium solubility is reduced (Sinha et al., 2013). Accordingly, the evaluated temperature range of the solvent phase (40-60 °C) aimed to compare, in relation to the original method (80 °C), the significance of this effect on the process. Also, the AS:S ratio was selected to evaluate the influence of the acetone volume on the supersaturation degree as this parameter could also affect the final concentration of ITR in the dispersions.

Table 2.4: The evaluated parameters of HIEAN and the resulting mean size and polydispersity of produced ITR particles

Run	Antisolvent temperature (°C)	AS:S ratio [(*)]	Particle size (nm)	PdI
I	40	10 : 1	269	0.105
II	60	10 : 1	321	0.166
III	40	10 : 2	995	0.113
IV	60	10 : 2	866	0.157
V	50	10 : 1.5	596	0.073
VI	50	10 : 1.5	477	0.126
VII	50	10 : 1.5	533	0.247

[(*)]Ratio of the volume of the antisolvent phase (AS – 20 mL) in relation to the solvent (S), which was modified to achieve the aimed ratios.

The model used to explain the results was evaluated using ANOVA. The regression was considered statistically significant with 95% confidence (p-value = 0.014) and the lack of fit was not considered to be significant (p-value = 0.230). Therefore, the model was considered valid for the analysis.

The modification of HIEAN conditions resulted in particles within a wide size range, from 269 to 995 nm (Table 2.4), showing how variations of those parameters, especially the AS:S ratio, are crucial for the final NP size. Indeed, smaller NPs, produced in runs I and II, were obtained when the AS:S ratio at a lower level (10:1 ratio) was used, in contrast to those produced using a higher level of this parameter, the 10:2 ratio, resulting in larger particles in Runs III and IV. The calculated effect of this factor (635.6 ± 59.44) (Table 2.) confirmed the positive and statistically significant impact of the antisolvent and solvent phase ratio on the process resulting in larger particles produced when this factor was used at a higher level (p-value = 0.009). Therefore, in order to produce particles with small sizes,

the optimised conditions of this method should employ this parameter closer to the level (-1), i.e. the AS:S ratio of 10:1.

The temperature and the interaction between both parameters had no statistical impact (p-value = 0.584 and 0.269, respectively) considering the evaluated range. However, at higher levels, i.e. temperatures greater than 60 °C, the temperature of the antisolvent could have a stronger effect on supersaturation, as solvent evaporation should be intensified at around and above its boiling point.

Table 2.5: Statistical analysis of the effects of selected factors in modified HIEAN.

Factor	Effect (nm)	*p-value*
Temperature	-38 ± 59	0.584
AS:S ratio	636 ± 59	0.009*
Interaction Temperature/AS:S ratio	-90 ± 59	0.269

(*) statistically different with 95% of confidence.

Although the produced particles were in the nanometric size range (Table 2.4), most of the samples were considered moderately polydisperse as their PdI was > 0.1 (Bhattacharjee, 2016), which is not ideal for the stability of these samples, as polydispersed dispersions are more prone to Oswald ripening (Clark et al., 2011). Therefore, optimisation of the nanoprecipitation method also aimed to reduce polydispersity of the nanoparticles.

2.2.4. Solvent evaporation under reduced pressure

When using the solvent phase at room temperature, there is a possibility that acetone is not evaporated to the same degree in comparison to the original condition used in the method, i.e. the solvent phase at 50 °C. The residual acetone can affect the stability of ITR dispersions by promoting Oswald ripening, where the smaller particles are solubilised and the solute diffuses into the larger particles (Mugheirbi and Tajber, 2015). Therefore, an additional step, evaporation under reduced pressure, was introduced following the formation of NPs in order to remove the residual acetone. This step was carried out keeping the liquid dispersions at 30 ºC and the impact of time and pressure were evaluated.

2.2.4.1. Influence of the evaporation step on the particles in dispersion

DLS was used to evaluate the average size of the NPs before and after the evaporation step (Table 2.6). The statistical analysis of these results revealed, in general, no significant influence of the evaporation step on the size of the particles in dispersion, regardless of the time and pressure used. The only exception observed was when the sample was evaporated for 30 min at 90 mbar, for which a significant increase in the particle properties before and after the process was measured (p-value = 0.010), possibly caused by heterogeneous nucleation leading to larger particles (D'Addio and Prud'homme, 2011).

Nevertheless, this result indicates that the evaporation step, in general, did not affect the NP particle size.

Table 2.6: The evaporation conditions and statistical analysis of results**.**

Time (min)	Pressure (mbar)	Initial size (nm)	Final size (nm)	*p-value*
20	90	233 ± 10	248 ± 4	0.080
30	90	654 ± 28	736 ± 12	0.010*
30	50	305 ± 17	307 ± 4	0.844
40	50	427 ± 23	397 ± 4	0.088

* Significant difference with 95 % of confidence.

2.2.4.2.Impact of the evaporation step on the solid-state properties of dried particles

Further analysis was carried out to investigate whether this additional step of evaporation could impact on the solid-state characteristics of the samples. DSC analysis of the dried samples (Fig. 2.1) revealed minimal differences in their thermograms (Table 2.7) and, in general, the samples presented a glass transition (T_g) at 62 ºC followed by one or two almost imperceptible endothermic events at 74 and 90 °C, an exothermic event and a melting point. The presence of T_g indicated that the produced samples were not crystalline and, therefore, the exothermic event is crystallisation into a more stable form (Yu, 2001). Furthermore, the small endothermic events at 74 and 90 °C are the liquid crystal transitions, respectively, from smectic to nematic (LC_1) and from nematic to isotropic liquid phase (LC_2) (Kozyra et al., 2018). This indicates that ITR was not amorphous, but a liquid crystal smectic mesophase (Shalaev et al., 2016). However, in the sample evaporated for 30 min at 90 mbar (Fig. 2.1c) and for 40 min at 50 mbar (Fig. 2.1e) only one mesophase transition was observed as the second transition overlapped with the exothermic event, which occurred earlier in those samples. This suggests lower stability of these samples as they crystallised at a lower temperature.

In general, liquid crystals, either smectic or nematic, mesophases have great potential for pharmaceutical application, as they could have increased stability in relation to amorphous material and/or increased apparent solubility in relation to crystalline materials (Shalaev et al., 2016).

Furthermore, the sample evaporated for 20 min at 90 mbar (Fig. 2.1b), had two endothermic transition around the melting point, at 160 ºC and other at 169 ºC, that could be due to crystallisation into polymorphic forms II and I, respectively (Zhang et al., 2016).
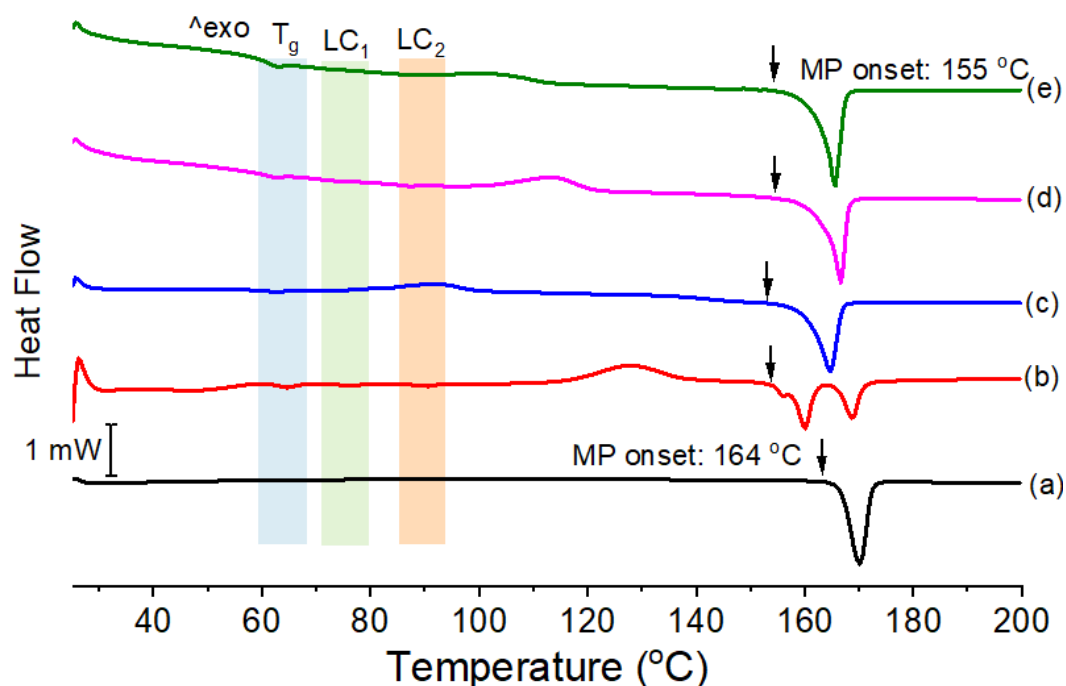
Fig 2.1: Thermograms of (a) ITR as received and the ITR NPs after rotary evaporation at (b) 20 min – 90mBAR, (c) 30 min – 90mBAR, (d) 30 min – 50mBAR, and (e) 40 min –50mBAR.

Table 2.7: Summary of thermal events observed in DSC analysis of ITR dispersions evaporated in different conditions.

Sample	Thermal event	Onset (°C)	Peak (°C)	Enthalpy (J/g)
ITR	Melt	164.4	169.8	-13.28
20min/90mBAR	T_g		62	
	LC_1		74.9	
	LC_2		89.8	
	Recrystallisation	111.3	127.1	55.6
	Melt (1)	154.2	160	-7.59
	Melt (2)	164.2	169	-12.63
30min/90mBAR	T_g		62.7	
	Recrystallisation	76.3	90.1	15.7
	Melt	155	160	-15.73
30min/50mBAR	T_g		62.9	
	LC_1		74.9	
	LC_2		89.8	
	Recrystallisation	99.0	114.3	12.3
	Melt	155	160	-15.30
40min/50mBAR	T_g		62.9	
	Recrystallisation	84.5	100.9	27.6
	Melt	155	160	-16.73

The diffractogram of the sample evaporated for 20 min at 90 mbar (Fig. 2.2 b) revealed the absence of well-defined Bragg peaks, except for a single peak at 6.2° 2θ, indicating that the samples were, indeed, liquid crystalline mesophases as found by DSC analysis (Fig. 2.1). The diffraction patterns of the other samples had additional Bragg peaks at 17.5, 18 and 20.6° 2θ that gradually increased in intensity when the evaporation time was prolonged and lower pressure was used. Therefore, the conditions of the evaporation can affect the solid-state of the samples, inducing some conversion of the material from a liquid crystal mesophase to a more ordered, crystalline state.
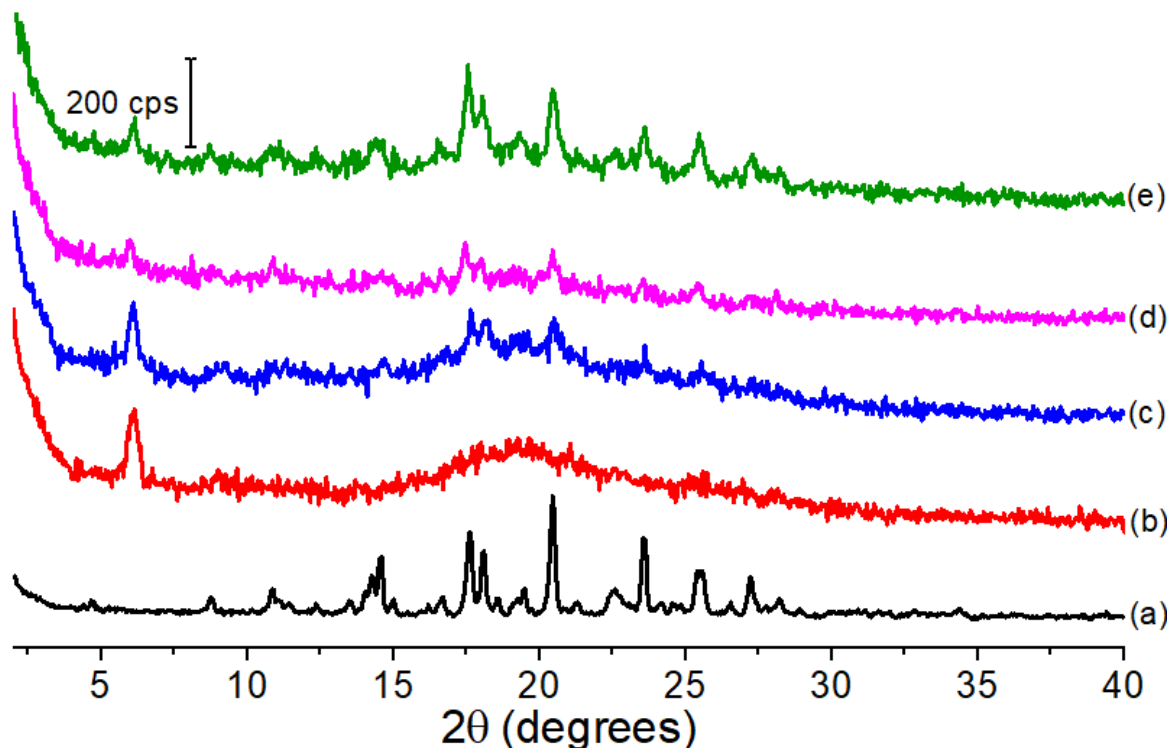
Fig. 2.2: Diffractograms of (a) ITR as received and the ITR NPs after rotary evaporation at (b) 20 min – 90mBAR, (c) 30 min – 90mBAR, (d) 30 min – 50mBAR, and (e) 40 min – 50mBAR.

2.2.4.3.Stability evaluation

A physical stability evaluation was performed using samples prepared by nanoprecipitation with and without the additional evaporation step, which was carried out in rota evaporator for 40 min at 50 mbar. The samples were stored at 4 °C (Fig. 2.3a) and at room temperature (25 °C, Fig. 2.3b) and their sizes were measured by DLS over time. The results obtained from the samples where no evaporation was employed revealed a rapid increase in the particle size at both temperatures (Fig. 2.3 in black square). At room temperature, particles increased in size and sedimented within 48 h, while at 4 °C they sedimented after 120 h. The samples prepared with the additional evaporation step revealed minor size differences detected during this evaluation (Fig. 2.3 in red circle), suggesting better colloidal stability.

The much lower stability of the non-evaporated samples is likely to be related to the presence of residual acetone in the system promoting Oswald ripening, as previously described in Section 2.3.2. Moreover, this was aggravated by the storage temperature, as the stability of both evaporated and non-evaporated samples were worse at 25 °C (Kumar et al., 2009; Wu et al., 2011). Therefore, the addition of the evaporation step was effective in removing the residual acetone from the system, leading to a remarkable improvement of physical stability.
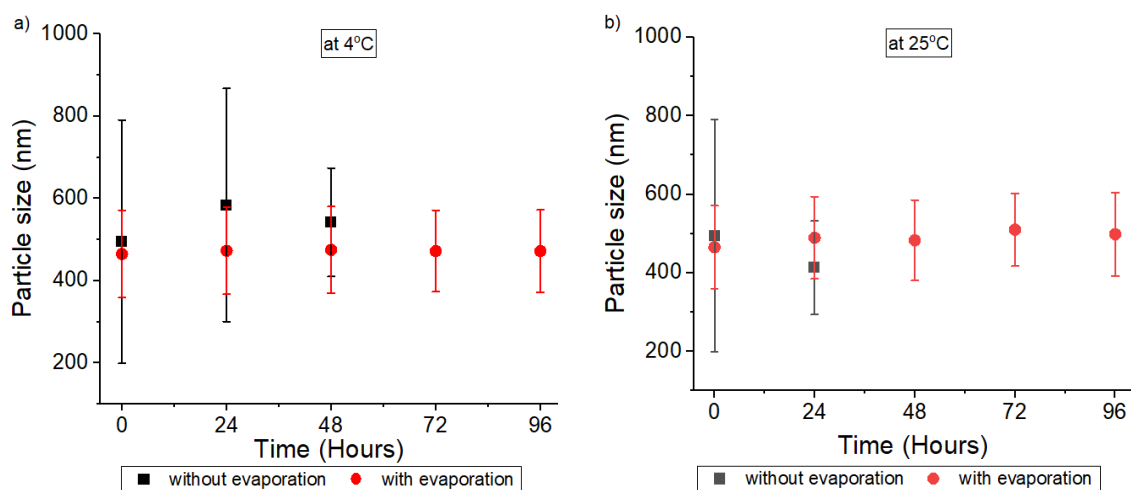
Fig. 2.3: Stability of ITR NPs with and without the evaporation stage stored at (a) 4 and (b) 25 ºC.

2.2.5. Optimisation of HIEAN method

For this purpose, the impact of the antisolvent phase at higher temperatures than those employed in Section 2.3.1, from 60 to 80 °C (Table 2.8), to induce greater solvent evaporation was evaluated. For the AS:S ratio, lower levels were assessed, where no more than 2 mL of the solvent phase was injected in 20 mL of antisolvent.

Table 2.8: Conditions used in the optimisation of the HIEAN method.

Sample	Antisolvent temperature (°C)	AS:S Ratio (v/v)	Particle size (nm)	PdI
#1	60	10:0.5	257 ± 41	0.065 ± 0.046
#2	60	10:1	451 ± 52	0.032 ± 0.037
#3	70	10:1	341 ± 64	0.060 ± 0.023
#4	80	10:0.5	235 ± 18	0.057 ± 0.012
#5	80	10:1	253 ± 16	0.054 ± 0.022

2.2.5.1. Evaluation of particles in dispersion

The particle size and PdI results of the produced samples are shown in Table 2.8. ANOVA showed that samples #1, #4 and #5 had comparable particle sizes (diameters)

however, they were significantly smaller than samples #2 and #3 (Table 2.8). Interestingly, the conditions used to produce #1 and #5 were the extreme conditions used (the lowest antisolvent temperature and the highest AS:S ratio for #1 as well as the highest antisolvent temperature and the lowest AS:S ratio for #5), yet both nanodispersions had similar sizes.

This could be due to the antisolvent temperature and the AS:S ratio affecting the supersaturation in a different way. Variations in supersaturation affect the nucleation rate which, normally, leads to the crystallisation of particles in different sizes (Sinha et al., 2013). For the HIEAN process described herein, the temperature had a critical effect on the nanoprecipitation, as heating the antisolvent phase to 80 °C produced samples with smaller particle size (samples #4 and #5) than those prepared at 60 and 70 °C (#2 and #3), except for the sample #1. As the boiling point of acetone is 56 °C, it is expected that it may be completely evaporated after injection of the solvent phase into the hot antisolvent, however, this is not the case (Mugheirbi and Tajber, 2015). Nevertheless, due to the faster evaporation rate of acetone at 80 °C, a higher drug supersaturation was created at this antisolvent temperature, which led to a higher nucleation rate and smaller particles in comparison to those produced at lower temperatures (60 and 70 °C). For sample #1, which was produced using the antisolvent at 60 °C (Table 2.8), a smaller volume of acetone (1 mL) was injected into the water in comparison to samples #2 and #3 (2 mL). In this case, as the solvent volume was low, even the slower evaporation was enough to induce a supersaturation that resulted in particles with sizes comparable to those produced in higher temperature (samples #4 and #5).

In addition to this effect caused by the volume of solvent, the different AS:S ratios resulted in samples with different ITR final concentrations, 0.1 mg/mL in samples #1 and #4, prepared using the 10:0.5 AS:S ratio (Table 2.8) and 0.2 mg/mL in samples #2, #3 and #5 that were prepared using the 10:1 AS:S ratio. In general, after the nucleation stage, the particles grow to reduce the supersaturation, therefore, the particles produced from a solution with a higher solute concentration could result in larger particles than those produced in same conditions but from a solution in a lower concentration (Mersmann, 1999). Indeed, this was observed when comparing samples #1 and #2, produced at 0.1 mg/mL of ITR final concentration, which had smaller particles than the others, produced at 0.2 mg/mL. However, when comparing samples #4 and #5, which had comparable particle sizes the temperature had a greater impact on the size than the AS:S ratio, most likely as at 80 °C acetone was rapidly evaporated and the difference of supersaturation in these systems became negligent.

Regardless of the process conditions used to produce the dispersions, the samples had low PdI values, lower than 0.1 (Table 2.8) and consequently, they were considered as monodisperse (Bhattacharjee, 2016).

2.2.5.2.Solid-state analysis

For this test, the dispersions were centrifuged, and the dried pellets were used the thermal analysis. The DSC curves (Fig. 2.4) revealed minimal differences among the samples (Table 2.9) and the thermograms also had the characteristics of a smectic mesophase, i.e. a T_g and two mesophase transitions, LC_1 and LC_2, similar to the samples in Section 2.3.2.2. Furthermore, in the sample produced at 70 °C and using the AS:S ratio of 10:1 (Fig. 2.4d) also had two melting points.

PXRD analysis (Fig. 2.5) also showed slight differences in the diffractograms of the samples, which had a single peak at $6°$ 2θ each, confirming the formation of a smectic mesophase. However, the sample produced using antisolvent at 60 °C and 10:0.5 ratio (Fig. 2.5b) had visible small peaks at 17.55 and 20.55° 2θ, suggesting the presence of some ITR crystalline form.
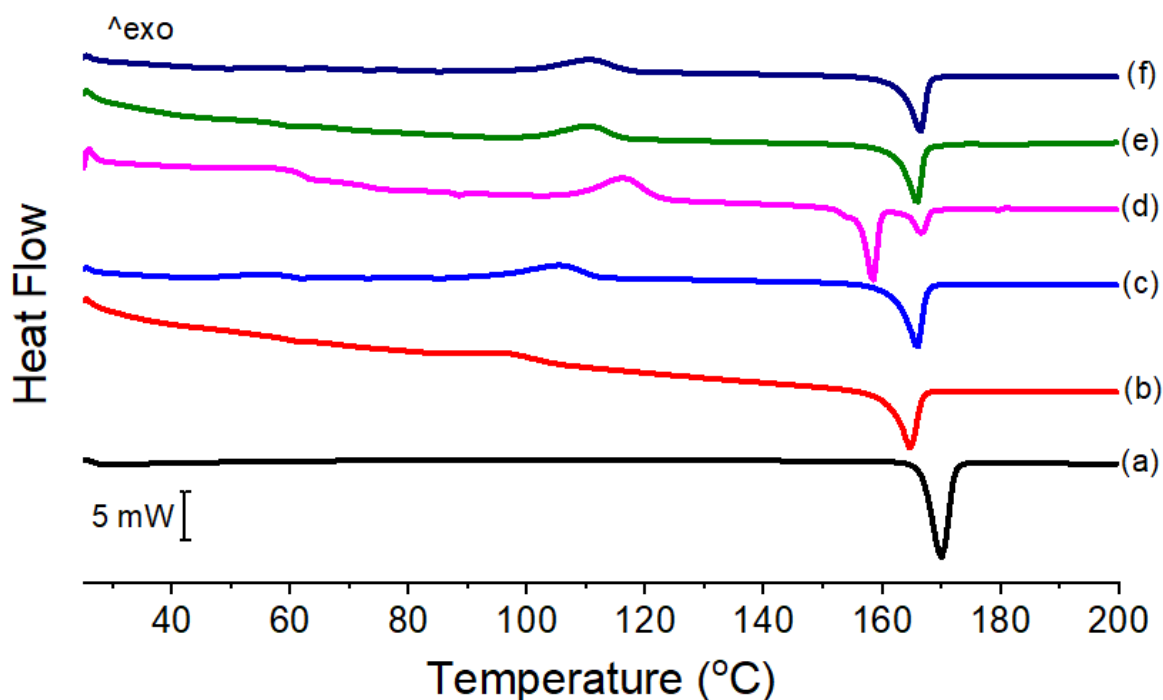
Fig. 2.4: Thermograms of (a) ITR as received and the ITR NPs prepared at (b) 60 °C – 10:0.5 ratio, (c) 60 °C – 10:1 ratio, (d) 70 °C – 10:1 ratio, (e) 80 °C – 10:0.5 ratio, and (f) 80 °C – 10:1 ratio.

Table 2.9: Summary of thermal events observed in DSC analysis of the ITR NPs prepared in different conditions**.**

Sample	Thermal event	Onset (°C)	Peak (°C)	Enthalpy (J/g)
ITR	Melt	164,4	169,8	-63,28
60°C/10:0.5 ratio	T_g		62	
	Recrystallisation	80.6	97.2	21.26
	Melt	156.4	164.7	-63.68
60°C/10:1 ratio	T_g		61.2	
	LC1		72.4	
	LC2		84	
	Recrystallisation	93.5	105.5	28.95
	Melt	156.4	165.9	-70.23
70°C/10:1 ratio	T_g		62,8	
	LC_1		74,0	
	LC_2		88.9	
	Recrystallisation	106.7	116.2	0.12
	Melt (1)	151.0	158.0	-66.15
	Melt (2)	163.8	166.3	-27.18
80°C/10:0.5 ratio	T_g		60.8	
	LC_1		72.4	
	LC_2		88.5	
	Recrystallisation	100.9	109.6	17.02
	Melt	155.9	165.5	-63.8
80°C/10:1 ratio	T_g		60.8	
	LC_1		73.1	
	LC_2		85.2	
	Recrystallisation	99.7	110.9	41.74
	Melt	155	160	-66.80
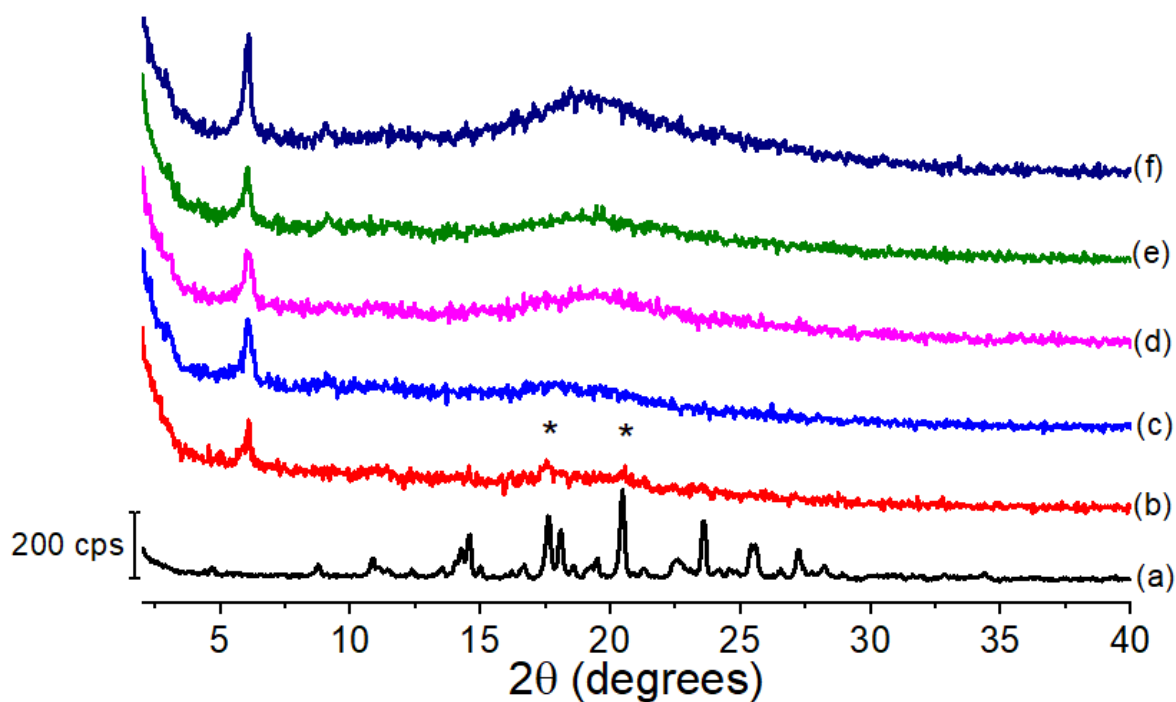
Fig. 2.5: Diffractograms of (a) ITR as received and the ITR NPs prepared at (b) 60 °C – 10:0.5 ratio, (c) 60 °C – 10:1 ratio, (d) 70 °C – 10:1 ratio, (e) 80 °C – 10:0.5 ratio, and (f) 80 °C – 10:1 ratio.

DSC and PXRD analyses of the samples obtained using different conditions of HIEAN showed a weak impact of the antisolvent temperatures and AS:S ratios used on the solid-state properties of the resulting NPs. Consequently, the characteristics of the samples in liquid dispersion were more important for the optimisation of the nanoprecipitation method, which was based on the particle size and yield. Therefore, using the antisolvent phase at 80 °C and the AS:S ratio of 10:1 was considered as the most advantageous conditions.

2.4. Conclusions

In summary, this work evaluated the HIEAN method, including the role of relevant process parameters, the effect of removal of residual solvent and the selection of optimal conditions for the preparation of nanoparticles with desired characteristics.

In the screening of process variables, only the AS:S ratio was initially considered critical to the particle size of the samples prepared by the nanoprecipitation method. This important role was due to its effect on the supersaturation generated, as alterations in the AS:S ratio implied in the modification of both solvent volume and ITR final concentration. Later, during the optimisation, the importance of the antisolvent temperature was more pronounced, as smaller particles were produced when this parameter was used at higher values than the boiling point of the solvent (>56 °C). In this case, the antisolvent temperature could affect the supersaturation due to an increased rate of acetone evaporation when the solvent phase was injected.

The inclusion of an additional residual solvent (acetone) evaporation step had no influence on the particle size of the ITR dispersions; however, prolonged evaporation at reduced pressure affected the solid-state properties of the particles, inducing some conversion of the material from a liquid crystal mesophase to a more ordered, crystalline state. Nevertheless, the ITR dispersions evaporated for 40 min at 50 mbar showed a remarkable stability enhancement when stored at 4 and 25 °C in comparison to the non-evaporated ITR dispersions. This improvement was attributed to the effective residual acetone removal by the evaporation step preventing the Oswald ripening.

The optimisation of the HIEAN conditions enabled the preparation of dispersions with desired characteristics, i.e. monodispersed nanoparticles with small sizes (<300 nm). Accordingly, the preparation of the particles using the antisolvent phase at 80 °C and the AS:S ratio of 10:1 yielded in a monodispersed dispersion with the particle size of 253 ± 16 nm, which had solid-state characteristics of a liquid crystal smectic mesophase. The preparation of ITR having such characteristics could represent improvements in some of its properties, such as apparent solubility, increased in relation to the crystalline form, and stability, increased in relation to its amorphous form. Therefore, presenting promising characteristics for a pharmaceutical application.

Chapter III: Development of modified itraconazole nanoparticles and investigation of polyethylene glycol polymers impact on their physicochemical and mucoadhesive properties

3.1.Introduction

Itraconazole (ITR) is an active pharmaceutical ingredient (API) with a broad-spectrum antifungal activity. It is one of a few azole agents used for the treatment of topical and systemic mycoses as well as for the prophylaxis in immune-suppressed patients (Campoy and Adrio, 2017; Denning and Hope, 2010). ITR has a very low solubility but a high absorption and, therefore, it is considered as a class II drug according to the Biopharmaceutics Classification System (BCS) (Papadopoulou et al., 2008). Indeed, ITR has a very low solubility in pure water (around 1 µg/mL), which increases in an acidic medium (4 µg/mL) (Hardin et al., 1988), however the poor solubility is the limiting factor for ITR absorption.

In general, the bioavailability of BCS class II compounds can be improved by the reduction of the API particles into nanometric sizes, i.e. nanonisation; this approach mainly improves the dissolution rates of APIs (Shah et al., 2016). The nanonisation can be achieved by top-down, bottom-up or a combination of both approaches. Methods based on the first approach using physical processes to reduce particle size, whereas the second is based on the precipitation of solubilised molecules (Pawar et al., 2014). Another approach to improve the poor characteristics of BCS class II drugs is by amorphisation of the API. This metastable form is in a higher energetic state and has its structure less ordered than the crystalline form. Therefore, amorphous materials have higher apparent solubilities (Grohganz et al., 2013). It has been shown that for ITR the combination of nanonisation with the disordered structure of particles is a suitable method of enhancing apparent solubility of this API as the maximum concentration detected during dissolution under supersaturated condition was a 6.5-fold higher for nanoparticles (NPs) when compared to microparticles of ITR (Mugheirbi et al., 2014).

As NPs may not be able to dissolve completely before reaching the site of absorption, the undissolved portion can end up in the gastrointestinal mucus layer after oral administration (Netsomboon and Bernkop-Schnürch, 2016; Sigurdsson et al., 2013). The mucus is a viscoelastic complex layer covering the epithelial cells of the eyes, respiratory and female reproductive tracts and the gastrointestinal system, from the mouth to anus. Its composition and physical characteristics are different according to its organ of origin and to the presence of pathological conditions. Under physiological conditions, the mucus is predominantly composed by water (95% w/w) and a complex mixture of salts, lipids and proteins (Johansson et al., 2013; Svensson and Arnebrant, 2010). Regardless of its origin, the mucus layer is responsible for the maintenance of lubrication and moisture and it also acts as a physical barrier against pathogens and potential noxious particles. Mucins constitute a polydisperse group of glycoproteins. Their molecular weight range from 0.5 to 20 MDa where approximately 80% are carbohydrates, such as N-acetylgalactosamine, N-acetylglucosamine, fucose, galactose and sialic acid that provide their anionic nature

(Svensson and Arnebrant, 2010). The protein core provides the hydrophobic regions of mucin due to a high proportion (>10%) of cysteine residues able to form disulphide bridges resulting in hydrophobic globules, also described as "cystine knots" (Johansson et al., 2013). In physiological conditions the mucus is a porous gel formed by the entanglement and hydration of mucin fibres, allowing it to retain particles larger than its porous mesh size (Cone, 2009). The combination of its morphology and the mucin composition turns the mucus into an effective physical barrier able to filter particles by charge and by size exclusion preventing them to reach the epithelium (Lieleg and Ribbeck, 2011).

In the case of nanoparticulate drug delivery systems, these particles can be designed to have strong or no interactions with the mucus layer. Those able to interact with mucus are considered "mucoadhesive" and they are developed to anchor on the mucus layer to increase their residence time and gradually release the drug close to the mucosa (das Neves et al., 2011). However, the residence time of these particles is limited to the turnover of mucus and, consequently, they potentially can be removed from the site before delivering the full dose of the entrapped drug (Murgia et al., 2018). On the other hand, particles unable to interact with the mucus are considered as "mucopenetrative" as they are able to diffuse through the mucus reaching the deeper regions of the layer and therefore, to be absorbed by the epithelium (Netsomboon and Bernkop-Schnürch, 2016). In recent years, those mucopenetrative particles have been receiving more attention, especially for the oral route of administration, due to their enhanced bioavailability when compared to the mucoadhesive carriers (Chen et al., 2013). Furthermore, mucopenetrative NPs are distributed more homogeneously across the intestine in contrast to the more locally concentrated depositions of mucoadhesive particles (Maisel et al., 2015).

The mode of NP interaction with the mucus layer can be modified using polymers attached to the NP surface. For instance, chitosan can interact with mucin via ionic, hydrogen and hydrophobic bonds. Consequently, this material is suitable for mucoadhesive formulations (Sosnik et al., 2014). Polyethylene glycol (PEG), on the other hand, can be used to prepare mucopenetrative NPs. This is possible because PEG polymers (PEGs) are normally non-ionic and able to neutralise the surface charge of such NPs, thus preventing them from attaching to the mucus (Huckaby and Lai, 2018). Furthermore, for the PEGylated NPs be mucopenetrative, it is necessary to create on the surface of these particles a high density layer composed of PEGs with molecular weight lower than 40 kDa (Maisel et al., 2016), with the chains arranged in a conformation known as a "dense brush", which is less susceptible to entanglement by the mucin chains of the mucus layer.

PEGylation is a valuable process employed in the manufacture of nanoparticulate drug delivery systems for another reason, as PEGs can also improve the stability of dispersed particles by reducing their aggregation and preventing their coalescence (Mueller et al., 2011). PEGylation also averts opsonisation of NPs in the bloodstream and reduces

their uptake by the mononuclear phagocyte system, which plays a key role in the clearance kinetics of PEGylated particles (Rabanel et al., 2014).

Nanonised particles produced either by nanomilling, as many currently marketed formulations or by bottom-up methods, may be composed of nearly entirely of the API to maximise the drug load and their surface modifications are limited to excipient adsorption, i.e. based on non-covalent bonding (Laitinen et al., 2013). In the present work, firstly, the aim was to identify and select polymers able to interact with the ITR NPs developed in Chapter 2. Secondly, the physicochemical properties of the produced particles and the impact that PEGylation had on the solid-state and nanometric properties of the systems were studied. Ultimately, the interactions of the PEGylated ITR NPs with gastrointestinal mucin were also investigated *in vitro* to determine whether they had mucopenetrative or mucoadhesive potential when administered orally.

3.2. Materials and Methods

3.2.1. Materials

Poly(ethylene glycol) 2,000 was purchased from Aldrich Chemical Co. Ltd (UK). Poly(ethylene glycol) 10,000, poly(ethylene glycol) methyl ether (MPEG) 2,000 and 10,000 and poly(ethylene glycol) dimethyl ether 2,000 (DMPEG) were purchased from Sigma-Aldrich (Ireland). 4 arm-poly(ethylene glycol) 5,000 and 10,000 Da were purchased from JenKem Technology (Dallas, USA). Poloxamer 188 (Lutrol® F 68) and Poloxamer 407 (Lutrol® F 127) were acquired from BASF (Germany). Mucin from porcine stomach (Type III, bound sialic acid 0.5-1.5 %, partially purified powder) was purchased from Sigma-Aldrich (Ireland). Polystyrene Nanoparticles (100 nm) were purchased from Bangs Laboratories, Inc. (USA). The details of all other materials and solvents used in this study are listed in Chapter 2.

3.2.2. Methods

3.2.2.1. Production of ITR NPs

ITR NPs were produced by the nanoprecipitation in antisolvent method using the optimised conditions described in Chapter 2. Briefly, a 2 mg/mL ITR solution (solvent phase) was prepared by dissolving 20 mg of the API in 10 mL of acetone. Then, an aliquot of this solution at 25 °C was rapidly injected using a 0.5 mm x 16 mm Sterican® needle into 20 mL of deionised water (Elix®, Merck Millipore, Ireland) (antisolvent phase) at 80 °C and a constant magnetic agitation at 1,300 rpm using a hot plate SD-162 (Stuart, UK). The dispersion was immediately transferred to a jacketed cylinder at 4 °C and cooled for 30 s under constant mix at 1,300 rpm. Finally, the cooled dispersion was transferred to a 100 mL round bottom flask and subjected to evaporation for 30 min and 60 mbar in a Rotavapor R-205 attached to a vacuum pump V-700 (Büchi, Switzerland) in a heating bath B-490 (Büchi, Switzerland) at 30 °C.

3.2.2.2. Production of ITR dispersions with polymers

The ITR dispersions were prepared with polymers at 0.5 molar fraction of the API, resulting in the ITR to polymer molar ratio of 2-1. The preparation of the dispersion with the poly(ethylene glycol) dimethyl ether 2,000 Da (DMPEG 2kDa) used the polymer at 0.1 molar fraction of the ITR, resulting in a molar ratio of 10-1. For this purpose, the polymers were weighted according to Table 3.1 and solubilised in 20 mL of deionised water (Elix®, Merck Millipore, Ireland) that was used as the antisolvent phase. The solvent phase and the conditions for the nanoprecipitation procedures were used exactly as described in Section 3.2.2.1. All samples were tested in triplicate.

Table 3.1: Polymers and weights used to prepare the dispersions with ITR

Polymer	Mass (mg)
Poly(ethylene glycol) 10,000 Da (PEG 10 kDa)	28.3±1.0
Poly(ethylene glycol) methyl ether 2,000 Da (MPEG 2 kDa)	5.7±1.0
Poly(ethylene glycol) dimethyl ether 2,000 Da (DMPEG 2 kDa)	1.1±1.0
4 arm-poly(ethylene glycol) 5,000 Da (4 ARM PEG 5 kDa)	14.2±1.0
4 arm-poly(ethylene glycol) 10,000 Da (4 ARM PEG 10 kDa)	28.3±1.0
Poloxamer 407	35.7±1.0
Poloxamer 188	24.3±1.0

3.2.2.3.Production of PEGylated NPs

The polymers, PEG 10 kDa, MPEG 10 kDa and 4 ARM PEG 10 kDa were evaluated at 0.5 or 1 of the molar fraction of ITR, resulting in the ITR to polymer molar ratios of 2-1 and 1-1, respectively. To produce PEGylated NPs, aqueous solutions of each polymer, at 30 mg/mL, were prepared and 0.94 or 1.88 mL of each of the solutions were diluted up to 20 mL using deionised water (Elix®, Merck Millipore, Ireland) for the 2-1 and 1-1 preparations, respectively. Afterwards, 2 mL of the ITR solution in acetone (2 mg/mL) was injected into the polymer solution at 80 ⁰C, the antisolvent for the process, following the procedure as described in Section 3.2.2.1.

3.2.2.4.Isolation of NPs

Isolation of NPs was performed as described in Chapter 2. For the PEGylated ITR NPs, the pellets were rinsed with 5 mL of deionised water and centrifuged again under the same conditions. After the second centrifugation, the supernatant was discarded and the pellets were dried for solid-state analyses and kept at 25 ⁰C.

3.2.2.5.Particle size and polydispersity index of NPs by dynamic light scattering (DLS)

DLS was performed as described in Chapter 2.

3.2.2.6.Zeta potential analysis of NPs

Zeta potential was calculated from the mean electrophoretic mobility values measured by Laser Doppler Velocimetry using a Zetasizer Nano series Nano-ZS ZEN3600 fitted with a red laser light beam (λ = 633 nm) (Malvern Instruments Ltd., UK). Aliquots of 1.0 mL were placed in a cell (DTS1060) for measurements without further dilution. The equilibration time was set to 2 min at 25 ⁰C. Measurements for each sample/batch were taken in triplicate. Results were corrected considering dynamic viscosity of the continuous

phase measured using a Vibro Viscometer SV-10 (A&D Ltd., Japan). The analysis was carried out in triplicate.

3.2.2.7.Adsorption studies of PEGs on the surface of premade ITR NPs

For the adsorption studies, 0.94 or 1.88 mL of a 30 mg/mL aqueous solution of PEG 10 kDa, MPEG 10 kDa and 4 ARM PEG 10 kDa was added to a non-PEGylated ITR NP dispersion previously prepared as described in Section 3.2.2.1. Those volumes of the polymer solutions resulted in the same polymer concentrations as those used to make PEGylated ITR NPs described in Section 3.2.2.3. The dispersions were then stirred at 200 rpm for 5 min at 4 ºC. The adsorption of these PEGs was assessed measuring the particle size of the dispersions using DLS, as described in Section 3.2.2.5, before and after the addition of the polymer solution (Rabanel et al., 2014). A negative control sample was prepared by subjecting the ITR NP dispersions to the same conditions in the absence of polymers. All samples were tested in triplicate.

3.2.2.7.Differential scanning calorimetry (DSC)

DSC was performed as described in Chapter 2.

3.2.2.8.Powder X-ray diffraction (PXRD)

PXRD was performed as described in Chapter 2.

3.2.2.9.Morphological analysis

A Zeiss Supra variable Pressure Field Emission Scanning Electron Microscope (SEM) (Germany) equipped with a secondary electron detector and accelerating voltage of 5 kV was used for the morphological examination of ITR particles. Aliquot samples of the dispersed NPs were placed directly on aluminium stubs, dried using nitrogen purge and sputter-coated with gold/palladium under vacuum before analysis (Mugheirbi et al., 2014).

3.2.2.10.Stability analysis

The physical stability of the ITR NPs (Section 3.2.2.1) and the PEGylated ITR NPs (Section 3.2.2.3) was investigated in liquid dispersions. For these experiments, the NPs were stored at 4 ºC and their sizes were measured using DLS (Section 3.2.2.5) after 7 and 21 days. All samples were tested in triplicate.

3.2.2.11.Evaluation of interactions of NPs with mucin by DLS

For this analysis, a 0.5 mg/mL mucin stock dispersion was prepared by dispersing 15 mg of purified mucin powder in 30 mL of a 30 mM NaCl solution and, then, filtered using a 0.2 µm hydrophilic PTFE filter (Fisherbrand™, Fisher Scientific, UK). Later, 37.5 µL of the NPs dispersion was injected into 5 mL of filtered mucin dispersion resulting in a final concentration of ITR NPs of 1.5 µg/mL. The mixtures were kept at 20 ºC in a jacketed

cylinder under 200 rpm of magnetic stirring. The particles size measurement of the aliquots taken at 0, 30, 60, 90 and 120 min of stirring was analysed by DLS, as described in Section 3.2.2.5. The analysis was carried out in triplicate.

3.2.2.12. Evaluation of diffusion of NPs in mucin by Nanoparticle Tracking Analysis (NTA)

The NTA was used to evaluate the particle size, concentration and diffusion coefficients of the NPs dispersed in a mucin solution. For this purpose, the filtered mucin stock dispersion, prepared as in Section 3.2.2.11 was diluted in 30 mM NaCl aqueous solution, then 50 µL of each NP dispersion was incubated in 1950 µL of this diluted mucin dispersion. The NPs were evaluated using a final concentration of 5 µg/mL and the mucin at 12.5 µg/mL. The mixtures were kept in a 1 mL syringe at 25 ± 2 °C during the analysis and continuously injected into the NTA system, a Nanosight NS300 (Malvern, UK). The analysis was carried out using a red laser (642 nm) and the images recorded using a sCMOS camera adjusted to camera level 7. Five videos of 60 s long were recorded for each sample at 0, 30, 60, 90 and 120 min after mixing the NPs dispersions in mucin solution and processed using NTA 3.2 software. The analysis was carried out in triplicate.

3.2.2.13. Quartz crystal microbalance with dissipation (QCM-D)

The potential interaction between the polymers or NPs and deposited mucin was investigated using a Quartz Crystal Microbalance with dissipation technology (QCM-D) (Q-Sense® E4, Q-Sense AB, Gothenburg, Sweden) attached to a peristaltic pump (IMS 935, Ismatec, Glattbrugg-Zurich, Switzerland). For this set of experiments, gold quartz crystals QSX 301 (Biolin Scientific, Sweden) were used as sensors. Prior to their first use and after each test, the sensors were cleaned following the protocol suggested by the manufacturer. Briefly, they were first sonicated in a 2% (w/v) sodium dodecyl sulphate aqueous solution for 5 minutes and then rinsed with deionised water. Afterwards, they were immersed in 10 mL of 5:1:1 solution of deionised water, ammonia (25%, v/v) and hydrogen peroxide (30%, v/v) at 75 °C for 5 min followed by a rinse with deionised water and dried with nitrogen gas. Just before experiments, the sensors were exposed to UV-zone treatment (UV/Ozone Pro Cleaner, Bioforce Nanotechnologies, USA) for 10 min.

For these experiments, first, 30 mM NaCl solution was perfused at a flow rate of 100 µL/min through the flow modules containing the gold sensors at 24°C. The frequency (*f*) and the dissipation (*D*) values were allowed to stabilise to set up the baseline reading. The mucin dispersion was prepared dispersing purified mucin powder in 30 mM NaCl solution resulting in a 25 mg/L mucin dispersion.

For the analysis of mucoadhesivity evaluation of polymers, solutions of PEG 10 kDa, MPEG 10 kDa and 4 ARM PEG 10 kDa were prepared at 0.1, 1, 10, 50 and 100 mg/mL in 30mM NaCl. The sequence of events carried out for divided in four stages where solutions

or dispersions were perfused at 100 µL/min through the system at 24 °C: (1) perfusion of mucin dispersion; (2) 30 mM NaCl solution to remove unbounded mucin; (4) the polymer solutions and (5) 30 mM NaCl to remove polymers that may induced changes in *f* and *D* but were not attached to mucin layer. Each of these solutions was perfused until the stabilisation of *f* and *D* values (Oh et al., 2015). During the experiments, *f* and D values in the 3rd, 5th, 7th and 9th, 11th and 13th overtones were monitored and recorded in real-time using the Q-Sense software (QSoft 401) and analysed using QSense Dfind software (Biolin Scientific, Sweden).

For the mucoadhesivity analysis of NPs dispersions, the ITR dispersions were diluted in 30mM NaCl to a final concentration of 1.5 µg/mL. A 1.5 µg/mL dispersion of polystyrene NPs was prepared diluting the dispersion in 30 mM NaCl solution was used as positive control. The background solution was had the same composition and prepared using the same conditions as for the NPs but without the API, i.e. a blank solution. The experiment was divided into five stages: (1) perfusion of mucin dispersion; (2) 30 mM NaCl solution to remove unbounded mucin; (3) background solution (BG) to investigate if the solution wherein the NPS were dispersed could interfere with the mucin layer; (4) 1.5 µg/mL NPs dispersion and (5) 30 mM NaCl to remove NPs that may induced changes in *f* and *D* but were not attached to mucin layer. During the experiments, *f* and D values in the 3rd, 5th, 7th and 9th overtones were monitored and recorded.

The Voigt-model (Voinova et al., 1999) was applied to calculate the mass (m) and the thickness of the adsorbed layers. The used parameters for this purpose were the fluid density (1.001 kg/m^3), the fluid viscosity (0.00071 kg/ms) and the attached mucin density (1450 kg/m^3) (Wiecinski et al., 2009). The analysis was carried out in triplicate.

3.2.2.14. Statistical analysis

Statistical analysis was carried out as described in Chapter 2.

3.3.Results and Discussion

3.3.1.Evaluation of the potential of polymers to modify ITR NPs

In this investigation, ITR NPs were prepared in the presence of polymers (Fig. 3.1) using an API to polymer molar ratio of 2:1. Then, the samples were analysed regarding their properties as dispersions using DLS and as dried materials using DSC to establish which polymers had a greater potential to interact with the ITR NPs.

Poly(ethylene glycol) (PEG)   Poly(ethylene glycol) methyl ether (MPEG)   Poly(ethylene glycol) dimethyl ether (DMPEG)

4-Arm-poly(ethylene glycol) (4 ARM PEG)   Poloxamer
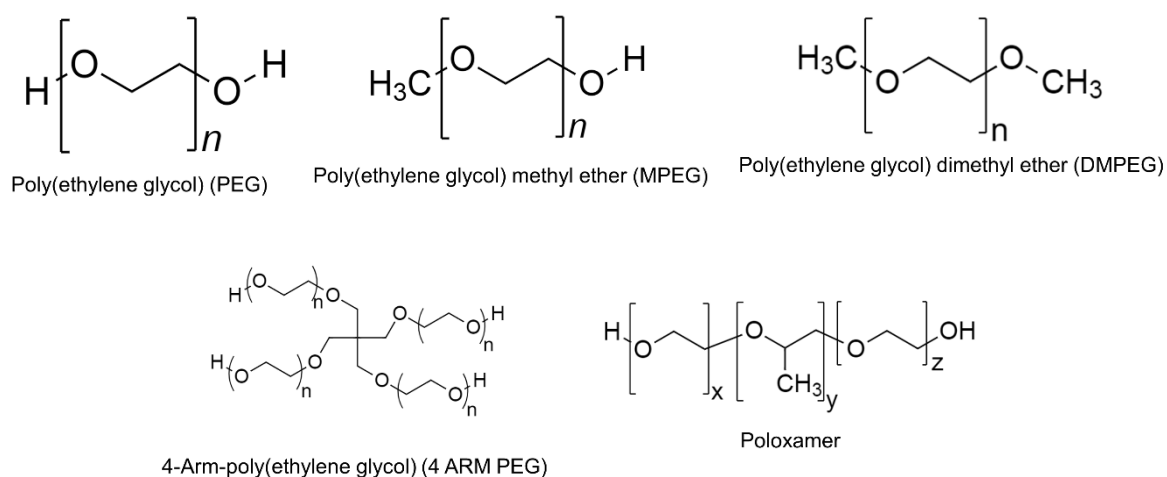
Fig. 3.1: Molecular structures of PEG, MPEG, DMPEG, 4 ARM PEG and Poloxamer polymers.

DLS analysis of the ITR dispersions (Table 3.2) showed that most of the samples had particles in the nanometric size range (<1 μm), except for ITR-Poloxamer 188 and ITR-Poloxamer 407, addition which resulted in unstable large particles with sizes of 2074±133 and 2502±1117 nm, respectively. These results were therefore excluded from the statistical analysis. ANOVA of the dispersions sizes revealed that the particle size of the ITR-DMPEG 2 kDa NPs was significantly different from the others despite a lower proportion of polymer (10:1) used in this sample. This could be due to a higher affinity of the DMPEG 2 kDa (Fig. 3.1) to the ITR NPs, increasing the number of the polymer chains adsorbed on the surface of these particles (McComiskey et al., 2018). Indeed, this was the only sample with a positive zeta potential value (+6.5 ± 0.6 mV) consequently, the electrostatic repulsion forces in these particles are reduced, increasing their propensity to aggregation despite the steric hindrance provided by the polymer. The zeta potential analysis of the other dispersions (Table 3.2) revealed that the ITR NPs had a strongly negative surface charge, of -30.1 ± 1.5 mV, in contrast to the preparations with polymers, which had their values partially neutralised. The statistical analysis of these results indicated that the dispersions with polymers had zeta potential values significantly different from the ITR NPs.

The analysis of the PdI values of the samples showed that the polymers had no impact on the polydispersity of the dispersions, which were considered monodispersed as their PdI were lower than 0.1. NPs made of ITR-Poloxamer 407 and ITR-Poloxamer 188

were the exceptions, as their PdI were 0.321±0.048 and 0.595±0.207, respectively and, therefore, having a high polydispersity values.

Table 3.2: Mean particle size, PdI and zeta potential of ITR NPs produced with polymers at 2:1 API:polymer molar ratio.

Sample	Particle Size (nm)	PdI	Zeta potential (mV)
ITR NP	253 ± 16	0.054 ± 0.022	-30.1 ± 1.5
ITR-PEG 2 kDa	257 ± 3	0.057 ± 0.010	-13.9 ± 0.4[*]
ITR-PEG 10 kDa	253 ± 3	0.020 ± 0.021	-13.0 ± 0.1[*]
ITR-MPEG 2 kDa	239 ± 3	0.048 ± 0.036	-17.6 ± 0.8[*]
ITR-DMPEG 2 kDa [a]	820 ± 160[*]	0.058 ± 0.067	+6.5 ± 0.6[*]
ITR-4-arm PEG 5 kDa	237 ± 4	0.008 ± 0.006	-16.2 ± 0.6[*]
ITR-4-arm PEG 10 kDa	240 ± 2	0.010 ± 0.007	-19.0 ± 0.3[*]
ITR-Poloxamer 407	2074 ± 133[b]	0.321 ± 0.048	-10.6 ± 0.3[*]
ITR-Poloxamer 188	2502 ± 1117[b]	0.595 ± 0.207	-11.0 ± 0.1[*]

[a] produced using 10:1 ITR:polymer ratio; [b] values excluded from statistical analysis, [*] values considered statistically significantly different by ANOVA

The thermal analysis of the dried samples (Fig. 3.2) showed that those prepared with polymers had DSC curves different to that of the ITR NPs (Fig. 3.2a) as no clear T_g, LC_1 and LC_2 were visible. This suggests that the solid-state properties of the ITR could be affected by the polymers, inducing the formation of crystalline material in place of the liquid crystal smectic mesophase. However, the thermograms of NPs composed of ITR-PEG 2 kDa and ITR-MPEG 2 kDa (Fig. 3.2b and d), a broad exothermic event suggests ITR crystallisation, therefore, disordered ITR could be present in those samples.

The presence of the polymer can be considered as not impacting on the melting point of ITR (Table 3.3). The values varied between 154 °C, observed for ITR-4 ARM PEG 5 kDa NPs (Fig. 3.2f) and ITR-Poloxamer 188 NPs (Fig. 3.2h), and 158 °C, for ITR-Poloxamer 407 NPs. In the unmodified ITR NPs (Fig. 3.2a) the melting point was 155 °C.

There was an endothermic event detected for ITR-PEG 10 kDa (Fig. 3.2c), ITR-4 ARM PEG 10 kDa (Fig. 3.2g), ITR-Poloxamer 188 (Fig. 3.2h) and ITR-Poloxamer 407 (Fig. 3.2i) NPs. This event was at temperatures close to the melting point of the respective polymer (PEG 10 kDa: 58 – 63 °C; 4 ARM PEG 10 KDa: 55-60 °C; Poloxamer 188: 52 °C; Poloxamer 407: 53 – 57 °C), indicating their presence in the dried samples. In addition, as no melt of polymers with lower molecular weight (2 and 5 kDa) were found, this suggests that longer polymer chains might have stronger interactions with the NPs.
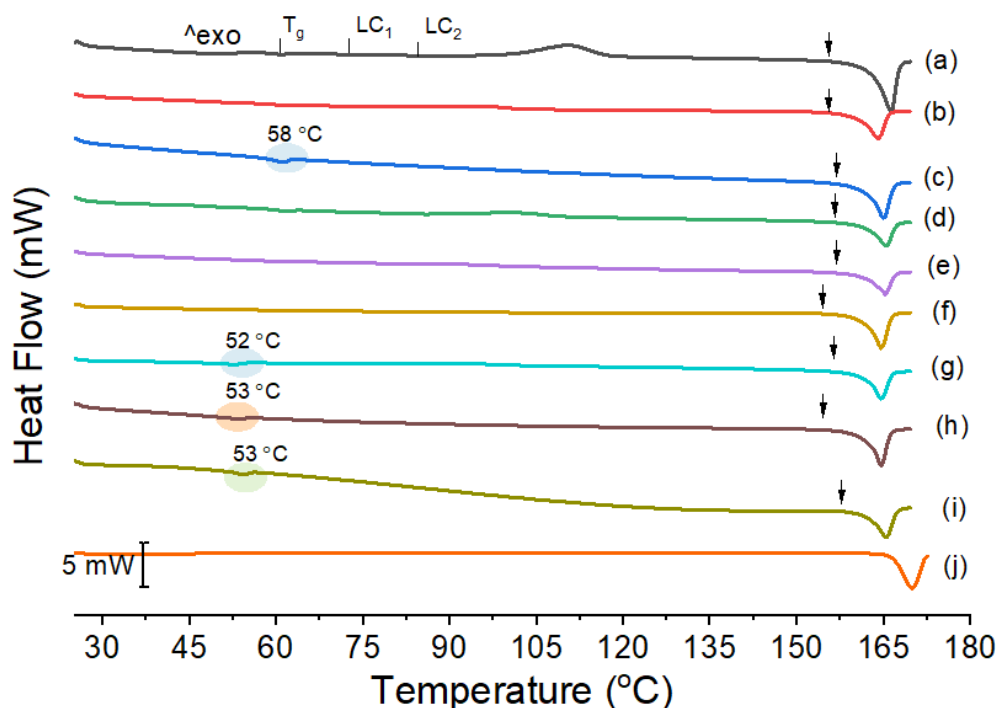
Fig. 3.2: DSC thermograms of (a) ITR NPs, (b) ITR-PEG 2 kDa, (c) ITR-PEG 10 kDa, (d) ITR-MPEG 2 kDa, (e) ITR-DMPEG 2 kDa, (f) ITR-4 ARM PEG 5 kDa, (g) ITR-4 ARM PEG 10 kDa, (h) ITR-Poloxamer 188, (i) ITR-Poloxamer 407, and (j) ITR as received. The highlighted areas indicate the melting point of the polymers. The arrows indicate the onset of the ITR melting.

Table 3.3: Summary of thermal events observed in DSC analysis of the ITR samples prepared with polymers.

Sample	Thermal event	Onset (°C)	Peak (°C)	Enthalpy (J/g)
ITR NP	T_g		60.8	
	LC_1		73.1	
	LC_2		85.2	
	Recrystallisation	99.7	110.9	41.74
	Melt	155	160	-66.80
ITR-PEG 2k	Melt	160.7	163.8	-68.7
ITR-PEG 10k	Endothermic	57.7	62.1	-5.58
	Melt	161.8	164.8	-62.5
ITR-MPEG 2k	Melt	162.0	165.3	-65.03
ITR-4 ARM PEG 5 kDa	Melt	161.7	164.5	-69.97
ITR-4 ARM PEG 10 kDa	Endothermic	47.5	52.6	-6.73
	Melt	161.9	164.5	-65.7
ITR-Poloxamer 188	Endothermic	50.6	53.8	-2.89
	Melt	161.9	164.4	-63.15
ITR-Poloxamer 407	Endothermic	51.7	54.3	-4.1
	Melt	162.0	165.1	-58.1
ITR	Melt	164,4	169,8	-63,28

In summary, this preliminary evaluation identified that the molecular weight and structure of the polymers affected properties of the produced ITR particles. NP dispersions with DMPEG 2kDa, Poloxamer 188 and Poloxamer 407 had larger particle sizes (> 800 nm), were not considered for further development, as NPs with mucoadhesive characteristics for oral administration should, ideally, have sizes below 500 nm (Ensign et al., 2012). Polymers with a molecular weight of 10 kDa had stronger interactions with the ITR particles therefore, PEG 10 kDa and 4-ARM PEG 10 kDa were selected for further analysis. MPEG 10 kDa was also included in the following studies to complement the analysis regarding the influence of the molecular structure of the polymers on the properties of ITR NPs.

3.3.2 Investigation of the mucoadhesive properties of PEGs

The QCM-D was used to investigate potential interactions of the polymers selected in the Section 3.3.1 (PEG 10 kDa, MPEG 10 kDa and 4 ARM PEG 10 kDa) with a deposited mucin layer.

For this experiment, the commercial mucin solution was used at 25 mg/L, which was demonstrated by Oh et al. (2015) to be able to form a visco-elastic film on the QCM-D sensor as well to attach polymer chains on its surface similarly to the porcine gastric mucin extracted in lab. Nevertheless, the authors observed lower viscosity in the commercial mucin, which was attibuted to the purification process.

The perfusion of mucin solution through the device induced a negative frequency shift (represented as blue lines in Fig. 3.3) until a plateau was achieved for all registered overtones, indicating that mucin was deposited on the sensor surface and a saturation point was achieved. Simultaneously, a positive dissipation shift (represented as red lines in Fig. 3.3) was also observed, reflecting the deposition of a viscoelastic layer on the surface of the crystal, as a dissipation shift higher than 1 ppm indicates that a non-rigid layer is deposited on the sensor (Oh et al., 2015). Indeed, mucin is known to be responsible for providing the viscoelastic characteristics of mucus and the deposited layer also had this characteristic (Bansil and Turner, 2006). Under this experimental circumstances, and for obtaining more accurate estimations of the mass and thickness of the layer deposited on the sensor, the data had to be processed using a mathematical model (Voight-Voinova viscoelastic model) that included the changes in the dissipation factor (Rodahl and Kasemo, 1995).

After preparing a stable mucin layer on the sensor, a test was conducted by rinsing the sensor with the saline solution. In a sequence, the solution of each polymer at different concentrations (0.1, 1, 10, 50 and 100 mg/mL) were perfused and, finally, the sensors were rinsed with saline again to establish the nature of the interaction polymer- mucin.
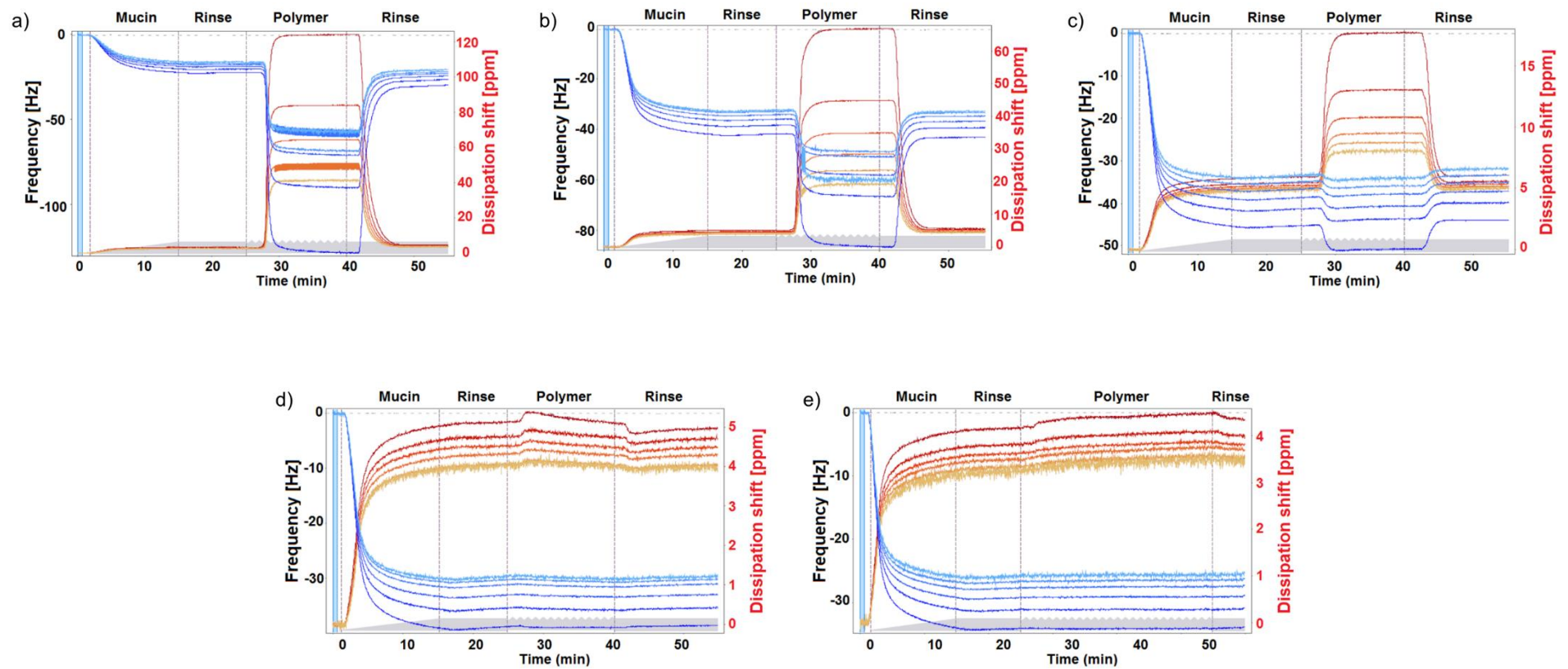
Fig 3.3: Representative traces for frequency (*f*) and energy dissipation (*D*) (from 3rd, 5th, 7th, 9th, 11th, and 13th overtones, respectively from darker to lighter tones) recorded by the device perfusing a solution of PEG 10 kDa at (a) 100mg/mL, (b) 50 mg/mL, (c) 10 mg/mL, (d) 1mg/mL and (e) 0.1mg/mL. Frequency is represented as the blue lines and its values shown in the left axis. Dissipation is represented as the red lines and its values shown in the right axis. The dot lines indicates the start of each stage.

3.3.2.1 Concentration effect

The analysis of the recorded overtones in the experiments carried out using polymer solutions at 0.1 and 1 mg/mL (Fig.3.3d and e) detected no variation in f and D when the polymers were perfused, indicating no mass adsorption at these concentrations. On the other hand, at higher concentrations, 10, 50 and 100 mg/mL, the experiments showed a clear shift of f and D (Fig. 3.3a-c), which returned to their original values in the following stage when the saline solution was perfused. This f and D shifts indicate that the polymers could interact with the mucin in concentrations above 1 mg/mL, however, as these parameters returned to their original values, their interaction occurred only during the polymer perfusion stage. A possible explanation for these findings is that at high concentrations, the polymer chains loops were forced into the mucin layer resulting in a temporary entanglement. As the H-bonds and van der Waals were too weak to anchor the polymers on the mucin layer, the subsequent saline perfusion could weaken this association and remove the polymers from the mucin layer. Moreover, analysis of the overtones showed different responses, resulting in a spread of their curves indicating that the polymers had superficial interactions with the mucin layer, as the overtones have specific penetration depth according to their frequency (Oh et al., 2015).

Statistical analysis of the mass adsorbed on the sensor in the different stages of the experiment are shown below (Fig. 3.4). This analysis revealed that the mass was significantly different only during the polymers perfusion stage at 10, 50 and 100 mg/mL, regardless of the polymer type (Fig 3.4). Therefore, the polymers deposited on the mucin layer were completely removed when the saline solution was perfused.
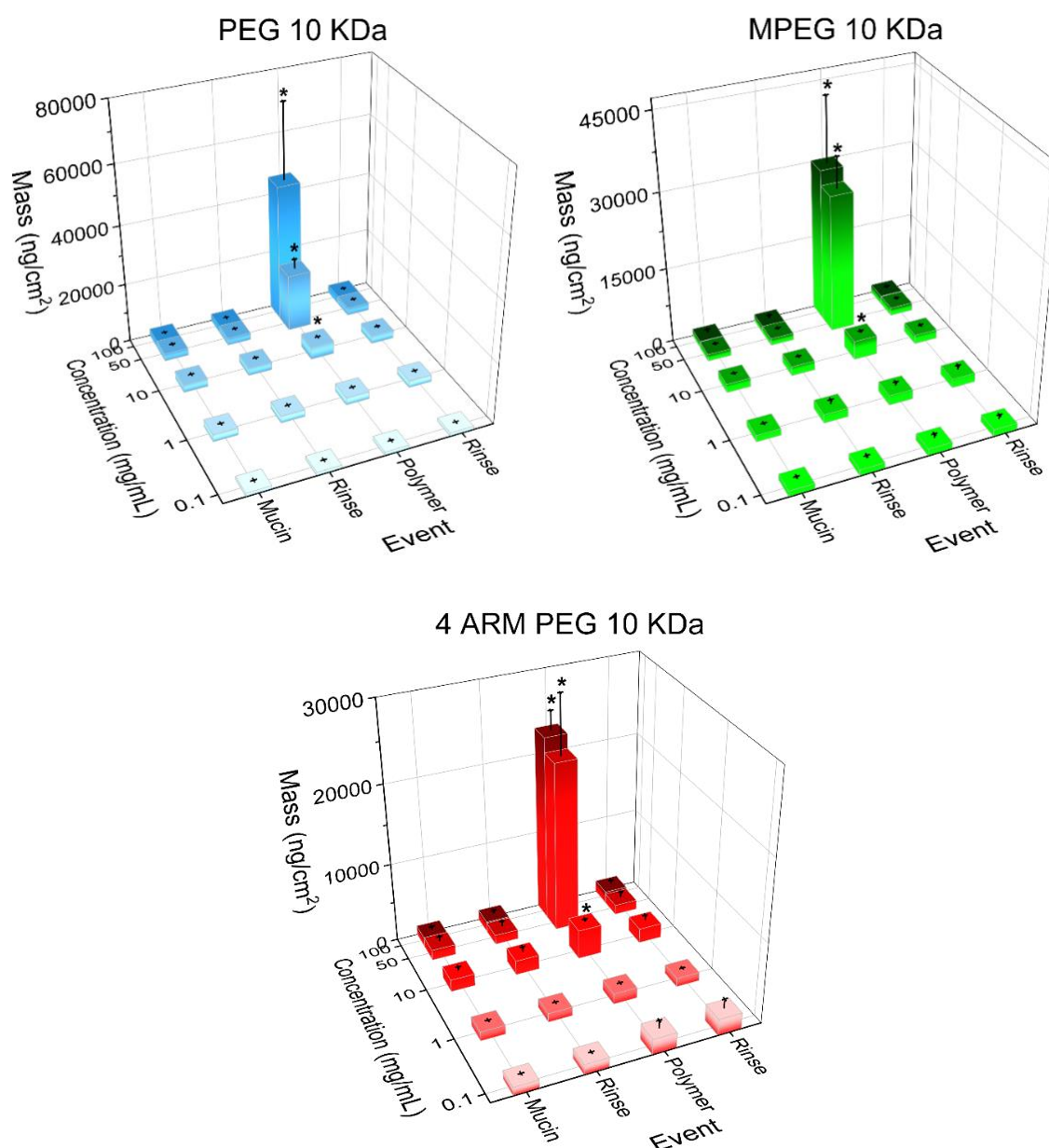
Fig 3.4: The mass adsorption (ng/cm^2) on the sensor after each event from analysis using PEG 10 kDa, MPEG 10 kDa and 4 ARMPEG 10 kDa at 0.1, 1, 10, 50 and 100 mg/mL. The (*) indicate significantly different stages.

3.3.2.2 Effect of the molecular structure of the PEGs

Polymers with mucoadhesive properties are normally cationic and examples of such polymers are chitosan, thiolated chitosan and polyallylamine (Oh et al., 2015). As PEGs are neutral polymers, they must be attached to the mucin layer, even temporarily, by other adhesion mechanisms (Liechty, W. B., Kryscio, D.R., Slaughter, B. V. and Peppas, 2010). As these polymers have elongated and flexible chains, they could assume different conformations in solution promoting their entanglement with the mucin fibres, which can be intensified by their multiple H-bond acceptors and the few terminal H-bond donors of the PEGs (Fig. 3.1) (Alessi et al., 2005; Norman et al., 2007; Serra et al., 2009).

Comparing the different PEGs, their *f* and *D* shifts were similar for the equivalent concentrations consequently, the calculated adsorbed mass during the polymer perfusion (Fig. 3.5) showed no significant difference, regardless of the concentration used. As a result, the structural differences of these PEGs, namely the number of terminal hydroxyl groups and linear or branched chains, had no influence on their interactions with mucin.
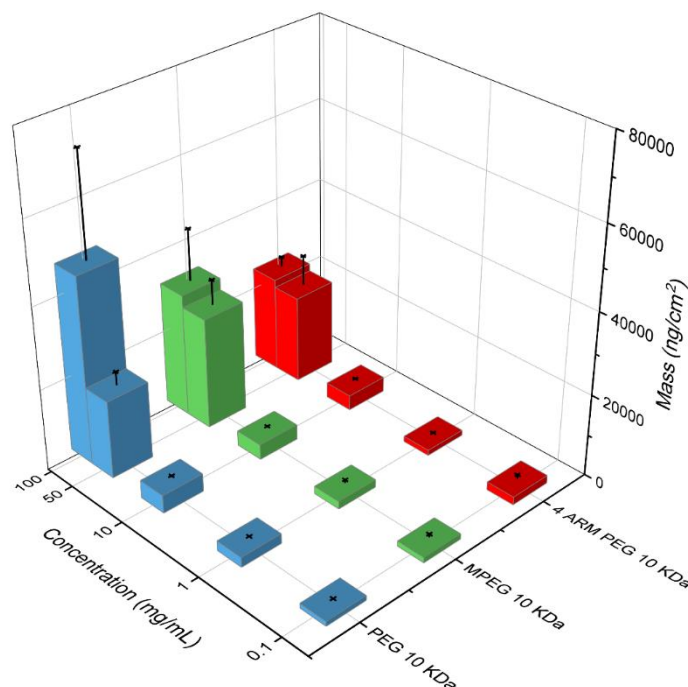
Fig 3.5: The mass adsorbed (ng/cm^2) during the polymer perfusion stage of PEG 10 kDa, MPEG 10 kDa and 4 ARM PEG 10 kDa solutions perfusion at 0.1, 1, 10, 50 and 100 mg/mL.

3.3.3 Characterisation of non-pegylated and pegylated ITR NPs

For the modification of the ITR NPs, the PEG 10 kDa, MPEG 10 kDa and 4 ARM PEG 10 kDa were used in ratios of API and polymer of 2-1 and 1-1. These PEGylated ITR NPs had their physicochemical and mucoadhesive properties analysed in comparison to the non-PEGylated ITR NPs.

3.3.3.1 Particle size, PdI and zeta potential

DLS analysis results (Table 3.4) showed that all NP samples were produced in a close size range, from 241 to 286 nm and no significant difference in relation to the particle diameters was found by one-way ANOVA. In addition, all NPs had low PdI (<0.1), thus they were considered monodisperse dispersions. As the ITR NPs had average sizes below 300 nm, these particles are smaller than the cut-off of the gastrointestinal mucus layer, 500 nm, which is one of the key properties required for NP penetration through this barrier (García-Díaz et al., 2018). In addition, the small sizes of these NPs should additionally increase ITR absorption and bioavailability (Rabinow, 2004).

The zeta potential of non-PEGylated ITR NPs was -30.1±1.5 mV (Table 3.4), providing adequate stability of the particles in the dispersion. In contrast, the surface charge of PEGylated NPs was partially neutralised, suggesting the presence of polymers on the surface of particles.

Table 3.4: Particle size (diameter), polydispersity index (PdI) and zeta potential measured by DLS for non-PEGylated and PEGylated ITR NPs.

Sample	Size (nm)	PdI	Zeta Potential (mV)
ITR NP	253 ± 16	0.054 ± 0.022	-30.1 ± 1.5
ITR-PEG 2-1 NP	255 ± 23	0.092 ± 0.083	-13.0 ± 1.0 *
ITR-PEG 1-1 NP	251 ± 10	0.023 ± 0.018	-10.4 ± 2.4 *
ITR-MPEG 2-1 NP	286 ± 22	0.053 ± 0.021	-18.6 ± 2.2 *
ITR-MPEG 1-1 NP	280 ± 13	0.042 ± 0.055	-21.1 ± 2.4 *
ITR- 4 ARM PEG 2-1 NP	241 ± 8	0.029 ± 0.017	-20.0 ± 4.0 *
ITR- 4 ARM PEG 1-1 NP	242 ± 4	0.050 ± 0.020	-17.0 ± 2.0 *

* value statistically different ($p < 0.05$) assessed by one-way ANOVA

3.3.3.2 Adsorption studies of PEGs on the surface of pre-made ITR NPs

As nanonised particles of APIs will normally not have their surface modified by covalent bonding with PEGs, the polymer adsorption ability on the surface of ITR NPs was evaluated (Van Eerdenbrugh et al., 2008). For this purpose, solutions of PEGs were added to the non-PEGylated ITR dispersion and the initial and final sizes of NPs were measured. For a proper interpretation of these results, some assumptions must be made. Firstly, the polymer adsorption is likely to occur randomly around the surface of the particles. Therefore, the thickness of the adsorbed layer is probably heterogeneous and should be referred to as an average. In addition, DLS analysis is an indirect measurement, wherein the Brownian movement of the particles are measured and used to estimate the size of a sphere having similar behaviour. Thus, the average thickness of the adsorbed layers was estimated by the particle radii difference before and after adding the polymers and compared to ITR blank NPs, which had no polymer added and were used as a control.

The results revealed that, indeed, the polymers were able to adsorb on the ITR NPs surface forming a coverage layer, however one-way ANOVA showed that the ITR-PEG 2-1 and ITR-4ARMPEG 2-1 were not statistically different from the control (Fig.3.6). Therefore, a higher concentration of these polymers might be necessary to form an adsorbed layer with significant thickness, in contrast to MPEG, which could produce layers with a considerable thickness when used in both proportions (2-1 and 1-1). This could have resulted from a higher affinity of the MPEG to the hydrophobic surface of the ITR NPs

promoted by the terminal methyl group of this polymer (McComiskey et al., 2018). Consequently, the molecular structure of the polymer had an important influence on the polymer surface adsorption.
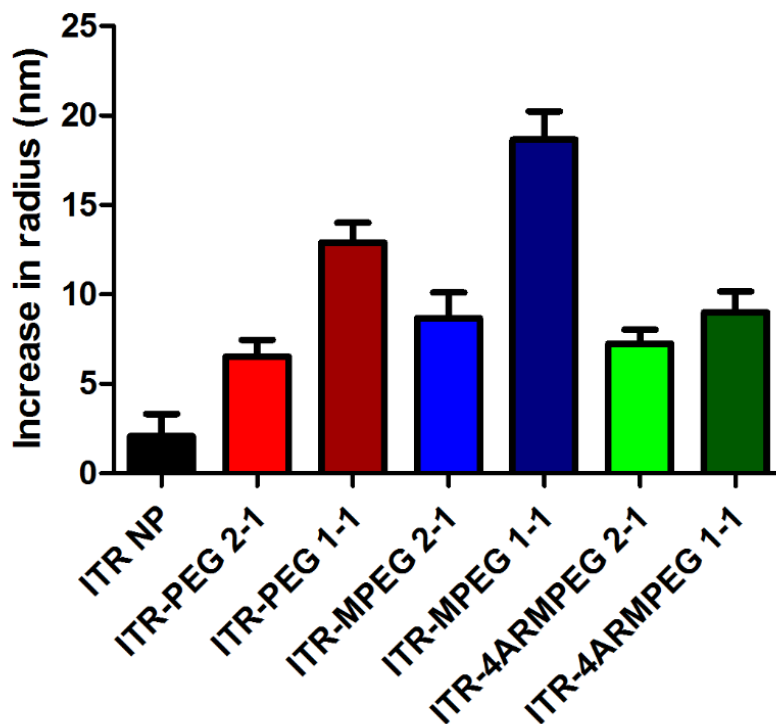
Fig. 3.6: The increase in the radius of NPs before and after polymer solution. ITR blank NPs were used as a control.

3.3.3.3 Solid-state characterisation of NPs

The diffractogram of the non-PEGylated, dried ITR NPs revealed the absence of well-defined Bragg peaks, except for a single peak at 6.2º 2θ (Fig. 3.7). The ITR phase presenting this pattern is described in the literature as being of a vitrified smectic mesophase (Chapter 2). This state of condensed matter is characterised by an orientational and one-dimensional positional orders, therefore they are less ordered than crystalline but more ordered than the amorphous state (Shalaev et al., 2016). The diffractograms of the PEGylated NPs samples also presented a peak at 6º 2θ, however of lower intensity. In addition, the samples of ITR-MPEG 1-1 NP, ITR-4 ARM PEG 2-1 NP and ITR-4 ARM PEG 1-1 NP had Bragg peaks with low intensities at 17.5, 18.1 and 20.6° 2θ, characteristic of the crystalline form of ITR (Fig. 3.7). Therefore, the use of PEG polymers during the HIEAN process led to NPs containing ITR in the smectic phase or a mixture of smectic and crystalline ITR. No crystalline polymers were detected by PXRD in the PEGylated NPs.
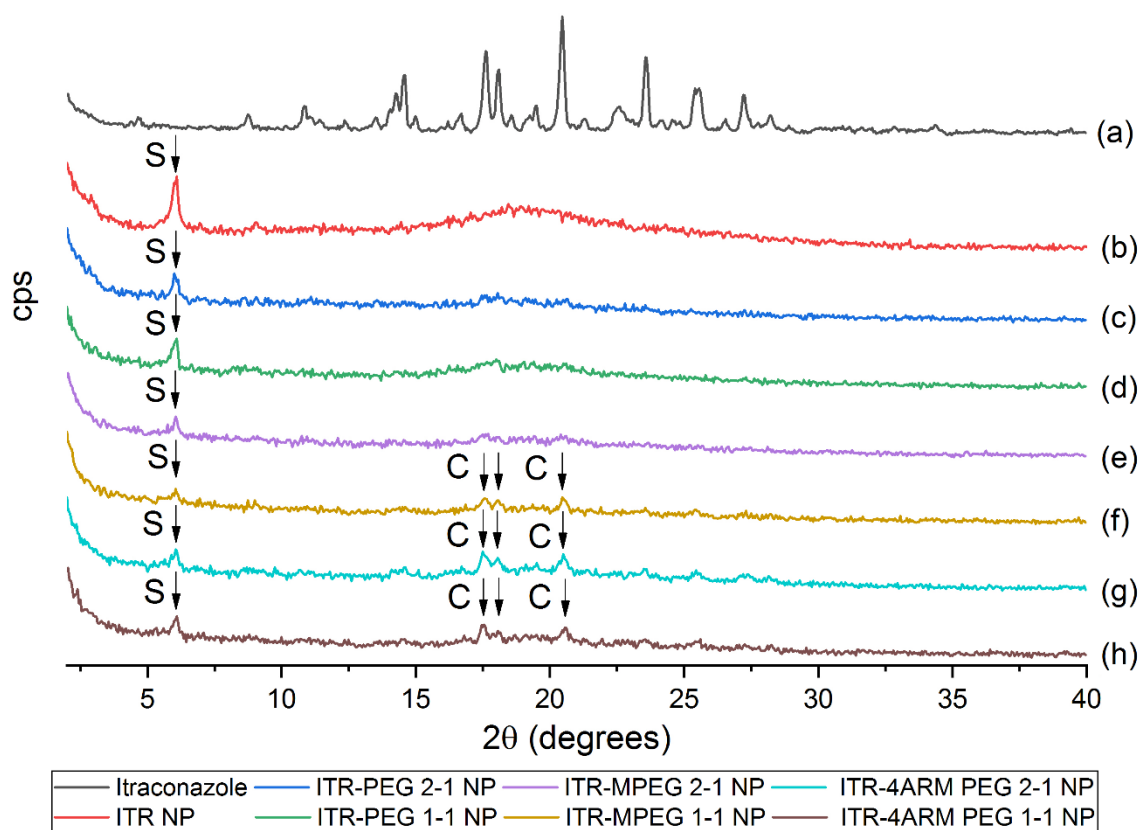
Fig. 3.7: X-ray diffractograms of (a) crystalline itraconazole, (b) dried non-PEGylated NPs, (c) ITR-PEG 2:1 NP, (d) ITR-PEG 1:1 NP, (e) ITR-MPEG 2:1 NP, (f) ITR-MPEG 1:1 NP, (g) ITR-4 ARM PEG 2:1, and (h) ITR-4 ARM PEG 1:1 NP. The arrows marked with "S" indicate the smectic peak and the peaks marked with "C" indicate crystalline peaks of ITR.

Thermal analysis of the ITR starting material crystalline powder and the produced NPs are shown in Fig 3.8. The thermogram of ITR "as received" showed a single melting endothermic peak with an onset at 163 ºC, indicating that the starting material was the pure crystalline polymorphic form I of ITR (Zhang et al., 2016). The thermograms of the non-PEGylated and PEGylated NPs showed additional thermal events, a transition at approximately 61 °C and ascribed to the glass transition event (T_g), followed by two almost imperceptible endothermic events at around 74 and 86 °C, corresponding to mesophase transitions from smectic to nematic and from nematic to isotropic liquid phases, respectively, (Kozyra et al., 2018) and then an exothermic crystallisation and a sharp melting peak. The DSC results confirm the outcome of PXRD analysis (Fig. 3.7) as ITR is present in its mesophase form. The liquid crystalline transitions were less visible, but still apparent in thermograms of PEGylated NPs, although, in most samples, the second transition was not visible, as it overlapped with the crystallisation exothermic event (Fig. 3.8 - highlighted in orange).
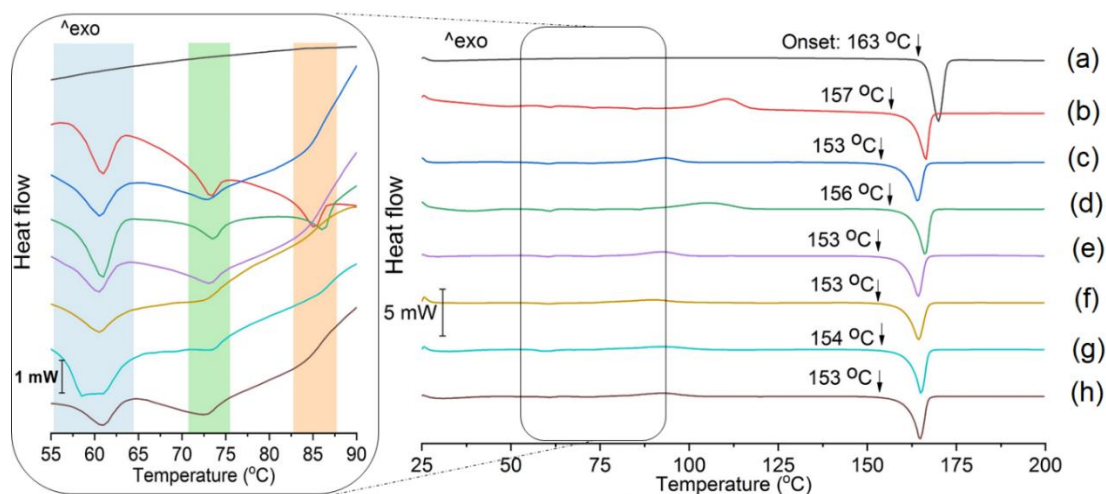
Fig. 3.8: DSC thermograms of (a) crystalline itraconazole, (b) dried non-PEGylated NPs, (c) ITR-PEG 2:1 NP, (d) ITR-PEG 1:1 NP, (e) ITR-MPEG 2:1 NP, (f) ITR-MPEG 1:1 NP, (g) ITR-4 ARM PEG 2:1, and (h) ITR-4 ARM PEG 1:1 NP. The area highlighted in blue indicates the temperature range of polymers melt and ITR T_g, in green the mesophase transition from smectic to nematic and in orange from nematic to isotropic liquid phase.

Table 3.5: Summary of thermal events observed in DSC analysis of the non-PEGylated and PEGylated ITR NPs.

Sample	Thermal event	Onset (°C)	Peak (°C)	Enthalpy (J/g)
ITR	Melt	164,4	169,8	-63,28
ITR NP	T_g		60.8	
	LC_1		73.1	
	LC_2		85.2	
	Recrystallisation	99.7	110.9	41.74
	Melt	155	160	-66.80
ITR-PEG 2-1	T_g		60.5	
	Recrystallisation	83.7	93.1	14.65
	Melt	160.3	164.0	-67.9
ITR-PEG 1-1	T_g		60.8	
	LC_1		73.6	
	LC_2		86.1	
	Recrystallisation	91.9	105.4	32.18
	Melt	162.6	165.8	-70.1
ITR-MPEG 2-1	Endothermic	55.8	60.5	-1.9
	Recrystallisation	76.9	90.5	19.4
	Melt	159.9	163.9	-73.0
ITR-MPEG 1-1	Endothermic	54.1	60.5	-2.0
	Recrystallisation	72.8	89.8	10.88
	Melt	160.3	164.3	-69.0

Table 3.5 (Continuation): Summary of thermal events observed in DSC analysis of the non-PEGylated and PEGylated ITR NPs.

Sample	Thermal event	Onset (°C)	Peak (°C)	Enthalpy (J/g)
ITR-4ARMPEG 2-1	Endothermic	56.3	58.5	-3.5
	Recrystallisation	80.1	93.2	22.5
	Melt	161.7	164.5	-72.8
ITR-4ARMPEG 1-1	Endothermic	57.3	60.8	
	Recrystallisation	80.2	92.8	19.0
	Melt	161.5	164.6	-72.3

A clear detection of the polymer presence in the thermograms of PEGylated NPs was difficult as the melting points of polymers, 59-62 °C for PEG, 60-65 °C for MPEG and 55-60 °C for 4 ARM PEG, overlap with the T_g event of ITR (Fig. 3.8). However, the polymer could be visible for sample ITR-PEG 1-1 as a larger enthalpy of the relaxation peak underlying the T_g (2.27 J/g in comparison to 1.43 J/g for ITR NP, Table 3.5) or as a small endothermic peak, especially evident for sample ITR-4 ARM PEG 2-1, where a peak 58.5 °C preceding the T_g event at 61 °C can be seen (Fig. 3.8g). Other alterations in the thermograms could also be associated with the PEG presence in NPs, as no polymer decomposition was detected up to 200 °C by thermogravimetry. For instance, the ITR melting peak (Fig. 3.8a), which had the onset temperature shifted from around 163 °C in the starting ITR material to 157 °C in the non-PEGylated NP sample, was even further depressed in the PEGylated NPs. The lowest onset (at 153 °C) was observed for samples ITR-PEG 2-1, ITR-MPEG 2-1, ITR MPEG 1-1 and ITR-4ARMPEG 1-1. The melting point depression occurs when a drug and the polymer are miscible resulting in the chemical potential reduction of this mixture in relation to the chemical potential of the pure drug. As the melting point occurring when the chemical potential of a compound equals the chemical compound of its molten form the melting point of a miscible of pair of drug and polymer mix is depressed in relation to an immiscible pair (Marsac et al., 2009).

In summary, the DSC analysis confirmed the presence of polymer in the NP samples. Moreover, DSC and PXRD also detected that PEGs increased of the molecular organisation of ITR molecules in the NPs, as the PEGylated NPs were found more crystalline than the non-PEGylated ITR NPs.

3.3.3.4 Morphological analysis

The morphology of the non-PEGylated and PEGylated ITR NPs was assessed by SEM (Fig. 3.9). The images revealed that precipitation of ITR in the absence of any polymer resulted in homogenous, spheroidal in shape particles (Fig. 3.9a). Similar morphologies

were also observed for the PEGylated samples ITR-PEG 2-1, ITR-PEG 1-1 NP and ITR-MPEG 2-1 (Fig. 3.9b, c and d). In contrast, samples ITR-MPEG 1-1, ITR-4 ARM PEG 2-1 and ITR-4 ARM PEG 1-1, were mixtures of spherical and flaky particles (Fig 3.9b, d and e).
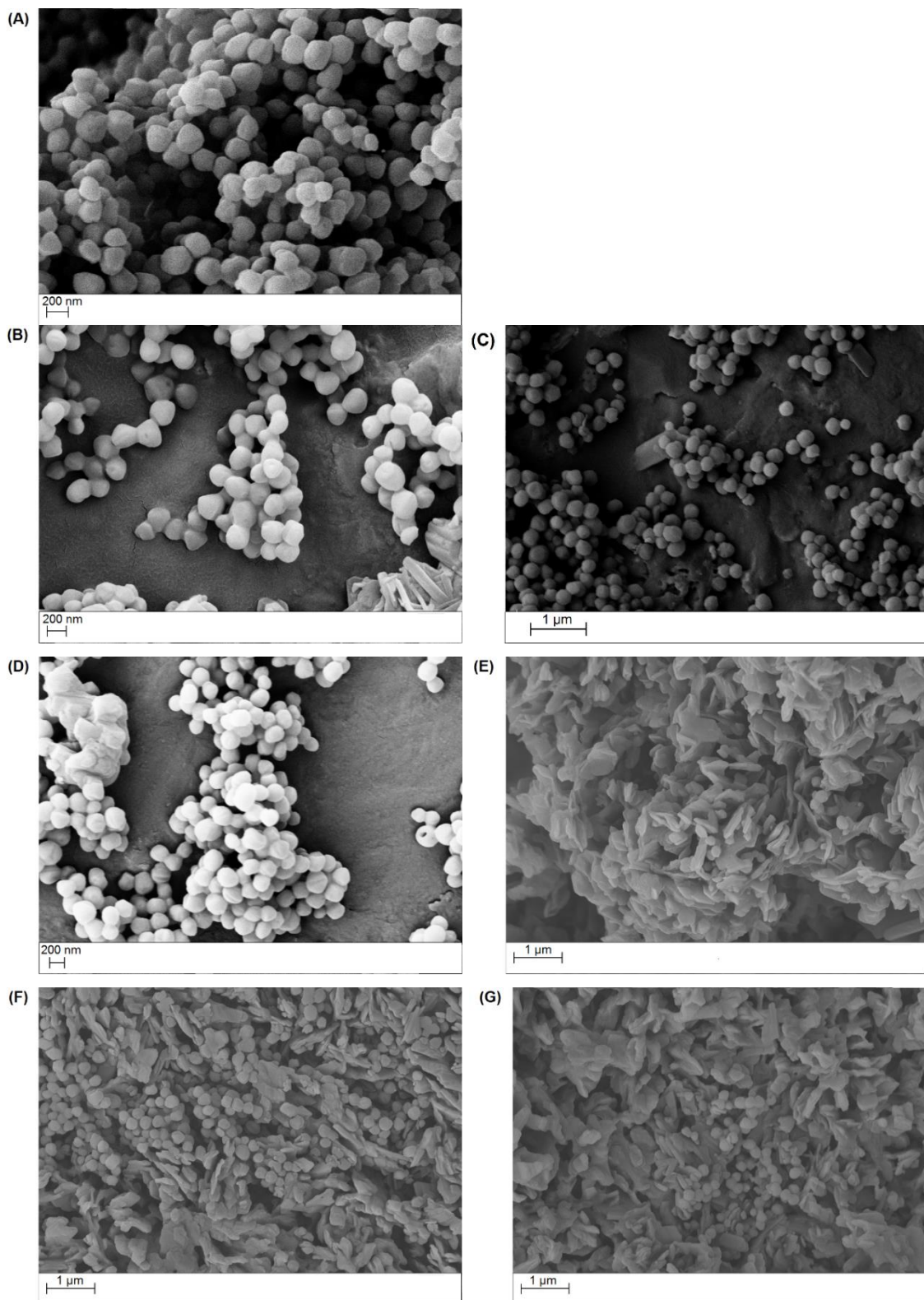
Fig. 3.9: SEM images of: (a) non-PEGylated ITR NP and the PEGylated samples: (b) ITR-PEG 2-1, (c) ITR-PEG 1-1, (d) ITR-MPEG 2-1, (e) ITR-MPEG 1-1, (f) ITR- 4 ARM PEG 2-1, (g) ITR- 4 ARM PEG 1-1.

These images show the influence of the polymers on the morphology of the PEGylated particles, which was possibly caused by adsorption of polymer on the more hydrophobic face of the crystal, inhibiting its growth while the non-adsorbed faces continued to elongate (Sriamornsak and Burapapadh, 2015). Another possibility for these elongated shapes observed in the ITR-MPEG 1-1, ITR-4 ARM PEG 2-1 and ITR-4 ARM PEG 1-1 SEM images could be a result of their increased crystallinity of the API. As observed in the PXRD analysis (Fig. 3.7), these samples had patterns indicating the presence of crystalline material, and, indeed, the crystalline ITR is normally observed having a bladelike shape, similar to those observed in the SEM images (Mugheirbi and Tajber, 2015).

3.3.3.5 Stability of NPs in liquid dispersions

The stability of the non-PEGylated and PEGylated ITR NPs in dispersions was assessed, without any sample preparation, over time and the results are shown in Fig. 3.10. After the period of 21 days, the particle size of non-PEGylated ITR NPs remained unchanged (229±4 nm after the preparation and 230±1 nm after 21 days of storage). This size conservation likely resulted from electronic repulsion promoted by surface charge reflected in low zeta potential (Table 3.4). On the other hand, the PEGylated NPs conserved their sizes up to 7 days (Fig. 3.10). At 21 days, most of the samples have visibly developed flocs, but were re-suspendable, with the exception of ITR-PEG 2-1 NPs, which had non-resuspendable sedimentation (cake) and was excluded from the last measurement. The explanation for the reduced stability of the PEGylated ITR NPs might be related to the partial neutralisation of their zeta potential by the presence of PEG, consequently, the electrostatic repulsive interactions were reduced. The adsorption of polymer chains may have provided some stabilisation by steric hindrance. However, this was inefficient compared to the electrostatic stabilisation, hence the particles underwent aggregation and sedimentation.
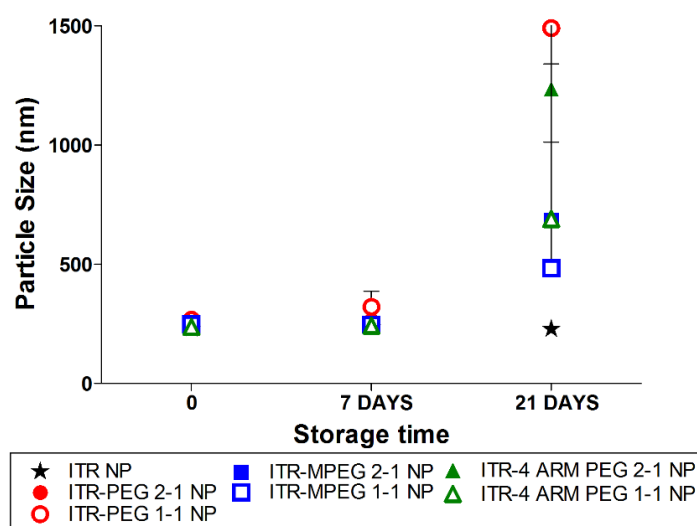
Fig. 3.10: Stability of the dispersed non-PEGylated and PEGylated ITR NPs.

3.3.3.6 Investigation of mucoadhesive properties of the non-PEGylated and PEGylated ITR NPs

Having observed that the PEG polymers can result in alterations of physicochemical properties of the NPs, it was of interest to investigate if those modifications could impact the manner they interact with mucin.

DLS analysis of the filtered mucin showed a very polydisperse mixture of compounds having particles with volumetric sizes distribution from smaller than 50 nm up to 400 nm (Fig. 3.11). The non-PEGylated ITR NPs incubated in the mucin dispersion conserved their average size, presenting mostly unchanged volumetric distribution even after a longer exposition (2 hours) (Fig. 3.11). Large particles (> 2000 nm) were also present, but it was likely to be resulted from the agglomeration of the mucin compounds, as no clear alteration of the NPs population was observed. This result suggests absence of interactions between the non-PEGylated ITR NP and the mucin dispersion, possible due to the strongly charged surface of the particles (-30.1 mV, Table 3.4) with repulsive electrostatic forces preventing interactions with the mucin, which is also negatively charged (Bogataj et al., 2003)

On the other hand, the incubation of PEGylated NPs in the mucin dispersion resulted in the reduction of peak and increase of average size in the later measurements that could be promoted by the interaction of the polymers with the mucin compounds (Fig. 3.11). This behaviour might have been caused by the partial surface charge neutralisation (Table 3.4) despite the presence of PEGs that should have afforded them mucopenetrative characteristics (Xu et al., 2015). It is possible that the polymer chains on the surfaces of NPs did not adopt the required conformation known as "dense brush" leading to the entanglement of mucin chains (Huckaby and Lai, 2018).

Although the DLS analysis being able to provide valuable information regarding the interactions of the NPs and mucin in dispersion, this technique may be inaccurate to evaluate the particle size distribution in case of very polydispersed samples (Bhattacharjee, 2016). This is because the diffracted light from large particles could obfuscate the detection of smaller. Therefore, further analysis using other methods, such as the NTA are required to improve this discussion.
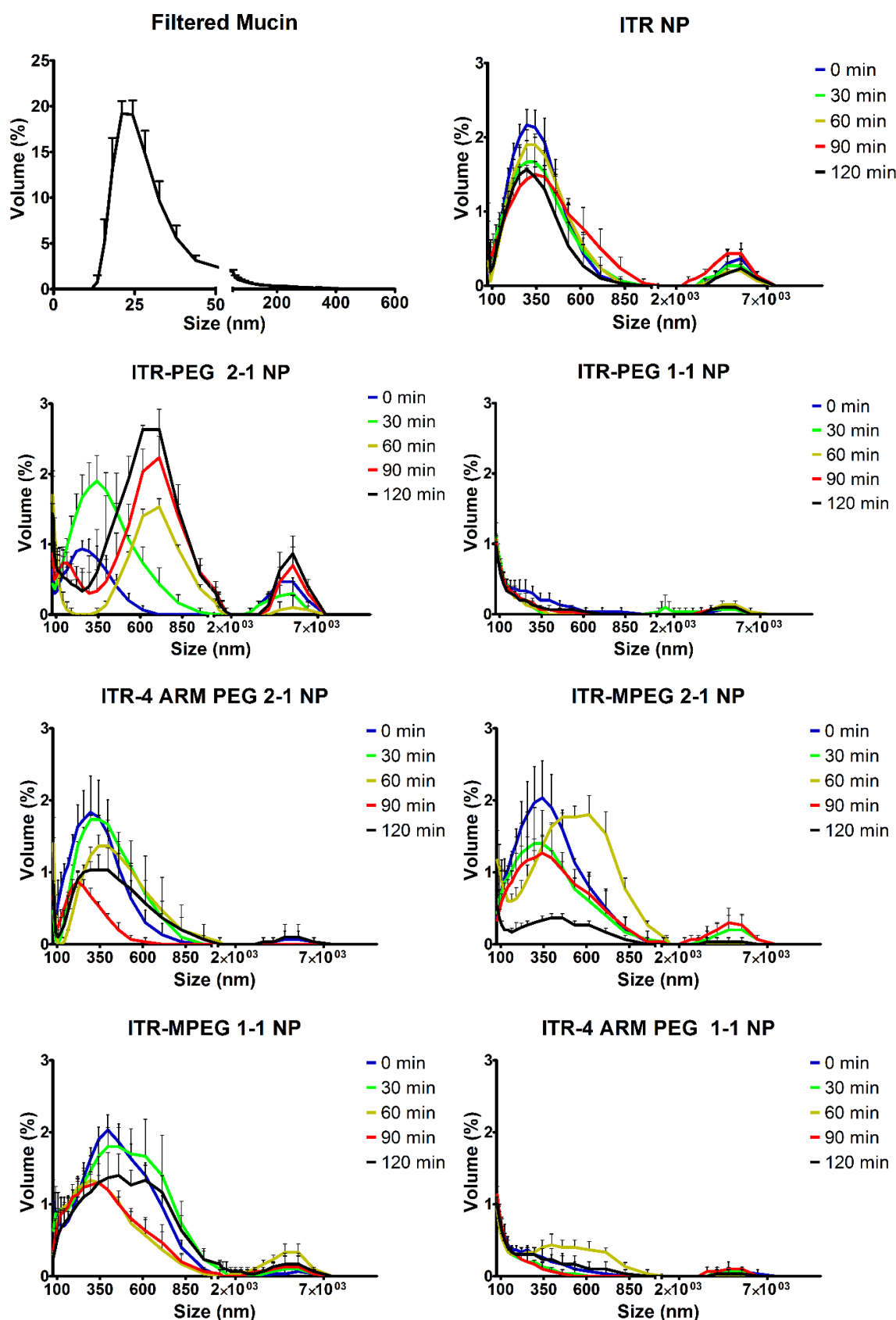
Fig. 3.11: Particle size distribution (by DLS) of the mucin dispersion, as well as the PEGylated and non-PEGylated ITR NPs, incubated with the mucin dispersion.

NTA was used to evaluate different properties of the NPs, including particle size, concentration and diffusion in a 30 mM saline solution and stability up to 120 min of

incubation in a 12.5 µg/mL mucin dispersion. In general, the NTA has remarkable advantages over the DLS, including a broader size range detection, higher resolution and it allows to visualize the sample (Filipe et al., 2010). On the other hand, the NTA may requires a more refined sample preparation, as it has a more limited range of sample concentration that the instrument is able to analyse. Also, NTA analysis are more time consuming and less reproducible than DLS analysis (Filipe et al., 2010). Therefore, the combination of both techniques could provide a more accurate overview of the samples.

The particle size analysis aimed to detect potential changes in size in the saline solution and the mucin dispersion. The results were analysed using student's t-test with 95% of confidence and no significant changes in size were observed (Table 3.6). Therefore, no indication of particle aggregation or adsorption of mucin chains were observed.

Table 3.6: D_m/D_s, particle size of non-PEGylated and PEGylated ITR NPs in saline solution, in mucin dispersion and p-value of sizes comparison.

Sample	D_m/D_s	Particle size in saline[*] (nm)	Particle size in mucin[**] (nm)	p-value
ITR NP	1.27	318.5 ± 42	347 ± 94	0.659
ITR-PEG 2-1 NP	1.05	389 ± 58	409 ± 193	0.873
ITR-PEG 1-1 NP	1.30	303 ± 66	315 ± 91	0.861
ITR-MPEG 2-1 NP	0.83	260.5 ± 9	347 ± 99	0.205
ITR-MPEG 1-1 NP	0.86	258 ± 14	221 ± 81	0.627
ITR- 4 ARM PEG 2-1 NP	0.84	215 ± 23	278 ± 59	0.174
ITR- 4 ARM PEG 1-1 NP	0.95	225 ± 5.5	249 ± 87	0.666

[*] 30 mM NaCl aqueous solution; [**] after 120 min of incubation in 12.5 µg/mL mucin dispersion.

A significant advantage of NTA over DLS analysis is the possibility of measuring the concentration of particles in dispersion (Filipe et al., 2010). The analysis of the NPs concentration during the incubation in a mucin dispersion showed a similar trend for all samples and a continuous decrease in NP concentration over time (Fig. 3.12). A decrease in the concentration of dispersed particles is normally caused by their aggregation forming larger entities or could be due to the dissolution of these particles. Considering that the NPs were prepared having a ITR final concentration of 0.2 mg/mL, which, then, was diluted into 5 µg/mL for the NTA tests, one could assume that the observed NP concentration decrease was likely to be caused due to the particles dissolution, as the media was no longer saturated after the dilution. Another possible explanation is the attachment of the NPs on the tubes of the instrument through the NTA system. Nevertheless, both, non-PEGylated and PEGylated ITR NPs are expected to at least partially dissolve after oral administration and the undissolved particles will be subjected to transcellular uptake either by enterocytes, and M cells in Peyer's patches (Ensign et al., 2012; Gao et al., 2012)
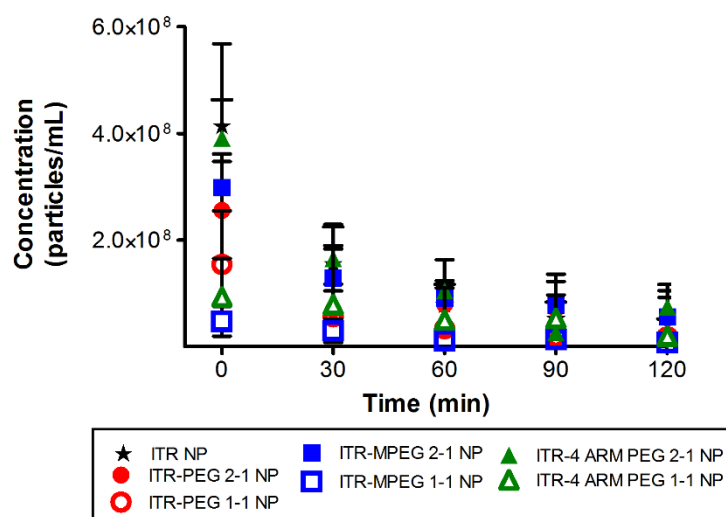
Fig. 3.12: Concentration of dispersed NPs (5 µg/mL) in a 12.5 µg/mL mucin dispersion measured by NTA at 0, 30, 60, 90 and 120 min of incubation.

NTA also was used to compare diffusion of the NPs in the saline solution and the mucin dispersion. In this technique, videos of particles in dispersion are recorded and processed by measuring the 2D displacement of the particles during a period of time, also known as mean square displacement (Gallego-Urrea et al., 2011), and related to the diffusion coefficient (*D*):

$$\bar{x}^2 + \bar{y}^2 = 4 \cdot D \cdot t \qquad \text{(Eqn. 3.1)}$$

where $\bar{x}$ and $\bar{y}$ are the displacement in the axis x and y and *D* is measured during a time period *t*. In a hypothetical situation where the NPs do not significantly interact with their surroundings, these particles present completely free and random movements known as Brownian motions. However, in the presence of compounds able to interact with those NPs, those movements are modified resulting in non-Brownian motions (Newby et al., 2018). This is the case for mucoadhesive NPs, which have their diffusion more constrict in a mucus layer in relation to water as their movements are hindered by their interactions with the mucin chains. In fact, this variation in movement can be detected by NTA and compared using the diffusion coefficient of the particles in mucin (D_m) in relation to the same particles in saline (D_s) (Lai et al., 2009; Maisel et al., 2016; Wang et al., 2008; Xu et al., 2015).

The calculated D_m/D_s ratio of the non-PEGylated and PEGylated ITR NPs (Table 3.4) revealed that ITR-PEG 1-1 NP had the highest ratio while ITR-MPEG 2-1 had the lowest, respectively 1.30 and 0.83. The observed variation could be due to the zeta potential influence (Table 3.4), as partial neutralisation of the PEGylated NPs reduced the electronic repulsive forces that prevent the mucin adsorption on the surface of these particles, consequently reducing the diffusion in this media (Svensson and Arnebrant, 2010). However, as all the D_m/D_s values are close to 1, it can be assumed that the samples have

comparable diffusion in both media and can be considered as having mucopenetrative properties (Lai et al., 2009).

The QCM-D was used to investigate potential interactions of the NPs with a deposited mucin layer. The adsorbed mucin layers had 12.0±1.3 nm of average thickness that was unaffected after the perfusion of 30 mM NaCl solution (12.1±1.3 nm, p-value = 0.934).
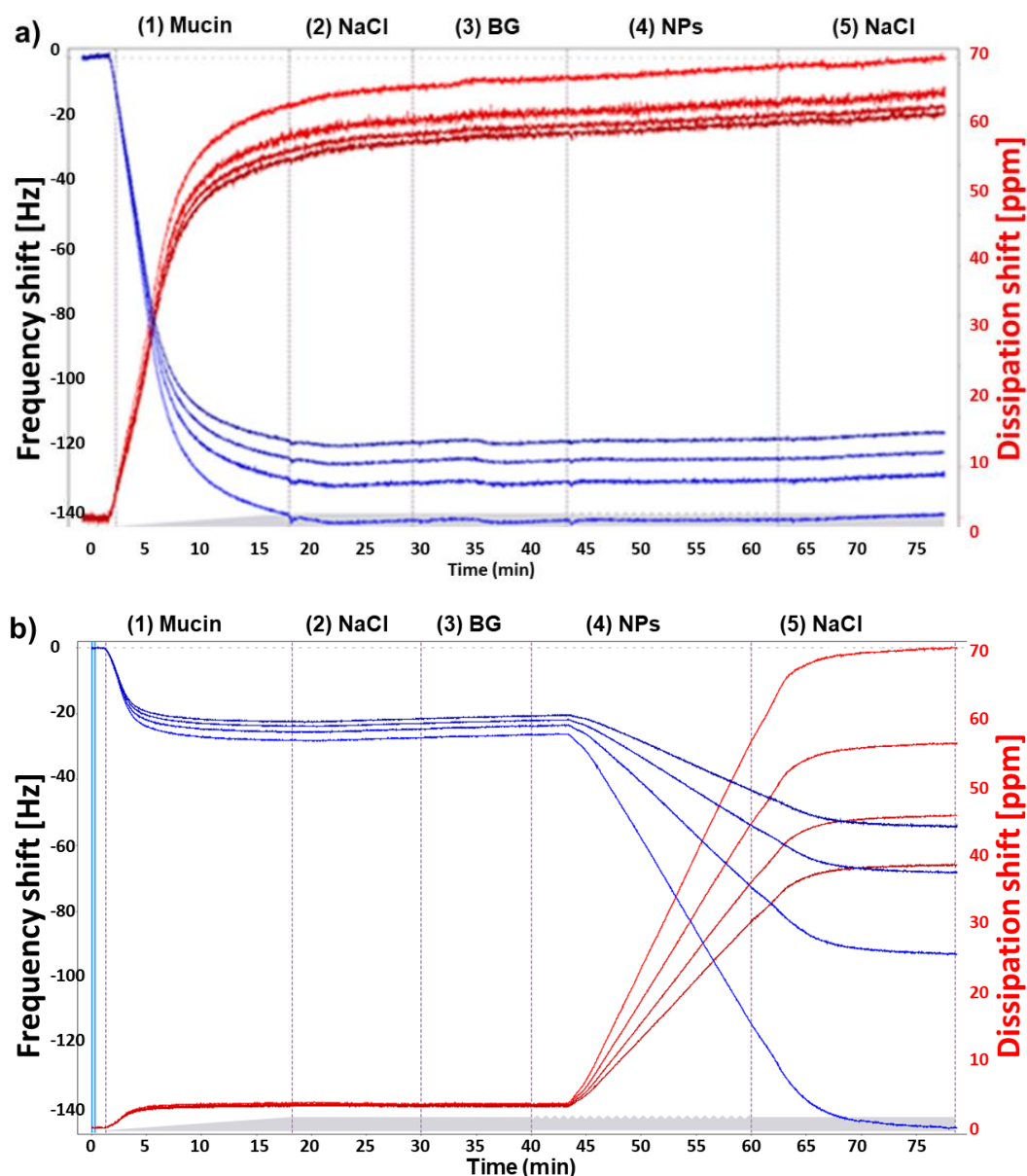
Fig. 3.13: (a) Representative traces for frequency (f) and energy dissipation (D) (from the 3rd, 5th, 7th and 9th overtones) recorded by QCM-D. Frequency is represented as a blue line and its values are shown in the left axis. Dissipation is represented as a red line and its values are shown in the right axis. The dot lines indicate the start of each step. Step 1: Perfusion of mucin results in the deposition of mucin on the sensors as represented by changes in f and D. Step 2: perfusion of 30 mM NaCl. Step 3: perfusion of background (BG) solution. Step 4: perfusion of NPs. Step 5: perfusion of 30 mM NaCl. Note that the absence of changes in f and D after the adsorption of mucin through the different steps indicates that the NPs and none of the solutions perfused during the experiment exert interactions with the mucin layer. (b) Results of polystyrene NPs (positive control) indicating interactions with the mucin layer.

Once a reproducible a stable mucin layer was achieved, the effect of the different solutions and NPs perfused in further steps (Fig. 3.13 a) was also analysed using the Voight viscoelastic model to estimate the adsorbed mass on the sensor after each event (Appendix 1). In the meanwhile, a positive control, a polystyrene NPs dispersed in 30 mM NaCl solution was used to assure the adhesive properties of the mucin layer (Fig. 3.13b).The results obtained revealed no significant changes in the mass after the perfusion of the non-PEGylated ITR NPs, indicating that the particles were not interacting with the mucin layer. This finding strongly correlates with the results obtained by DLS and NTA, wherein attractive interactions were not formed between these NPs and the mucin compounds. Therefore, the non-PEGylated ITR NPs can be considered as having mucopenetrative potential. Interestingly, our results differ with previous studies as the assumption is that nanonised particles are generally mucoadhesive (Gao et al., 2012; Shah et al., 2016). The perfusion of PEGylated NPs did not reveal either significant increase of the adsorbed mass indicating the absence of interactions of those NPs with the mucin layer. These results agree with those obtained by NTA (Table 3.6) but are in contrast with the results of DLS analysis (Fig. 3.11). As PEGylated ITR NPs had their zeta potential partially neutralised (Table 3.4) reducing the repulsive electrostatic forces, some weak interactions with the mucin chains in the stationary fluid were enabled, as in the DLS essay only a low shear stress is present. On the other hand, these interactions were too weak to immobilise the NPs on the mucin layer and, therefore, unable to induce significant changes under flow conditions, as it happened during NTA and QCM-D experiments, where higher shear stress was present.

Hence, for a more complete overview of the manners NPs interact with the mucin, multiples aspects should be considered, such as the adhesive and diffusion properties of the investigated material. Nonetheless, the accurate classification regarding the muco-penetrative or adhesive properties of NPs is dependent to the evaluation of further aspects intrinsic of *in vivo* situation, such as water movement in gastrointestinal environment and three-dimensional arrangement of mucus layer to name a few (Netsomboon and Bernkop-Schnürch, 2016).

3.4 Conclusions

Preliminary evaluation showed that Poloxamer polymers were unsuitable candidates for modification of ITR NPs. The most promising molecules were PEG 10 kDa and 4 ARM PEG, as they resulted in NPs with sizes below 500 nm, suitable for oral administration. These polymers could be detected by thermal analysis suggesting stronger interaction with ITR.

The evaluation of the mucoadhesive properties of PEG 10 kDa, MPEG 10 kDa and 4 ARM PEG 10 kDa showed that only at very high concentrations of 10, 50 and 100 mg/mL the polymers could interact with the mucin layer. However, the interactions were weak, and the saline solution perfusion was able to reversibly remove the polymers from the QCM sensor.

Following preliminary studies, non-PEGylated and PEGylated ITR nanoparticles were produced using an optimised method of nanoprecipitation in antisolvent. The PEGylation of ITR NPs had no impact on the average particle size and PDI. However, the zeta potential of the PEGylated NPs was partially neutralised, resulting in reduced stability in dispersion, as the steric hindrance provided by the adsorbed polymer was not as effective as the electrostatic repulsive forces in the non-PEGylated NPs.

The analysis of the solid-state properties of the non-PEGylated ITR NPs indicated this sample as being a smectic mesophase, in contrast to some PEGylated NPs that were more crystalline. Furthermore, the ITR-MPEG 1-1 NP, ITR-4 ARM PEG 2-1 NP and ITR-4 ARM PEG 1-1 NP samples also had particles shapes affected by the polymers, leading to the formation of a mix of spherical and flaky shapes, instead of the homogeneous spherical particles as in the non-PEGylated ITR NPs.

The investigation of the mucoadhesive properties revealed no evidence that the non-PEGylated ITR NPs could interact with mucin, therefore, this system was considered as having a mucopenetrative potential. On the other hand, the PEGylated NPs were seen to exhibit mucoadhesive potential in stationary conditions (DLS analysis), but when flow conditions were applied (NTA and QCM-D) the particles had mucopenetrative properties.

As demonstrated in this work, the investigation of the mucoadhesive properties of nanoparticles should not be limited to a single technique, but multiple aspects, including particles diffusion, attachment and aggregation, should be considered for more accurate classification of a system as being mucopenetrative or mucoadhesive.

Chapter IV: Identification and physicochemical analysis of itraconazole cocrystals

4.1.Introduction

In Chapters 2 and 3, the properties of ITR were modified, firstly, by preparing nanoparticles composed entirely by the API, and, then, by PEGylating these particles. In this chapter, a different modification of the solid-state properties was used that involved conversion of ITR into a cocrystal.

A pharmaceutical cocrystal can be defined as a multicomponent crystal wherein at least one is the active pharmaceutical ingredient (API) and the other(s), the coformer(s) are in a well-defined stoichiometric and bonded by non-covalent interactions (Schultheiss and Newman, 2009; Thakuria et al., 2013). These interactions are mainly intermolecular hydrogen bonds between functional groups forming a "supramolecular synthons", moreover, additional weaker interactions as van der Waals forces, π-stacking or halogen bonds also aid to stabilize the cocrystal (Berry and Steed, 2017; Desiraju, 1995). Ionic cocrystals are a subgroup of the molecular cocrystals, which have ionised coformers in their multicomponent structure instead of having neutral molecules (Duggirala et al., 2016). Consequently, charge assisted hydrogen bonds contribute to the stabilisation of the crystal structure. The purpose of ionic cocrystals is to use the advantages of salt and cocrystallisation to improve the characteristics of an API (Cerreia Vioglio et al., 2017).

First ITR cocrystals were produced combining this API with dicarboxylic acids used as coformers, including fumaric acid, succinic acid, L-malic acid, L-tartaric acid, D-tartaric acid and DL-tartaric acid (Remenar et al., 2003). The Remenar's work also reported a remarkable improvement of ITR dissolution with approximately a 20-fold enhancement for the cocrystals prepared with L-malic and L-tartaric acids, which had dissolution profiles comparable to the commercial form of ITR (Sporanox® capsule 100 mg - Jassen Pharmaceutica).

Structural analysis of ITR and succinic acid cocrystal revealed that this form has a trimeric building block where two molecules of the API were oriented antiparallel and bridged by the coformer. The main interaction found to be responsible for the intermolecular arrangement of this structure were H-bonds formed by the hydroxyl moiety on both sides of the acid with the N4 of the 1,2,4-triazole ring of each ITR molecule (Fig. 4.1) (Remenar et al., 2003). Further analysis of this cocrystal revealed an additional weak halogen bonding of the dichlorophenyl group of one ITR molecule that interacts with the oxygen or nitrogen atoms of the 1,2,4-triazol-5-one ring of the adjacent ITR molecule causing a tilt of the *sec*-butyl groups in these molecules (Nonappa et al., 2013).
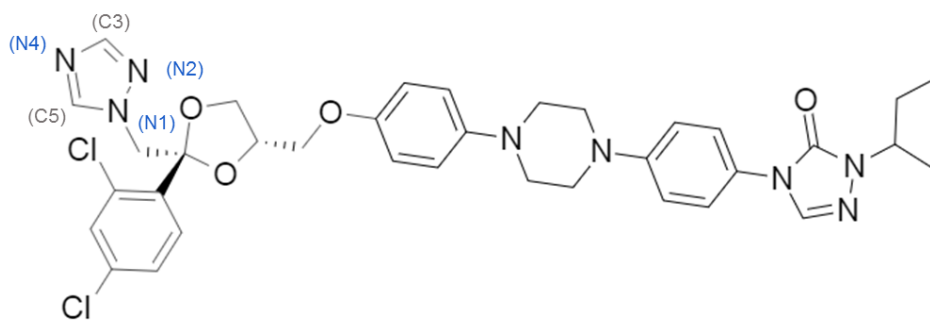
Fig. 4.1: Representation of the molecular structure of ITR.

Until recently, the ITR cocrystals reported in literature were produced using aliphatic dicarboxylic acid with up to seven carbons in their chain (Shevchenko et al., 2013). However, an ITR cocrystal with suberic acid, an aliphatic dicarboxylic coformer with 8 carbons in its chain, could also be produced by rapid solvent removal (Weng et al., 2019). Therefore, this chapter aimed to identify new ITR cocrystals by two experimental screenings: one in Trinity College Dublin ("Experimental Screening 1") and another in an R&D department of a pharmaceutical company, Zentiva (Prague, Czech Republic) referred to as "Experimental Screening 2". In the first screening, "Experimental Screening 1", the objective was to evaluate whether aromatic coformers with functional groups other than aliphatic dicarboxylic acids (Fig.4.2) could form ITR cocrystal. The second screening, "Experimental Screening 2", was part of the activities performed during the industrial secondment and used standard procedures of the company. In this screening, the objective was to investigate a new range of coformers, including acids, amino acids and salts (Fig. 4.3). In this case, a range of salts were used to evaluate if ITR could form ionic cocrystals, as no information is currently available in the literature regarding ionic cocrystals of ITR.
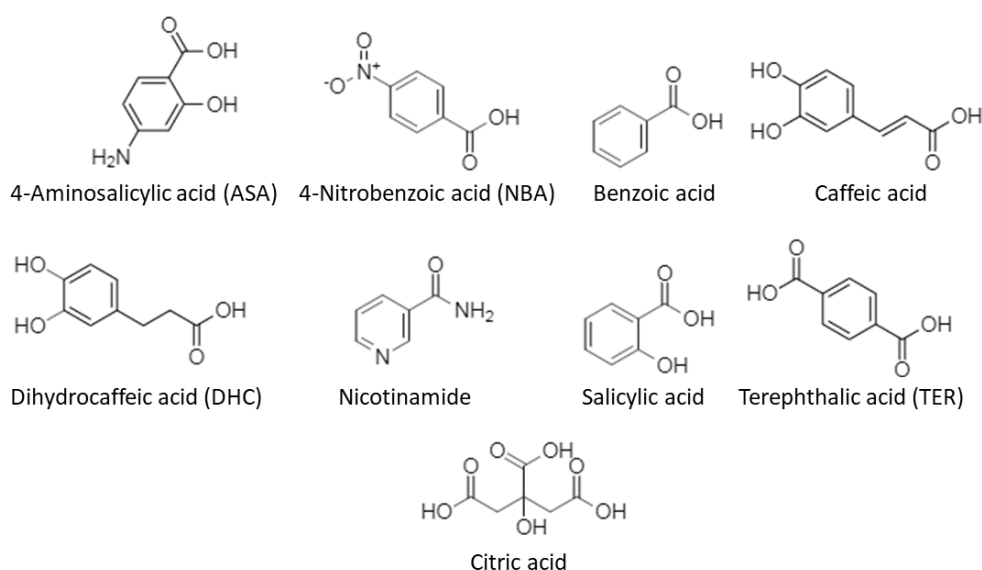
Fig. 4.2: Coformers used in the "Experimental Screening 1".

Acids:

Acetic acid   Benzoic acid   Citric acid   Nicotinic acid

Oxalic acid   Succinic acid   Tartaric acid   Terephthalic acid

Amino acids:

L-Alanine   Betaine   Glycine   L-Proline

Sarcosine   L-Serine   Valine

Salts:

Ammonium acetate   Sodium benzoate   Sodium citrate   Magnesium citrate

Sodium oxalate   Potassium benzoate   Potassium sodium tartrate
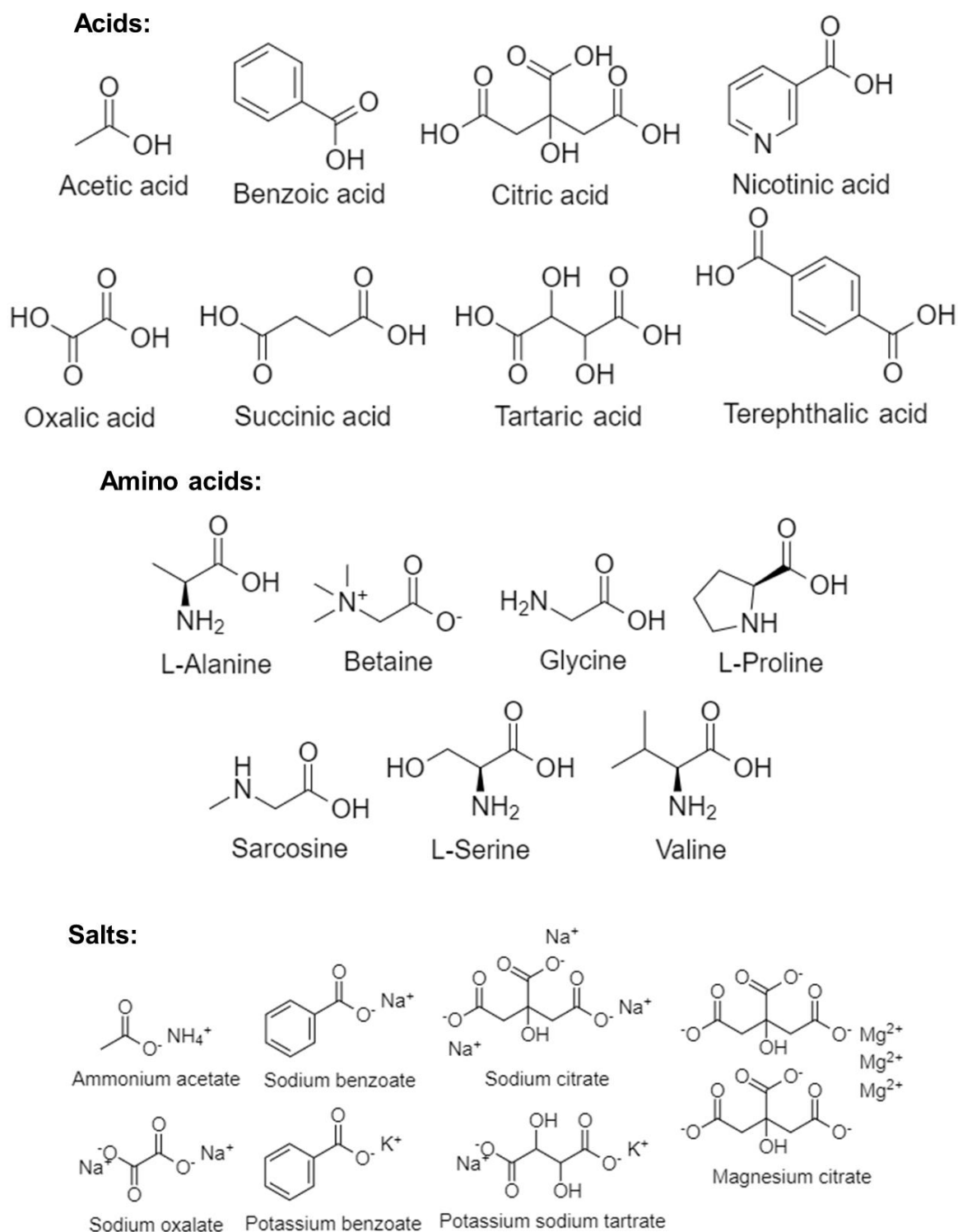
Fig. 4.3: Coformers used in the "Experimental Screening 2".

Furthermore, in this chapter, a new cocrystalline form of ITR was identified and extensively evaluated regarding its solid-state properties including the crystal structure. Finally, this new cocrystal and others reproduced in the screening were evaluated to determine the impact cocrystallisation might have on ITR solubility and dissolution.

4.2.Materials and Methods

4.2.1.Materials

The following coformers: 4-aminosalicylic acid (ASA), 4-nitrobenzoic acid (NBA), benzoic acid, citric acid, caffeic acid, dihydrocaffeic acid (DHC), nicotinamide and terephthalic acid (TER) were purchased from Sigma-Aldrich (Ireland), while these coformers: nicotinic acid, oxalic acid (OXA), benzoic acid, D,L-tartaric acid, citric acid, succinic acid (SUC), potassium sodium tartrate, ammonium acetate, magnesium citrate, sodium citrate, sodium benzoate, potassium benzoate, sodium oxalate, L-proline, sarcosine, glycine, valine, alanine, L-serine, betaine as well as the solvents: methanol (MeOH), acetone, dichloromethane (DCM) and dimethyl sulfoxide (DMSO) (HPLC grade) were kindly provided by Zentiva (Czech Republic). MeOH (HPLC grade) was purchased from Sigma-Aldrich (Ireland). Details of all other materials and solvents used in this study are listed in Chapter 2.

4.2.2.Methods

4.2.2.1.Neat grinding (NG)

For these preparations, 40 mg of ITR and an amount of a coformer (Fig. 4.2) corresponding to 2:1, 1:1 and 1:2 of API-coformer molar ratios were carefully weighted. Afterwards, the compounds were ground for 30 s using an agate mortar and pestle.

4.2.2.2.Wet grinding (WG)

Wet grinding was carried out following the procedure described for the neat grinding (Section 4.2.2.1), with the addition of two drops of methanol in the mixture of powders. For this method, only coformers presented in Fig 4.2 were used.

4.2.2.3.Slurry method

In this method, solutions of ITR at 0.74, 2.20, 0.5 and 28 mg/mL were prepared in methanol (MeOH), acetone, dimethyl sulfoxide (DMSO) and dichloromethane (DCM), respectively. Then, 1.0 mL aliquot of each solution was transferred to a 1.5 mL glass vial and a quantity of each coformer (Fig. 4.3) was added in a 1:50 API-coformer molar ratio. Then, the preparations were mixed at 50 °C for 8 hours and at room temperature thereafter for next 4 days using an IKA RT 15 magnetic stirrer (Germany). After this period, the slurries prepared using the ITR solution in DCM were filtered under vacuum using a glass filter of porosity grade 4. The other systems were dried at 30 °C and 100 mbar in a 3608-6CE vacuum oven (ThermoFisher Scientific™, USA). The solid dried samples were analysed further as described below.

4.2.2.4.Ball milling (BM)

300 mg of ITR were weighted and added to an amount of a coformer (Fig. 4.3) corresponding to a 2:1 API-coformer molar ratio. Then, the powders were transferred to a 25 mL stainless steel grind jar with two 15 mm stainless steel balls. Before grinding, two drops of acetone were added to the powders. The mixtures were ground in two cycles of 10 min at 25 Hz using a Retsch Mixer Mill MM 200 (Germany).

4.2.2.5.Scaled up ball milling

The ITR cocrystals with succinic acid (ITR-SUC), oxalic acid (ITR-OXA) and terephthalic acid (ITR-TER) were produced in larger scales. For each of these cocrystals, 2000 mg of ITR was weighted and added to 166.7 mg of succinic acid, 178.7 mg of oxalic acid or 235.6 mg of terephthalic acid, corresponding to a 2:1 API-coformer molar ratio. The ball milling procedure was carried out as described in the Section 4.2.2.4, adding 14 drops of acetone before each milling cycle.

4.2.2.6.Slow evaporation

A solution of ITR and TER was prepared by weighing 5.96 mg of the API and 0.7 mg of the coformer to prepare a 2-1 mole/mole mixture; and 5.96 mg and 1.4 mg of ITR and TER, respectively, to prepare a 1-1 mole/mole ratio. The powders were transferred into glass vials and solubilised in 10 mL of methanol by sonication in a U300H ultrasonic bath (Ultrawave, UK) to obtain clear solutions. Then, the solutions were filtered using 0.45 μm PTFE syringe filters (Fisherbrand, UK). Parafilm was used to cover the top of the vials and small holes were pierced to allow the solvent evaporation. The solutions were left at room temperature and humidity conditions until crystallisation occurred.

4.2.2.7.Freeze drying

Firstly, a 10 mg/mL solution of ITR in dioxane was prepared by weighing 1.0 g of the API and solubilising in 100 mL of the solvent. The solution was divided into 3 round-bottomed flasks and frozen using liquid nitrogen while rotating in Rotavapor R-205 (Büchi, Switzerland). The samples were dried for 18 hours using a freeze drier ALPHA 2-4 LSC (Martin Christ, Germany) with manifold for connection of NS 29/32 flasks under a vacuum of 2×10^{-3} mbar, 5-6 m^3/h suction and ice condenser adjusted to -85 °C. No secondary drying step was applied.

4.2.2.8.Raman spectroscopy

The Raman spectra of powders were measured directly in glass vials using a Raman Spectrometer RFS 100/S (Bruker, Germany). The spectra were acquired by averaging 64 scans taken with resolution 4 cm^{-1} and laser power 250 mW.

4.2.2.9.Powder X-ray diffraction (PXRD) – Experimental Screening 1

PXRD was performed as described in Chapter 2.

4.2.2.10.PXRD – Experimental Screening 2

PXRD patterns were obtained with laboratory X´PERT PRO MPD (PANalytical, Netherlands) diffractometer, used radiation CuKα ($\lambda = $ 1.542Å), generator settings: excitation voltage 45 kV, anodic current 40 mA. Scan description: scan type – gonio, measurement range 2 - 40º 2θ, step size 0.02º 2θ, time per step 200 s. The samples were measured on zero-background silica sample holder. Incident beam optics: programmable divergence slits (irradiated length 10 mm), 10 mm mask, 1/4º anti-scatter fixed slit, 0.02 rad soller slits. Diffracted beam optics: X'Celerator detector, scanning mode, active length 2.122º, 0.02 rad soller slits, anti-scatter slit 5.0 mm, Ni filter.

4.2.2.11.Differential scanning calorimetry (DSC) – Experimental Screening 1

DSC was performed as described in Chapter 2 subjecting the samples up to 400 °C with a heating rate of 10 °C/min.

4.2.2.12. DSC – Experimental Screening 2

DSC was performed as in Section 4.2.2.11 using a Mettler Toledo DSC 822e/700 (Switzerland).

4.2.2.13.Thermogravimetric analysis (TGA)

Thermogravimetric analysis was performed by carefully weighting dried samples in aluminium crucibles and heating them in a thermobalance TG 209 (Netzsch, Germany) up to 400 °C with a heating rate of 10 °C/min under nitrogen purge in a 100 mL/min flow rate.

4.2.2.14.Morphological analysis

Scanning electron microscopy (SEM) analysis was carried out as described in Chapter 3, placing the powder samples on carbon tabs.

4.2.2.15.Single crystal X-ray analysis

A monocrystal of ITR-TER with approximate dimensions 0.030 mm x 0.140 mm x 0.150 mm was used for the X-ray crystallographic analysis. The X-ray intensity data were measured at 100 ± 2 K on a Bruker Apex Kappa Duo with an Oxford Cobra Cryosystem low-temperature device using a MiTeGen micromount. Bruker APEX software was used to correct for Lorentz and polarization effects. This study was carried out by Dr. Brendan Twamley, Trinity College Dublin.

4.2.2.16. Fourier-transform infrared spectroscopy (FT-IR)

The dried powders were subjected to FT-IR spectroscopy on a PerkinElmer Spectrum 100 (USA), equipped with a universal attenuated total reflection (ATR) device and a ZnSe crystal. The FT-IR spectra of the samples were recorded in a wavelength range from 500 to 4000 cm^{-1}. The spectra were acquired by averaging 4 scans taken with resolution 4 cm^{-1}.

4.2.2.17. Contact angle

The contact angle of a liquid on the surface of the samples was used to predict their wettability. For this purpose, each sample (ITR starting material, freeze-dried ITR, ITR-TER, ITR-OXA and ITR-SUC cocrystals) were compacted into 4.5 cm in diameter disks and placed on the lifting table of a Drop Shape Analyser DSA 25 (Krüss, Germany). Then, an automated dosing syringe containing water at 20 °C was used to deposit a single drop of 14 μL on the surface of the disks. The images of the water drop on the surface of the disks were recorded for 10 min by a high-resolution USB 3.0 camera and processed by ADVANCE software (Krüss, Germany) to calculate the contact angle. Each sample had the contact angle measured in duplicate.

4.2.2.18. Intrinsic dissolution rate (IDR)

For this purpose, disks with a diameter of 8 mm were prepared by compressing 50±2 mg of powder in a stainless-steel cylindrical die system at approximately 100 kg/cm^2 for 120 s. Then, the opposite side of the steel die was sealed using a rubber plug, leaving a 0.503 cm^2 surface of the disk exposed. The stainless-steel dies were used as the disk holders and were loaded automatically by the robotic arm of the Pion inForm (Pion, United Kingdom) and immersed in the dissolution media. For each test, 40 mL of the medium (150 mM NaCl + acetate-phosphate buffer) was preheated to 37 °C and pH was adjusted with 0.5 M HCl to 1.2. The agitation was set to 100 rpm. A spectral scan (190-720 nm) was collected every 30 seconds and concentration was calculated against the calibration curve obtained previously under identical conditions. This analysis was carried out in triplicate.

4.2.2.19. Powder dissolution of ITR systems mixed with lactose

For this procedure, samples were prepared by weighing an amount of ITR (starting material), FD ITR, ITR-TER, ITR-OXA and ITR-SUC containing an equivalent of 100 mg of ITR and mixing with lactose monohydrate in a 1 to 6 ratio (API-excipient (w/w)) to allow proper wettability and dispersibility in the liquid medium. Sporanox® was used as the reference formulation and the pellets were removed from the capsule before the use in the dissolution experiments. The dissolution analysis was performed using a solution prepared by mixing of 33 mM NaCl with 67 mM HCl (artificial gastric juice (AGJ)) and containing 0.05% (v/v) of Tween 20. pH of this mixture was then adjusted to 1.2 with 0.5 M HCl. The

experiments were carried out using a standard USP II dissolution apparatus (Sotax, Switzerland) attached to a UV-Vis spectrophotometer Specord 200 Plus (Analytic Jena, Germany). The powders were added directly to the media (900 mL) kept at 37 °C and agitated at 75 rpm for the first 45 min and at 150 rpm for the final 15 min. The aliquots were automatically taken at predefined time points (2, 5, 10, 15, 20, 25, 30, 45, 50 and 60 min) and the ITR concentration was assessed by measuring the absorbance at 255 nm. This analysis was carried out in triplicate.

4.2.2.20. Powder dissolution of ITR systems mixed with other excipients

A second dissolution test evaluated dissolution of the API when physically mixed with the same excipients as those present in Sporanox® (Jassen Pharmaceutica (Gilis et al., 1997)). For this purpose, 350 mg of ITR (starting material) and FD ITR or the amount of the ITR-TER, ITR-OXA and ITR-SUC cocrystals containing the equivalent of 350 mg of the API were carefully weighted and mixed with the other excipients in the concentrations listed in Table 4.1 for 5 minutes in 200 mL plastic bottles using a Turbula® mixer (WAB group, Switzerland). Sporanox® formulation was used as described in Section 4.2.2.19.

Table 4.1: Composition of the powders used in the dissolution analysis

Excipient (%, w/w)	Formulation				
	ITR	FD ITR	ITR-OXA	ITR-SUC	ITR-TER
API	21.74	21.74			
Cocrystal			23.22	23.13	23.70
Sucrose	41.74	41.74	40.95	41.0	40.69
HPMC[*]	32.61	32.61	31.99	32.03	31.79
PEG[**]	3.91	3.91	3.84	3.84	3.82
Total (%)	100	100	100	100	100
Powder mass (mg)[***]	460	460	501.1	498.32	514.2

[*]Hydroxypropyl methyl cellulose 2910 (5 mPa.s) (HPMC); [**]Polyethylene glycol 6,000 Da (PEG); [***] Mass of powder containing 100 mg of ITR used in the dissolution test.

The dissolution analysis was carried out as described in Section 4.2.2.19, using 900 mL peak vessels in a dissolution apparatus 708-DS (Agilent, USA) coupled to an Agilent UV-Vis spectrophotometer Cary 60. This analysis was carried out in triplicate.

4.2.2.21. Statistical analysis

Statistical analysis was carried out as described in Chapter 2.

4.3.Results and Discussion

4.3.1.Experimental Screening 1

In this screening, binary samples were prepared by neat (NG) and wet grinding (WG) using a pestle and mortar and later analysed using DSC and PXRD, in which one new cocrystal (ITR-TER) and three combinations showing the formation of eutectic phases (ITR-DHC, ITR-NBA and ITR-ASA) were identified. No evidence of interactions with ITR with caffeic acid, nicotinamide, benzoic acid, salicylic acid and citric acid was found. Although eutectic phases were not the focus of this work, their identification is interesting, as they also have pharmaceutical applications, for instance, they could be used to improve the solubility and dissolution of poor soluble drug (Leuner, 2000). In general, eutectics and cocrystals are multi-component systems formed by non-covalent interactions of the API with coformers. However, in eutectics, the compounds have limited interactions and are unable to form one continuous phase, consequently, these are an heterogeneous mix composed by individual crystals of the API and coformer (Cherukuvada and Nangia, 2014). In contrast, the parental molecules of cocrystals have stronger interactions and are able to form a new phase, i.e. a homogeneous crystalline structure (Qiao et al., 2011).

The formation of the ITR-TER cocrystal was perhaps possible because TER is a dicarboxylic acid (Fig. 4.2) and able to interact with ITR in a complementary arrangement, similar to that of aliphatic dicarboxylic acids (Remenar et al., 2003). Moreover, the ITR-TER combination is the first cocrystal produced with an aromatic coformer, suggesting that other aromatic dicarboxylic acids might produce similar results and should be evaluated as potential candidates to form cocrystals with ITR. In contrast, DHC, NBA and ASA were unable to form cocrystals despite being able to interact with ITR, probably because these interactions were limited to their single carboxylic acid moiety. As a result, the crystal structure of the API and coformers was unchanged and, upon heating, their interactions resulted in an entropic gain, which favoured the eutectic formation (Stoler and Warner, 2015).

To identify a probable explanation for the eutectic formation, two factors were considered: the difference in the pK_a values between the API and coformer also Hansen solubility parameters ($\Delta\delta_t$) (Table 4.2). The analysis of the pK_a values could provide information on the nature of the interactions between the API and coformer, as this parameter is related to the acid-base interactions (Cruz-Cabeza, 2012). Accordingly, the pK_a values of the coformers able to form eutectic mixtures: DHC, NBA and ASA, are 3.84, 3.41 and 2.05, respectively (Table 4.2), which were the only tested coformers, except for the salicylic acid and the pK_{a1} of the citric acid, having a very close or lower values in comparison to pK_a of ITR, 3.7 (Table 4.2). On the other hand, the difference in the Hansen solubility parameters between the API and the coformer ($\Delta\delta_t$) is used to predict the

miscibility of substances and the parameter is based on the total cohesive energy according to the dispersion, polar and hydrogen bond factors (Mohammad et al., 2011). In general, the drug/coformer pair might form an eutectic mixture when $\Delta\delta_t < 7$ MPa$^{0.5}$ (Greenhalgh et al., 1999). However, the $\Delta\delta_t$ values for the DHC/ITR and ASA/ITR pairs were 11.78 and 7.09 MPa$^{0.5}$, respectively, and these combinations yielded eutectic mixtures, while $\Delta\delta_t$ for the salicylic acid/ITR, benzoic acid/ITR and nicotinamide/ITR combinations was 2.74, 0.15 and 2.38 MPa$^{0.5}$, respectively, (Table 4.2), however, these combinations did not form a eutectic phase. Therefore, this parameter was also unable to explain the formation of the eutectic mixtures.

Table 4.2: pK_a and Hansen solubility parameter values of ITR and the coformers used in Experimental Screening 1

Coformer	pK_a	δ_t (MPa$^{0.5}$)	$\Delta\delta_t$ (MPa$^{0.5}$)
ITR	3.7[(*)]	22.6	
ASA	2.05	29.69	7.09
Citric acid	3.1/ 4.7/ 6.4	31.06	8.46
Salicylic acid	2.97	25.34	2.74
NBA	3.41	24.49	1.89
TER	3.54/4.46	26.78	4.18
DHC	3.84	34.38	11.78
Benzoic acid	4.19	22.45	0.15
Caffeic acid	4.62	34.8	12.20
Nicotinamide	13.39	24.98	2.38

(*) pK_a of the conjugated ITR (Hansen, 2007; Hardin et al., 1988; Lide, 1991; Malpani et al., 2011; Mohammad et al., 2011; Papagianni, 2007; Peña et al., 2006; Speight, 2017; *The Merck Index*, 2013; Thiry et al., 2016; Zuorro et al., 2019)

No correlation between pK_a and $\Delta\delta_t$, was found (Fig. 4.4) and the pK_a seemed more critical for the eutectic formation than the $\Delta\delta_t$, as the eutectic mixtures only formed with coformers with pK_a close or lower than pKa of ITR, as no relation could be identified regarding the $\Delta\delta_t$ values. This indicates that an acid-base interaction of the coformers with the API was the probable explanation for the formation of these eutectic mixtures.
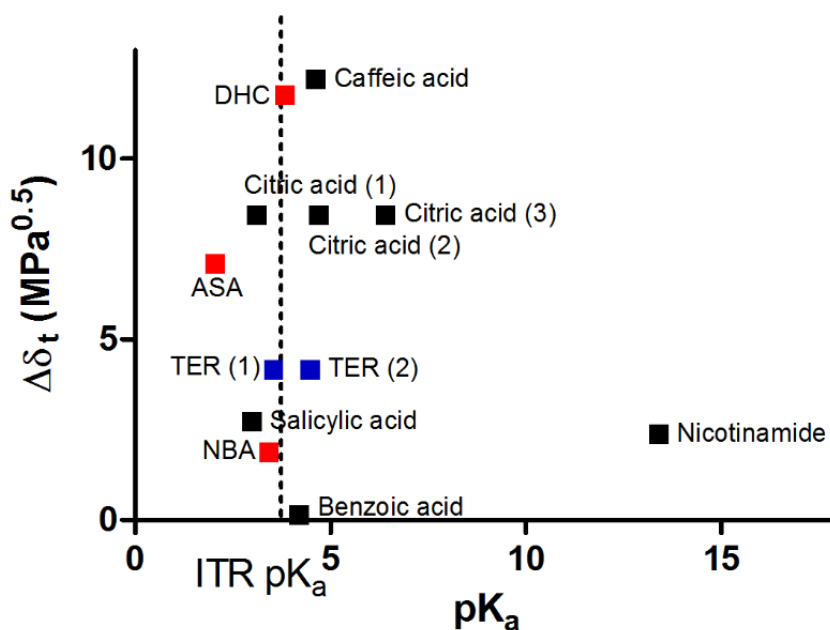
Fig. 4.4: The difference of the Hansen solubility parameter in relation to ITR ($\Delta \delta_t$) over the pK_a of the tested coformers. The dashed line indicates the ITR pK_a. Coformers with multiple pKa are indicated as (1) for pK_{a1}, (2) for pK_{a2} and (3) for pK_{a3}. The formation of eutectic mixture is indicated by (■); cocrystal by (■); and no interaction by (■).

4.3.1.1. ITR and TER mixtures

PXRD analysis of the samples prepared by NG (Fig. 4.4) revealed that the mixtures had similar diffractograms to ITR with two Bragg peaks at 17.45 and 17.95° 2θ corresponding to TER. In contrast, the samples prepared by WG had additional Bragg peaks at 3.5, 7.0 and 21.2° 2θ, which are absent in the parent materials, indicating the formation of a new phase. Therefore, the WG method appeared to be more efficient in producing the ITR-TER cocrystal than NG probably, because the cocrystallisation process was facilitated by the presence of methanol. Indeed, the use of solvents in cocrystallisation screening is common, as they can act as a "catalyser", although the mechanisms for this is not completely clear (Karagianni et al., 2018).

Fig. 4.4: Diffractograms of ITR and TER binary mixtures in a API-coformer ratio of (a) 1-2, (b) 1-1, and (c) 2-1 produced by wet grinding (WG); (d) 1-2, (e) 1-1, and (f) 2-1 produced by neat grinding (NG) in "Experimental Screening 1"; and the (g) TER and (h) ITR starting materials. * indicates the distinct peaks of the cocrystal.

DSC analysis of the binary ITR-TER mixtures showed thermograms with a sharp endothermic peak at 198 ^{o}C (Fig. 4.5), which was absent in the parent compounds, ITR and TER, and indicated melting of the cocrystal. Furthermore, the ITR-TER mixtures also had an endothermic peak with an onset at 164 ^{o}C (Fig. 4.5), which was assigned to melting of ITR. In the ITR-TER 1-1 (WG) and ITR-TER 1-2 (WG) samples this peak was almost imperceptible (Fig. 4.5), with enthalpies of 2.58 and 0.74 J/g (Table 4.3), respectively. In contrast, this peak in the samples ITR-TER 1-1 (NG) and ITR-TER 1-2 (NG) had an enthalpy of 13.48 and 18.43 J/g, respectively (Table 4.3), indicating that methanol used in the WG could contribute to the greater conversion of ITR into the cocrystal. In the samples ITR-TER 1-1 (NG) and ITR-TER 1-1 (WG), a broad endothermic peak was also detected with an onset at 310 ^{o}C, while in the samples ITR-TER 1-2 (NG) and ITR-TER 1-2 (WG) this peak had an onset at 320 ^{o}C. In both cases, this peak is likely of the depressed melting of TER, which, in the absence of ITR, melted at 350 ^{o}C (Fig. 4.5 in red). Finally, the ITR-TER mixtures also had an exothermic event at 375 ^{o}C, which was also present in the thermogram of ITR and suggestive of thermal degradation of the API at this temperature.

Fig. 4.5: DSC thermograms of ITR and TER binary mixtures in a API-coformer ratio of (a) 1-2, (b) 1-1, and (c) 2-1 produced by wet grinding (WG); (d) 1-2, (e) 1-1, and (f) 2-1 produced by neat grinding (NG) in "Experimental Screening 1"; and the (g) TER and (h) ITR starting materials. The area highlighted in blue indicates the ITR melting peak; in orange the cocrystal melting peak and in green, TER melting and ITR degradation.

Table 4.3: Summary of thermal events observed in DSC analysis of the ITR and TER starting materials and the binary mixtures in "Experimental Screening 1".

Sample	Thermal event	Onset (°C)	Peak (°C)	Enthalpy (J/g)
ITR	Melt	159.9	168.2	-91.2
	Exothermic	326.9	382.2	282.3
TER	Melt	300.9	395.0	-672.59
ITR-TER 2-1 NG	Melt (API)	163	167.4	-40.2
	Melt (CC)	199.6	200.9	-46.1
ITR-TER 1-1 NG	Melt (API)	167.7	169.1	-10.61
	Melt (CC)	197.9	199.7	-71.9
ITR-TER 1-1 NG	Melt (API)	163.4	167.0	-18.43
	Melt (CC)	197.7	200.2	-57.7
ITR-TER 2-1 WG	Melt (API)	163.8	167.3	-19.65
	Melt (CC)	200.77	201.96	-69.41
ITR-TER 1-1 WG	Melt (API)	164.97	167.68	-2.58
	Melt (CC)	198.06	200.38	-70.34
ITR-TER 1-2 WG	Melt (API)	164.48	167.5	-0.75
	Melt (CC)	197.11	199.66	-59.08

4.3.1.2. ITR and DHC mixtures

PXRD analysis of the ITR-DHC mixtures (Fig. 4.6) indicated that no new phase was formed, as the mixtures had diffractograms similar to ITR with some peaks due to the presence of DHC, observed mainly at 25.4° 2θ. Therefore, the binary samples were mixtures composed of the API and coformer crystals.
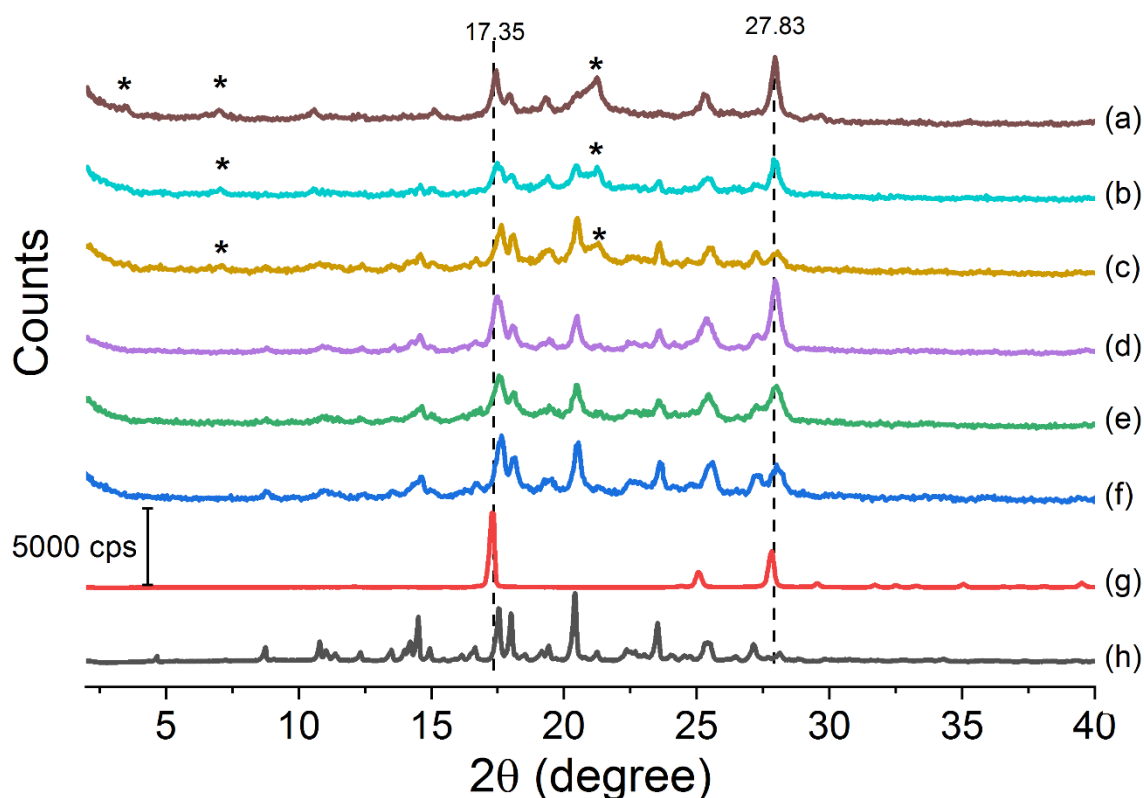

Fig. 4.6: Diffractograms of ITR and DHC binary mixtures in a API-coformer ratio of (a) 1-1 produced by wet grinding (WG); (b) 1-2, (c) 1-1, and (d) 2-1 produced by neat grinding (NG) in "Experimental Screening 1"; and the (e) DHC and (f) ITR starting materials

Thermal analysis showed that the ITR-DHC mixtures had endothermic events at a lower temperature than the melting events of ITR and DHC, at 164 and 136 °C, respectively (Fig. 4.7). For the samples prepared by NG, the endothermal events were broad, with the ITR-DHC 1-2 (NG) sample showing the lowest onset, at 65 °C, while the ITR-DHC 1-1 (NG) and ITR-DHC 2-1 (NG) mixtures had the peaks at 87 and 86 °C, respectively (Table 4.4). In contrast, in the ITR-DHC 1-1 (WG), the endothermic event was sharp and had an onset at 89 °C. This difference was probably caused by the methanol, which facilitated the interaction between the parent molecules. ITR-DHC 1-1 (WG) and ITR-DHC 2-1 (NG) also displayed a second endothermic event with onsets at 103 and 118 °C, respectively, that could be of depressed melting of ITR or DHC, caused by some miscibility of these substances (Stoler and Warner, 2015). Therefore, the above findings suggest that ITR and DHC can form a eutectic mixture, as no indication of formation of cocrystal was found in the PXRD analysis (Fig. 4.6) (Cherukuvada and Nangia, 2014).
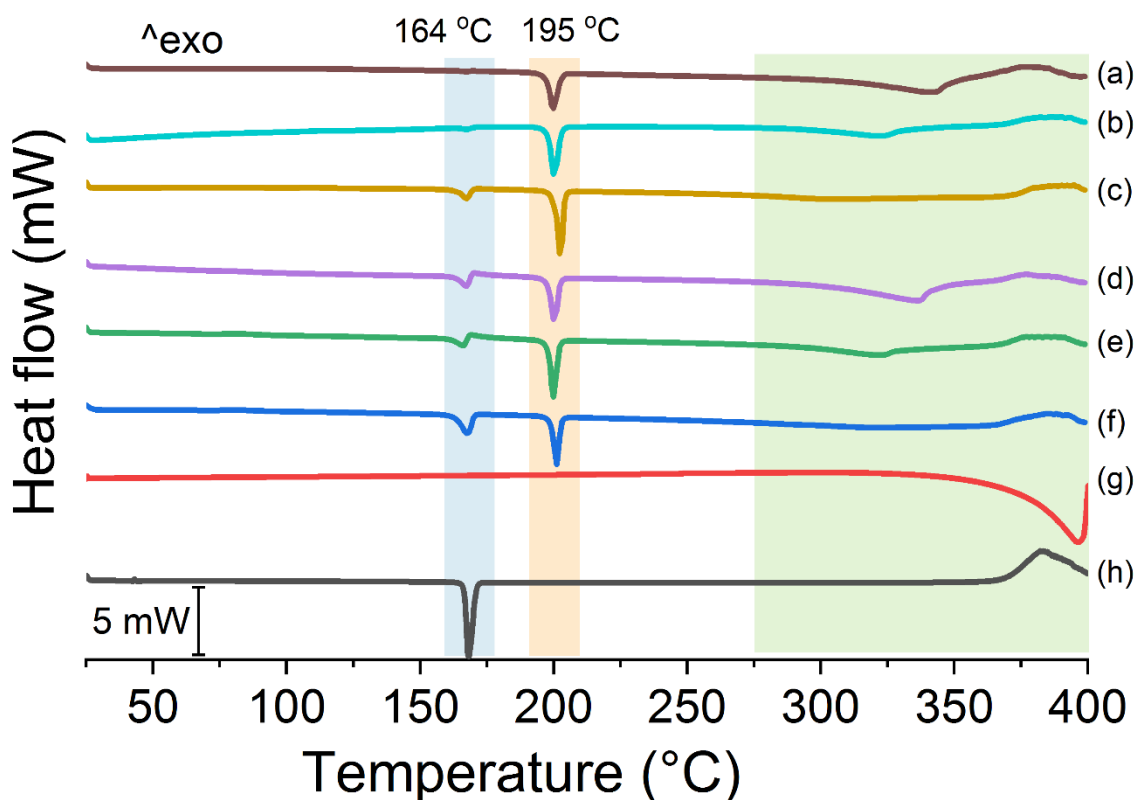
Fig. 4.7: DSC thermograms of ITR and DHC binary mixtures in a API-coformer ratio of (a) 1-1 produced by wet grinding (WG); (b) 1-2, (c) 1-1, and (d) 2-1 produced by neat grinding (NG) in "Experimental Screening 1"; and the (e) DHC and (f) ITR starting materials.

Table 4.4: Summary of thermal events observed in DSC analysis of the ITR and DHC starting materials and the binary mixtures.

Sample	Thermal event	Onset (°C)	Peak (°C)	Enthalpy (J/g)
ITR	Melt	159.9	168.2	-91.2
DHC	Melt	134.7	142.6	-39.6
ITR-DHC 2-1 NG	Eutectic	86.6	107.4	-107.9
	Melt (CF)	118.0	146.1	-168.9
ITR-DHC 1-1 NG	Eutectic	87.4	106.2	-100.8
ITR-DHC 1-2 NG	Eutectic	62.8	84.5	-87.9
ITR-DHC 1-1 WG	Eutectic	89.2	97.7	-81.7
	Melt (CF)	103.1	133.9	-171.2

4.3.1.3. ITR and NBA mixtures

The diffractograms of the ITR-NBA mixtures (Fig. 4.8) were of physical mixtures with prominent Bragg peaks at 17.25, 25.05, 26.85, 27.8 and 28.75° 2θ that indicated the presence of the coformer. However, no peaks of a new phase were observed.

Fig. 4.8: Diffractograms of ITR and NBA binary mixtures in a API-coformer ratio of (a) 1-1 produced by wet grinding (WG); (b) 1-2, (c) 1-1, and (d) 2-1 produced by neat grinding (NG) in "Experimental Screening 1"; and the (e) NBA and (f) ITR starting materials.

DSC analysis of ITR-NBA mixtures (Fig. 4.9) showed endothermic events at lower temperatures than either of the melting points of ITR and NBA. The onset value of the endothermic peak (eutectic) for ITR-NBA 1-2 (NG) was at the lowest temperature, 120 °C, and that of ITR-NBA 2-1 (NG) the highest, 127 °C (Table 4.5). In addition, it was also observed that ITR-NBA 2-1 (NG) and ITR-NBA 1-1 (NG) had broader peaks. In ITR-NBA 1-1 (WG) a small peak at 146 °C was related to the depressed melting event of ITR. Therefore, the mixture of ITR-NBA was unable to form a new phase and, instead, a eutectic mixture was also formed.
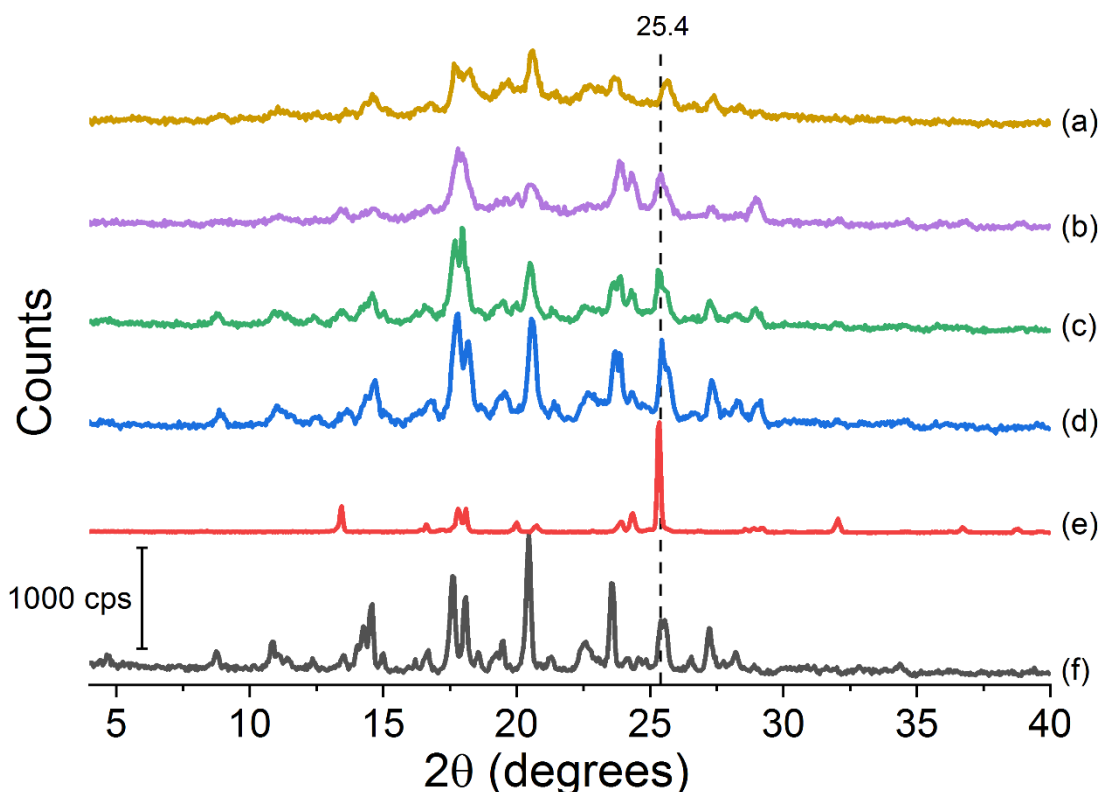
Fig. 4.9: DSC thermograms of ITR and NBA binary mixtures in a API-coformer ratio of (a) 1-1 produced by wet grinding (WG); (b) 1-2, (c) 1-1, and (d) 2-1 produced by neat grinding (NG) in "Experimental Screening 1"; and the (e) NBA and (f) ITR starting materials.

Table 4.5: Summary of thermal events observed in DSC analysis of the ITR and NBA starting materials and the binary mixtures.

Sample	Thermal event	Onset (°C)	Peak (°C)	Enthalpy (J/g)
ITR	Melt	159.9	168.2	-91.2
NBA	Melt	239.9	240.0	-173.5
ITR-NBA 2-1 NG	Eutectic	136.0	146.1	-28.1
	Melt (API)	152.9	159.4	-3.85
ITR-NBA 1-1 NG	Eutectic	130.8	140.6	-72.2
ITR-NBA 1-2 NG	Eutectic	130.9	133.9	-59.3
ITR-NBA 1-1 WG	Eutectic	123.3	136.9	-61.7
	Melt (API)	146.1	149.1	-3.7

4.3.1.4. ITR and ASA mixtures

Similar to the ITR-DHC and ITR-NBA samples, the diffractograms of the ITR-ASA samples (Fig. 4.10) also showed no evidence of a new phase formation and the materials were physical mixtures of the ITR and ASA crystals. In this case, the Bragg peaks at 16.9,

25.95 and 26.8° 2θ identified the presence of the coformer in the samples, while the other peaks were of ITR.
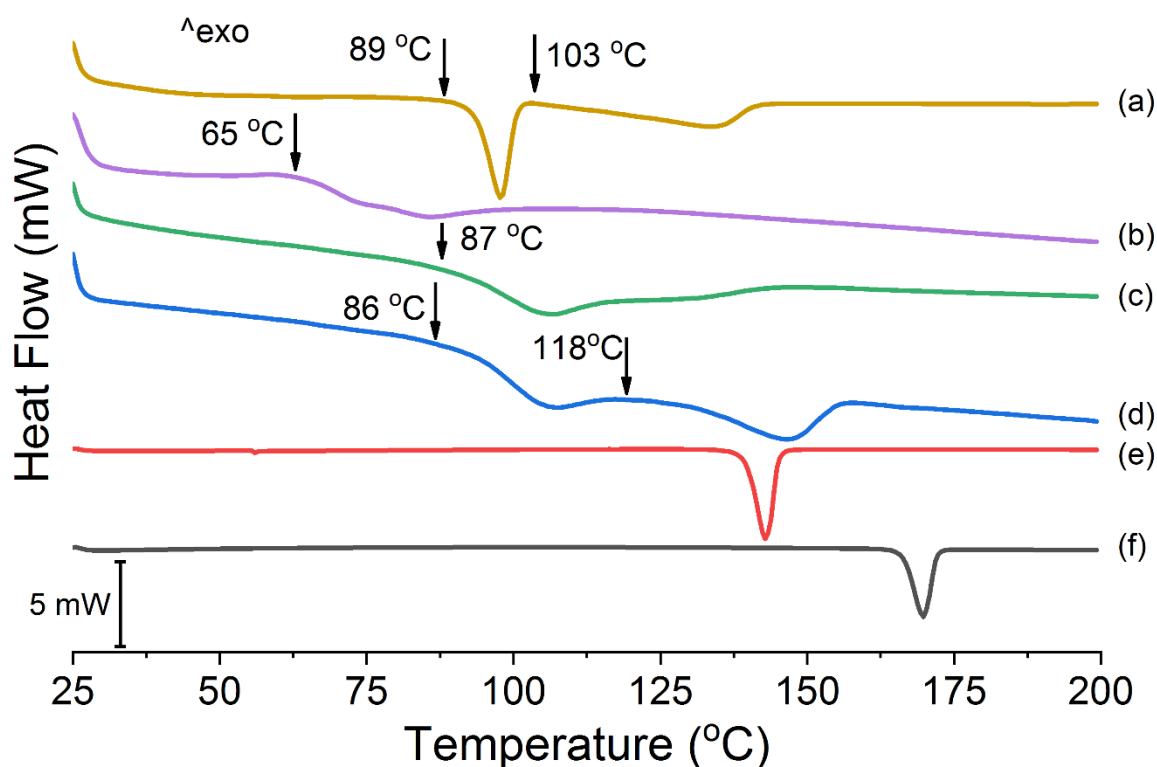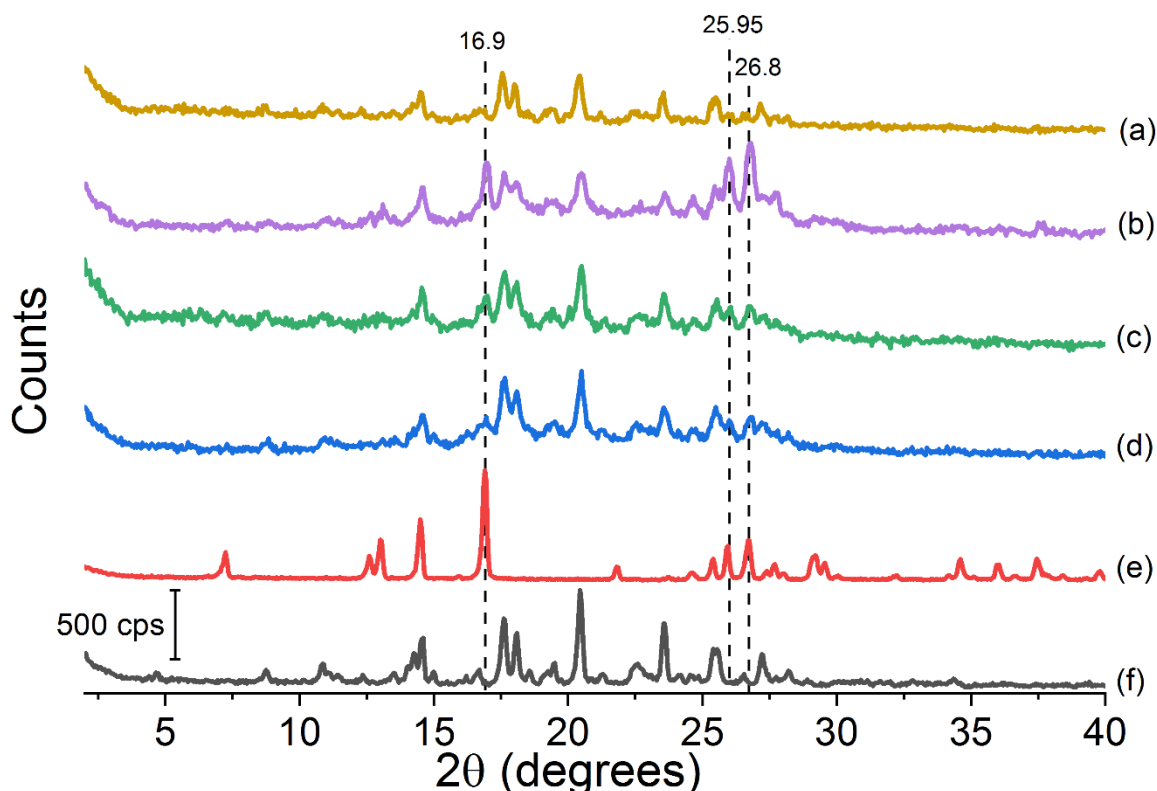

Fig. 4.10: Diffractograms of ITR and ASA binary mixtures in a API-coformer ratio of (a) 1-1 produced by wet grinding (WG); (b) 1-2, (c) 1-1, and (d) 2-1 produced by neat grinding (NG) in "Experimental Screening 1"; and the (e) ASA and (f) ITR starting materials.

Thermal analysis of the ITR-ASA binary mixtures (Fig 4.11) showed multiple endothermic events, however, most of them they overlapped making a precise analysis of their onset temperatures unreliable. Nevertheless, a variation in the onset temperature of the eutectic peak was observed, varying from 124 °C in ITR-ASA 2-1 (NG) and ITR-ASA 1-2 (NG) to 127 °C in ITR-ASA 1-1 (NG) (Table 4.6). In addition, the eutectic peak of the samples seemed to overlap with the depressed melting point of ASA, which is at 144 °C for the pure substance (Fig. 4.11). Furthermore, the ITR-ASA mixtures had an endothermic event with onset at approximately at 141 °C that could be due the ITR depressed melting point, with exception for ITR-ASA 1-1 (NG), which had no thermal event at this temperature.
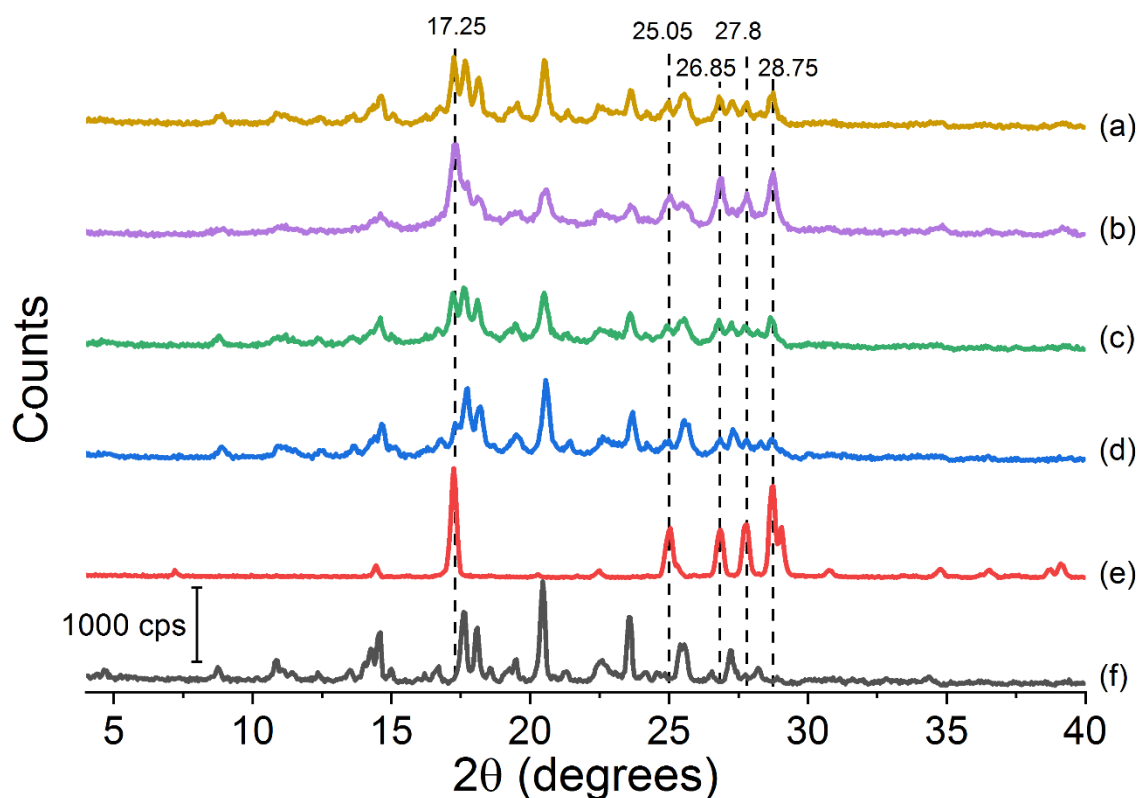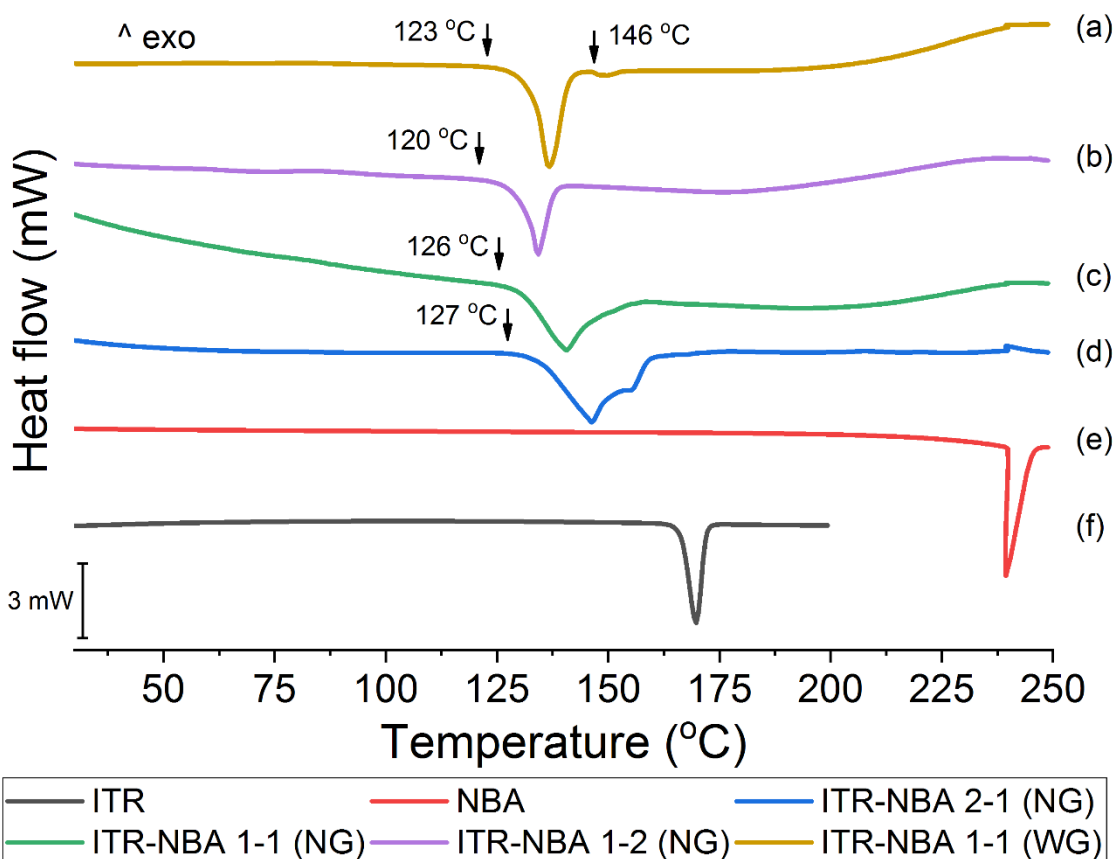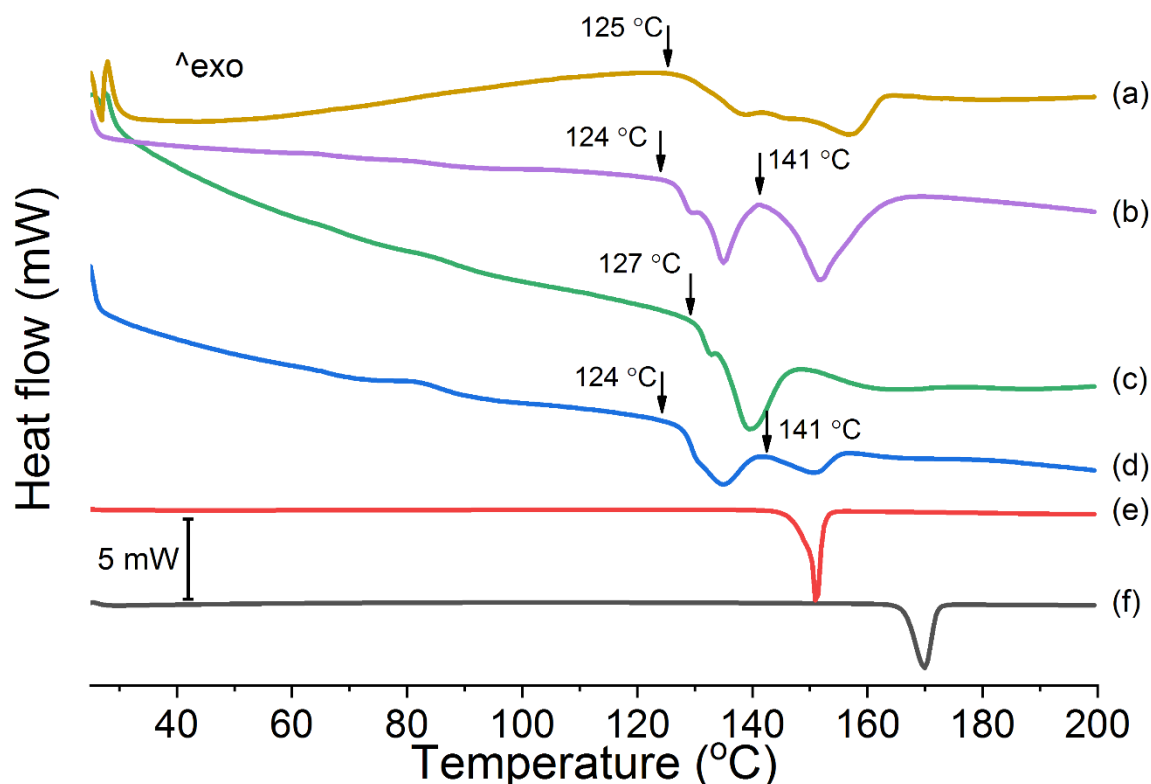
Fig. 4.11: DSC thermograms of ITR and ASA binary mixtures in a API-coformer ratio of (a) 1-1 produced by wet grinding (WG); (b) 1-2, (c) 1-1, and (d) 2-1 produced by neat grinding (NG) in "Experimental Screening 1"; and the (e) ASA and (f) ITR starting materials.

Table 4.6: Summary of thermal events observed in DSC analysis of the ITR and ASA starting materials and the binary mixtures.

Sample	Thermal event	Onset (°C)	Peak (°C)	Enthalpy (J/g)
ITR	Melt	159.9	168.2	-91.2
ASA	Melt	137.0	151.0	-388.9
ITR-ASA 2-1 NG	Eutectic	124.1	136.4	-29.1
	Melt (API)	141.1	150.1	-25.9
ITR-ASA 1-1 NG	Eutectic	127	138.9	-61.2
ITR-ASA 1-2 NG	Eutectic	124	134.9	-59.3
	Melt (API)	141	151.4	-151.5
ITR-ASA 1-1 WG	Eutectic	125	138	-61.7
	Melt (API)		156	-3.7

4.3.2. Experimental Screening 2

The "Experimental Screening 2", was part of the activities performed during the industrial secondment and used standard procedures of the company. Accordingly, ball milling (BM) and slurry methods were used to prepare the samples, which were analysed, firstly, using Raman spectroscopy to identify possible new forms, and, then, using DSC and PXRD to confirm the cocrystallisation.

In this screening, the slurry method was used due to its advantages over other cocrystallisation methods, which is the possibility of carrying out a large number of experiments. Another interesting advantage of this method is that no prior knowledge of the correct API-coformer ratio for the cocrystallisation is needed, as in the slurry method one or both API and coformer are used in concentrations higher than their solubility in a solvent, consequently their excess creates a chemical potential towards cocrystallisation, when this is possible (Douroumis et al., 2017; Zhang et al., 2007). Another advantage is its simple and versatile setup allowing for production of a large number of samples in diversified conditions at once and the conditions more favourable for cocrystallisation might also be observed. On the other hand, its scalability is poor due to possible long cocrystallisation times to obtain considerable yields and additional purification steps are required to produce a purer cocrystal (Malamatari et al., 2017). Alternatively, ball milling has the advantage of being faster and requiring a minimal volume of solvent for the process and it is considered as a "greener" manufacturing option (Weyna et al., 2009).

In the "Experimental Screening 2" no new cocrystal or ionic-cocrystal were identified. However, two cocrystals were reproduced using the slurry method (ITR-OXA and ITR-TER) and three cocrystals were prepared using ball milling (ITR-SUC, ITR-OXA and ITR-TER). These results suggest that, indeed, the coformer must be a dicarboxylic acid to form ITR cocrystals, in agreement with the literature (Remenar et al., 2003; Shevchenko et al., 2013; Weng et al., 2019). This might be because only these coformers have the appropriate conformation and sufficiently strong interactions with ITR molecules to form stable supramolecular arrangements required for a new phase formation.

The "Experimental Screening 2" failed to identify new phases with amino acids, in contrast to the results published elsewhere, which claim to have produced ITR cocrystals with glycine, proline and serine (Shete et al., 2015). This might be as the pK_a of the amino group (pK_{a2}) of amino acids is high (Table 4.7) and, despite two H-bond donors in their molecules (Fig. 4.3), these compounds are unlikely to form H-bond with ITR (Cruz-Cabeza, 2012). On the other hand, dicarboxylic acids OXA, SUC and TER have lower pK_{a2} (Table 4.3) enabling the formation of a cocrystal with ITR.

Also, no ionic cocrystal was formed from the mix of ITR with the salts. Possibly, because ITR is a neutral molecule and has no H-bond donor group, consequently, unable to form charge-assisted hydrogen bonds that are required to stabilise the ionic cocrystal (Duggirala et al., 2016). Indeed the ionic interactions with ITR were also problematic when the API was prepared as a salt using hydrochloric acid (Shevchenko et al., 2012). In that work, the authors described the preparation of two ITR salts, the ITR-2HCl and the ITR-3HCl. However, both forms had low stability, as they degraded at 90 °C during thermal analysis and underwent a conversion to a hydrate during dissolution.

Table 4.7: pK$_{a1}$ and pK$_{a2}$ of the coformers used in Experimental Screening 2

Coformer	pK$_{a1}$	pK$_{a2}$
Acids[(*)]		
Oxalic acid	1.23	4.19
Succinic acid	4.21	5.64
Terephthalic acid	3.54	4.46
Amino acids		
Alanine	2.34	9.69
Betaine	2.38	
Glycine	2.34	9.60
Proline	1.99	10.60
Sarcosine	2.36	11.64
Serine	2.21	9.15
Valine	2.32	9.62

(*) Acids able to form ITR cocrystal; (Bruice, 2007; Comuzzo and Battistutta, 2019; Lide, 1991; Pearce, 1978)

4.3.2.1. ITR-TER

PXRD analysis of the ITR-TER cocrystals produced in this screening is shown in (Fig. 4.12). In this case, ITR-TER (BM) had a diffraction pattern distinct from those of the starting materials, particularly due to the peaks at 3.5, 7.0, 10.5, 15.05, 17.8, 19.3 and 21.2° 2θ. The powder X-ray patterns of the samples made by slurry method (ITR-TER (MeOH) and ITR-TER (acetone)) were similar to that of TER, however, some Bragg peaks of low intensity at 7 and 10.5° 2θ were noticed that could indicate some cocrystal conversion in these samples.

Comparing these results to those obtained in the previous screening (Section 4.3.1.1), it was noticed that ball milling yielded a product with the most distinct cocrystal diffractogram pattern, indicating to be the most efficient method of this cocrystal manufacture. In fact, the grinding method, neat and wet, as well as the slurry method are valuable methods for experimental screening, as no special instrument is required and they are effective to identify new solid forms (Fucke et al., 1969; Zhang, 2007). However, as demonstrated in this Chapter, these methods may not achieve high conversion rate as a high-energy method, as the ball milling.

Fig. 4.12: Diffractogram patterns of ITR and TER cocrystal produced by (a) ball milling (BM), and slurry in (b) acetone and (c) MeOH in Experimental Screening 2; and (d) TER and (e) ITR starting materials. The * indicate the distinct peaks of the cocrystal.

Thermal analysis of the ITR-TER samples produced in this screening (Fig. 4.13) showed that ITR-TER (BM) had a sharp endothermic peak at 198 °C corresponding to melting of the cocrystal and a small peak with an onset at 164 °C, related to melting of ITR. As the cocrystal melting peak had a normalised enthalpy of 83.70 J/g and the ITR melting peak of 4.01 J/g (Table 4.8), this indicated that this sample was composed mainly of the cocrystal and some residual ITR. On the other hand, the samples prepared by slurry method, ITR-TER (MeOH) and ITR-TER (acetone), had a low in magnitude peaks with an onset at 195 °C, which corresponded to melting of the cocrystal. This peak had the normalised enthalpies of 8.13 and 8.12 J/g (Table 4.8), respectively, approximately a 10-fold lower than the enthalpy of the cocrystal melting peak in ITR-TER (BM). As the thermograms of the ITR-TER (MeOH) and ITR-TER (acetone) samples had a sharp peak at approximately 390 °C of TER melting, this indicates that they were composed mainly of the coformer mixed with the cocrystal.

Fig. 4.13: DSC thermograms ITR and TER cocrystal produced by (a) ball milling (BM), and slurry in (b) acetone and (c) MeOH in Experimental Screening 2; and (d) TER and (e) ITR starting materials. The area highlighted in blue indicates the ITR melting peak, in orange, the cocrystal melting peak and in green, the TER melting and ITR degradation.

Table 4.8: Summary of thermal events observed in DSC analysis of the ITR and TER starting materials and their binary mixtures in "Experimental Screening 2".

Sample	Thermal event	Onset (°C)	Peak (°C)	Enthalpy (J/g)
ITR	Melt	159.9	168.2	-91.2
	Exothermic	326.9	382.2	282.3
TER	Melt	300.9	395.0	-672.59
ITR-TER (MeOH)	Melt (CC)	162.6	198.1	-8.13
	Melt (CF)	302.8	392.8	-747.4
ITR-TER (Acetone)	Melt (CC)	168.5	198.6	-8.12
	Melt (CF)	305.5	396.8	-490.8
ITR-TER (BM)	Melt (API)	155.3	168.5	-4.0
	Melt (CC)	195.9	204.1	-83.7
	Exothermic	311.0	379.05	347.1

4.3.2.2.ITR-OXA

The ITR-OXA cocrystal was produced from DCM slurry screening and by BM. The diffractograms of the ITR-OXA systems (Fig. 4.14) showed that the sample prepared by slurry (Fig. 14.4 in blue) is similar to that of coformer (Fig. 4.14 in red) however, Bragg peaks of very low intensity at 6.7 and 16.7° 2θ indicate the cocrystal presence. On the other hand, the ITR-OXA (BM) sample (Fig. 4.14 in green) was different in relation to the starting materials (Fig. 4.14 in black and red), with new peaks observed at 6.7, 10.8, 16.7, 21.4 and 21.7° 2θ. This PXRD pattern was similar to that of the ITR-OXA cocrystal published by Schevchenko and it was the cocrystal in its solvated form with acetone (Shevchenko et al., 2013).
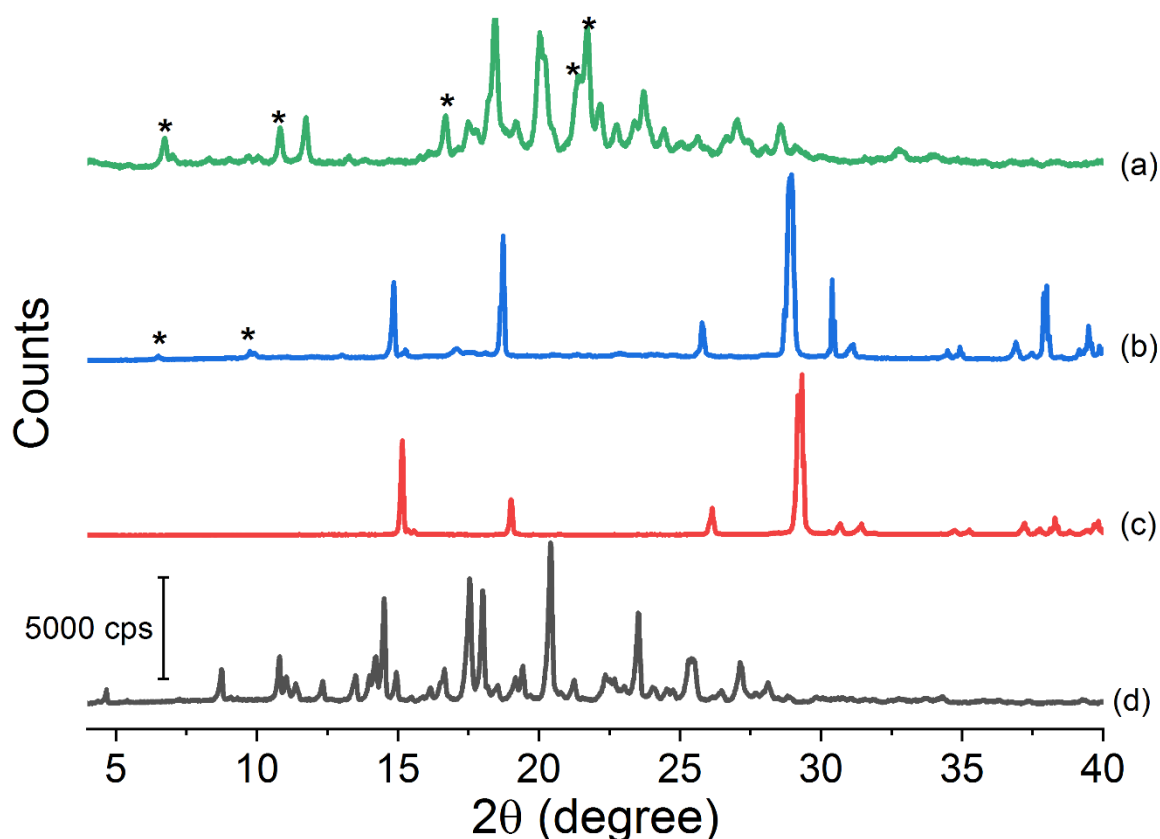
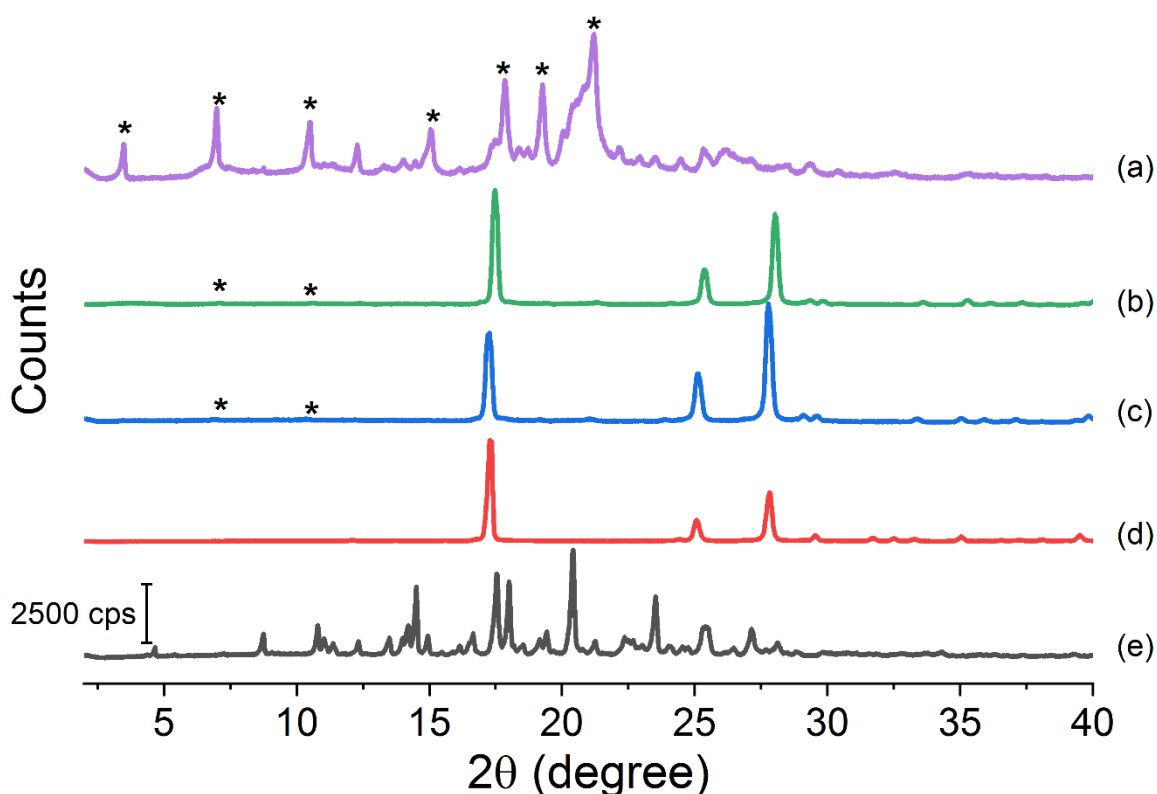**Fig.4.14:** Diffractograms of ITR and OXA cocrystal produced by (a) ball milling (BM), and slurry in (b) DCM in Experimental Screening 2; and (c) OXA and (d) ITR starting materials. The * indicate the distinct peaks of the cocrystal.

The DSC thermograms (Fig. 4.15) revealed that OXA (Fig. 4.c) had two endothermic events, the first with an onset at 99.5 °C corresponding to dehydration and the second, at 188 °C related to melting (Vojta et al., 2016). For the ITR-OXA samples, the sample obtained by slurry cocrystallisation (Fig. 4.15 b) also had a sharp peak of dehydration at 94 °C but was devoid of a clear melting peak (Table 4.9). On the other hand, the sample ITR-OXA prepared by BM (Fig. 4.15a) had no indication of dehydration by DSC, but it had an endothermic event with an onset at 154 °C, that could be a phase transition, nevertheless, further investigation is required for an accurate conclusion on this thermal event. Melting of

the ITR-OXA cocrystal was observed at 174 °C. Although no indication of dehydration of ITR-OXA (BM) was observed in the DSC thermogram, TGA (Fig. 4.16) detected a mass loss of 2.19 % at 106.7 °C corresponding to its dehydration.

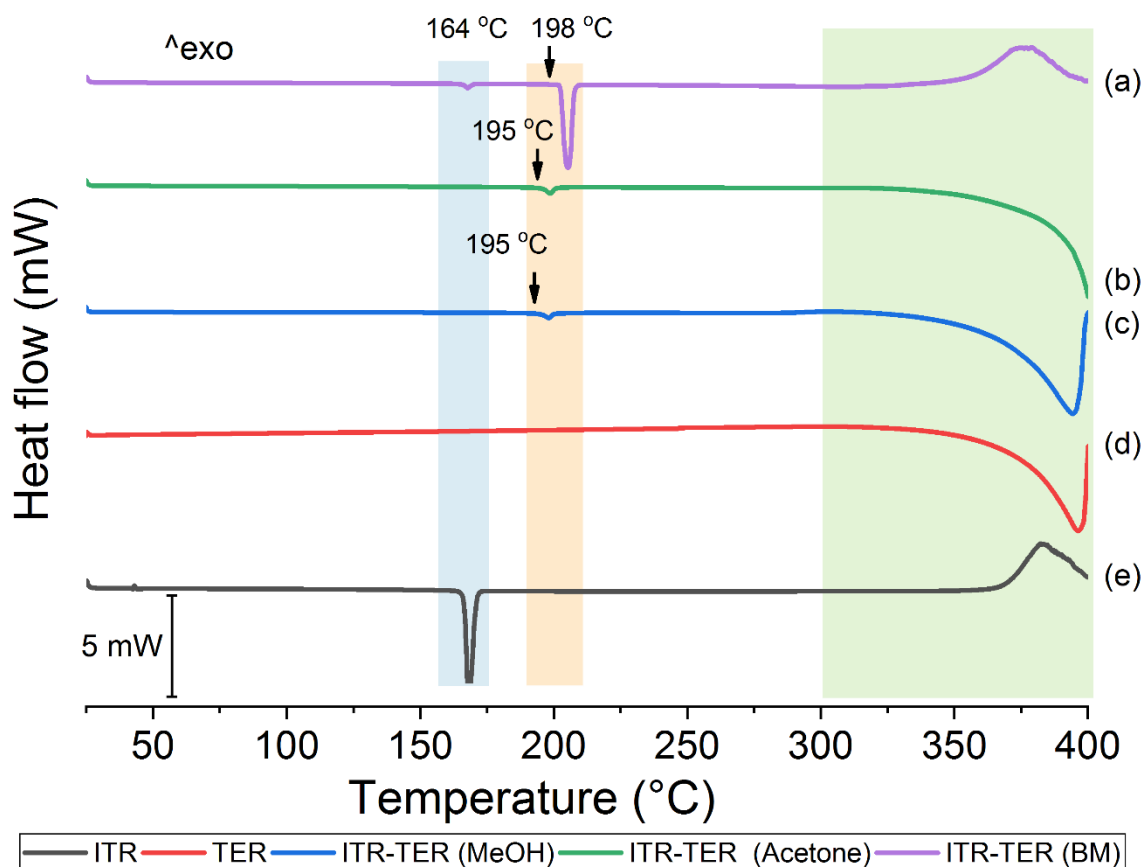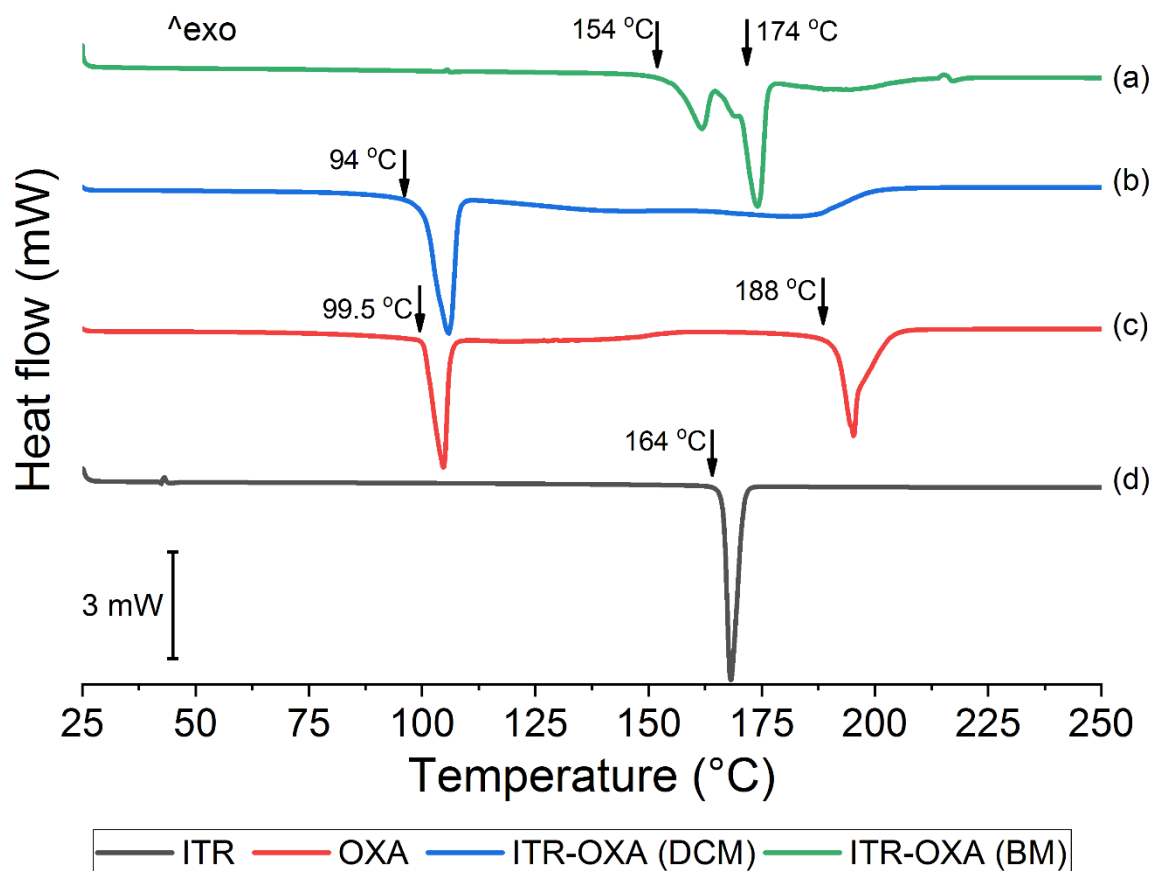**Fig. 4.15:** DSC thermograms of ITR and OXA cocrystal produced by (a) ball milling (BM), and slurry in (b) DCM in Experimental Screening 2; and (c) OXA and (d) ITR starting materials.

Table 4.9: Summary of thermal events observed in DSC analysis of the ITR and OXA starting materials and the binary mixtures.

Sample	Thermal event	Onset (°C)	Peak (°C)	Enthalpy (J/g)
ITR	Melt	159.9	168.2	-91.2
	Exothermic	326.9	382.2	282.3
OXA	Dehydration	99.5	100.9	-540.1
	Melt	188.5	191.5	-532.1
ITR-OXA (DCM)	Dehydration	99.5	100.5	-499.4
ITR-OXA (BM)	Melt (API)	154	169.7	-12.8
	Melt (CC)	170.1	174	-46.2
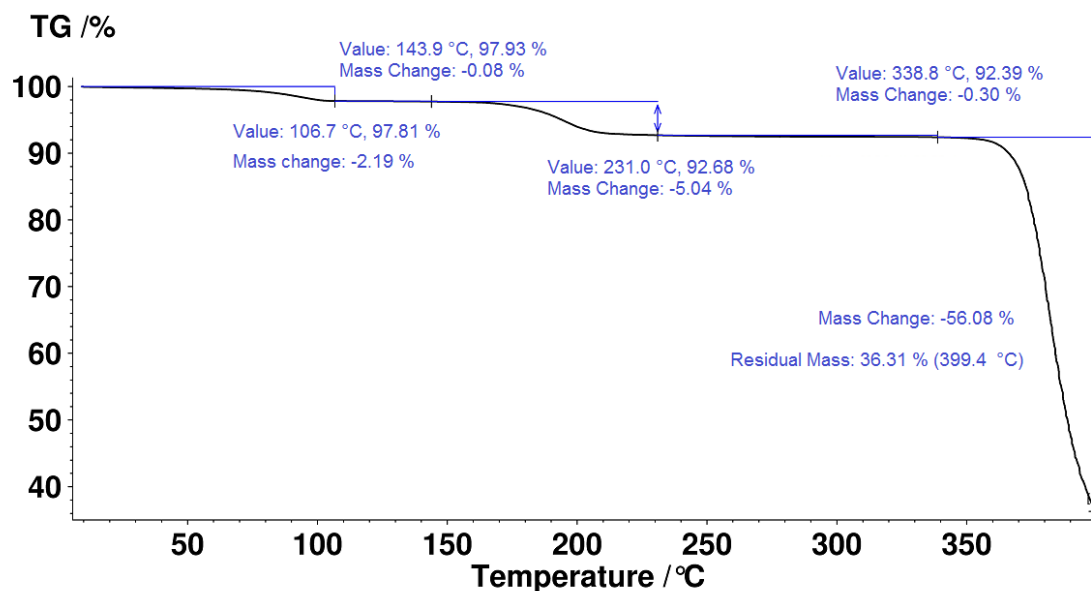
Fig. 4.16: Thermogravimetric analysis of ITR-OXA cocrystal prepared by ball milling (BM).

4.3.2.3.ITR-SUC

The diffractogram of the ITR-SUC cocrystal (Fig.4.17) was comparable to that published in the literature, with peaks at 7.1, 9.1, 10.1 and 17.2° 2θ, which were used as a reference to distinguish this form to the parent compounds (Remenar et al., 2003).
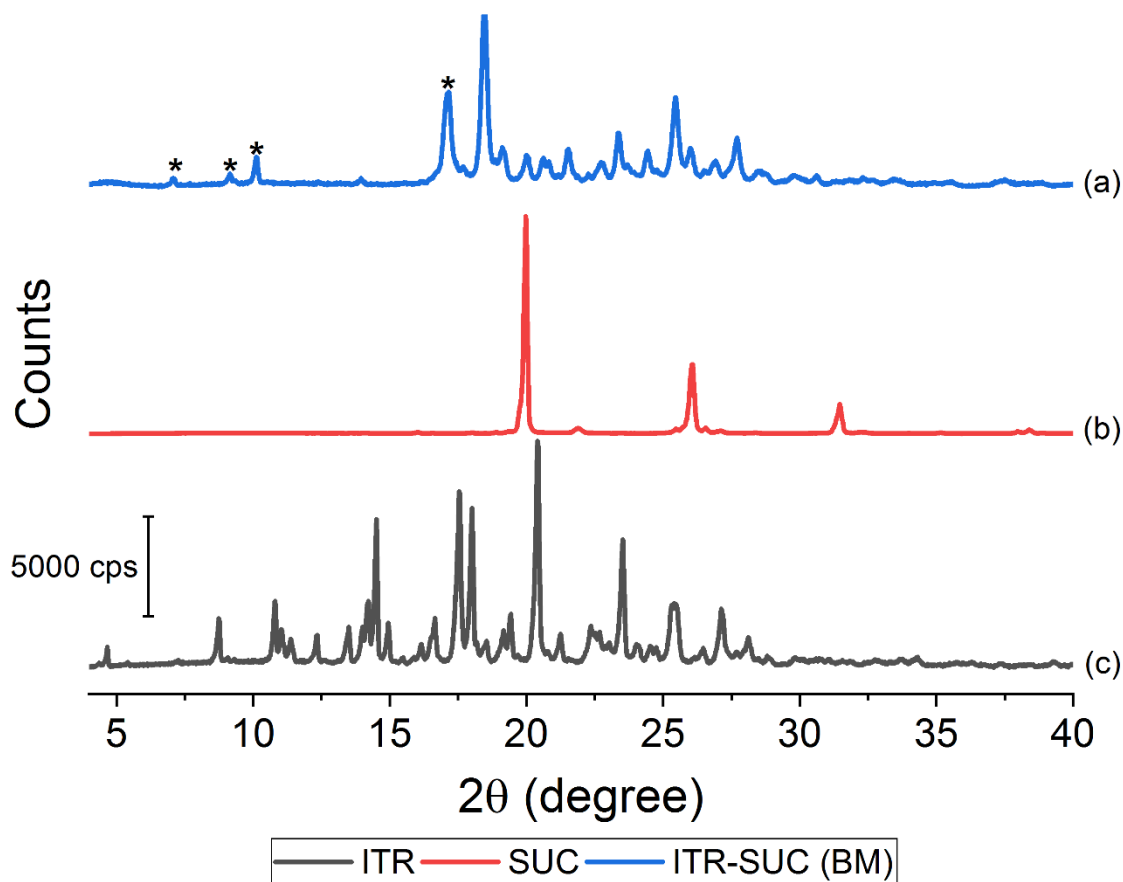
Fig.4.17: Diffractogram patterns of (a) ITR-SUC cocrystal produced by ball milling (BM), in Experimental Screening 2; and the (b) SUC and (c) ITR starting materials. The * indicate the distinct peaks of the cocrystal.

DSC analysis of the ITR-SUC cocrystal (Fig. 4.18) showed that it melted at 154 °C, a lower temperature than those of either pure ITR (164 °C) or SUC (186 °C) (Table 4.10). Therefore, the preparation of ITR-SUC by ball milling was efficient, as no other thermal event was observed in this sample.
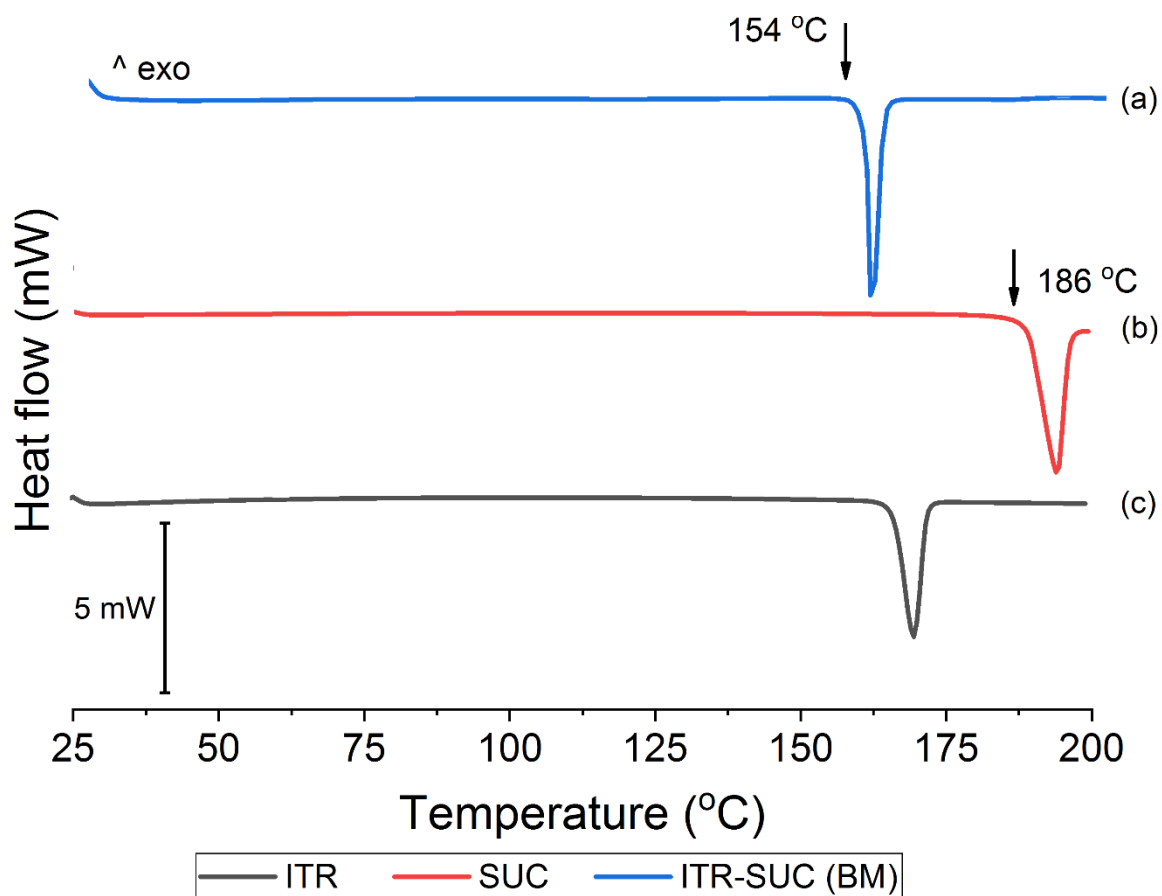
Fig. 4.18: DSC thermograms of (a) ITR-SUC cocrystal produced by ball milling (BM), in Experimental Screening 2; and the (b) SUC and (c) ITR starting materials.

Table 4.10: Summary of thermal events observed in DSC analysis of the ITR and SUC starting materials and their binary mixtures.

Sample	Thermal event	Onset (°C)	Peak (°C)	Enthalpy (J/g)
ITR	Melt	159.9	168.2	-91.2
SUC	Melt	186	395.0	-476.75
ITR-SUC (BM)	Melt (CC)	154	158.6	-84.66

4.3.3. Elucidation of the crystalline structure of ITR-TER

Following the successful identification of a new ITR cocrystal with TER, further analysis was carried out to elucidate its crystalline structure.

4.3.3.1.Raman spectroscopy

Initially, during the "Experimental Screening 2", Raman spectroscopy was used to identify possible new forms. However, this analysis can also provide valuable information about the interactions between the API and the coformer. The spectrum of the cocrystal (Fig.4.19) was different when compared to that of ITR, which could indicate interactions between the API and the coformer forming supramolecular interactions (Delori et al., 2012). In the pure coformer, H-bonded dimers are formed by the –COOH groups, with the C=O moiety acting as the H-bond acceptor and the -OH moiety being the H-bond donor. In the cocrystal, the acid dimer arrangement is destroyed, which may result in a shift of the peak assigned to the C=O stretching band to a higher wavelength,1696 cm^{-1} in the cocrystal spectrum, while in the coformer it is at 1633 cm^{-1}. This effect was also observed by Schevchenko et al. (Shevchenko et al., 2013) who investigated the formation of ITR cocrystal with aliphatic dicarboxylic acid of varying chain length, including succinic acid, malonic acid, and oxalic acid. In this work, the authors detected a peak shift of the C=O vibration to a higher wavelength in all the produced cocrystals.
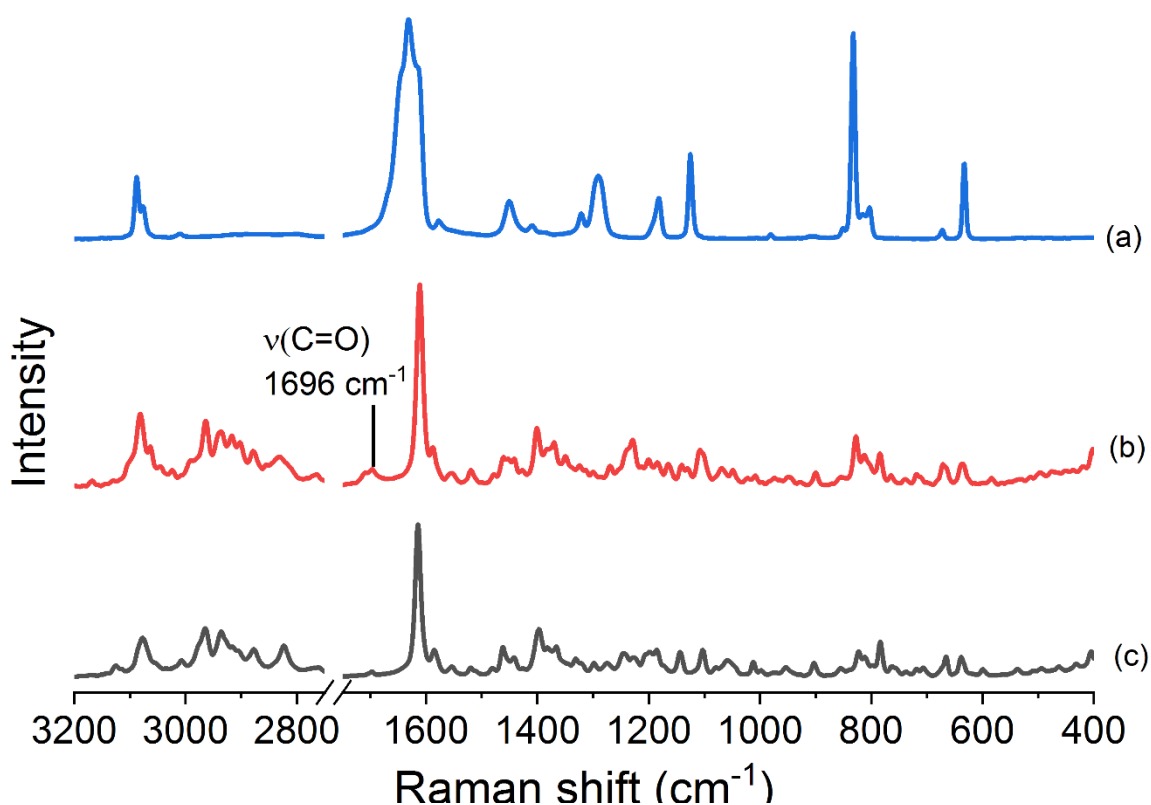
Fig. 4.19: Raman spectra of (a) TER starting material, (b) ITR-TER cocrystals produced by ball milling (BM) in Experimental Screening 2, and (c) ITR starting material.

4.3.3.2.FT-IR

FT-IR spectra (Fig. 4.20) recorded for the ITR-TER cocrystal were different in relation to its starting materials and the most relevant bands are listed in Appendix 2. The formation of a supramolecular interaction, in addition to an evidence presented by Raman spectroscopy (Fig. 4.19), was also observed in the FT-IR spectra (Fig. 4.20). In the ITR-TER cocrystal spectrum, a strong band was found at 1705 cm^{-1}, which was also present in the ITR and TER spectra, at 1698 cm^{-1} and 1675 cm^{-1}, respectively (Fig. 4.20). Strong peaks at this wavelength range are normally caused due to C=O stretching (Williams and Fleming, 1995). As this peak appears at a higher wavelength in the cocrystal than in the parent compounds, this suggests that the new H-bond network in the cocrystal might be weaker.

Another area of interest was identified in the fingerprint region, between 1200 and 1300 cm^{-1}. In the TER spectrum, a broad strong peak at 1281 cm^{-1} corresponding to the carbonyl carbon stretching was seen, while in ITR, a peak at 1271 cm^{-1} is assigned to aromatic C-N stretching (Karthikeyan et al., 2015; Nonappa et al., 2013). In the cocrystal, medium strength bands were detected around this area, possibly due to the interacting groups in the new cocrystal.
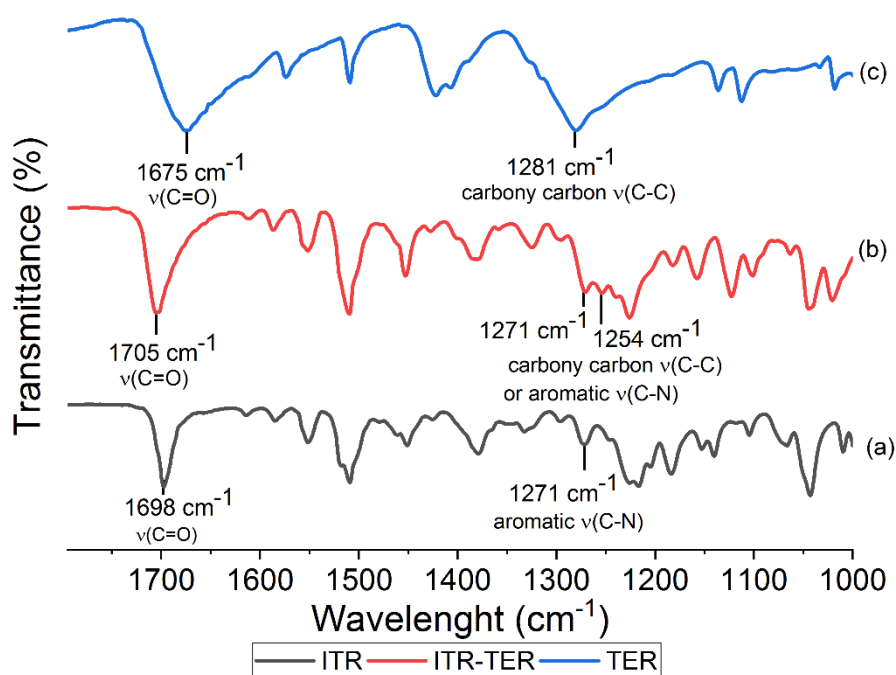
Fig.4.20: FT-IR spectra of (a) ITR, (b) ITR-TER cocrystal and (c) TER.

4.3.3.3.Single crystal X-ray analysis

Single crystal X-ray diffraction showed that the cocrystal had a triclinic unit cell composed of 4 molecules (Z=4) in a P$\overline{1}$ space group (Table 4.11). The asymmetric unit crystal was formed by two ITR molecules and two half of TER molecules (Fig. 4.21). In this arrangement, the ITR molecules are in an antiparallel orientation with a TER molecule

trapped in the space between them. Additionally, the TER molecules presented a rotational symmetry element. This analysis also identified H-bonds formed by the hydroxyl of the carboxyl acid and the N4 of the azole ring of ITR (Fig. 4.21), in agreement with Raman (Fig. 4.19) and FT-IR analyses (Fig. 4.21). This interaction is also observed in other cocrystals of ITR (Remenar et al., 2003; Shevchenko et al., 2012), however, in ITR-TER an intrinsic second H-bond was identified formed by the hydrogen-bonding to the C3 of the azole group and the carbonyl of the coformer (Fig. 4.21).

Table 4.11: Crystallographic data of the ITR-TER cocrystal

Empirical formula	$C_{39}H_{41}Cl_2N_8O_6$	
Formula weight (Da)	788.70	
Temperature of measurement (K)	100±2	
Wavelength (Å)	1.54178	
Space group	$P\bar{1}$	
Unit cell dimensions (Å, °)	a = 10.3910±6	α= 81.310± 5
	b = 14.3714± 10	β= 81.019± 6
	c = 25.418±2	γ = 89.951± 4
Volume ($Å^3$)	3705.2±5	
Z	4	
Calculated density (mg/m^3)	1.414	
Absorption coefficient (mm^{-1})	2.075	
Crystal size (mm^3)	0.15 x 0.14 x 0.03	
Theta range for data collection (°)	1.780 to 66.203	
Reflections collected	12852	
Completeness to theta = 66.203°	97.5 %	
Refinement method	Full-matrix least-squares on F^2	
Data / restraints / parameters	12852 / 435 / 1076	
Goodness-of-fit on F^2	1.093	
Final R indices [I>2σ (I)]	R_1 = 0.1069, wR_2 = 0.2616	
R indices (all data)	R_1 = 0.1188, wR_2 = 0.2689	
Largest diff. peak and hole	0.703 and -1.004 e.$Å^{-3}$	

   This analysis also found disordered aliphatic chains at the end of the ITR molecules. This disorder was probably caused by attractive interactions in the antiparallel molecules of ITR, in which a weak halogen bonding of dichlorophenyl and the oxygen or nitrogen in the triazole group could be tilting the sec-butyl reducing the dihedral angle of this group (Fig. 4.21) (Nonappa et al., 2013).
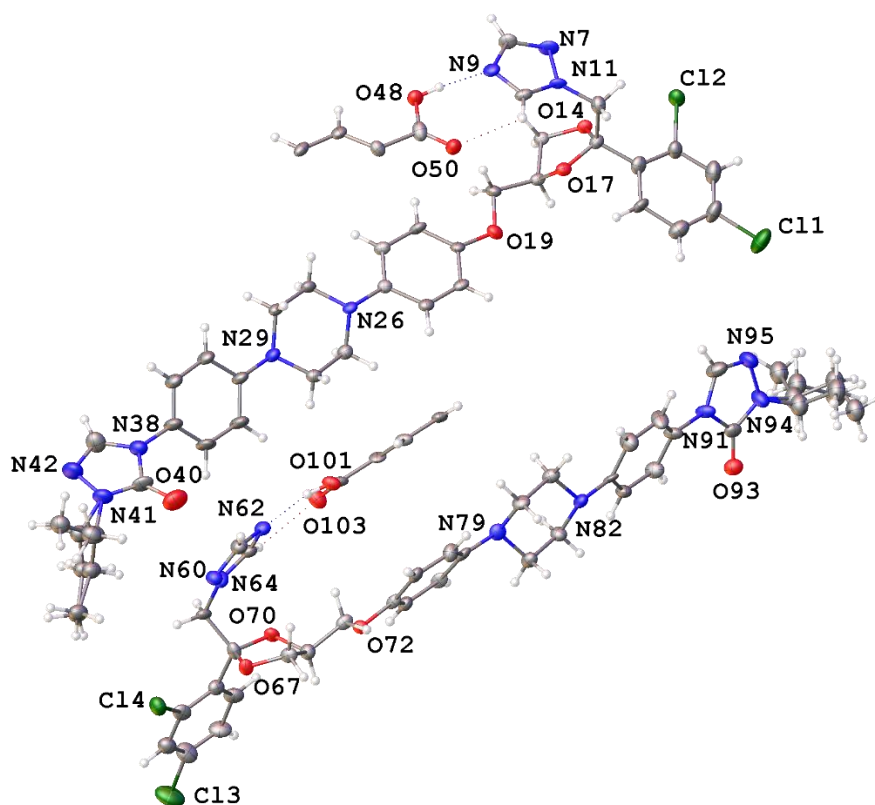
Fig. 4.21: The asymmetric unit in the ITR-TER cocrystal structure.

In comparison to the single crystal X-ray analysis of the ITR cocrystal with SUC (Cambridge Structural Database record: REWTUK (Nonappa et al., 2013)), the ITR-TER had some structural differences. Although they both have their crystal lattice formed by 4 molecules, the cocrystal with SUC was described as a monoclinic system with a $P2_1/c$ space group. Furthermore, the intermolecular synthon also had a different arrangement, as the carbonyl group did not form H-bond as in the ITR-TER cocrystal, and those formed by the OH moiety of the carboxylic acid had a critical role in the stabilisation of the supramolecular arrangement.

4.3.4. Comparison of ITR in different forms

The final part of this chapter aimed to compare ITR in its crystalline Form I (starting material) and the form obtained after freeze drying to the multicomponent forms: ITR-OXA, ITR-SUC and ITR-TER cocrystals. The commercial formulation of ITR, Sporanox® capsules (Janssen), was used as a reference in this evaluation. The Sporanox® pellets are produced spray-layering a solution of the API mixed with hydroxypropylmethylcellulose on sugar beads (Kalepu and Nekkanti, 2015). Ultimately, this study aimed to test if the cocrystalline forms show an advantage over the pure ITR in terms of physicochemical properties and dissolution characteristics.

ITR-OXA, ITR-SUC and ITR-TER cocrystals were produced by ball mill, however, in a larger scale than those prepared in the Experimental Screening 2. DSC and PXRD analysis of these cocrystals showed similar solid-state properties in comparison to the

equivalent material produced in different scales (Appendix 2). Therefore, no adjustments on the preparation conditions, including the milling time and frequency of milling, were necessary for the scale up.

The solid-state analysis of the freeze-dried ITR (FD ITR) using PXRD revealed that its diffractogram patterns (Fig. 4.22a) had no well-defined Bragg peaks, except one at 5.9° 2θ indicating that this sample was a vitrified smectic mesophase. Despite FD ITR being prepared by a different method, the solid state of this sample is similar to that of the non-PEGylated ITR NP as shown in Chapter 2 and 3. The results of thermal analysis of FD-ITR (Fig. 4.22, b) showed that this sample had a glass transition at 60 °C, followed by two endothermic events, at 71 and at 83 °C, corresponding to the liquid crystal transition LC_1 and LC_2 (Table 4.12). The DSC curve of the FD ITR sample also showed an exothermic event at 116 °C, indicating crystallisation of disordered ITR and then melting of the crystalline form at 159 °C. Therefore, the solid-state analysis of FD ITR showed that freeze drying of ITR solution in dioxane resulted in a disordered material similar in nature to those produced by nanoprecipitation by antisolvent (Chapter 2 and 3).
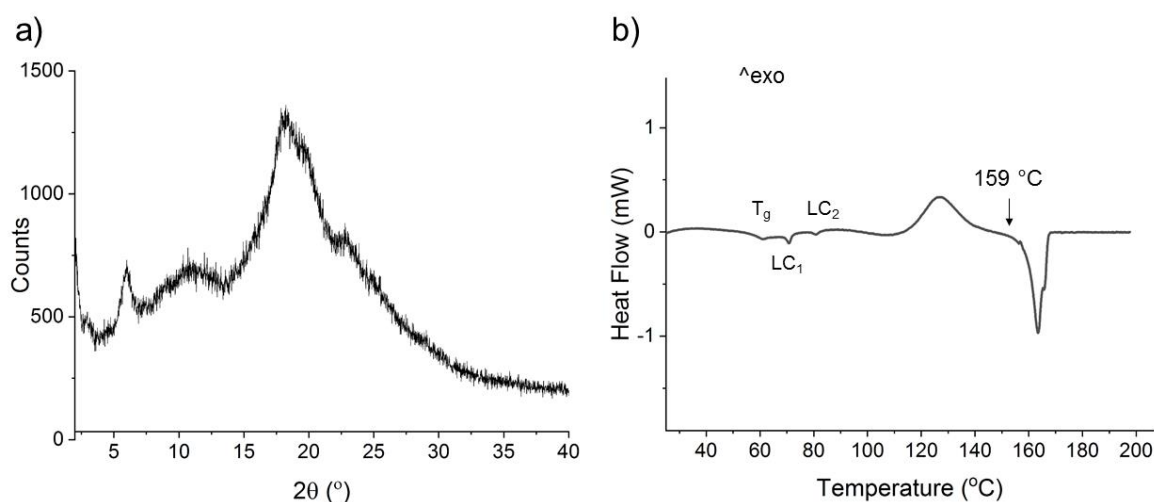
Fig. 4.22: The (a) diffractogram patterns and the (b) thermogram of the freeze-dried ITR (FD ITR).

Table 4.12: Summary of thermal events observed in DSC analysis of the FD ITR

Sample	Thermal event	Onset (°C)	Peak (°C)	Enthalpy (J/g)
FD ITR	T_g		60.1	
	LC_1		70.6	
	LC_2		80.4	
	Recrystallisation	108.8	126.7	4.9
	Melt (CF)	159.1	163.7	-5.3

4.3.4.1.Morphological analysis

The morphological analysis revealed that the ITR powder "as received" (Fig. 4.23a) was composed of large rod-like structures, with particles up to 30 µm. The SEM images of the cocrystals (Fig. 4.23b-d) showed that these samples had smaller particles, as expected from milled material, however, each having a characteristic morphology. For instance, images of the ITR-TER sample (Fig 4.23b) showed clusters formed by round particles smaller than 1 µm. The ITR-SUC cocrystal (Fig. 4.24c) was composed by angular polyhedral particles with sizes smaller than 5 µm. Finally, the ITR-OXA sample (Fig. 4.23d) had elongated particles smaller than 3 µm. FD ITR (Fig. 4.23e) also had a distinct morphology in comparison to the starting ITR material (Fig. 4.23a) and was composed by flake particles in a wide range of sizes. The SEM images of Sporanox® (Fig. 4.23f and g) revealed that the spherical pellet had a smooth surface and a diameter of approximately 840 µm. The outside layer was approximately 130 µm of thickness.
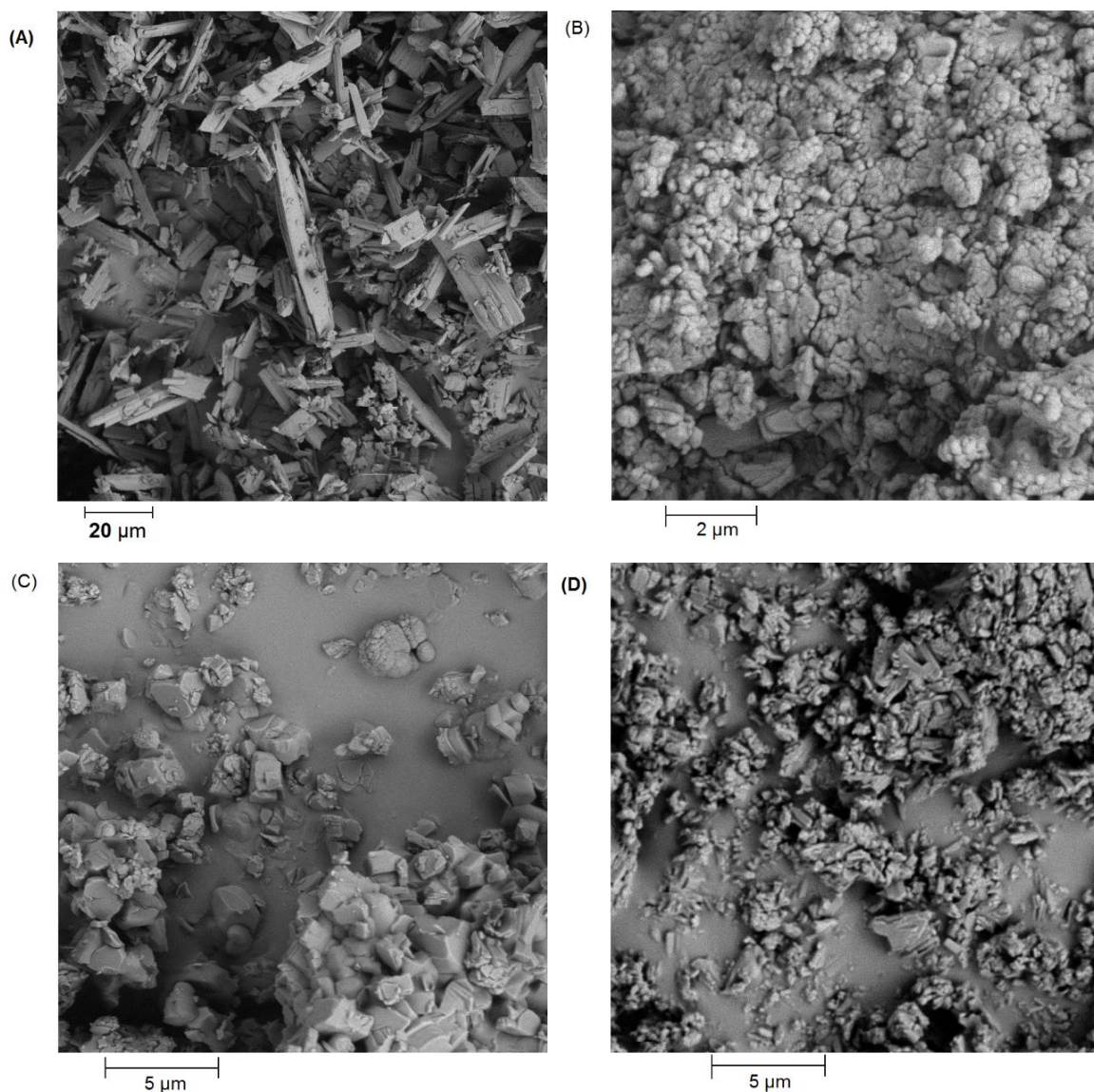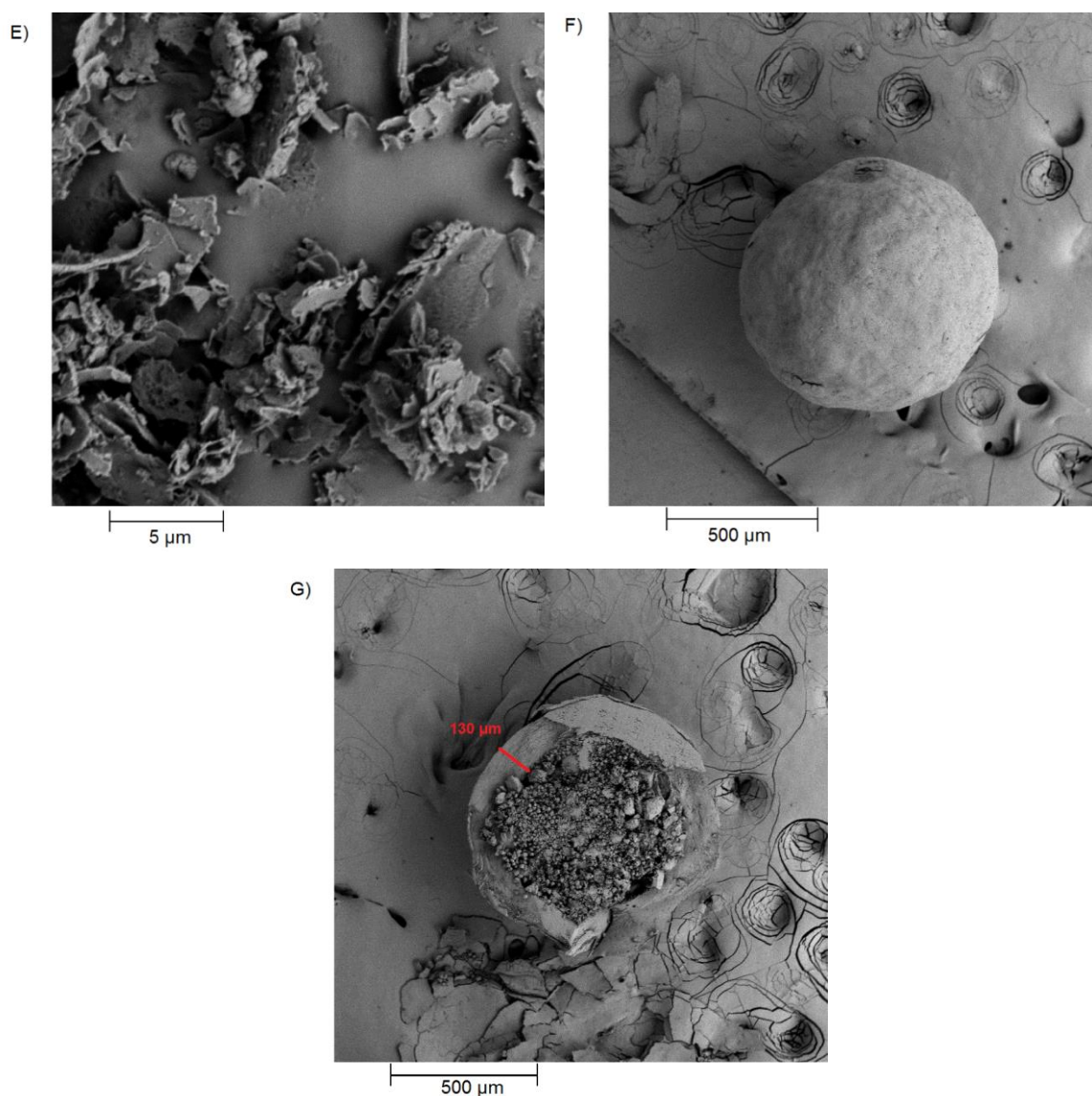
Fig. 4.23: SEM images of (a) crystalline ITR, (b) ITR-TER, (c) ITR-SUC, (d) ITR-OXA, (e) FD ITR and (f) intact and (g) sectioned Sporanox® pellet.

4.3.4.2. Contact angle analysis

The contact angle of a water drops on the surface of disks prepared by compacting ITR, FD ITR, ITR-OXA, ITR-SUC and ITR-TER was measured to estimate wettability of these samples. The photos taken during this experiment showed that the shape of the water drops remained spherical on the surface of all the disks (Fig. 4.24), highlighting the hydrophobicity of these materials.

The samples had a low variability of their contact angle values (Table 4.13), with ITR-SUC and ITR-TER having the lowest and the highest values, 126.485±1.49 and 130.535±1.66°, respectively. Furthermore, the values did not significant changed after 10 min of evaluation, indicating that the prolonged contact of the disks with the water drop had no effect on their wettability. Therefore, this result indicated that the samples had poor wettability, as they had contact angle values greater to 90° (Florence and Attwood, 2006).

Moreover, no improvement in wettability was observed for FD ITR or in the cocrystals in comparison to crystalline ITR.
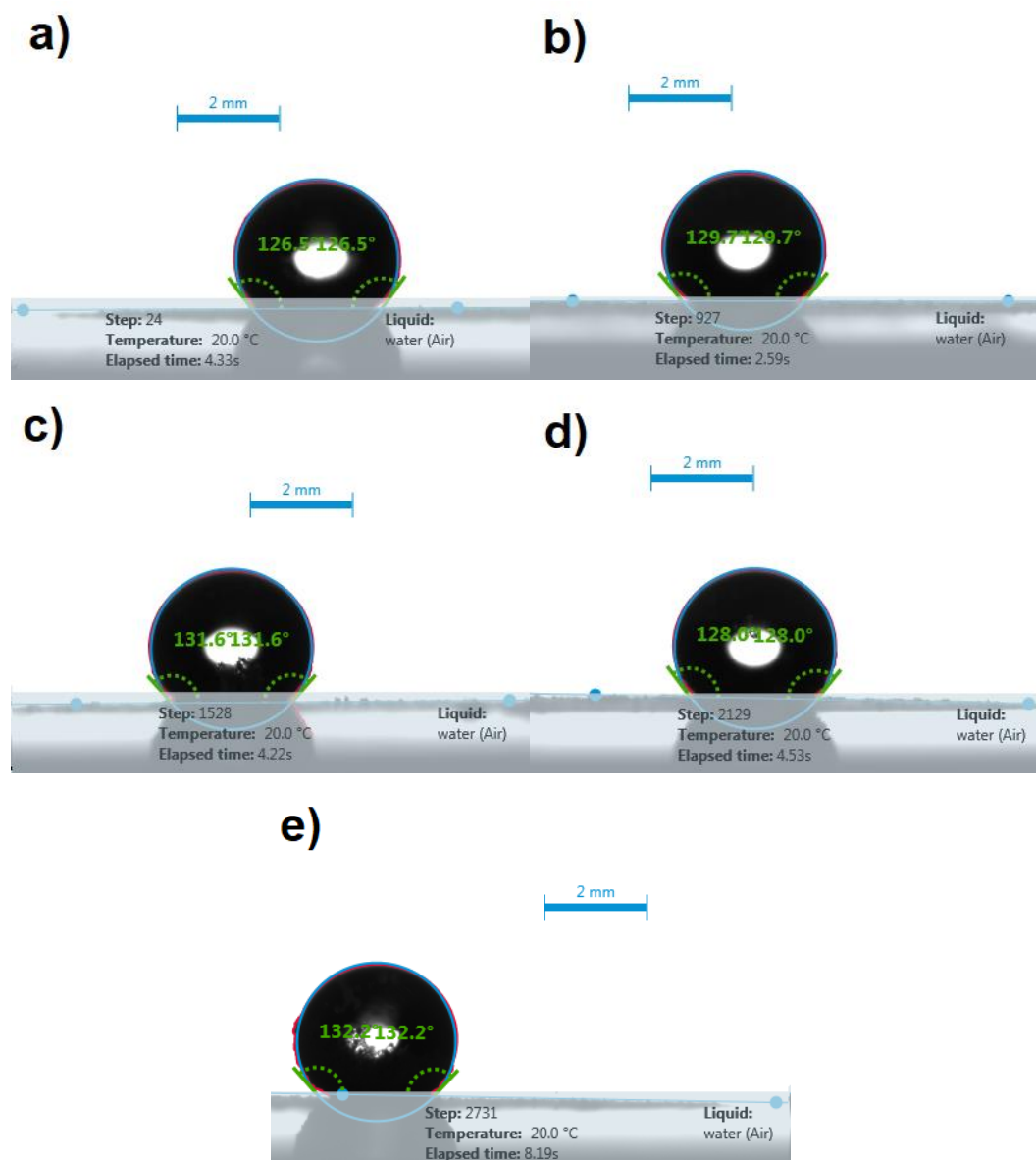
Fig. 4.24: Images of water drops on the surface of disks of compacted (a) crystalline ITR, (b) FD ITR, (c) ITR-OXA, (d), ITR-SUC (e) ITR-TER.

Table 4.13: Contact angle of a water drop at the start and end of the measurement and p-values

Sample	Initial (°)	Final[*] (°)	*p-value*
ITR	126.840 ± 0.38	126.465 ±0.32	0.267
FD ITR	128.865 ± 0.79	127.040 ± 1.65	0.160
ITR-OXA	128.715 ± 2.88	125.955 ± 3.51	0.352
ITR-SUC	126.485 ± 1.49	124.780 ± 1.95	0.295
ITR-TER	130.535 ± 1.66	129.730 ± 1.94	0.614

[*] after 10 min of drop deposition

4.3.4.3.Intrinsic dissolution rate (IDR)

The IDR analysis in medium at pH 1.2 was carried out using an inForm instrument, which is an instrument able to prepare dissolution media automatically using the parameters previously programmed, including information about the temperature and pH conditions, as this instrument has sensors to monitor these parameters. Furthermore, the inForm was designed to perform the dissolution analysis using small volumes up to 40 mL using its a robotic arm to lower the disks holders in the dissolution media, therefore, enabling instantaneous UV measurements (Bergström et al., 2019).

This analysis (Fig. 4.25) revealed a different behaviour of the samples, with ITR showing the lowest IDR, of 2.33 ± 1.1 $\mu g.min^{-1}.cm^{-2}$, in comparison to FD ITR, which achieved the highest dissolution rate of 54.14 ± 2.22 $\mu g.min^{-1}.cm^{-2}$. The faster IDR of FD ITR in relation to ITR was related to the disordered state of the API in the former. As identified in the solid-state characterisation (Fig. 4.22), the API in FD ITR was in the liquid crystal smectic mesophase, which is a higher energy form in comparison to the crystalline state of ITR (the starting material). Therefore, the high free energy of FD ITR promoted the quicker dissolution of the API (Babu and Nangia, 2011).

One-way ANOVA revealed that the investigated samples had statistically different IDR values, except for ITR and ITR-TER. In this case, cocrystallisation was unable to improve the dissolution rate of the API, likely due to the poor aqueous solubility of the coformer, TER, which has solubility in water of 17 µg/mL at 25 °C (Park and Sheehan, 2000), close to ITR aqueous solubility of 1 µg/mL at pH 6.8 (Stevens, 1999). The influence of the coformer in IDR was evident for the other cocrystals, as the rank order of aqueous solubility of pure coformers was TER < SUC < OXA (OXA: 130-140 mg/mL and SUC: 83 mg/mL (Litsanov et al., 2014; Tyner and Francis, 2018)), the same as for the IDR values of the equivalent cocrystals: ITR-TER < ITR-SUC < ITR-OXA (Fig. 4.25).

Raman spectroscopy analysis (Appendix 2) of the disks showed no difference in the samples before and after the IDR test therefore, they conserved their solid-state characteristics during this experiment.
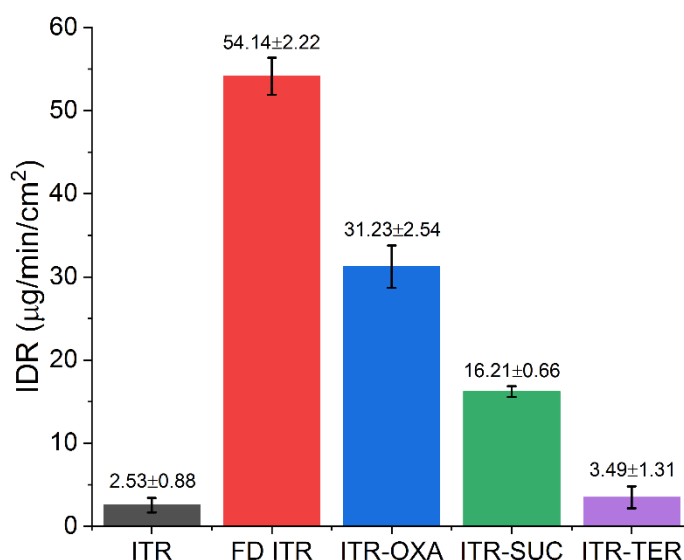
Fig. 4.25: IDR of the API as start material (ITR), freeze dried (FD ITR), and the cocrystals ITR-OXA, ITR-SUC and ITR-TER

4.3.4.4. Powder dissolution

Powder dissolution analysis was carried out in two stages: one with the samples mixed with lactose monohydrate in a 1-6 API-excipient ratio (w/w) to improve wettability and dispersibility of the drug powders and another with the samples physically mixed with the same excipients as in the Sporanox® formulation. In both dissolution experiments, Sporanox® was used as the reference. For this purpose, the pellets were removed from the capsules and used without further alterations.

In the dissolution experiment where the samples were mixed with lactose, the results showed that the Sporanox® had a superior dissolution profile in comparison to the other samples (Fig. 4.26). ITR from Sporanox® had an almost constant dissolution rate until it reached its maximum percent of drug dissolved, $\%_{max}$, of 66.9±2.1% (Table 4.14) after 40 min. In comparison to ITR, which had a $\%_{max}$ of 3.7±0.1% (Table 4.14), the concentration of solubilised ITR released form Sporanox® was greater by a 18-fold, highlighting the enhanced dissolution performance of this commercial form.

FD ITR and ITR-SUC had faster initial dissolution rates in comparison to other ITR forms (Fig. 4.26). The time required to reach the maximum percent of dissolved drug, T_{max}, was 20 min for FD ITR and 15 min for ITR-SUC, while the other sample this time was between 40 and 60 min (Table 4.14). This effect could be due to the differences in solubility between the various forms combined with their different sizes, as shown on the SEM images (Fig. 4.23). Nevertheless, the dissolution profile of FD ITR showed a decrease in the amount of the dissolved material from 18.6±2.8% to 14.6±0.4% after 60 min, being statistically different by t-test (p-value = 0.03). This slight "parachute effect" might be caused by crystallisation of the dissolved API in order to reduce the chemical potential of the supersaturation generated when the disordered API was dissolved (Babu and Nangia,

2011). This was confirmed using PXRD, and it was apparent that the material remaining after dissolution of FD ITR crystallised to form I of ITR (Appendix 2).

Among the cocrystals, the ITR-SUC had the highest $\%_{max,}$ of 7.8±0.8% (Table 4.14), while the dissolution profile of ITR-OXA mostly overlapped with that of ITR. The cocrystal had a slightly higher $\%_{max}$, 4.5±0.1%, while ITR had the $\%_{max}$ of 3.7±0.1% (Table 4.14). This result may contrast with the IDR study (Fig. 4.25), which showed a faster dissolution rate of ITR-OXA in relation to ITR. In this study, the very small difference in the % of solubilised drug between ITR and ITR-OXA could be caused by incongruent dissolution from the cocrystal and removal of the coformer from its surface. This is due to the very different solubilities of OXA (130-140 mg/mL) in comparison to that of ITR (0.001 mg/mL) (Stevens, 1999; Tyner and Francis, 2018). A conversion to crystalline ITR form I was observed by PXRD analysis of the remaining ITR-OXA (Appendix 2). Therefore, cocrystallisation of an API with a coformer that with very different aqueous solubility might not be able to enhance the dissolution rate of the API (Grossjohann et al., 2012).

Dissolution studies of ITR-TER showed that the amount of the drug dissolved increased until the final measurement at 60 min (Fig. 4.26), reaching a $\%_{max}$ of 5.8±0.4% however, this value had no significant difference in comparison to those referent of the ITR (Table 4.14). In this case, the results of powder dissolution of ITR-TER and ITR agreed with their IDR results (Fig 4.25), which showed that cocrystallisation with TER did not increase ITR dissolution. However, the PXRD trace of the undissolved ITR-TER after the dissolution test showed no alteration of the solid state after dissolution (Appendix 2), suggesting that this cocrystal have an enhanced stability in aqueous media in relation to the other samples.
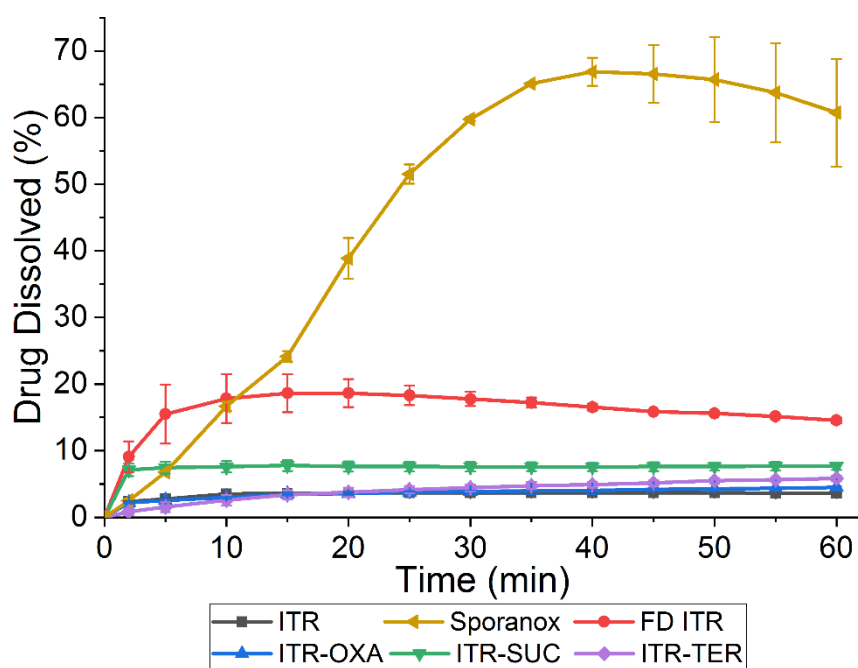
Fig. 4.26: Dissolution profile of Sporanox® and the mixtures of ITR, FD ITR, ITR-OXA, ITR-SUC and ITR-TER with lactose monohydrate in a 1-6 ratio (w/w) of API and excipient.

Table 4.14: The %$_{max}$ and T$_{max}$ values for Sporanox® and the mixtures of ITR, FD ITR, ITR-OXA, ITR-SUC and ITR-TER with lactose monohydrate in a 1-6 ratio (w/w) of API and excipient.

Sample	%$_{max}$ (%)	T$_{max}$ (min)
Sporanox®	66.9±2.1	40
ITR	3.7±0.1	40
FD ITR	18.6±2.1	20
ITR-OXA	4.5±0.1	60
ITR-SUC	7.8±0.8	15
ITR-TER	5.8±0.4	60

The dissolution analysis using the samples mixed with the same excipients as those present in the Sporanox® formulation (Fig. 4.27) yielded different results in comparison to the test using the physical mixtures with lactose (Fig. 4.26). In this experiment, Sporanox® also had a superior dissolution profile when compared to the other samples (Fig. 4.26), reaching 86.1±1.0% of dissolved drug. Only 2.4±0.1% dissolved from the crystalline ITR (Table 4.7). FD ITR had the second highest dissolution profile (Fig. 4.27). This sample continuously released ITR reaching a %$_{max}$ of 36.0±1.0% (Table 4.15). No "parachute" effect was observed, in contrast to the previous analysis (Fig. 4.26). This could be caused by the stabiliser effect of the polymers PEG 6 kDa and HPMC, preventing crystallisation of solubilised API into its crystalline form (Van Eerdenbrugh et al., 2008). The PXRD trace of the undissolved FD ITR recovered after the dissolution test showed no alterations of its solid-state characteristics (Appendix 2), suggesting that the FD ITR had an enhanced stability in this experiment.
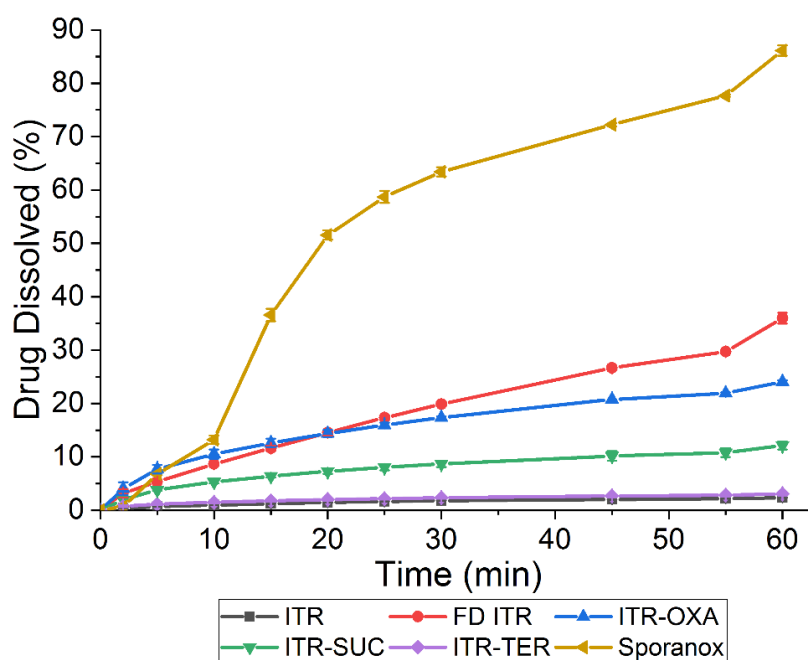
Fig. 4.27: Dissolution profile of Sporanox® and the ITR, FD IDR, ITR-OXA, ITR-SUC and ITR-TER mixed with excipients present in the Sporanox® capsule.

Table 4.15: The %max values of Sporanox® and the ITR, FD ITR, ITR-OXA, ITR-SUC and ITR-TER mixed with excipients present in the Sporanox® capsule.

Sample	$\%_{max}$ (%)
Sporanox®	86.1±1.0
ITR	2.4±0.1
FD ITR	36.0±1.0
ITR-OXA	24.1±0.3
ITR-SUC	12.13±0.8
ITR-TER	3.1±0.1

In relation to the cocrystals, ITR-OXA reaching the greatest $\%_{max}$ of 24.1±0.3% (Table 4.7). The ITR-SUC cocrystal had a $\%_{max}$ of 12.1±0.8%, while ITR-TER had the lowest drug release of 3.1±0.1%. ITR-TER was the only sample, which showed no significant difference in $\%_{max}$ in relation to the crystalline ITR when compared by ANOVA. In comparison to the previous analysis, ITR-OXA and the ITR-SUC had improved dissolution profiles, probably due to the stabiliser effect of the PEG 6 kDa and HPMC polymers, as observed for the FD ITR sample. PXRD analysis of ITR-OXA and ITR-SUC after the dissolution test (Appendix 2) showed no change when compared to the samples before dissolution.

Another factor to be considered in these results is the particle size of these samples. Although the SEM not being ideal to determine the accurate average particle sizes, the SEM images (FIG. 4.23) revealed that the ITR-OXA were produced having smaller sizes than the ITR-SUC, approximately 3 and 5 µm, respectively, while much larger particles were observed for the crystalline ITR, with particles up to 30 µm (Fig. 4.23). According to the Noyes-Whitney equation (Eq. 1.1) (Noyes and Whitney, 1897), the dissolution rate (dm/dt) is expressed as:

$$\frac{d_m}{d_t} = \frac{AD(C_s - C)}{h} \qquad \text{(Eqn.1.1)}$$

where *A* is the surface area of the solid, *D* is the diffusion coefficient, C_s is the saturation solubility, *C* is the drug concentration and *h* is the thickness of diffusion layer. Therefore, the samples produced in smaller sizes are likely to have faster dissolution rate, as observed for the ITR-OXA in relation to the other cocrystals. Nevertheless, the ITR-TER was unable to improve the dissolution rate in relation to the crystalline ITR even having particles in smaller particles (Fig. 4.23b), highlighting the importance of the coformer selection.

4.4.Conclusions

In summary, this work demonstrated that the number of multicomponent forms of ITR is limited, as the extensive screening showed that only three eutectic phases and one new cocrystal were identified after screening 29 ITR-excipient pairs. A new cocrystal was produced using TER, which is the first aromatic coformer described as being able to cocrystallise with ITR. Moreover, despite not being an initial objective of tis work, the formation of eutectics also could further understanding as how coformers can interact with ITR. The coformers that formed eutectic phases with ITR were dihydrocaffeic acid, 4-nitrobenzoic acid and 4-aminosalicylic acid and have a carboxylic acid moiety in their molecular structure and their pK_a values are close or lower than that of ITR as common properties.

The elucidation of the crystalline structure of ITR-TER revealed that this new form is similar to other known ITR cocrystals with a 2-1 stoichiometry, where the ITR molecules are in an anti-parallel arrangement and the coformer "trapped" in the space formed between the two ITR molecules. However, this supramolecular arrangement had a different heterosynthon to the existing cocrystals based on aliphatic dicarboxylic acids, as the C3 of the azole group and the carbonyl of the coformer formed an additional H-bond.

A comparison of the dissolution behaviour of the various forms of ITR including crystalline ITR, freeze dried ITR and ITR cocrystals with oxalic acid, succinic acid and terephthalic acid showed that they had different profiles and dissolution characteristics. FD ITR showed a remarkable improvement in terms of dissolution considering IDR and powder dissolution in relation to crystalline ITR. This was due to the high energy state of the API achieved by freeze-drying. For the cocrystals, their IDR values and powder dissolution profiles correlated with the aqueous solubility of the coformers. The increasing rank order of the dissolution rates of API from the cocrystals was ITR-TER < ITR-SUC < ITR-OXA. Furthermore, physically mixing FD ITR, ITR-OXA and ITR-SUC with the same excipients present in the Sporanox® formulation, including PEG 6 kDa and HPMC, enhanced the stability of these forms in the dissolution media preventing their crystallisation into the form I of the API.

Chapter V: Development of ITR-TER nano-cocrystals and their use as dry powders for pulmonary administration

5.1.Introduction

In Chapter 4, a new cocrystal of ITR with terephthalic acid (TER) was identified. However, the solubility and the dissolution studies showed that this multi-component system had characteristics similar to crystalline ITR. However, it was found that the ITR-TER cocrystal did not undergo a form change into the parent drug (ITR) upon dissolution in contrast to other ITR cocrystals produced with succinic acid and oxalic acid indicating that this new form had improved physical stability.

As demonstrated in Chapters 2 and 3, ITR had different physicochemical characteristics when the particle size was reduced into the nanometric scale. Therefore, it was hypothesised that nanonisation of the ITR-TER cocrystal could lead to alteration of its characteristics. The preparation of nanometric cocrystals, i.e. nano-cocrystals (NCC), is a relatively unexplored topic, nevertheless, it has been already proved that NCCs are able to successfully enhance the properties of APIs (Huang et al., 2017; Karashima et al., 2016). For instance, the comparison of multiple forms of phenazopyridine, a BCS class II anaesthetic, revealed that the drug from NCCs produced with phthalimide was completely released after 180 min in contrast to the hydrochloride salt form and the same cocrystal in a micrometric size, which had 67 and 43% drug release after the same time, respectively (Huang et al., 2017). In addition, the oral bioavailability study showed that the C_{max} and the AUC of the NCC form were improved by a 1.39- and 2.44-fold, respectively, in relation to the salt form. In another study, carbamazepine-saccharin and furosemide-caffeine NCCs also had improved dissolution profiles in comparison to their respective API in the nanometric size and non-nanometric cocrystals (Karashima et al., 2016).

The application of nanonised cocrystals was also used to improve the characteristics of ITR (De Smet et al., 2014). In the work of De Smet, ITR NCC with adipic acid with a particle size of 549 ±51 nm was produced by wet milling and then spray dried or layered on beads to produce a dry powder. The dissolution analysis of the spray-dried NCC and the NCC layered on beads showed complete release after 8 and 20 min, respectively, in contrast to the commercial form of the ITR, Sporanox® (Janssen Pharmaceutica, Belgium) which had only 35% ITR release after 60 min. The bioavailability studies of ITR when these formulations were orally administered to dogs, also showed modified pharmacokinetics characteristics as the spray dried NCC had a faster release, a 1.3-fold higher C_{max} and reduced T_{max} in relation to Sporanox, while the beads formulation had C_{max} and AUC a 1.9- and 2.2-fold, respectively, increased comparing to the commercial form (De Smet et al., 2014).

Similar to the nanonised API, the NCCs can be produced by top-down methods, including wet milling and high-pressure homogenisation, or by a bottom-up approach, using techniques such as antisolvent precipitation, supercritical fluid and solvent evaporation (Fontana et al., 2018; Padrela et al., 2018; Sander et al., 2010; Spitzer et al., 2015). Among

them, top-down methods are less complicated and requiring minimal solvent addition, therefore considered as a "green" approach (Trask et al., 2004; Verma et al., 2009). However, the size reduction using top-down methods is limited to a critical point where the energy input of the process is unable to cause further cracks on the particle (Loh et al., 2015). On the other hand, the bottom-up methods are based on the crystallisation of solutes from solution, therefore, they have a greater potential to produce particles with smaller and narrow size distribution than top-down methods (Sinha et al., 2013). Nevertheless, for the NCC preparation using an antisolvent precipitation method, the API and coformer must have similar solubility in the solvent-antisolvent pair to achieve a congruent cocrystallisation, where the formation of the cocrystal is more probable than the crystallisation of the isolated parent components (Alhalaweh and Velaga, 2010; McClurg, 2016).

Furthermore, the development of the ITR-TER NCC could be particularly interesting for application in a pulmonary formulation. This administration route is used for systemic drug delivery and for local treatment against pulmonary diseases including infections and inflammation (Newman, 2018). However, for each of these purposes, solubility of the drug have a critical importance, as freely soluble drugs are likely to be promptly absorbed when inhaled and reaching the bloodstream in a short time therefore, they have a better potential for systemic delivery (Velaga et al., 2018). On the other hand, the slow drug release of poorly soluble APIs increases the residence time of the particles in the lungs, consequently, favouring the local action (Velaga et al., 2018).

Nanoparticles (NPs) are likely to have a poor deposition in the lungs when inhaled, because particles having sizes lower than 1 µm are likely to be exhaled easily (Sosnowski, 2015). Indeed, the particle size is a key factor for the pulmonary deposition, as particles with sizes between 1 and 5 µm are likely to be deposited in the lower airways, while those larger than the higher limit range are also unable to reach the lungs as they are subject to inertial impaction and swallowed (Loira-Pastoriza et al., 2014). Therefore, a common form to enhance the pulmonary administration of NPs is to incorporate them into larger structures, which have a more suitable size range. These nanoparticle-embedded microparticle structures are known as "Trojan particles" (Anton et al., 2012), which are produced normally by spray-drying or freeze-drying the NPs with encapsulating materials, such as mannitol and poly(vinyl alcohol) (Cheow et al., 2011; Yamasaki et al., 2011). Then, after the deposition of the Trojan particle, these encapsulating materials are removed, releasing the NPs on the lungs.

Therefore, in this Chapter, a method of ITR-TER NCC preparation by antisolvent precipitation was developed considering a number of factors. Initially, the solvent phase was selected by evaluating the mixture of acetone and methanol to establish which ratio of these solvents is able to solubilise, at highest possible concentration, the API and the coformer in the ITR-TER stoichiometry of 2-1. Then, ITR-TER dispersions with and without

lecithin were produced, characterised and evaluated regarding their colloidal stability. The influence of the ultrasound application on the particle size of the ITR-TER dispersions was also evaluated. The final stage of the method development aimed to optimise the preparation conditions and scale-up to enable the production of an appropriate batch size for spray drying, which was the method of making Trojan particles. These Trojan particles containing the developed ITR-TER NCC embedded into microparticles were produced with mannitol, trehalose and raffinose. The solid-state and aerodynamic properties of the dried powders were then evaluated.

5.2.Materials and Methods

5.2.1.Materials

Soybean lecithin with 90% purity was purchased from Alfa Aesar (UK). D-mannitol, D-(+)-trehalose dihydrate, ethanol (analytical grade) and acetonitrile (HPLC grade) were purchased from Sigma-Aldrich (Ireland). D-(+)-raffinose pentahydrate was purchased from ITW Reagents (Germany). The details of all other materials and solvents used in this study are listed in Chapter 4.

5.2.2.Methods

5.2.2.1.Solubility analysis

An amount of ITR in excess of the expected solubility was placed in 4 mL glass vials and 2 mL an acetone and methanol mixture at 1.0, 0.9, 0.8, 0.7, 0.6 and 0.5 (v/v) of solvent fraction in respect of acetone content were added. The tubes were sealed, immersed in a beaker with water at 25 and 50 °C and mixed at 1,300 rpm using a hot plate stirrer SD-162 (Stuart, UK) for 24 hours. Then, the samples were filtered using PTFE 0.45 μm syringe filters (Fisherbrand™, Fisher Scientific, UK) and the filtrates diluted 10-fold in the mobile phase (acetonitrile and phosphate buffer mixture at a 60:40 (v/v) ratio as described in Section 5.2.2.8). The API concentration was determined using HPLC as described in Section 5.2.2.8. This analysis was carried out in duplicate.

5.2.2.2.ITR-TER cocrystal preparation by antisolvent precipitation

Initially, solutions of 2 mg/mL of ITR and 0.235 mg/mL of TER were prepared by dissolving 20 mg of the API and 2.35 mg of the coformer in 10 mL of a mixture of acetone and methanol (70:30, v/v) and filtering the solution using a 0.45 μm PTFE filter (Fisherbrand™, Fisher Scientific, UK). Afterward, 2 mL of this solution at 25 °C was rapidly injected using a 0.5 mm x 16 mm Sterican® needle into 20 mL of deionised water (Elix®, Merck Millipore, Ireland) at 90 °C under a constant magnetic agitation at 1,300 rpm using an SD-162 hot plate stirrer (Stuart, UK). The dispersions were immediately transferred to an ice-bath for a few seconds before being transferred to a 100 mL round bottom flask and subjected to evaporation at 30 ºC (heating bath B-490, Büchi, Switzerland) for 30 min and 60 mbar in a Rotavapor R-205 attached to a vacuum pump V-700 (Büchi, Switzerland).

5.2.2.3.Preparation of ITR-TER dispersions containing lecithin

For this purpose, a 1 mg/mL dispersion of lecithin was prepared by dispersing 10 mg of the compound in 10 mL of ethanol. Then, 122 or 244 μl of this dispersion was injected in 20 mL of deionised water at 90 °C under constant magnetic agitation at 1,300 rpm using an SD-162 hot plate stirrer (Stuart, UK). These diluted dispersions of lecithin were used as the antisolvent phase to produce the ITR-TER dispersions containing, respectively, 2.5 and 5

% (w/w) of lecithin in relation to the total of solid contents. Then, 2 mL of a solution containing 2 mg/mL of ITR and 0.235 mg/mL of TER in a mixture of acetone and MeOH (at 25 °C) prepared as described in Section 5.2.2.2 was injected using a 0.5 mm x 16 mm Sterican® needle to the antisolvent phase kept at 90 °C. For the kinetic analysis of the particle size growth, aliquots were taken after this step at pre-determined time points and evaluated as described in Section 5.2.2.9. For the sonication analysis, the dispersions were transferred to a 50 mL beaker and placed in an ice bath and then the procedure followed as described in Section 5.2.2.4. For the analysis of the effect of lecithin as a particle stabiliser, the dispersions were transferred to an ice-bath for a few seconds before being transferred to a 100 mL round bottom flask and subjected to evaporation at 30 ºC (heating bath B-490, Büchi, Switzerland) for 30 min and 60 mbar in a Rotavapor R-205 attached to a vacuum pump V-700 (Büchi, Switzerland).

5.2.2.4. Sonication of ITR-TER dispersions

Pre-made ITR-TER dispersions without and with 5% (w/w) of lecithin were sonicated using a VC130 PB Vibra-Cell™ ultrasonic processor (Sonics & Materials, USA) for 30 minutes in an ice bath and magnetic agitation at 400 rpm (IKA, Germany). The probe with a 13 mm tip diameter was immersed allowing some space for the magnetic stirrer. The ultrasound was applied setting the input to 100% of amplitude and producing an output of approximately 16±2 Watt. For the evaluation of the impact of ultrasonication on the particle size of the ITR-TER dispersion, aliquots were taken at times 0, 5, 10, 15 and 30 min of the ultrasound application and the particle size was measured by DLS as described in Section 5.2.2.9. This evaluation was performed in triplicate.

5.2.2.5. Optimisation of the ITR-TER NCC method

The following process parameters: the ITR concentration in the solvent phase and the antisolvent:solvent ratio (AS:S; v/v) were selected as factors for a full factorial experimental design at 2 levels, (+1) and (-1), and an additional repetition at central point (Table 5.1). This optimisation aimed to evaluate the effect of these parameters on the particle size of the ITR-TER dispersions considering an increase of the ITR final concentration. All samples were prepared in triplicate.

Table 5.1: Selected factors and levels used for parameter screening of nanoprecipitation method.

Parameter	Level		
	(-1)	(0)	(+1)
ITR concentration[*] (mg/mL)	2	4	6
AS:S ratio (v/v)	10:1	7.5:1	5:1

(*) in solvent phase; AS: antisolvent phase; S: solvent phase

5.2.2.6.Scale-up of the ITR-TER preparation method

Initially, 100 mL of deionised water (Elix®, Merck Millipore, Ireland) in a 250 mL round-bottom flask were heated at 90 °C in a water-bath using a hot plate SD-162 (Stuart, United Kingdom). Then, 6.7 mL of a 1 mg/mL lecithin dispersion in ethanol prepared as described in Section 5.2.2.3 were added and mixed under constant magnetic agitation at 1,300 rpm. This was used as the antisolvent phase. Also, a solution of 6 mg/mL of ITR and 0.706 mg/mL of TER was prepared dissolving 150 mg of the API and 17.66 mg of the coformer in 25 mL of a mixture of acetone and methanol in a volume ratio of 70:30 (v/v). A U300H ultrasonic bath (Ultrawave, UK) at 40 °C was used to produce a clear solution that was used as the solvent phase. Then, 20 mL of the solvent phase was rapidly injected using a10 mL pipette into the antisolvent phase and the formed dispersion was allowed to equilibrate for a few seconds before transferring to a beaker and cooled down using an ice-bath. Finally, the dispersion was sonicated for 30 min as described in Section 5.2.2.4. This evaluation was performed in triplicate.

5.2.2.7.Spray drying of ITR-TER dispersions

ITR-TER dispersions were converted into Trojan particles using a spray-dryer Büchi Mini Spray Dryer B-290 (Büchi, Switzerland) operating in the open cycle mode configuration with a two-fluid nozzle. ITR-TER dispersions were prepared as in the Section 5.2.2.6 and a sugar, either mannitol, raffinose or trehalose, was added to the liquid dispersion of ITR-TER at 85.3% (w/w) of the total solid content (Table 5.2). The inlet temperature for the process was set at 140 °C and the feeding pump rate was adjusted to 15% (flow of 5.4 ml/min). Nitrogen was used as the atomising gas (flow at 40 mm high) with air used as the drying medium (flow of 504 L/min, aspirator rate of 80%). These settings yielded the outlet temperature of approximately 70°C. A high-efficiency cyclone separator was employed for collection of the spray-dried product. The production yield was calculated as the weighted of the powder recovered in relation to the total solid content. All samples were prepared in duplicate.

Table 5.2: Composition of the spray-dried powders

Excipient (%,w/w)	Formulation		
	ITR-TER-MAN	**ITR-TER-RAF**	**ITR-TER-TRE**
ITR-TER NCC	14[*]	14[*]	14[*]
Lecithin	0.7	0.7	0.7
Mannitol	85.3		
Raffinose		85.3	
Trehalose			85.3

(*) The equivalent of 12.5% (w/w) of the API

5.2.2.8.ITR quantification by high-performance liquid chromatography (HPLC)

Concentrations of ITR were measured using a Waters Symmetry® C18 column (4.6 mm diameter, 150 mm length, particle size 5 µm) attached to an Alliance HPLC with a Waters 2695 Separation module quipped with a Waters 1525 Binary HPLC pump, Waters 717 plus autosampler and operating with a Waters 2487 dual λ absorbance detector.

For this analysis, a phosphate buffer was prepared by dissolving 13.6 g of potassium dihydrogen phosphate in 2 litres of ultra-pure water (Elix®, Merck Millipore, Ireland). Then, the pH was adjusted to 6.8 using 3M KOH solution. Before use, the phosphate buffer was filtered under vacuum using a 0.2 µm hydrophilic polypropylene membrane filter (Pall, USA) and sonicated in a U300H ultrasonic bath (Ultrawave, UK). The mobile phase used for the ITR quantification was a mixture of the phosphate buffer and acetonitrile at 40:60 (v/v). For the analysis, 20 µL injection volume was used with an isocratic flow rate of 1 ml/min for 14 min. The ITR concentration was measured by a UV detection wavelength of 260 nm. The concentration range for the calibration curve of ITR was 4-40 µg/mL. Empower 3 software (Waters, USA) was used for evaluation of the results. This analysis was carried out in triplicate.

5.2.2.9.Particle size and PdI analysis using dynamic light scattering (DLS)

DLS was performed as described in Chapter 2. For the kinetic analysis of particle size, no equilibration time was used, and the instrument was programmed to execute 15 consecutive measurements with a total measurement time of approximately 40 min. This evaluation was performed in triplicate.

5.2.2.10.Zeta potential

Zeta potential was performed as described in Chapter 3.

5.2.2.11.Differential Scanning Calorimetry (DSC)

DSC was performed as described in Chapter 4.

5.2.2.12.Powder X-ray diffractogram (PXRD)

PXRD was performed as described in Chapter 3.

5.2.2.13.Fourier transform infrared spectroscopy (FT-IR)

FT-IR was performed as described in Chapter 4.

5.2.2.14.Morphological analysis

Scanning electron microscopy (SEM) was carried out as described in Chapter 3.

5.2.2.15.Quantification of ITR in the spray-dried powders

For this purpose, 2 mg of each of the spray-dried powders were carefully weighted and dissolved in 10 mL of the mobile phase (Section 5.2.2.16) using a U300H ultrasonic bath (Ultrawave, UK) until a clear solution was obtained. Then, 1 mL aliquots of this solution were taken and filtered using PTFE 0.45 µm syringe filters (Fisherbrand™, Fisher Scientific, UK). ITR was quantified using HPLC as described in Section 5.2.2.8. The results are expressed as an average and used to calculate the drug loading (Eqn. 5.1) and the encapsulation efficiency (Eqn 5.2) (Schafroth et al., 2012).

$$\text{Drug Loading (\%, w/w)} = \frac{\text{amount of drug in spray-dried powder}}{\text{amount of spray-dried powder}} \times 100 \qquad \text{(Eqn. 5.1)}$$

$$\text{Encapsulation efficiency (\%, w/w)} = \frac{\text{amount of drug in spray-dried powder}}{\text{initial drug amount}} \times 100 \qquad \text{(Eqn. 5.2)}$$

5.2.2.16.Particle size analysis of the spray-dried powders

The geometric particle size distribution was determined by laser light diffraction using a Malvern Mastersizer 3000 (Malvern Instruments, UK). Particles were dispersed using an Aero S (Malvern Instruments, UK) dry feed instrument using 4 bar pressure. An obscuration of 0.5-10% was obtained manually adjusting the feed rate. This analysis was carried out in triplicate.

5.2.2.17.Next Generation Impactor (NGI) analysis

For each formulation, 3 hydroxypropylmethylcellulose (HPMC) capsules (size 3 Vcaps®, Capsugel, USA) were filled with the spray-dried powder containing an equivalent dose of 2.5±0.2 mg of ITR (Duret et al., 2012). A dry powder inhalation device (Cyclohaler®, N.V. Medicopharma, Netherlands) was connected to the mouthpiece of a Next Generation Impactor (Copley Scientific Limited, UK). The capsule containing the inhaled powder was placed in the holder of the inhaler device, punctured, and a vacuum pump was used to produce the air stream of 60 L/min for 4 s (Tewes et al., 2013). The powder that remained in the capsule and the powder deposited in the device, mouthpiece, throat, in stages (S) 1-7 (corresponding to the following cut off diameters: S1: 8.06 µm, S2: 4.46 µm, S3: 2.82 µm, S4: 1.66 µm, S5: 0.94 µm, S6: 0.55 µm, S7: 0.36 µm), and micro-orifice collector (MOC) were collected and dissolved in 5 mL of mobile phase (Section 5.2.2.8). Afterwards, 1 mL aliquots were taken, filtered using PTFE 0.45 µm syringe filters and the content of ITR was quantified by HPLC as described in Section 5.2.2.8. The fine particle fraction (FPF), i.e. the total amount of particles with aerodynamic diameters smaller than 5.0 µm recovered from stage 2 to MOC, was calculated by interpolation from the inverse of the standard normal cumulative mass distribution less than stated size cut-off against the natural logarithm of the cut-off diameter of the respective stages. The FPF, considered as the respirable

fraction, was expressed as a percentage of the total emitted dose. The mass median aerodynamic diameter (MMAD) of the particles and the geometric standard deviation (GSD) were determined using the Copley Inhaler Testing Data Analysis Software (C.I.T.D.A.S.) version 3.10 (Copley Scientific Limited, UK).

5.2.2.18.Particle size analysis of resuspended powders

For this purpose, a quantity of 1.0±0.1 mg of each of the spray-dried samples, ITR-TER-MAN, ITR-TER-RAF and ITR-TER-TRE, was carefully weighed and resuspended using 2 mL of deionised water and homogenised using a vortex SA7 (Stuart, UK) for 2 minutes. The particle size of resuspended powder was analysed by DLS (Section 5.2.2.9) and by nanoparticle tracking analysis (NTA). NTA was performed as described in Chapter 3 using a NanoSight syringe pump to inject the samples into the system.

The particle size of the resuspended powders was compared to the characteristics of ITR-TER dispersions before spray-drying. For this purpose, 50 µL of the ITR-TER dispersions (Section 5.2.2.6) were diluted in 2.2 mL of deionised water, resulting in a nominal ITR concentration of 2.7 µg/mL and also analysed by DLS and NTA. Both analysis were performed in triplicate.

5.2.2.19.Statistical analysis

Statistical analysis was carried out as described in Chapter 2.

5.3.Results and Discussion

In this chapter, the ITR-TER cocrystal was produced as NPs, i.e. nano-cocrystals (NCCs) for pulmonary formulation. As the cocrystal have low aqueous solubility and high stability as determined in Chapter 4, these characteristics could enable a prolonged residence time of the particles in the lungs with lower risks of conversion to pure ITR and slowly releasing the API in the lungs for its local action against fungal infections (Tolman and Williams, 2010; Yang et al., 2008).

5.3.1.Development of ITR-TER nano-cocrystals

ITR-TER NCCs were developed using antisolvent precipitation. The preference for this method was based on the possibility of modifying the conditions that affect the size in order to achieve the ITR-TER particles in the nanometric size range, as performed in Chapter 2. Furthermore, in comparison to the ball milling, antisolvent precipitation has a better potential to produce smaller particles, as this is a bottom-up approach where the particles are formed from by nucleation and subsequent growth from a supersaturated solution allowing to prepare small particles with a narrow size distribution (Sinha et al., 2013). On the other hand, milling is a top-down method based on the size reduction of existing particles, which limits the lower size that could possibly be obtained (Loh et al., 2015). Therefore, antisolvent precipitation seemed as more promising for the preparation of smaller ITR-TER NCCs, despite the ball-milled ITR-TER cocrystal had sizes lower than 1 μm in Chapter 4.

5.3.1.1.Determination of the composition of the solvent phase

The first step in the development of the ITR-TER NCC nanoprecipitation method was to select the solvent phase. As investigated in Chapter 4, the ITR-TER cocrystal has a 2-1 API-coformer stoichiometry therefore, ideally, both compounds should have considerable solubility in a solvent to reduce its volume usage and improve the yield. However, the solubility of ITR and TER in the previously used solvents, acetone and methanol, is very low (Table 5.3) limiting the production yield of this method.

Table 5.3: Reported solubility of ITR and TER in acetone and methanol at 25 °C.(McComiskey et al., 2018; Park and Sheehan, 2000; Sriamornsak and Burapapadh, 2015)

	Solvent	
	Acetone (mg/mL)	Methanol (mg/mL)
ITR	2.5	0.745
TER	insoluble	0.792

The solubility of ITR was evaluated at 25 and 50 °C using a mix of acetone with methanol in different solvent fractions, in which the former as used as the main solvent and

the latter as the cosolvent (Fig. 5.1). ANOVA analysis showed that, regardless of the acetone fraction and temperature, ITR had a significantly lower solubility in pure acetone. Considering the higher solubility of the API in acetone than in methanol (Table 5.3), this result indicated that an acetone and methanol mixture, at any ratio, could remarkably increase the ITR solubility in relation to those solvents used alone. In addition, the highest solubility of ITR was 7.1 mg/mL when solubilised at 25 °C using the 0.9 acetone fraction, while at 50 °C, 19.3 mg/mL of the API could be solubilised in a 0.7 acetone fraction. Therefore, the temperature had a positive impact on the ITR solubility, as the API was a 2.72-fold more soluble at 50 °C.

Considering an antisolvent precipitation method to prepare the ITR NPs described in Chapters 2 and 3, and the 2-1 API to coformer stoichiometry of the ITR-TER cocrystal as determined in Chapter 4, both compounds must be solubilised in the solvent phase respecting this stoichiometry to increase the cocrystallisation probability preventing precipitation of the cocrystal constituents separately. The mixed solvent system with the acetone to methanol volume ratio of 70:30 (v/v) enabled the solubilisation of the highest concentration of the API and coformer respecting this stoichiometry that was prepared at 6 mg/mL and 0.706 mg/mL, respectively at 50 °C.
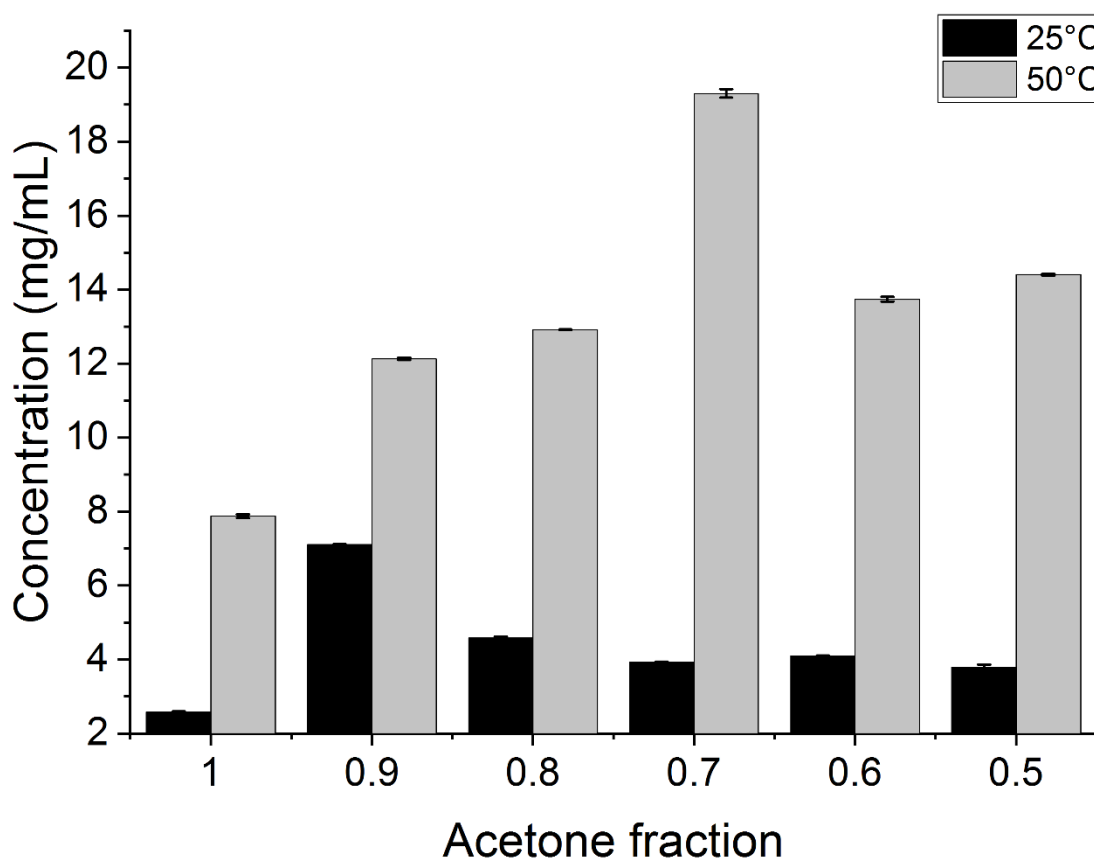
Fig. 5.1: Solubility of ITR in the acetone-methanol mixture at 25 and 50 °C.

5.3.1.2.Effect of lecithin as a particle stabiliser

Initial studies aimed at producing NCC without any stabiliser. As shown in Table 5.4, the particles produced with no lecithin had large particle sizes, of 2361±512 nm. Therefore, it was clear that, in order to make nanosized particles, a stabiliser was needed. It was decided that lecithin might be a suitable excipient. Lecithin (Fig. 5.2) is an endogenous lipid that acts as a lung surfactant and it is considered to be biocompatible with lower hazard risks (Wauthoz and Amighi, 2014). For this reason, it is commonly used as a pharmaceutical excipient, particularly in pulmonary formulations (Li et al., 2015).
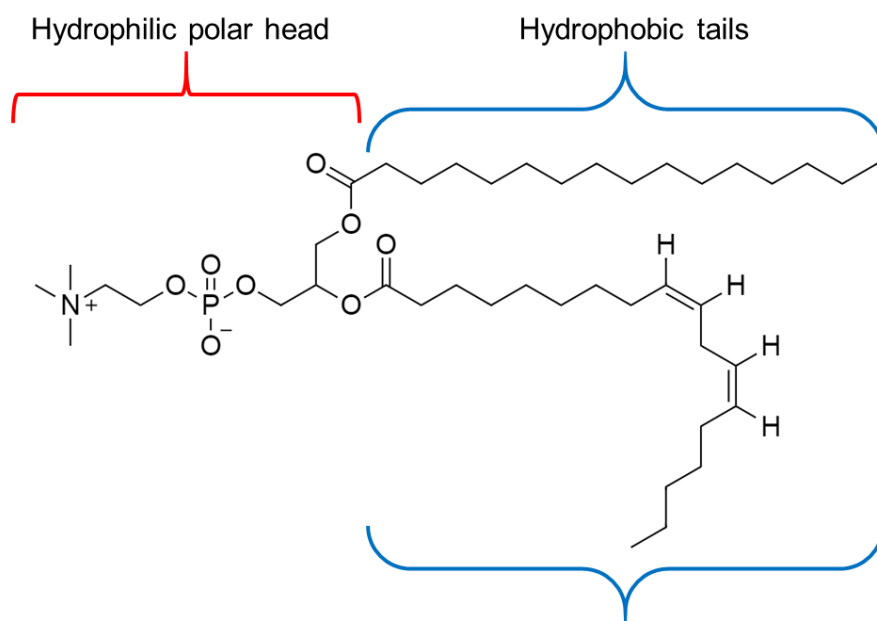
Fig. 5.2: Representation of the molecular structure of lecithin.

DLS analysis of the ITR dispersions prepared with 2.5 and 5% (w/w) of lecithin (Table 5.4) showed that the smallest particles were produced when 5% of lecithin was used, 1170±15 nm. The statistical analysis using ANOVA confirmed that the particle sizes of dispersions with no and 5% of lecithin were significantly different. Therefore, lecithin significantly affected the particle size of the dispersions; however, the stabiliser must be in a concentration higher than 2.5% (w/w) to induce those significant alterations.

Table 5.4: Average particle size, PdI and Zeta potential of the ITR-TER particles with 0, 2.5 and 5% (w/w) of lecithin.

Sample	Particle Size (nm)	PdI	Zeta Potential (mV)
0% Lecithin	2361 ± 512	0.412 ± 0.228	-15.4 ± 0.7
2.5% Lecithin	1559 ± 386	0.275 ± 0.083	-18.8 ± 0.7
5% Lecithin	1170 ± 15	0.078 ± 0.040	-21.3 ± 0.8

ANOVA of PdI values of the dispersions (Table 5.4) showed that the values were not statistically significant regardless of the lecithin concentration used. Nevertheless, only the

particles made using 5% of lecithin were in the range considered as monodispersed, the dispersion containing 2.5% of lecithin was considered as moderately polydisperse and the one with no stabiliser was considered as highly polydisperse (Bhattacharjee, 2016). As discussed in Chapter 2, PdI is a critical characteristic of dispersions as those dispersions which are more polydisperse are more often subject to Oswald ripening than those monodispersed (Wang et al., 2013). Therefore, the presence of lecithin could also contribute to an improvement in the physical stability of the dispersions by reducing their polydispersity and, consequently, minimising Oswald ripening.

The analysis of zeta potential showed that a more negative surface charge of the particles was measured when the lecithin concentration was increased (Table 5.4) and, in this case, ANOVA revealed that the differences were significant. This indicates that the zeta potential of particles was also affected by the adsorbed lecithin, possibly because the non-polar hydrophobic tail of this stabiliser (Fig 5.2) can interact with the hydrophobic surface of the ITR-TER particles, leaving its polar head (Fig 5.2) exposed and able to increase the surface charge of the particles. Furthermore, this suggests that lecithin could increase the stability of the particles by increasing the electrostatic repulsive forces between the particles in dispersion (Chuacharoen and Sabliov, 2016).

In order to evaluate the kinetics of the particle growth, particle size analysis of the ITR-TER dispersions over time using DLS was conducted. The results (Fig. 5.3) showed that particles made with no lecithin increased their sizes rapidly reaching a size above the nanometric range, of 1168±308 nm after 21 min. The particles produced using lecithin at 2.5 and 5% also quickly increased in size and reached a plateau at approximately 966±189 and 982±150 nm, respectively, after 24 and 27 min, respectively. Comparing the results of the kinetics study with those presented in Table 5.4, the only difference was noted for the dispersion without lecithin as a different particle size was measured. The variation could be because the aliquots of the dispersions for the studies on kinetics were taken immediately after injection the solvent phase and placed in the instrument for DLS measurements, while for results shown on Table 5.4, the samples were evaporated prior to size analysis.
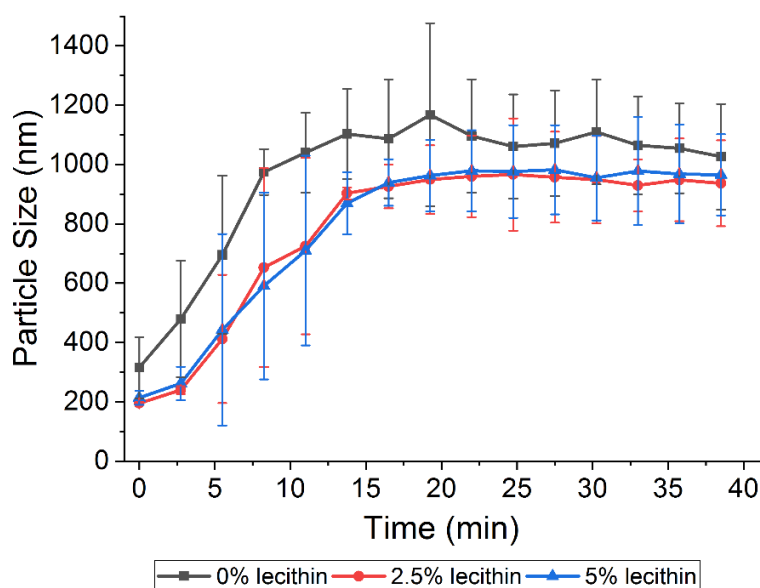
Fig. 5.3: DLS analysis of the particle size of ITR-TER NCC with 0, 2.5 and 5% of lecithin.

The solid-state analysis of the dried material was carried out using PXRD, DSC and FT-IR and the results were compared to those of the pure ITR-TER cocrystal as presented in Chapter 4 and with lecithin (starting material).

PXRD analysis (Fig. 5.4) showed that the ITR-TER particles had Bragg peaks of low intensity at 7.0, 10.5, 15.05, 17.84, 19.26 and 21.20° 2θ, which were also present in the ITR-TER cocrystal (Chapter 4), confirming the presence of this multicomponent form of ITR in these samples. The diffractogram of lecithin had no Bragg peaks, thus lecithin was an amorphous material and its presence in the samples could not be determined using PXRD.

Fig. 5.4: PXRD diffractograms of the (a) ITR-TER cocrystal, the ITR-TER particles containing (b) 0, (c) 2.5 and (d) 5% of lecithin, and (e) pure lecithin.

Thermal analysis of the ITR-TER dispersions containing 0, 2.5 and 5 % of lecithin (Fig. 5.5) showed DSC curves with only one main thermal event, being a sharp endothermic peak with an onset close to the melting point of the pure ITR-TER cocrystal (Table 5.5). Therefore, this indicated that the particles were composed of the cocrystal, indicating a congruent precipitation. Indeed, a small variation in the cocrystal melting temperature was observed between the ITR-TER prepared by ball milling (Fig 5.5a) and by precipitation in antisolvent (Fig. 5.5b). This could be a result of the different particle sizes of these samples, as in the milling process, clusters of approximately 1 µm were formed by round particles smaller (Chapter IV), consequently, increasing the surface area, responsible for the melting point depression (Jiang and Li, 2002). In the meanwhile, the precipitation in antisolvent resulted in particles with sizes over 2 µm (Table 5.4), and, hence, having a slightly higher melting point. Among the samples prepared with lecithin (Fig. 5.5c and d), a small variation in their melting points was observed that could be due to an inter-batch variation, nevertheless, to confirm this possibility, further investigation using other lecithin concentration is necessary. Therefore, no evidence was observed indicating significant effects of lecithin on the solid-state properties of the ITR-TER dispersions.
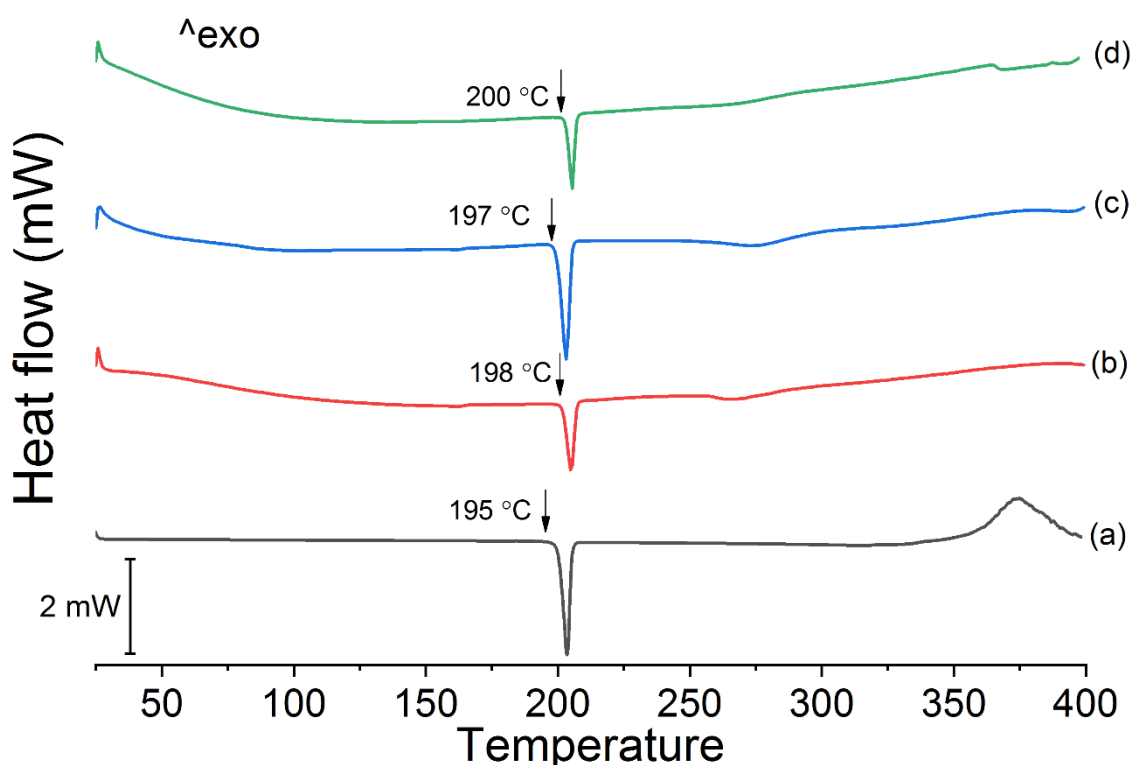
Fig. 5.5: DSC curves of the (a) ITR-TER cocrystal, the ITR-TER particles containing (b) 0, (c) 2.5 and (d) 5% of lecithin.

Table 5.5: Summary of thermal events observed in DSC analysis of the ITR-TER cocrystal and the ITR-TER particles containing 0, 2.5 and 5% (w/w) of lecithin.

Sample	Thermal event	Onset (°C)	Peak (°C)	Enthalpy (J/g)
ITR-TER	Melt (CC)	195.9	204.1	-83.7
	Exothermic	311.0	379.05	347.1
ITR-TER 0% lecithin	Melt	198	201.4	-8.8
ITR-TER 2.5% lecithin	Melt	197	203.4	-7.4
ITR-TER 5% lecithin	Melt	200	205.1	-6.6

FT-IR analysis (Fig. 5.6) showed that the spectra of the precipitated samples, regardless of the lecithin presence, were similar to that of the ITR-TER cocrystal. However, a strong peak at 1272 cm^{-1} of TER was also present in these samples. This peak was assigned to a C-C stretching (Karthikeyan et al., 2015), suggesting that a residual TER could be present in the samples.
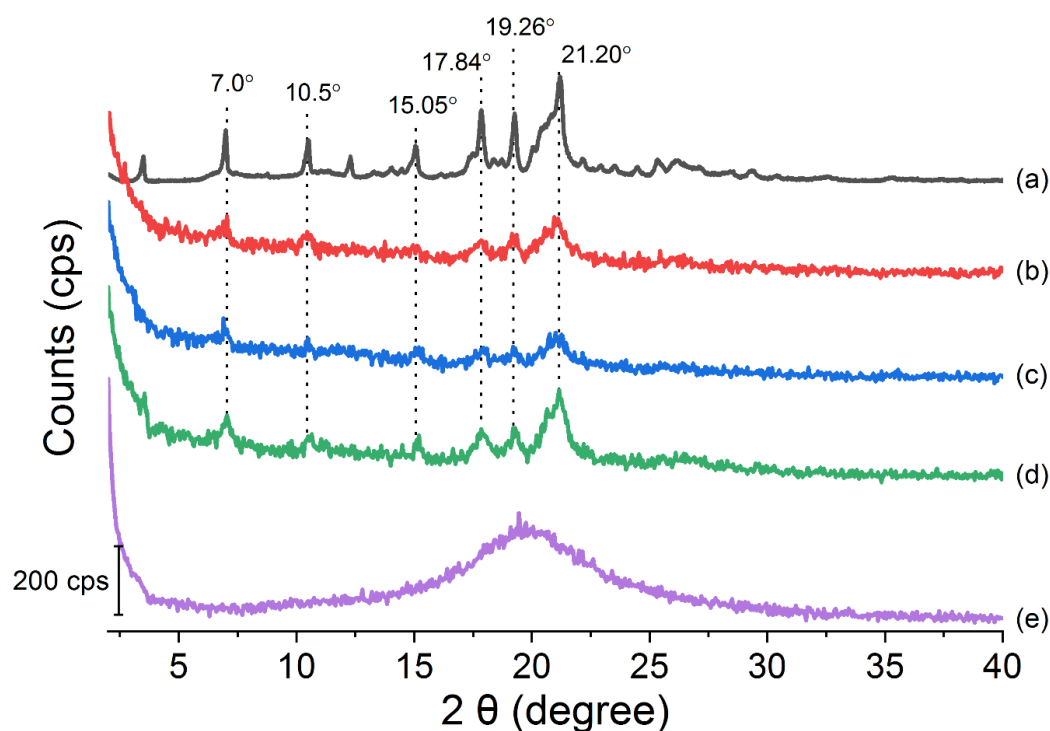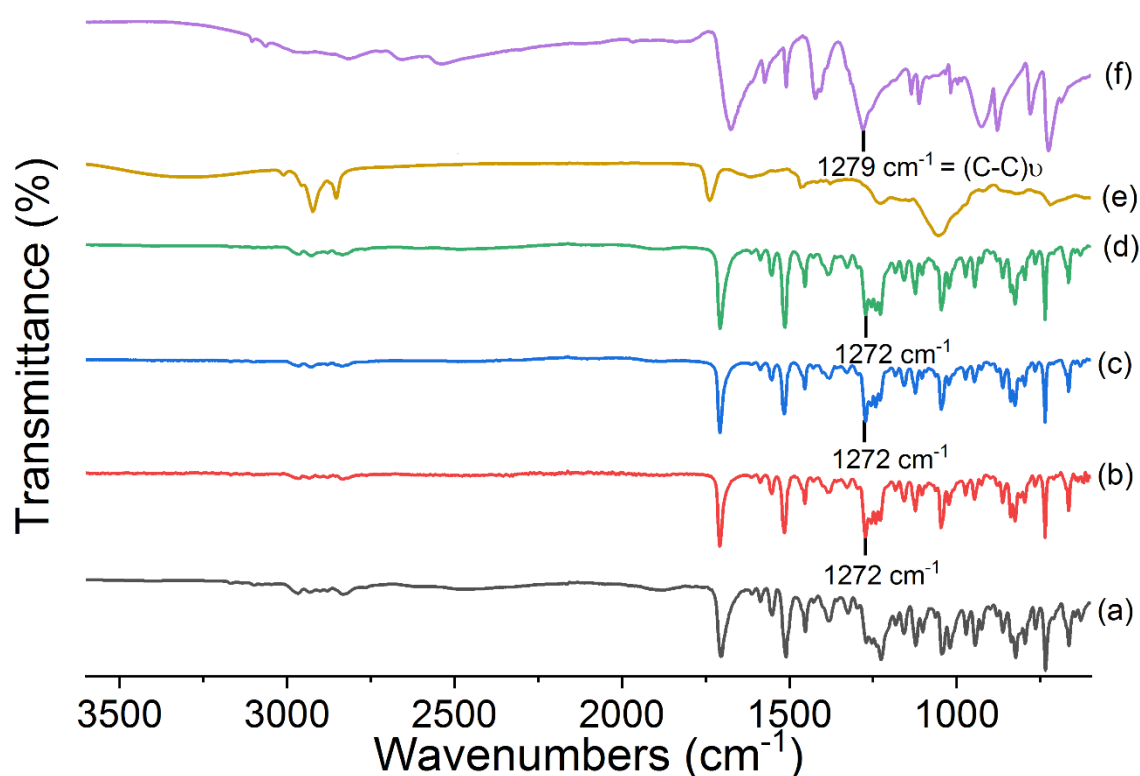

Fig. 5.6: FT-IR spectra of the (a) ITR-TER cocrystal, the ITR-TER particles containing (b) 0, (c) 2.5 and (d) 5% of lecithin, and the pure (e) lecithin and (f) TER.

5.3.1.3. Evaluation of ultrasound treatment on the size of NCC

This step of the method development aimed at reducing the average particle size of the dispersions. For this purpose, the samples were sonicated for 30 min using an ultrasound probe immediately after their preparation and their sizes were measured at times 0, 5, 10, 15 and 30 min.

DLS results (Fig. 5.7) showed the particles increased their sizes during the initial 5 min followed by a size reduction until the end of the experiment, however, ANOVA showed that this change in size was only significant in the ITR-TER dispersion prepared with 5% of lecithin. In fact, this size reduction was significant when the particle size decreased from 698±42 nm at time 5 min to 554±72 and 494±87 nm after 15 and 30 min, respectively. This size reduction effect caused by sonication, also known as "sonofragmentation", was possible because when the ultrasound was applied, acoustic cavitation occurred in the liquid (Sander et al., 2014). This phenomenon is the formation and growth of bubbles, which rapidly undergo an implosive disruption, locally releasing an intense heat of approximately 5000 K also an intense pressure of 10^5 kPa (Sander et al., 2014). In the sonofragmentation, the shockwaves caused by the acoustic cavitation promote high-velocity collisions among the ITR-TER particles resulting in their fracture and size reduction (Prozorov et al., 2004). On the other hand, this high energy applied by the sonication could also result in degradation of the ITR-TER particles, especially after prolonged periods. Hence, sonication was limited to 30 min of application under ice-bath.
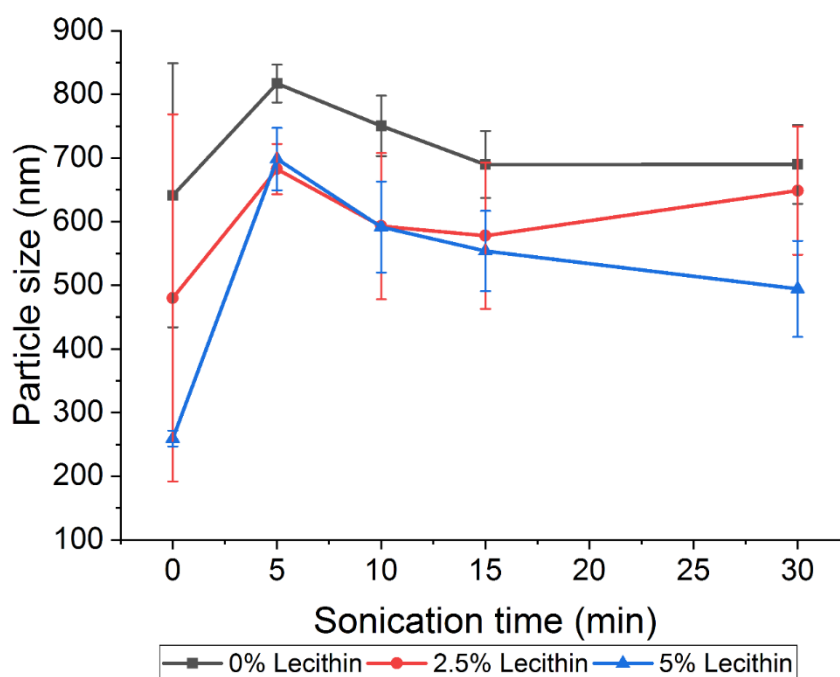
Fig 5.7: Particle size analysis of the ITR-TER dispersions containing 0, 2.5 and 5% of lecithin over 30 min of sonication.

The SEM images (Fig. 5.8) showed that the samples produced without sonication (Fig 5.8 a and b) were composed mainly by large rod-like structures with their longer dimensions of > 1 µm. In contrast, the sonicated samples (Fig 5.8 c and d) were mixtures of particles with different shapes and dimensions, with larger particles of approximately 1 µm in length and the other particles much smaller, of approximately 200 nm. This was likely to be caused by the sonication that randomly fragmented the larger particles into smaller entities, producing the observed heterogeneity. Furthermore, the particle shapes of the samples containing lecithin (Fig. 5.8 b and d) were very similar to those made with no

stabiliser (Fig. 5.8 a and c) therefore, lecithin appeared to have no effect on this characteristic, despite the sonication procedure was only significant for the dispersion containing 5% of lecithin.

In summary, the application of ultrasound for 15 or 30 min could reduce the particle size of the ITR-TER dispersions containing 5% of lecithin. Therefore, for all subsequent processing 30 min of sonication was used to prepare the dispersions.
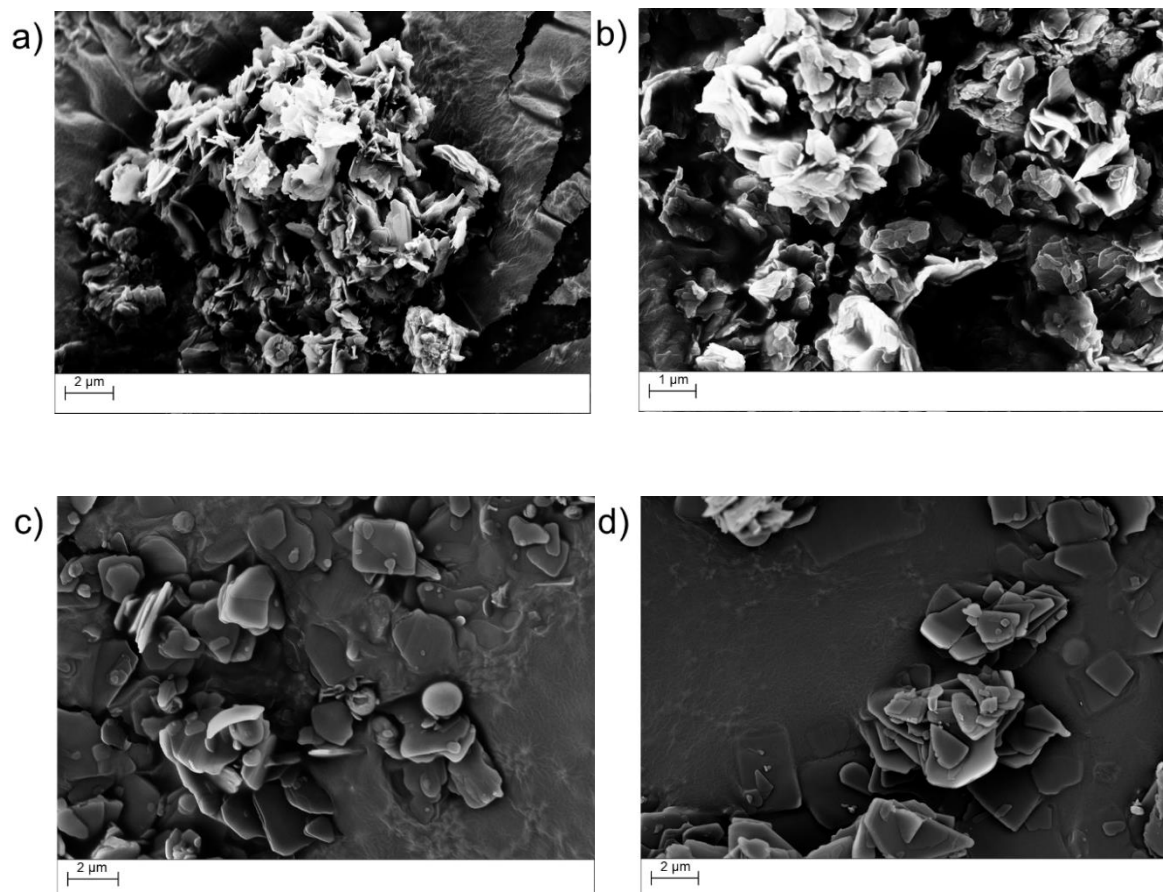
Fig 5.8: SEM images of ITR-TER particles prepared in different conditions: (a) 0 % lecithin without ultrasound, (b) 5% lecithin without ultrasound, (c) 0% lecithin with ultrasound, (d) 5% lecithin with ultrasound.

5.3.1.4.Optimisation of the nanoprecipitation method to prepare ITR-TER NCC

The conditions used in the precipitation method were optimised aiming to produce particles in a nanometric range and to increase the production yield. In all cases, 5% of lecithin was used and 30 minutes of sonication was employed. For the purpose of the process optimisation, the concentration of the API and coformer and the antisolvent:solvent (AS:S) ratio (v/v) were evaluated (Table 5.4). These factors were selected based on their critical effect on the size of particles produced by antisolvent precipitation, as described in Chapter 2. For simplicity, only the ITR concentration is stated below, although the other component, TER, was also included in the 2-1 molar ratio.

The model used to explain the results was evaluated using ANOVA. The regression was not considered statistically significant applying the 95% of confidence interval (p-value = 0.199) and the lack of fit was not considered to be significant (p-value = 0.584). Therefore, the model could not mathematically explain the effect of the parameters on the particle sizes probably because other factors that could influence the particle size, such as the sonication time, were not included in this investigation.

Nevertheless, all dispersions produced had average particle sizes < 1 μm (Table 5.6), where the #1 system had the smallest average, 565 ± 19 nm, and the #4 sample the largest, 894 ± 42 nm, statistically significantly different. The particle size of samples #2, #3 and #5 was comparable. However, considering that the final cocrystal concentration in the final dispersion, using sample #4 would be preferred due to the higher production yield. Therefore, the conditions used to make sample #4 were selected to be used in further preparations.

Table 5.6: Conditions used in the optimisation of the ITR-TER precipitation method, the resulting particle size and nominal cocrystal concentration in the dispersions

Sample	ITR concentration (mg/ml) [*]	AS:S ratio (v/v)	Particle Size (nm)	Nominal cocrystal concentration (mg/mL) [**]
#1	2	10:1	565 ± 19	0.224
#2	2	5:1	724 ± 36	0.447
#3	6	10:1	740 ±52	0.671
#4	6	5:1	894 ± 42	1.341
#5	4	7.5:1	791 ± 51	0.671

(*) in the solvent phase; (**) in the dispersions; AS: antisolvent phase; S: solvent phase

5.3.1.5. Scale-up of the nanoprecipitation method to prepare ITR-TER NCC

The final development stage of ITR-TER NCC preparation method was to scale up the production of the dispersions from 20 to 100 mL. This modification aimed to have a substantial dispersion volume and amount of particles for spray-drying and further tests using the dried powders (Section 5.3.6).

For this scale-up, it was necessary to modify the preparation setup, as the glassware used until this stage was not suitable for the proposed larger volume. The tubes used initially (Fig. 5.9a) were replaced by round-bottomed flasks (Fig. 5.9 b). The parameters used for the sonication step remained unchanged with the time of 30 minutes.
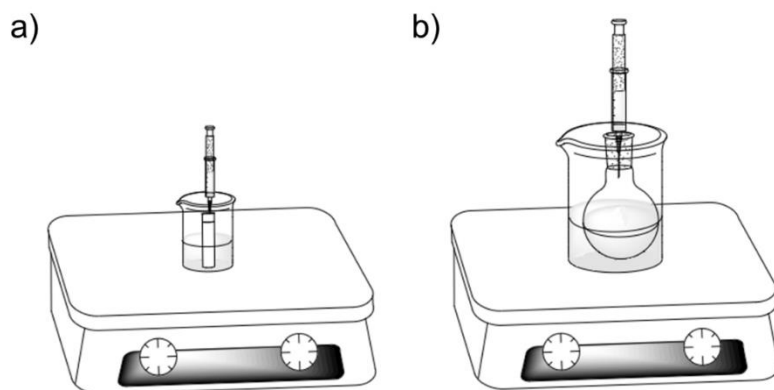
Fig. 5.9: Representation of the setups used to produce (a) 20 mL and (b) 100 mL of the ITR-TER NCC dispersions.

The characteristics of the dispersions produced on larger scale were evaluated by DLS (Table 5.7). This analysis showed that the dispersions containing 5% lecithin had a particle size of 909 ± 260 nm and PdI of 0.150 ± 0.078 therefore, these dispersions had particles within the desired nanoscale sizes, despite being moderately polydisperse. Furthermore, there was no significant difference in relation to the particle size of sample #4 (Table 5.6) and the scale-up batch. In contrast, dispersions with no stabiliser had larger particles with sizes of 1660 ± 889 nm and were highly polydisperse (PdI of 0.529 ± 0.343). Therefore, the setup modification was able to produce the ITR-TER particles within the nanometric scale however, lecithin was still necessary to achieve such particles.

Table 5:7: Particle size and PdI of the ITR-TER dispersions with 0 and 5% of lecithin produced using 100 mL scale

Sample	Size (nm)	PdI
0% Lecithin	1660 ± 889	0.529 ± 0.343
5% Lecithin	909 ± 260	0.150 ± 0.078

The solid-state analysis of the dried materials showed that the systems produced on a larger scale had diffraction patterns similar to that of the cocrystal previously described in Chapter 4 (Fig. 5.10), confirming the presence of the cocrystal in the samples.
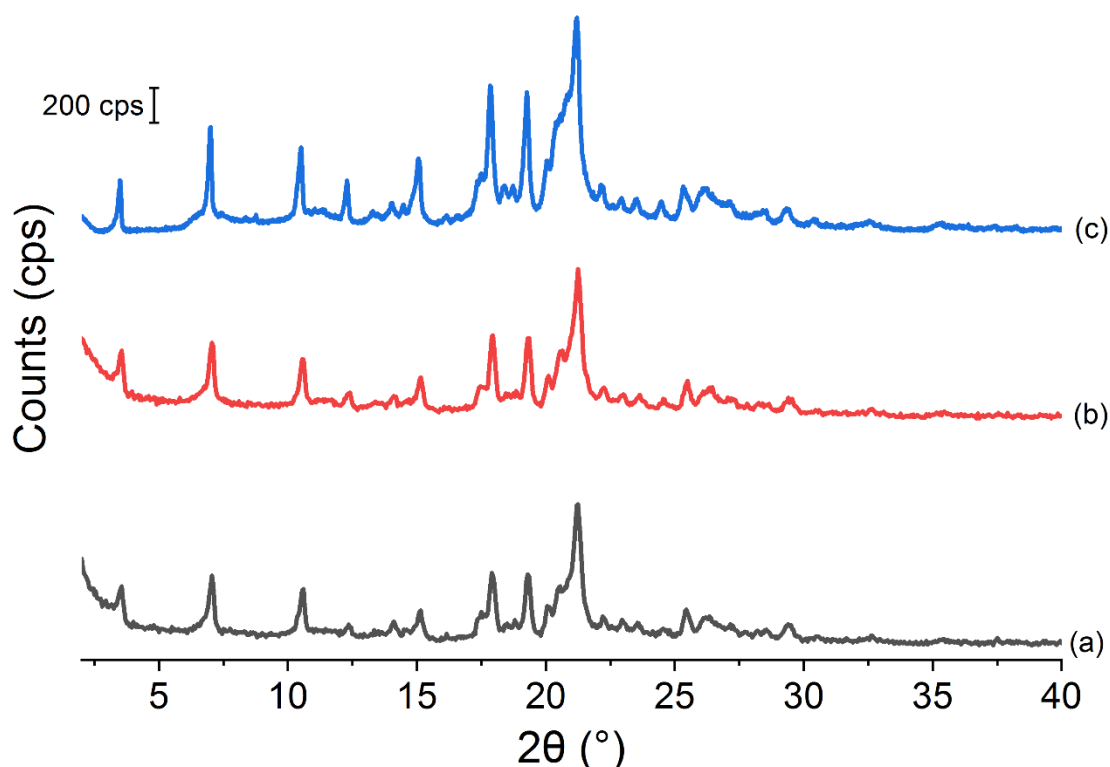
Fig. 5.10: PXRD diffractograms of the (a) dried ITR-TER dispersions containing 0 and (b) 5% of lecithin produced using 100 mL scale; and the (c) ITR-TER cocrystal.

The thermal analysis of the dried dispersions with 0 and 5% of lecithin showed a sharp endothermic peak having its onset at 204 °C in both samples (Fig. 5.11), which was correlated to the cocrystal melt. In addition, at a lower temperature, both samples had a smaller endothermic peak having its onset at 163 °C, which corresponded to the API melt. The normalised enthalpy of this peak in the sample with 0% of lecithin was -3.87 J/g (Table 5.8), while in those with 5% of lecithin this value was -3.22 J/g (Table 5.8), indicating a similar amount of residual ITR in those samples. Furthermore, no relevant difference between the samples in relation to those produced in smaller scale (Fig. 5.5).

In summary, the analysis of the ITR-TER dispersions using DLS and the characterisation of the solid-state properties by PXRD and DSC revealed that the characteristics of the material produced on larger scale were similar to those produced in a smaller scale, as both samples were composed mainly of ITR-TER NCC. Hence, the adjustments performed in the method to increase the batch size were successful.
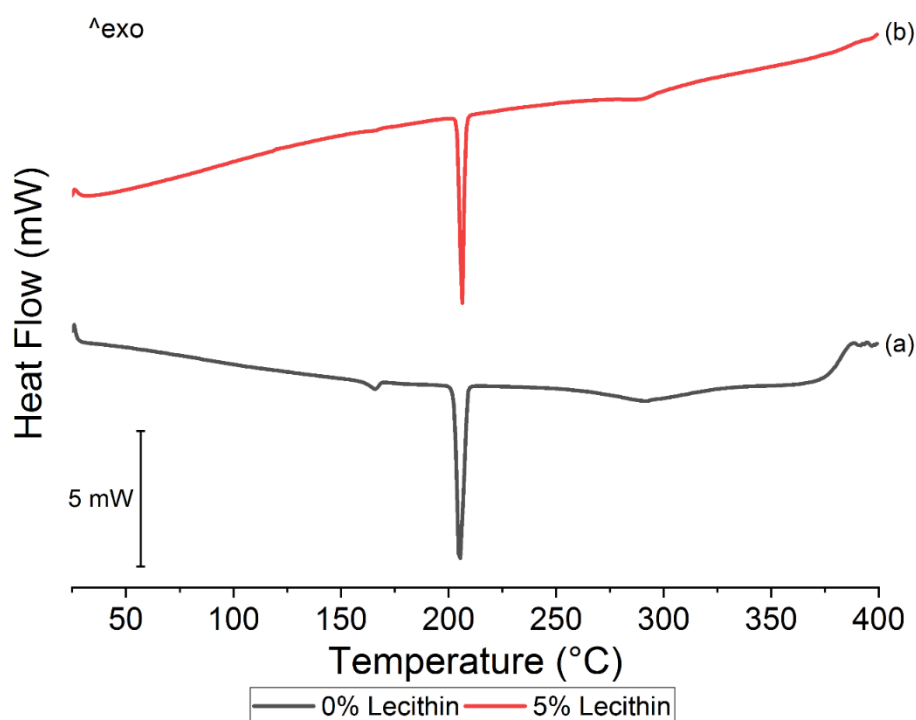
Fig. 5.11: Thermogram of the ITR-TER dispersions with (a) 0 and (b) 5% of lecithin produced using 100 mL scale.

Table 5.8: Summary of thermal events observed in DSC analysis of the ITR-TER 0 and 5% lecithin prepared using 100 mL scale.

Sample	Thermal event	Onset (°C)	Peak (°C)	Enthalpy (J/g)
ITR-TER 0% lecithin	Melt (API)	159.6	165.2	-2.2
	Melt (CC)	203.0	205.5	-76.0
ITR-TER 5% lecithin	Melt (API)	160.2	166.1	-0.81
	Melt (CC)	204.5	206.3	-75.47

5.3.2. Spray-dried ITR-TER Trojan particles for pulmonary administration

The method developed in the previous section enabled the preparation of stable ITR-TER dispersions with sizes lower than 1 μm. However, particles with this aerodynamic size are exhaled easily, therefore, the pulmonary administration of ITR-TER NCC would be inefficient. The ideal particle size range for this purpose is 1 – 5 μm, as particles in this range are likely to be deposited in the oropharynx or in the lower airways (Andrade et al., 2013). Therefore, in order to modify the characteristics of the NPs and make them more suitable for pulmonary administration, the ITR-TER NCCs were spray-dried with sugars, mannitol, raffinose and trehalose (Fig. 5.12) to encapsulate the NPs in microparticles and produce a system known as "Trojan particles" (Anton et al., 2012). As the sugars have high aqueous solubility (mannitol: 0.180 g/mL, raffinose: 0.14 g/mL, trehalose: 0.460 g/mL (Lammert et al., 1998; Rowe et al., 2012)), they will dissolve *in vivo* releasing the ITR-TER NCCs from the microparticles.
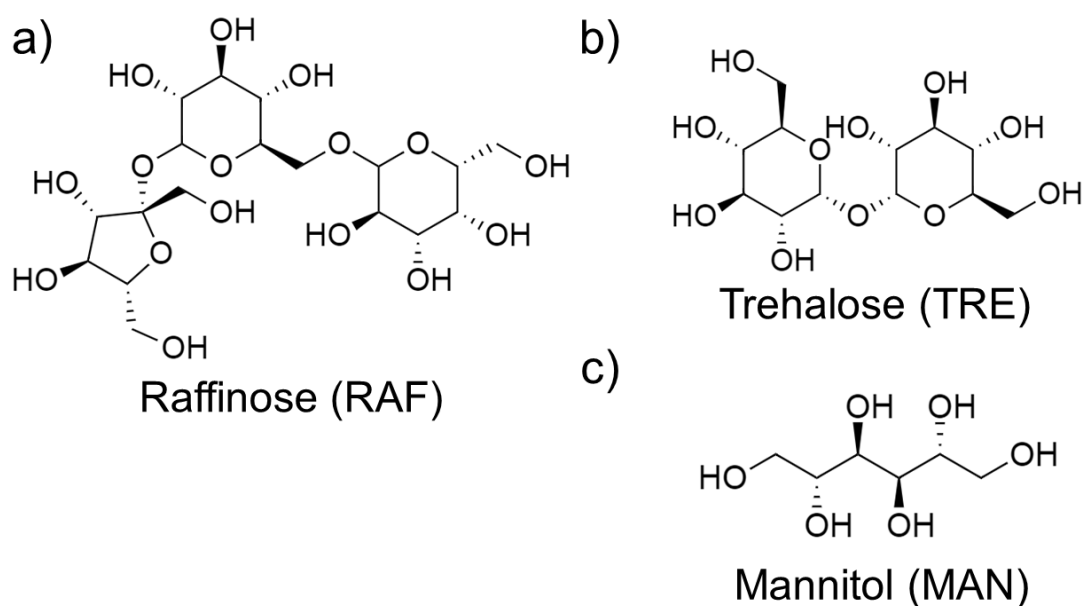
Fig. 5.12: Representation of the molecular structures of (a) raffinose, (b) trehalose, and (c) mannitol.

The calculation of the spray-drying yield showed that the sample prepared with trehalose (ITR-TER-TRE) had the lowest yield, of 43.81% (w/w), while the one prepared with mannitol (ITR-TER-MAN) had the highest production yield, of 54.8% (w/w) (Table 5.9). For the drug loading, i.e. the amount of the API in the spray-dried particles, the highest drug content was measured for ITR-TER-RAF, 12.04±0.39% (w/w), while the ITR-TER-MAN system had the lowest drug loading, 8.6±0.41% (w/w) (Table 5.9). As the powders were produced with the same ITR nominal concentration, 12.5% (w/w) (Table 5.2) and produced using the same drying conditions, this discrepancy might be caused due to a process loss. Accordingly, the lower ITR concentration in ITR-TER-MAN could be a result of the formation of smaller particles, as discussed in details later in Section 5.3.2.2, with particle separation leading to the finer particles being carried away from the cyclone and collection vessel by the gas to the exhaust. For the encapsulation efficiency (amount of drug in the powder in relation to the initial amount), the lowest value was recoded for ITR-TER-MAN, 68.80±3.39 % (w/w) and the highest for ITR-TER-RAF, 96.40±2.83.

Table 5.9: Spray-drying yield, drug loading and encapsulation efficiency of the spray-dried powders

Sample	Yield (%, w/w)	Drug Loading (%, w/w)	Encapsulation efficiency (%, w/w)
ITR-TER-MAN	54.8±4.5	8.6±0. 41	68.80±3.39
ITR-TER-RAF	47.3±7.3	12.04±0.39	96.40±2.83
ITR-TER-TRE	43.8±6.4	10.86±0.51	86.80±3.96

In general, spray drying is the method of choice to produce dried material from suspensions, however, the optimization of the drying conditions is often required to

maximize the yield. Ideally, a multifactorial design of experiments (DoE) is carried out for an extensive evaluation of the impacts of drying conditions, such as drying gas flow rate and inlet temperature and solution/suspension feed rate to name a few, could have on the characteristics of the dried powder (Dobry et al, 2009).

5.3.2.1. Solid-state characterisation of spray-dried powders

The solid-state characterisation of the spray-dried powders and sugars on their own (starting material powders) were carried out using PXRD and DSC. In the diffractograms of ITR-TER-MAN (Fig. 5.13), Bragg peaks characteristic of the crystalline mannitol and of the ITR-TER cocrystal were observed, indicating that the crystalline characteristics of both materials were conserved after spray-drying. On the other hand, the diffractograms of ITR-TER-RAF and ITR-TER-TRE had peaks of the ITR-TER cocrystal, at 7.05, 17.95 and 21.35° 2θ and no Bragg peaks corresponding to the crystalline forms of the sugars (Fig. 5.13). This is due to amorphisation of raffinose and trehalose caused by spray drying process (Ógáin et al., 2011).
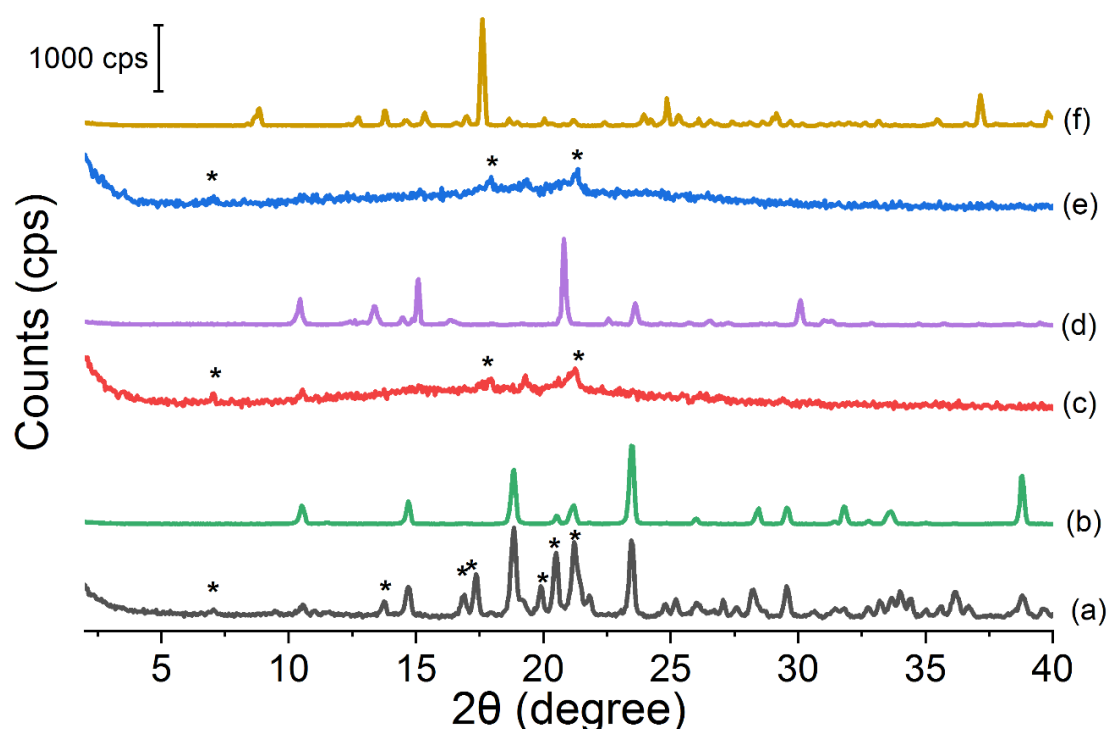
Fig. 5.13: PXRD diffractograms of the (a) ITR-TER-MAN, (b) mannitol, (c) ITR-TER-RAF, raffinose, (e) ITR-TER-TRE and (f) trehalose powders. The * indicates Bragg peaks of the ITR-TER cocrystal.

DSC analysis of the spray-dried samples (Fig. 5.14) showed that all had a common endothermic event with an onset at approximately 200 °C, corresponding to melting of the cocrystal. The normalised enthalpies were 9.51 J/g for ITR-TER-TRE, 6.07 J/g for ITR-TER-MAN and 8.16 J/g for ITR-TER-RAF (Table 5.10). In the ITR-TER-MAN sample, a sharp endothermic peak was also observed with an onset at 157 °C, corresponding to melting of mannitol. The normalised enthalpy of this peak was 256.22 J/g consistent with the majority

of this sample being mannitol (Table 5.10). The thermogram of ITR-TER-RAF showed a broad endothermic peak from 25 to approximately 100 °C that could be due the surface dehydration of the powder. This sample also had a broad endothermic peak at 223 °C related to melting of raffinose. A dehydration peak was also observed at 25-100 °C in ITR-TER-TRE and a broad endothermic peak at approximately 210 °C indicated melting of the anhydrous form of trehalose (Ógáin et al., 2011).
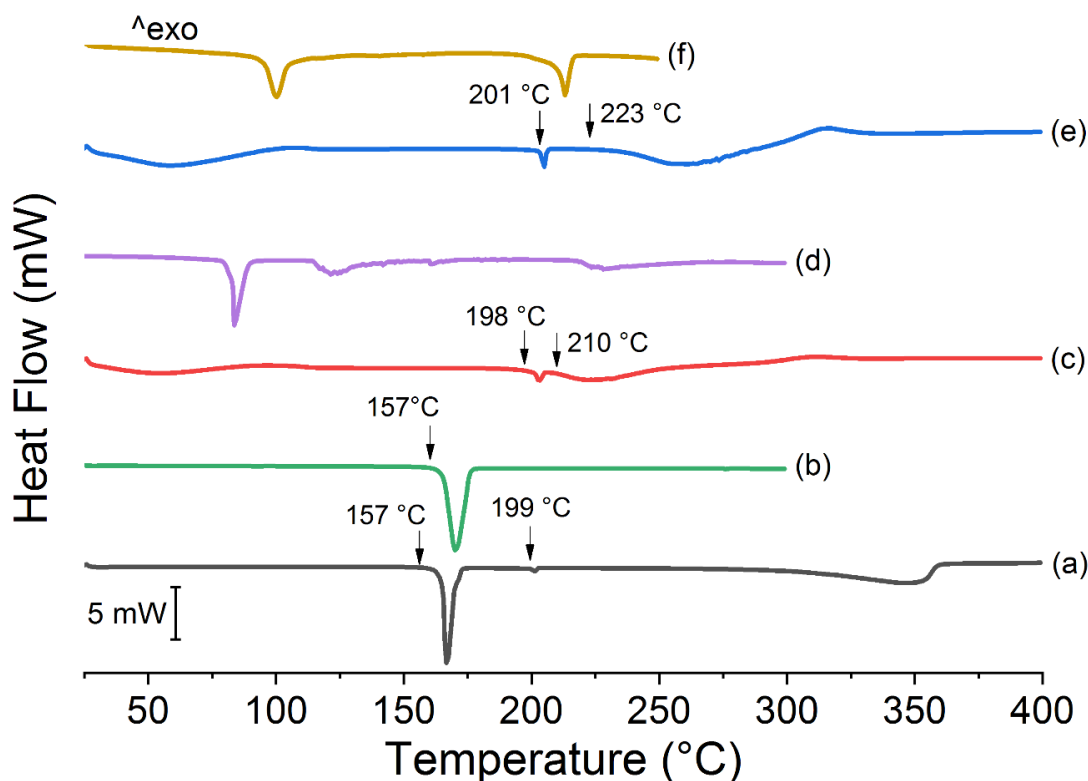
Fig. 5.14: DSC thermograms of the (a) ITR-TER-MAN, (b) mannitol, (c) ITR-TER-RAF, raffinose, (e) ITR-TER-TRE and (f) trehalose powders.

Table 5.10: Summary of thermal events observed in DSC analysis of the spray-dried powders and the sugars, mannitol, raffinose and trehalose.

Sample	Thermal event	Onset (°C)	Peak (°C)	Enthalpy (J/g)
ITR-TER-MAN	Melt (API)	165.1	167.0	-256.22
	Melt (CC)	199.6	201.3	-6.1
	Endothermic	292.6	347.3	-608.37
Mannitol	Melt	157		-60.96
ITR-TER-RAF	Melt	201.1	202.7	-8.16
Raffinose	Dehydration	76.3	83.3	-40.54
	Melt	112.1	122.4	-33.33
ITR-TER-TRE	Melt	203.2	204.8	-9.51
Trehalose	Dehydration	88.9	100.9	-58.33
	Melt	190.3	213.5	-52.99

5.3.2.2.Particle size and morphological analysis of Trojan particles

SEM was used for the analysis of the morphological characteristics of the spray-dried powders (Fig. 5.15). In general, these samples were made of round particles, which could improve the pulmonary deposition (Crowder et al., 2002). In addition, the samples were mixtures of fine particles, smaller than 1 µm and others much larger but smaller than 5 µm. This size range is also suitable for the pulmonary administration, as powders with this size range are more likely to be deposited in the lower airways with the particles with sizes below 1 µm likely to be exhaled (Carvalho et al., 2011).
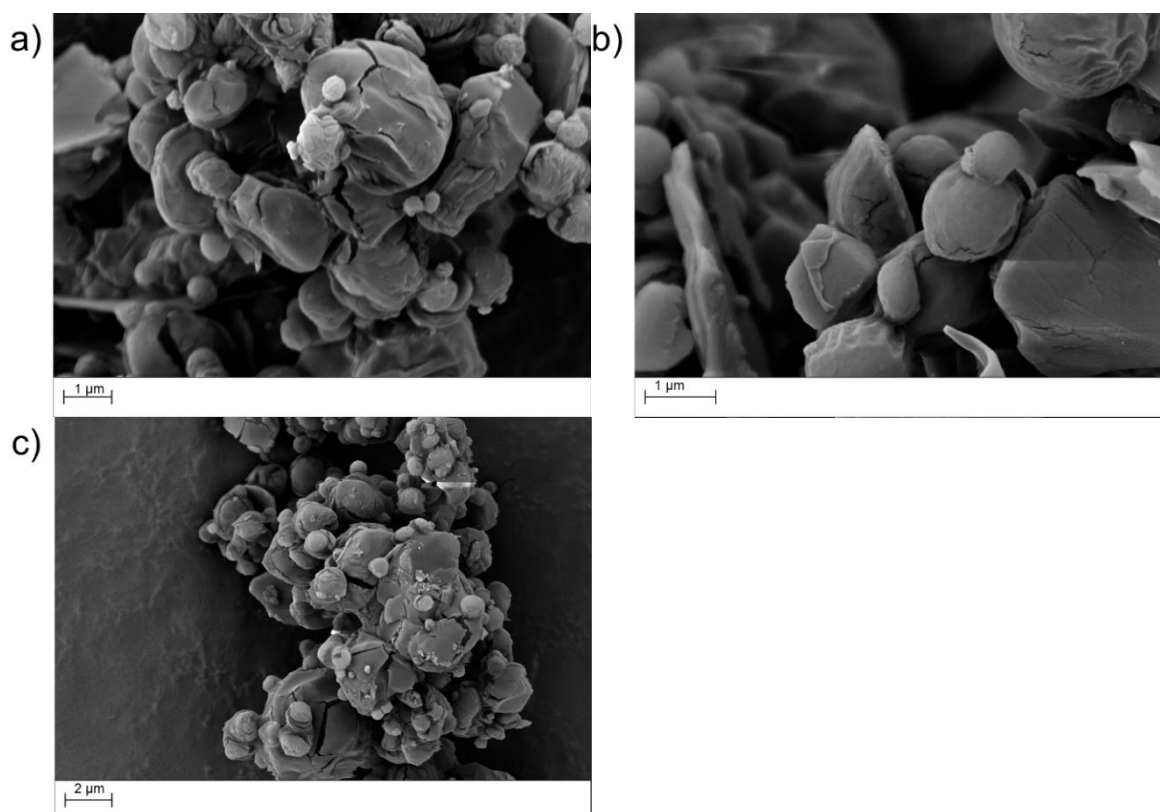
Fig. 5.15: SEM images of (a) ITR-TER-MAN, (b) ITR-TER-RAF and (c) ITR-TER-TRE.

The particle size analysis by laser light diffraction of the spray-dried powders are shown in Table 5.11 and expressed as the D10, D50 and D90 values that represent the points in the size distribution that include 10, 50 and 90% of the measured particles, respectively. The ANOVA test revealed that the particle size of the ITR-TER-MAN powder was significantly smaller than the other samples, considering D10, D50 and D90. The particle size of ITR-TER-RAF and ITR-TER-TRE were comparable in relation to their D10 and D50 values; however, their D90 values was statistically significantly different. The explanation of this size difference could be because the spray-drying process of mannitol in solution resulted in crystalline particles (Fig. 5.13a), while the ITR-TER-RAF and ITR-TER-TRE were amorphous (Fig. 5.13c and e). Indeed, the crystalline form is more ordered, consequently, having particles with a higher density, on the other hand, disordered

materials normally have lower density (Babu and Nangia, 2011). Therefore, considering that droplets are formed having similar sizes, regardless the sugar type, the drying process of the ITR-TER-MAN droplets resulted in smaller particles, i.e. higher density, while for the ITR-TER-RAF and ITR-TER-TRE larger particles were produced, i.e. lower density.

Table 5.11: D10, D50 and D90 values of the particle size distribution of the spray-dried powders

Sample	D10 (µm)	D50 (µm)	D90 (µm)
ITR-TER-MAN	1.38±0.014	4.85±0.064	16.0±0.065
ITR-TER-RAF	1.48±0.031	5.75±0.291	28.1±0.601
ITR-TER-TRE	1.46±0.060	5.60±0.040	17.8±0.145

Furthermore, the analysis of the size distribution revealed that ITR-TER-MAN had mostly a monomodal size distribution with a small peak at 86 µm indicating that this powder had one main population, although some larger particles are also present (Fig. 5.16). In contrast, the size distributions of ITR-TER-RAF and ITR-TER-TRE were bimodal with the former showing a small peak at 111 µm. This could be related to moisture affecting the particles as TRE and RAF were amorphous and prone to moisture sorption (Fakes et al., 2000; Zhao et al., 2018).
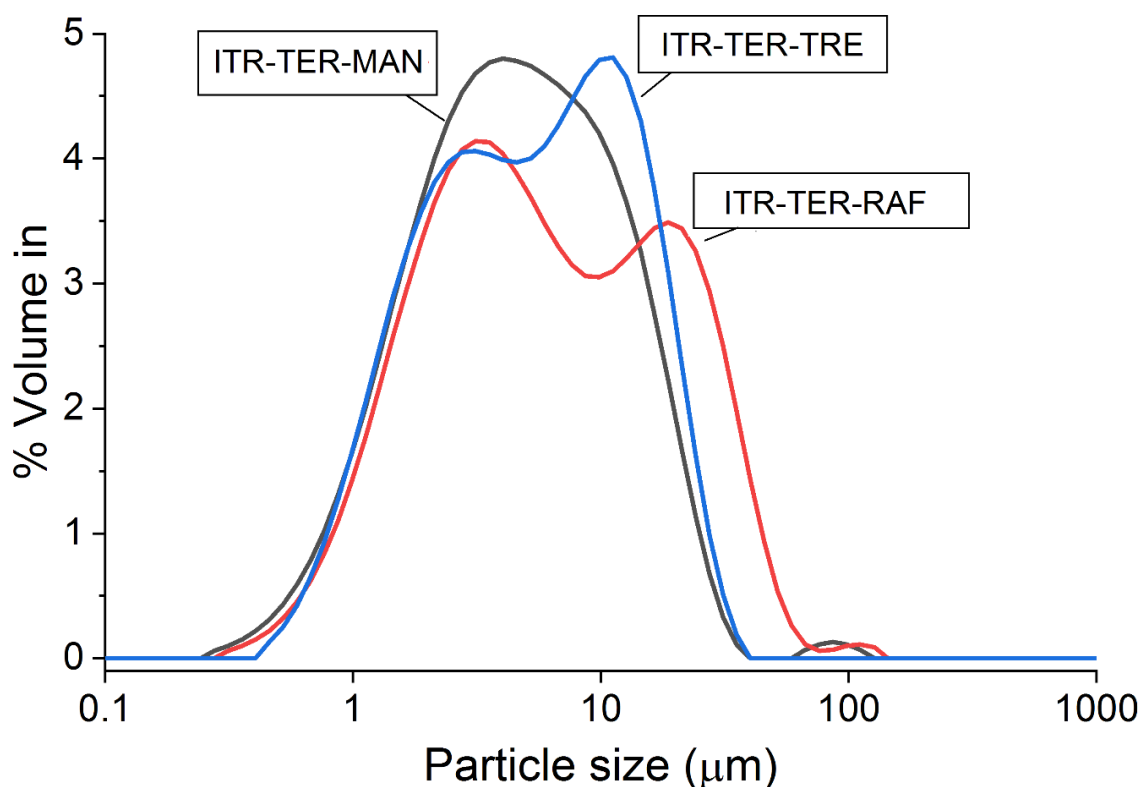

Fig. 5.16: Particle size distribution of the ITR-TER-MAN, ITR-TER-RAF and ITR-TER-TRE samples.

5.3.2.3.Particle size analysis of the redispersed powders

The redispersibility of the dried powders was investigated using DLS (Table 5.12) and NTA (Table 5.13) in order to evaluate whether the process could impact on the particle size of NCCs. For this purpose, the samples were redispersed at a 0.5 mg/mL in water and a vortex was used to improve homogeneity of the dispersed particles. The particle size analysis using DLS (Table 5.12) showed that the ITR-TER dispersions had a particle size of 1023 ± 272 nm before spray drying. For the redispersed powders, ITR-TER-MAN had the smallest size, 952 ± 169 nm, while the ITR-TER-TRE had the largest, 1022 ± 97 nm. Nevertheless, statistical analysis showed that none of the samples had a significant size change in relation to their original size. Therefore, the sugars seemed to be efficient in protecting the particle aggregations during the spray-drying process.

Table 5.12: Particle size measured of the ITR-TER dispersion before spray-drying and after redispersion by DLS.

Sample	Original size (nm)	Redispersed size (nm)	*p-value*
ITR-TER-MAN	1023 ± 272	952 ± 169	0.593
ITR-TER-RAF	1023 ± 272	968 ± 379	0.819
ITR-TER-TRE	1023 ± 272	1022 ± 97	0.856

The analysis of redispersibility using NTA (Table 5.12) showed that the samples were composed of much smaller particles. The ITR-TER dispersions had average particle sizes of 191 ± 59 nm and the redispersed powders had particle sizes from 135 ± 48 to 224 ± 22 nm, with ITR-TER-RAF showing the smallest particles and ITR-TER-MAN the largest. Only the ITR-TER-TRE sample was significantly different when compared with the original size. NTA also showed that no aggregation took place during the drying process, in agreement with the results from the DLS analysis (Table 5.11).

Table 5.12: Particle size of the ITR-TER dispersion before spray-drying and after redispersion measured by NTA.

Sample	Original size (nm)	Redispersed size (nm)	*p-value*
ITR-TER-MAN	191 ± 59	224 ± 22	0.821
ITR-TER-RAF	191 ± 59	135 ± 48	0.082
ITR-TER-TRE	191 ± 59	142 ± 27	0.031*

(*) considered statistically different with 95 % of confidence interval.

Comparing the results of both methods, around a 5-fold difference in the average particle size was measured. This could be NTA calculates the size by the displacement of the particles in dispersion, while DLS uses intensity of the scattered light to calculate particle sizes (Bhattacharjee, 2016). Consequently, in the presence of multiple size populations,

smaller particles might not be detected by DLS due to the high-intensity scattering of the large particles (Bhattacharjee, 2016; Boyd et al., 2011). Furthermore, as showed in the SEM images of the ITR-TER (Fig. 5.8), the NCCs were fragmented by the sonication producing smaller particles of approximately 200 nm and others, remained much larger, with size of approximately 1 µm. Indeed, the size distribution results by NTA detected multiple populations in the redispersed powders (Fig. 5.17); however, as demonstrated by D90, most of the particles had sizes below 300 nm. The other populations detected with sizes from 375 to 525 nm, from 675 to 780 and from 915 to 1015 nm (Fig. 5.17), are less than 10% of the total particles, and were the probable cause for discrepancy with the results observed by DLS (Table 5.9).
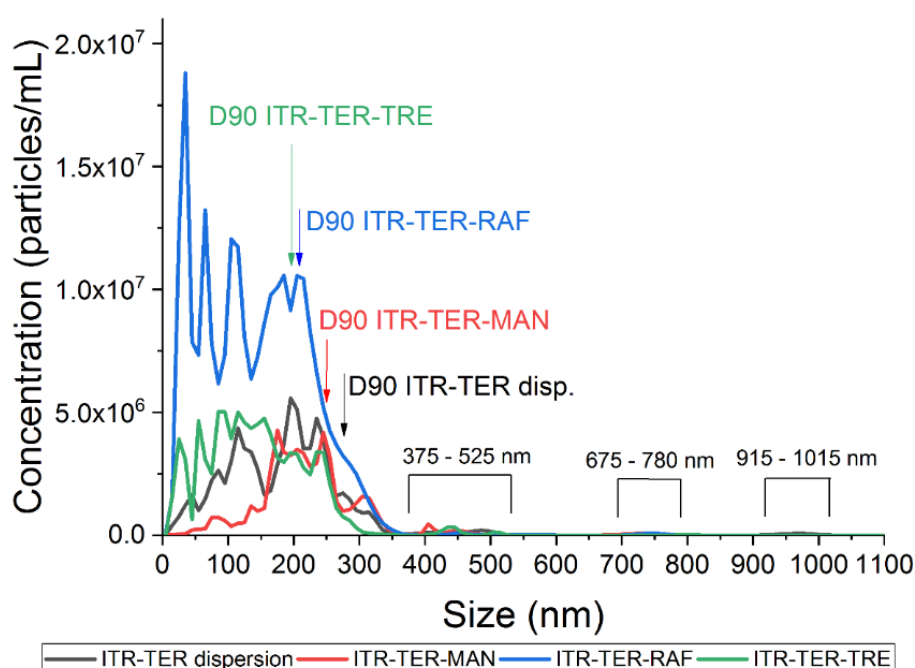
Fig. 5.17: Particle size distributions of the ITR-TER dispersion and the redispersed ITR-TER-MAN, ITR-TER-RAF and ITR-TER-TRE powders.

5.3.2.4. Analysis of the aerodynamic properties of Trojan particles

The *in vitro* evaluation of the pulmonary deposition of the spray-dried powders was carried out using the NGI (Fig. 5.18). This is method was especially developed for this purpose in order optimize the accuracy of this prediction, considering the factors as the inhalation pressure and the diameter of the airway pathway (Marple et al, 2003). Nevertheless, dead spaces are present in the NGI design, reducing the clinical realism of the powder behaviour when inhaled (Mohammed et al, 2012).

ITR-TER-MAN had the highest total emitted dose (TED), of 72.73±2.61% (w/w) (Fig. 5.18a), indicating that this powder had a better potential to be released from the capsule when inhaled. In contrast, ITR-TER-RAF and ITR-TER-TRE had larger powder fractions that remained in the capsules, of 25.11±13.47 and 32.65±14.50%, respectively (Fig. 5.18b

and c), with TEDs of 60.67±5.38 and 55.33±5.9%, respectively. This was probably because raffinose and trehalose are hygroscopic materials able to sorb moisture forming clusters that could affect the aerodynamic properties of the powders (Fakes et al., 2000; Zhao et al., 2018).

Other relevant parameters to these investigations are the mass median aerodynamic diameter (MMAD) and geometric standard deviation (GSD) (Simon et al., 2016). The former is the diameter at which half of the particles of the recovered powder, in mass, are larger or smaller, while the latter indicates uniformity of these particles, in which lower values indicate a higher homogeneity. Ideally, powders for a pulmonary application have values of MMAD lower than 5 µm to prevent loses to inertial impaction when inhaled (Carvalho et al., 2011). The MMAD of ITR-TER-MAN was 4.02 ± 0.13 µm and its GSD was 1.74±0.03 (Fig. 5.18a), which were the lowest values comparing all the Trojan particles, as ITR-TER-RAF and ITR-TER-TRE had MMAD of 5.28±0.54 and 5.89±2.56 µm and those of GSD 2.28±0.39 and 2.68±1.05, respectively (Fig. 5.18b and c). Therefore, the comparison of the MMAD values suggested that ITR-TER-MAN is subjected less to inertial impaction when inhaled and the GSD results indicated that this sample had a more homogenous size distribution than ITR-TER-RAF and ITR-TER-TRE. These results are in agreement with the particle size characterisation carried out using laser diffraction (Table 5.15), in which the D50 of the ITR-TER-MAN was also the lowest (4.85±0.064 µm) and the ITR-TER-RAF and ITR-TER-TRE had values greater than 5 µm, of 5.75±0.291 and 5.60±0.040 µm, respectively.

Another information obtained from the NGI analysis is the fine particle fraction (FPF) that is the fraction of the inhaled powder with sizes lower than 5 µm, therefore, this is the percentage of the powder in the capsule able to reach the lower airways (Sosnowski, 2015). Among the samples, ITR-TER-MAN had an FPF of 36.11±0.17% (Fig. 5.18a), while ITR-TER-RAF had 19.50±3.81% (Fig. 5.18b) and ITR-TER-TRE had 14.57±13.2% (Fig. 5.18c). The statistical analysis of the FPF results using ANOVA revealed that only ITR-TER-MAN and ITR-TER-TRE had significantly different results, therefore, when inhaled, a larger fraction of the former sample is expected to reach deeper regions of the lungs.

In general, the NGI analysis showed that ITR-TER-MAN had better aerodynamic properties, in terms of TED, MMAD, GSD and FPF values than ITR-TER-RAF and ITR-TER-TRE, which were comparable. Therefore, ITR-TER-MAN is expected to have a better performance as a pulmonary formulation.

MMAD (µm)	GSD	TED (%)	FPF (%)
4.02 ± 0.13	1.74 ± 0.03	72.73 ± 2.61	36.11 ± 0.17

MMAD (µm)	GSD	TED (%)	FPF (%)
5.28 ± 0.54	2.28 ± 0.39	60.67 ± 5.38	19.50 ± 3.81

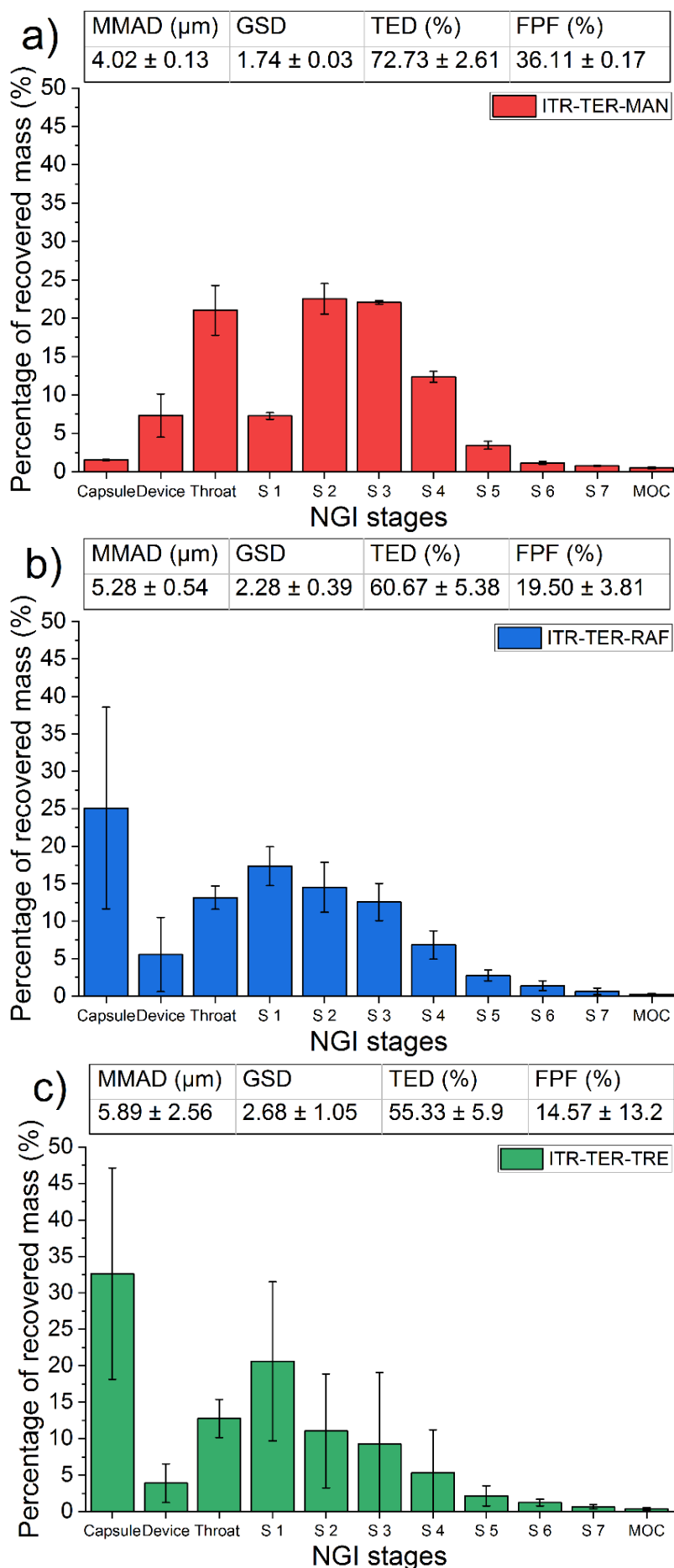| MMAD (µm)	GSD	TED (%)	FPF (%)
5.89 ± 2.56	2.68 ± 1.05	55.33 ± 5.9	14.57 ± 13.2

Fig. 5.18: *In vitro* deposition analysis of (a) ITR-TER-MAN, (b) ITR-TER-RAF and (c) ITR-TER-TRE powders using NGI.

5.4.Conclusions

In this chapter, a method based on antisolvent precipitation was developed to prepare ITR-TER cocrystals in a nanometric size range and in a batch size suitable for preparation of Trojan particles. The method development consisted of the evaluation of multiple parameters that may have impacted on the characteristics of the ITR-TER NCC. Firstly, a mixture of acetone and methanol in a volume ratio of 70:30 (v/v) enabled ITR and TER solubilisation at the highest concentration respecting the 2-1 stoichiometry of the ITR-TER cocrystal. Secondly, the evaluation of lecithin as a stabiliser of the ITR-TER dispersions showed that its use at 5% (w/w) in relation to the total solid content results in particles with smaller sizes and lower zeta potential values in comparison to the batch made without lecithin. Lecithin at this concentration also enabled the preparation of monodispersed particles, while polydisperse particles were produced with no stabiliser. Furthermore, the presence of the stabiliser did not affect the solid-state characteristics of the ITR-TER with the cocrystal produced at all lecithin concentrations used. The evaluation of ultrasound application on the ITR-TER dispersions detected a significant size reduction of the particles when sonication was applied continuously for at least 15 min. SEM images of the sonicated dispersions showed small heterogeneous particles of approximately 200 nm in size that could be fragments of larger structures, in contrast to the non-sonicated dispersions which had only particles of approximately 1 μm in size. Therefore, the ultrasound application efficiently reduced the size of the particles to nanometric dimensions. The conditions of the antisolvent precipitation method were then optimised to increase the final ITR concentration and preserving the nanometric size of the cocrystal particles. Finally, the modifications of the method setup to scale-up the batch size from 20 mL to 100 mL had no effects on the characteristics of the ITR-TER dispersions in comparison to those produced on smaller scale; therefore, the new setup was successful to increase the batch size scale by a 5-fold.

Trojan particles were produced by spray-drying of ITR-TER NCC with mannitol, raffinose and trehalose and the physicochemical and aerodynamic properties of the dry powders were evaluated. In general, the spray-dried powders had round particles, in contrast to elongated particles of ITR-TER NCCs. Particle round in shape are more favourable for the pulmonary administration. Furthermore, the powders instantaneously redispersed in water releasing the NCC, which had, in general, sizes smaller than 250 nm as measured by NTA and the Trojan particles are expected to readily release ITR-TER NCC in the lungs. The median particle size of ITR-TER-MAN was smaller in comparison to the others, 4.85±0.06 μm, which was in agreement with the results obtained from the NGI, as its MMAD was 4.02±0.13 μm and its GSD was 1.74±0.03. This enabled ITR-TER-MAN to have the largest respirable fraction, of 36.11 ± 0.17%. This indicated that a larger fraction of ITR-TER-MAN could be deposited in deeper regions of the lungs in comparison to the

other powders. In general, the physicochemical characterisation and the *in vitro* evaluation of the pulmonary deposition of the dry powders indicated that ITR-TER-MAN is expected to be more suitable for pulmonary administration than the other Trojan particles presented in this work.

Chapter VI: General Discussion and Conclusions

In this thesis, the physicochemical properties of ITR were modified using different approaches including the development of nanonised ITR, PEGylated ITR nanoparticles (NPs), cocrystallisation and the preparation of the cocrystal in a nanoparticle format, i.e. a nano-cocrystal (NCC). Each one of these approaches had a different purpose, which was studied and presented in the chapters. Briefly, in Chapter 2, a nanoprecipitation method was modified and the effects of the process parameter on the characteristics of ITR NPs were evaluated. In Chapter 3, the method developed in Chapter 2 was used to prepare non-PEGylated and PEGylated ITR NPs and the physicochemical and mucoadhesive properties of these NPs were evaluated. Chapter 4 focused on the identification of multi-component forms of ITR, identifying one new cocrystal. The structure, solid state properties and dissolution of this cocrystal were investigated. Finally, in Chapter 5, the identified cocrystal was used to prepare NCCs using antisolvent precipitation. The produced nanoparticles were then embedded in sugar microparticles to develop of a dry powder for pulmonary administration.

6.1. Optimisation of the antisolvent precipitation method to produce ITR NPs

The development of ITR NPs in Chapter 2 was a continuation of a previous work of Mugheirbi and co-workers aimed at preparing NPs by antisolvent precipitation (Mugheirbi et al., 2014). In this case, the critical step of the method, the solvent phase injection into the antisolvent solvent, was modified to minimise the probability of heterogeneous nucleation and, consequently, preventing the formation of large, micron-sized particles. Furthermore, an additional step was incorporated to remove the residual solvent (acetone) from the dispersions, which resulted in a significant stability improvement. The final objective in this chapter was to optimise the nanoprecipitation method in order to produce a monodispersed dispersion with small particle sizes.

In general, the conditions used in the method were modified to increase the degree of ITR supersaturation, as this parameter is critical to increasing the nucleation rate, consequently, smaller particles are produced (Mullin, 2001). Several parameters could be modified to increase the degree of supersaturation including the solvent selection, the mixing, the antisolvent temperature, the volume ratio of antisolvent to solvent (AS:S) and others (Sinha et al., 2013). In Chapter 2, the analysis focused on the antisolvent temperature and the AS:S ratio to evaluate the impact of these parameters on the NP characteristics. In the initial analysis, only the AS:S ratio was found critical for the produced particle size, as alterations in this parameter affected the volume of solvent and the total of ITR injected, which had a direct consequence on the supersaturation. On the other hand, antisolvent temperatures used (40 to 60 °C) had no significant influence on the particle size. Nevertheless, when the antisolvent was used at a higher temperature (60-80 °C), i.e. higher than the acetone boiling point (56 °C), smaller particles were produced, due to its

contribution to remove the solvent more quickly, hence, increasing the supersaturation degree.

The inclusion of an additional residual solvent (acetone) evaporation step had no impact on the particle size of the ITR dispersions; however, prolonged evaporation at reduced pressure affected the solid-state properties of the particles, increasing their degree of crystallinity. Nevertheless, the ITR dispersions evaporated for 40 min at 50 mbar showed a remarkable stability enhancement when stored at 4 and 25 °C in comparison to the non-evaporated ITR dispersions. This was possible because removing the residual solvent prevented the Oswald ripening phenomenon (Thorat and Dalvi, 2012).

The optimised conditions of the antisolvent precipitation method, i.e. using the antisolvent phase at 80 °C and the AS:S ratio of 10:1, yielded a monodispersed ITR dispersion with the particle size of 253 ± 16 nm, which had solid-state characteristics of a liquid crystal smectic mesophase.

6.2. Non-PEGylated and PEGylated ITR NPs

In this thesis, a range of ITR NPs were produced using antisolvent precipitation method. The system referred to as "ITR NP" in Chapter 2 is the same to the "non-PEGylated ITR NP" in Chapter 3. These "simpler" NPs had no stabiliser and were composed of the pure drug dispersed in water. The other nanoparticulate system described in Chapter 3, the PEGylated ITR NPs, are different than the non-PEGylated ITR NP due to PEGs adsorbed on their surface. In this study, the influence of the molecular structure of the polymer was analysed using three types of PEG polymers with the same molecular weight (10 kDa), in which one was a linear chain polymer (PEG), other was linear and methylated (MPEG) and the third was a branched (4 ARM PEG) polymer.

The comparison between the non-PEGylated and the PEGylated ITR NP revealed the impact the polymers had on the NPs. One of these differences was the stabilisation mechanism, as the non-PEGylated ITR NP had a zeta potential of -30.1 ± 1.5 mV, therefore, were stabilised by electrostatic repulsive forces, while the PEGylated ITR NPs had their surface potential partially neutralised by the polymers and the zeta potential values varied from -10.4 ± 2.4 to -21.1 ± 2.4 mV. Consequently, in the PEGylated ITR NPs, the electrostatic repulsive forces were reduced and the steric hindrance was not as effective to prevent aggregation, resulting in a decrease in colloidal stability when stored for 21 days. The PEGylated NPs had larger particle sizes while the non-PEGylated NPs remained mostly unchanged during the same period.

Further analysis also revealed differences in the solid-state properties of these NPs. The non-PEGylated ITR NPs had a disordered state, known as a smectic liquid crystal mesophase. In a contrast, ITR-MPEG 1-1 NPs, ITR-4 ARM PEG 2-1 NPs and ITR-4 ARM

PEG 1-1 NPs were partially crystalline, therefore PEGylation affected the solid-state properties in these samples.

The surface PEGylation of ITR NPs aimed to modify their interactions with the mucin layer. In case of NPs able to interact with the mucus, i.e. mucoadhesive NPs, their prolonged residence time might improve the absorption of the drugs (Netsomboon and Bernkop-Schnürch, 2016). This approach was used in ITR preparations for vaginal, pulmonary and oral uses (Jafarinejad et al., 2012; Mirza et al., 2016; Suksiriworapong et al., 2017; Vanić and Škalko-Basnet, 2013). In those samples, the API was encapsulated in carriers containing mucoadhesive polymers, including Carbopol, chitosan and thiolated PEGs. However, the development of mucopenetrative NPs might be more advantageous, particularly for the oral use due to their enhanced bioavailability in comparison to the mucoadhesive NPs. Also, these particles were found to distribute more homogeneously across the intestine in contrast to the more locally concentrated depositions of mucoadhesive particles (Chen et al., 2013; Maisel et al., 2015). Furthermore, the evaluation of the mucoadhesive properties of nanonised ITR as well as PEGylated nanonised ITR had not been explored to date.

A range of techniques, such as DLS, NTA and QCM-D, were used to investigate the mucoadhesive properties of the non-PEGylated and PEGylated ITR NPs. The DLS experiments provided information about the interaction of the particles with the dispersed mucin in a stationary condition, while the QCM-D evaluated the same aspect but using flow conditions. The use of NTA aimed to investigate the diffusion of the particles in mucin. The results showed that the non-PEGylated ITR NPs were unable to interact with the mucin in stationary and flow conditions, while the PEGylated NPs could only interact with mucin in the stationary conditions using DLS, regardless the PEG type. Therefore, PEGylation affected the mucoadhesive property of the nanonised ITR. Moreover, the evaluation of the different aspects of mucoadhesivity of NPs using multiple techniques contributed to a more reliable and robust characterisation and should be considered in similar studies.

Furthermore, a decrease in NP concentration was observed using NTA when the non-PEGylated and PEGylated ITR NPs were incubated in a saline solution. As no evidence of aggregation of these particles were found, this decline in concentration was most likely related to their dissolution. Therefore, after oral administration, these particles are expected to partially dissolve and the undissolved particles subjected to a transcellular uptake by enterocytes and M cells in Peyer's patches (Ensign et al., 2012; Gao et al., 2012). Another possible explanation for the concentration decrease is the attachment of the NPs on the tubes of the NTA system.

6.3. Formation of eutectics mixtures and cocrystallisation

In Chapter 4, the experimental screening resulted in the identification of one new cocrystal of ITR formed with the terephthalic acid (TER). To date, the identified cocrystals of ITR were produced using a dicarboxylic acid as a coformer, including succinic acid (SUC), oxalic acid (OXA) and tartaric acid, which are molecules commonly used for cocrystallisation (Remenar et al., 2003; Shevchenko et al., 2013). Recently, a cocrystal of ITR with suberic acid was also produced from solution using a rapid solvent evaporation (Weng et al., 2019). In this case, the used coformer, suberic acid, has 8 carbons in its chain and is the longest molecule shown to cocrystallise with ITR.

Like other known cocrystals of ITR described in the literature, the ITR-TER cocrystal was also produced with a dicarboxylic acid, however, in contrast to the others, TER is an aromatic molecule. The crystallographic analysis of the ITR-TER cocrystal showed that this form has a 2:1 API to coformer stoichiometry and its asymmetric unit is formed by two molecules of ITR in an anti-parallel arrangement with the TER molecule placed in the gap formed between the two ITR molecules. This intermolecular arrangement is stabilised by heterosynthons formed between the two carboxylic acid molecules of the coformer and the azole ring of the ITR, wherein the hydroxyl of the carboxylic acid forms a H-bond with the N2 of the azole ring and the other carbonyl forms a second H-bond with the hydrogen bonded to the C3 of the azole ring. This structure is very similar to the succinic acid cocrystal of ITR however, in this form the heterosynthon is based on the H-bond between the hydroxyl moiety of the carboxylic acid of the coformer with the N2 of the azole ring of the API (Nonappa et al., 2013).

The ITR-TER cocrystal had an intrinsic dissolution rate (IDR) of 3.49 ± 1.3 $\mu g/min/cm^2$, which was not statistically significant in comparison to the crystalline form of the ITR (2.53 ± 0.9 $\mu g/min/cm^2$). The maximum dissolved drug ($\%_{max}$) from the ITR-TER cocrystal and crystalline ITR also was comparable, including dissolution studies where the samples were physically mixed with lactose and another experiment where they were mixed with excipients as those present in the Sporanox® solid formulation. Therefore, the ITR-TER cocrystal showed no superior *in vitro* dissolution characteristics in relation to the crystalline ITR, which could be due the low aqueous solubility of the coformer, approximately 17 $\mu g/mL$ (Park and Sheehan, 2000). In contrast, the other evaluated cocrystals, ITR-SUC and ITR-OXA, had greater IDR values, 16.20 ± 0.66 and 31.22 ± 2.54 $\mu g/min/cm^2$, respectively. In the dissolution experiment carried out on physical mixtures of the cocrystals with lactose, the ITR-SUC cocrystal had a $\%_{max}$ of $7.8\pm0.9\%$, which was slightly greater than those of the ITR-OXA cocrystal and crystalline ITR, 4.5 ± 0.1 and $3.7\pm0.1\%$, respectively. In the dissolution analysis where the samples were mixed with the excipients as those in the Sporanox® formulation, the ITR-SUC and ITR-OXA cocrystals showed a $\%_{max}$ of $12.1\pm0.8\%$ and $24.1\pm0.3\%$, respectively, while only $2.4\pm0.1\%$ of the API could be dissolved from

crystalline ITR. Therefore, both cocrystals, ITR-SUC and ITR-OXA, could improve the dissolution profiles of the API. This increase in the % drug solubilised could be correlated with the aqueous solubility of their respective coformers, approximately 83 and 135 mg/mL (Litsanov et al., 2014; Tyner and Francis, 2018). Furthermore, the difference observed between the two dissolution experiments could be due to the stabiliser effects of the polymers present in the Sporanox® formulation, hydroxypropyl methylcellulose and PEG, preventing crystallisation of ITR.

Although the ITR-OXA and ITR-SUC had enhanced dissolution profiles in relation to the crystalline ITR, they seemed to unable to achieve the improvements observed in other ITR cocrystals described in literature. In fact, a dissolution profiles of the ITR cocrystals with malic acid and tartaric acid into 0.1 N HCl, achieved a remarkable enhancement of their dissolution profile, as they had an increase of 20-fold in their $\%_{max}$ in relation to the crystalline ITR (Remenar et al., 2003). This enabled these cocrystals to have dissolution profiles comparable to the Sporanox®.

The experimental screenings also identified three eutectic mixtures of ITR formed with 4-aminosalicylic acid (ASA), 4-nitrobenzoic acid (NBA) and dihydrocaffeic acid (DHC). The eutectic mixtures identified in the screening might have the potential for pharmaceutical applications.

The reports on the eutectics mixtures with ITR are scarce and the formation of a eutectic mixture was only observed with phenol. The temperature of the eutectic point of this mix was lower than 25 °C and the system liquefied at room temperature (Park et al., 2012b). In this work, the authors found that the hydroxyl group of phenol could interact with the carbonyl group of the API. The authors showed that a solution containing this eutectic mixture could be used for a topical use and the *in vivo* analysis showed that ITR could permeate through the skin despite having characteristics not appropriate for transdermal delivery: high molecular weight, poor aqueous solubility and high log partition coefficient (Park et al., 2012a, 2012b).

6.4. ITR-TER nano-cocrystals

In Chapter 5, a nanoparticulate system of the ITR-TER cocrystal was produced using an antisolvent precipitation method. In this case, the preparation conditions were modified such as to produce the ITR-TER cocrystals in the nanometric size with a batch size suitable for the preparation of the Trojan particles (nano-in-microparticles). The antisolvent phase was used at high temperature to promote faster solvent evaporation, as this was demonstrated to be critical for the preparation of nanometric particles (presented in Chapter 2).

Multiple parameters were evaluated during the method development, including the solvent selection, based on the capacity to solubilise the API and the coformer and

respecting the 2:1 stoichiometry of the ITR-TER cocrystal. A mixture of acetone and methanol in a volume ratio of 70:30 (v/v) was selected to prepare the solvent phase containing the drug at 6 mg/mL and the coformer 0.706 mg/mL at 50 °C.

Another modification included addition of a stabiliser, as without it a polydispersed dispersion of the ITR-TER cocrystal with particle size of 2361 ± 512 nm was produced. The evaluation of lecithin as a potential stabiliser of the ITR-TER dispersion showed that at 5% (w/w), smaller particles were produced (1170 ± 15 nm). The stabiliser had an impact on the zeta potential value of the dispersion, with the lecithin-stabilised particles showing a zeta potential value of -21.3 ± 0.8 mV, in comparison to those with no lecithin of -15.4 ± 0.7 mV. This indicated that the lecithin could contribute to the stabilisation of particles by increasing the electrostatic repulsive forces. The presence of the stabiliser did not affect the solid-state characteristics of the ITR-TER system with the cocrystal produced at all lecithin concentrations used.

Although the lecithin at 5% (w/w) could reduce the size of the ITR-TER, the produced particles were still out of the aimed nanometric range. Therefore, an additional step of ultrasound application in the dispersions was used to further reduce sizes of the particles. The manufacture of NPs was possible using the sonication continuously for at least 15 min. SEM images of the sonicated dispersions showed small heterogeneous particles of approximately 200 nm in size that could be fragments of larger structures, in contrast to the non-sonicated dispersions, which had only particles of approximately 1 μm in size.

In Chapter 5, the nanoprecipitation method was optimised to produce ITR-TER nano-cocrystals (NCCs) based on the results obtained in Chapter 2. The optimisation aimed to increase the final API concentration and preserve the nanometric size of the cocrystal particles. The optimised parameters were the ITR concentration in the solvent phase and the AS:S ratio. As a result, a 6-fold higher production yield was achieved using 6 mg/mL of ITR in the solvent phase and the AS:S ratio of 5:1. This compares to 2 mg/mL of ITR and a 10:1 AS:S ratio used in the process as described in Chapter 2.

Finally, the modifications of the method setup to scale-up the batch size from 20 mL to 100 mL had no effect on the characteristics of the ITR-TER dispersions and the new setup was successful in increasing the batch size by a 5-fold.

The development of the ITR-TER NCCs resulted in a very different system, in relation to morphological and physicochemical characteristics, in comparison to the non-PEGylated and PEGylated ITR NPs. This difference is mostly caused by the presence of a coformer that impacts on the arrangement of molecules in the crystal lattice and translating into the supramolecular level dictating the shape and size of particles (Berry and Steed, 2017).

Only one report on ITR NCCs was found with the NPs of ITR prepared with adipic acid using wet milling. This sample had the particle size of 529 ± 69 nm (De Smet et al.,

2014). Bioavailability analysis of these particles in dogs, when administered orally, showed a faster drug release in comparison to Sporanox®, as the time when the highest API concentration was detected (T_{max}) of the ITR NCCs was 3 hours, while for the commercial form it was 6 hours, demonstrating the benefits of combing cocrystals and nanoparticles.

The development of the ITR-TER NCCs was based on the premise that its low solubility could promote a longer residence time in the lungs and contribute to the more effective treatment of local fungal infections (Tolman and Williams, 2010; Yang et al., 2008). For this purpose, dry powders of the ITR-TER NCCs embedded into microparticles of sugars. Such particles are known as Trojan particles (Tsapis et al., 2002).

6.5. Formulation of a dry powder for inhalation

Bioavailability of ITR after oral administration is subject to high variability, because, when the ITR capsules are administered, it is required an acidic gastric environment, also the capsule should be administered in fed state to improve the ITR absorption. Therefore, patients presenting gastrointestinal abnormalities, e.g. hypochlorhydria and frequent vomiting, are subject to have reduced ITR absorption from the capsules (Willems et al., 2001). In addition, the gastrointestinal synthons are common in approximately 20% of the patients, causing a compliance reduction to prolonged treatments (Lestner and Hope, 2013). Therefore, to reduce the side effects, and at the same time improve the efficacy of the treatment against infections, several formulations of ITR for pulmonary administration were developed recently (Card et al., 2008). These include nanoparticulate drug delivery systems in aerosols (Alvarez et al., 2007; Yang et al., 2010), as nebulisation dispersions (Pardeike et al., 2011) and in dry powders (Duret et al., 2012, 2014; Jafarinejad et al., 2012; Moazeni et al., 2012). A few studies have used ITR cocrystals for pulmonary application, wherein the enhanced dissolution profile of the cocrystals was explored to increase the ITR systemic absorption (Karashima et al., 2017; Weng et al., 2019). In one of these studies the plasma concentration of ITR was measured when the dry powders were administered intratracheally in rats. The results showed that animals treated with the formulations containing the ITR cocrystals with succinic acid and tartaric acid had the area under the curve (AUC) in the initial 8 hours after administration 24 and 19-folder higher, respectively, than the subjects treated with the formulation containing crystalline ITR (Karashima et al., 2017). In another study, dissolution analysis of the spray dried ITR cocrystal with suberic acid showed a fast dissolution over the initial 15 min, reaching the plateau of 80% dissolved ITR. In this case, the authors attributed the fast release of the API to the amorphous nature of the spray-dried powder and its large surface area, although the thermodynamic instability of the cocrystal in water could also contribute to this result (Weng et al., 2019).

The pulmonary formulations presented in Chapter 5 aimed to explore the ITR-TER cocrystal to increase the residence time of the particles in the lungs. This was based on the

poor solubility of the cocrystal, as described in Chapter 4. Drug delivery systems having prolonged residence time have the potential to increase their efficiency to treat fungal infections locally in the lungs (Eedara et al., 2019; Loira-Pastoriza et al., 2014). Furthermore, this local action implies reduced absorption of the drug to the bloodstream, minimising the systemic side effects (Loira-Pastoriza et al., 2014).

The pulmonary formulations developed consisted of the ITR-TER NCCs embedded into microparticles and presented as dry powders (Trojan particles). For this purpose, the nanoparticles were prepared with 5% (w/w) of lecithin, used as a stabiliser, and spray-dried with sugar to form larger particles with more suitable sizes for pulmonary administration. Particles with sizes between 1 and 5 μm are more likely to be deposited deeper in the respiratory tract when inhaled, while NPs are likely to be exhaled, consequently, rapidly eliminated (Kaur et al., 2012). Lecithin is a biocompatible excipient, as the lungs also contain phospholipidic surfactants similar to lecithin (Li et al., 2015). For this reason, lecithin is commonly used in pulmonary formulations (Wauthoz and Amighi, 2014).

It was important that the Trojan particles are able to release the NCCs. This was evaluated by redispersing the powders in water and measuring the particle size of the dispersions using DLS and NTA before and after spray drying. The results showed that the particle size of the redispersed powder was comparable to that measured before spray drying, implying that ITR-TER NCCs could be released instantaneously following inhalation.

The Trojan particles based on mannitol, raffinose and trehalose were evaluated in terms of the solid-state and aerodynamic properties. The formulation prepared with mannitol, ITR-TER-MAN, were crystalline in contrast to amorphous systems prepared with raffinose, ITR-TER-RAF, and trehalose, ITR-TER-TRE. The analysis of *in vitro* particle deposition using NGI showed that the ITR-TER-MAN system had the highest content of fine particles, i.e. particles with sizes lower than 5 μm, of 36.11±0.17 as well as the lowest MMAD and GSD, 4.02±0.13 μm and 1.74±0.03, respectively. This means that this formulation had the highest fraction of particles with sizes lower than 5 μm, which could represent a more efficient pulmonary deposition. In contrast, the ITR-TER-RAF and ITR-TER-TRE had a lower FPF of 19.50±3.81 and 14.57±13.2%, respectively, and higher MMAD, 5.28±0.54 and 5.89±2.56 μm, respectively. Therefore, the ITR-TER-MAN is expected to have a superior *in vivo* performance following inhalation considering the evaluated formulations.

6.6. Main findings

- The antisolvent temperature and the antisolvent to solvent ratio were important parameters impacting on the particle size of ITR NPs produced using a heat induced antisolvent precipitation.

- The inclusion of the solvent (acetone) evaporation step under reduced pressure resulted in reducing the Oswald ripening improving the colloidal stability of ITR NPs.

- PEGylation of ITR NPs resulted in dispersions with different physicochemical characteristics in comparison to non-PEGylated NPs; the changes included zeta potential values and solid-state properties.

- Interactions of PEGylated ITR NPs with mucin were detected in stationary conditions, while non-PEGylated ITR NPs did not interact with mucin in stationary and flow conditions.

- A new cocrystal of ITR with terephthalic acid and eutectic mixtures of ITR with with 4-aminosalicylic acid (ASA), 4-nitrobenzoic acid (NBA) and dihydrocaffeic acid (DHC) ASA, NBA and DHC were uncovered.

- The new ITR-TER cocrystal is the first multicomponent system of this API that is based on an aromatic coformer.

- The API-coformer stoichiometry in the ITR-TER was 2:1 and its crystalline structure is formed by two molecules of ITR in an antiparallel arrangement with one molecule of TER placed between them. H-bonds between the carboxylic acid of the coformer and the azole ring of the API were found responsible for the stabilisation of this structure.

- The intrinsic dissolution rate of the ITR-TER cocrystal was comparable to that of the crystalline form of ITR.

- The ITR-TER cocrystal could be nanonised when using antisolvent precipitation. The mixture of 70:30 (v/v) of acetone and methanol used as solvent phase allowed to use a 6 mg/mL of ITR in the solvent phase and using the AS:S ratio at 5:1. The stabilisation of the ITR-TER NCC was achieved using 5% (w/w) of lecithin in relation to the solid content. Sonication applied for at least 15 min could reduce the particle size into the nanometric size range. The setup modification enabled a 5-fold increase in the yield without altering the nanometric size and the solid-state properties of the ITR-TER NCCs.

- The dry powders for pulmonary administration were produced embedding the ITR-TER NCC into microparticles of mannitol, raffinose and trehalose using a spray-drier. Among them, the ITR-TER-MAN had smallest median size, 4.85±0.06 μm, furthermore, its MMAD was 4.02±0.13 μm and its GSD was 1.74±0.03. This enabled ITR-TER-MAN to have the largest respirable fraction, of 36.11 ± 0.17%. Therefore, this powder had the best aerodynamic properties for a potential pulmonary administration.

6.7.Future work

- Evaluate the feasibility of the set up developed to scale-up the ITR-TER NCC preparation for the non-PEGylated and PEGylated ITR NPs. Investigate the impacts of this set up on the solid-state properties of the produced NPs.

- Perform an *in vitro* study using intestinal cell lines, as Caco-2, to investigate whether PEGylation of the nanonised ITR could influence on the internalisation of the API by these cells.

- Investigate the dissolution profiles PEGylated and PEGylated ITR NPs considering administration via oral route. Additionally, perform an *in vivo* study using animals to investigate the bioavailability and other pharmacokinetic properties of the non-PEGylated and PEGylated ITR NPs to determine whether the surface modification can alter the API absorption when orally administered.

- Further investigation of the properties of eutectic mixtures formed with the ITR by the determination of their phase diagram using DSC and PXRD to establish the stoichiometry of the eutectic points. Evaluate these samples using FT-IR analysis in order to study the nature of the interactions between the API and coformers. Additionally, perform dissolution experiments of the ITR eutectic mixtures to assess potential improvements in the dissolution profile that these multi-component forms could have in relation to the crystalline form.

- Use design of experiments (DoE) to optimise the spray dry conditions used for the preparation of the dry powder formulations. Accordingly, this study would provide information about the drying conditions in which the powders are produced with enhanced the aerodynamic properties, consequently, improving their potential for pulmonary application.

- Use the nanonised ITR produced in antisolvent precipitation to develop Trojan microparticles. Evaluate if the ITR NPs have their solid-state properties are preserved as a smetic mesophase liquid crystal after spray-drying using DSC and PXRD analysis. Furthermore, stablish a parallel between the Trojan particles containing the ITR NPs and the NCC.

- Investigate the physicochemical stability of the Trojan particles, including analysis on the conservation of their solid-state, as well as their aerodynamic properties.

- Investigation of Trojan particles possible behaviour when administered considering multiple aspects. Firstly, evaluate their interaction with mucin, using the QCM-D, NTA and DLS. Secondly, determine the dissolution profiles of the pulmonary dry powders using a relevant media to assess the drug release from these formulations, consequently, providing information if the NPs would have a prolonged residence time

in the lungs. Finally, perform an *in vitro* study using airway cell lines, such as Calu-3, to investigate the permeability of the drug by these cells.

References

Abbott, K.C., Hypolite, I., Poropatich, R.K., Hshieh, P., Cruess, D., Hawkes, C.A., Agodoa, L.Y., Keller, R.A., 2001. Hospitalizations for fungal infections after renal transplantation in the United States. Transpl. Infect. Dis. 3, 203–211. https://doi.org/10.1034/j.1399-3062.2001.30404.x

Alessi, M.L., Norman, A.I., Knowlton, S.E., Ho, D.L., Greer, S.C., 2005. Helical and coil conformations of poly(ethylene glycol) in isobutyric acid and water. Macromolecules 38, 9333–9340. https://doi.org/10.1021/ma051339e

Alhalaweh, A., Velaga, S.P., 2010. Formation of Cocrystals from Stoichiometric Solutions of Incongruently Saturating Systems by Spray Drying. Cryst. Growth Des. 10, 3302–3305. https://doi.org/10.1021/cg100451q

Alvarez, C.A., Wiederhold, N.P., McConville, J.T., Peters, J.I., Najvar, L.K., Graybill, J.R., Coalson, J.J., Talbert, R.L., Burgess, D.S., Bocanegra, R., Johnston, K.P., Williams, R.O., 2007. Aerosolized nanostructured itraconazole as prophylaxis against invasive pulmonary aspergillosis. J. Infect. 55, 68–74. https://doi.org/10.1016/j.jinf.2007.01.014

Amidon, G.L., Lennernäs, H., Shah, V.P., Crison, J.R., 1995. A Theoretical Basis for a Biopharmaceutic Drug Classification: The Correlation of in Vitro Drug Product Dissolution and in Vivo Bioavailability. Pharm. Res. 12, 413–420. https://doi.org/10.1023/A:1016212804288

Andes, D., Pascua, A., Marchetti, O., 2009. Antifungal therapeutic drug monitoring: Established and emerging indications. Antimicrob. Agents Chemother. 53, 24–34. https://doi.org/10.1128/AAC.00705-08

Andrade, F., Rafael, D., Videira, M., Ferreira, D., Sosnik, A., Sarmento, B., 2013. Nanotechnology and pulmonary delivery to overcome resistance in infectious diseases. Adv. Drug Deliv. Rev. 65, 1816–1827. https://doi.org/10.1016/j.addr.2013.07.020

Anton, N., Jakhmola, A., Vandamme, T.F., 2012. Trojan Microparticles for Drug Delivery. Pharmaceutics 4, 1–25. https://doi.org/10.3390/pharmaceutics4010001

Armstrong-James, D., Meintjes, G., Brown, G.D., 2014. A neglected epidemic: fungal infections in HIV/AIDS. Trends Microbiol. 22, 120–127. https://doi.org/10.1016/j.tim.2014.01.001

Ashbee, H.R., Barnes, R.A., Johnson, E.M., Richardson, M.D., Gorton, R., Hope, W.W., 2014. Therapeutic drug monitoring (TDM) of antifungal agents: Guidelines from the british society for medical mycology. J. Antimicrob. Chemother. 69, 1162–1176. https://doi.org/10.1093/jac/dkt508

Babu, N.J., Nangia, A., 2011. Solubility Advantage of Amorphous Drugs and

Pharmaceutical Cocrystals. Cryst. Growth Des. 11, 2662–2679. https://doi.org/10.1021/cg200492w

Badawi, A.A., El-Nabarawi, M.A., El-Setouhy, D.A., Alsammit, S.A., 2011. Formulation and Stability Testing of Itraconazole Crystalline Nanoparticles. AAPS PharmSciTech 12, 811. https://doi.org/10.1208/s12249-011-9651-9

Bansil, R., Turner, B.S., 2006. Mucin structure, aggregation, physiological functions and biomedical applications. Curr. Opin. Colloid Interface Sci. 11, 164–170. https://doi.org/10.1016/j.cocis.2005.11.001

Barone, J.A., Moskovitz, B.L., Guarnieri, J., Hassell, A.E., Colaizzi, J.L., Bierman, R.H., Jessen, L., 1998. Enhanced bioavailability of itraconazole in hydroxypropyl-beta-cyclodextrin solution versus capsules in healthy volunteers. Antimicrob. Agents Chemother. 42, 1862–5.

Basavoju, S., Boström, D., Velaga, S.P., 2008. Indomethacin–Saccharin Cocrystal: Design, Synthesis and Preliminary Pharmaceutical Characterization. Pharm. Res. 25, 530–541. https://doi.org/10.1007/s11095-007-9394-1

Bassetti, M., Righi, E., Costa, A., Fasce, R., Molinari, M.P., Rosso, R., Pallavicini, F.B., Viscoli, C., 2006. Epidemiological trends in nosocomial candidemia in intensive care. BMC Infect. Dis. 6, 21. https://doi.org/10.1186/1471-2334-6-21

Bassi da Silva, J., Ferreira, S.B. de S., de Freitas, O., Bruschi, M.L., 2017. A critical review about methodologies for the analysis of mucoadhesive properties of drug delivery systems. Drug Dev. Ind. Pharm. 43, 1053–1070. https://doi.org/10.1080/03639045.2017.1294600

Bavishi, D.D., Borkhataria, C.H., 2016. Spring and parachute: How cocrystals enhance solubility. Prog. Cryst. Growth Charact. Mater. 62, 1–8. https://doi.org/10.1016/j.pcrysgrow.2016.07.001

Berenguer, J., Ali, N.M., Allende, M.C., Lee, J., Garrett, K., Battaglia, S., Piscitelli, S.C., Rinaldi, M.G., Pizzo, P.A., Walsh, T.J., 1994. Itraconazole for experimental pulmonary aspergillosis: Comparison with amphotericin B, interaction with cyclosporin A, and correlation between therapeutic response and itraconazole concentrations in plasma. Antimicrob. Agents Chemother. 38, 1303–1308. https://doi.org/10.1128/AAC.38.6.1303

Bergström, C.A.S., Box, K., Holm, R., Matthews, W., McAllister, M., Müllertz, A., Rades, T., Schäfer, K.J., Teleki, A., 2019. Biorelevant intrinsic dissolution profiling in early drug development: Fundamental, methodological, and industrial aspects. Eur. J. Pharm. Biopharm. 139, 101–114. https://doi.org/10.1016/j.ejpb.2019.03.011

Berry, D.J., Steed, J.W., 2017. Pharmaceutical cocrystals, salts and multicomponent systems; intermolecular interactions and property based design. Adv. Drug Deliv. Rev. 117, 3–24. https://doi.org/10.1016/j.addr.2017.03.003

References

Bhattacharjee, S., 2016. DLS and zeta potential – What they are and what they are not? J. Control. Release 235, 337–351. https://doi.org/10.1016/j.jconrel.2016.06.017

Bodey, G.P., 1992. Azole antifungal agents. Clin. Infect. Dis. 14 Suppl 1, S161-9. https://doi.org/10.2307/4456409

Bogataj, M., Vovk, T., Kerec, M., Dimnik, A., Grabnar, I., Mrhar, A., 2003. The Correlation between Zeta Potential and Mucoadhesion Strength on Pig Vesical Mucosa. Biol. Pharm. Bull. 26, 743–746. https://doi.org/10.1248/bpb.26.743

Boogaerts, M.A., Maertens, J., Van der Geest, R., Bosly, A., Michaux, J.L., Van Hoof, A., Cleeren, M., Wostenborghs, R., De Beule, K., 2001. Pharmacokinetics and safety of a 7-day administration of intravenous itraconazole followed by a 14-day administration of itraconazole oral solution in patients with hematologic malignancy. Antimicrob. Agents Chemother. 45, 981–985. https://doi.org/10.1128/AAC.45.3.981-985.2001

Boyd, R.D., Pichaimuthu, S.K., Cuenat, A., 2011. New approach to inter-technique comparisons for nanoparticle size measurements; using atomic force microscopy, nanoparticle tracking analysis and dynamic light scattering. Colloids Surfaces A Physicochem. Eng. Asp. 387, 35–42. https://doi.org/10.1016/j.colsurfa.2011.07.020

Bruice, P.Y., 2007. Organic Chemistry, 5th ed. Pearson International Edition, Santa Barbara.

Campoy, S., Adrio, J.L., 2017. Antifungals. Biochem. Pharmacol. 133, 86–96. https://doi.org/10.1016/j.bcp.2016.11.019

Card, J.W., Zeldin, D.C., Bonner, J.C., Nestmann, E.R., 2008. Pulmonary applications and toxicity of engineered nanoparticles. Am. J. Physiol. Cell. Mol. Physiol. 295, L400–L411. https://doi.org/10.1152/ajplung.00041.2008

Carvalho, T.C., Peters, J.I., Williams III, R.O., 2011. Influence of particle size on regional lung deposition – What evidence is there? Int. J. Pharm. 406, 1–10. https://doi.org/10.1016/j.ijpharm.2010.12.040

Cerreia Vioglio, P., Chierotti, M.R., Gobetto, R., 2017. Pharmaceutical aspects of salt and cocrystal forms of APIs and characterization challenges. Adv. Drug Deliv. Rev. 117, 86–110. https://doi.org/10.1016/j.addr.2017.07.001

Chen, D., Xia, D., Li, X., Zhu, Q., Yu, H., Zhu, C., Gan, Y., 2013. Comparative study of Pluronic® F127-modified liposomes and chitosan-modified liposomes for mucus penetration and oral absorption of cyclosporine A in rats. Int. J. Pharm. 449, 1–9. https://doi.org/10.1016/j.ijpharm.2013.04.002

Chen, Y., Li, L., Yao, J., Ma, Y.-Y., Chen, J.-M., Lu, T.-B., 2016. Improving the Solubility and Bioavailability of Apixaban via Apixaban–Oxalic Acid Cocrystal. Cryst. Growth Des. 16, 2923–2930. https://doi.org/10.1021/acs.cgd.6b00266

Cheow, W.S., Ng, M.L.L., Kho, K., Hadinoto, K., 2011. Spray-freeze-drying production of

thermally sensitive polymeric nanoparticle aggregates for inhaled drug delivery: Effect of freeze-drying adjuvants. Int. J. Pharm. 404, 289–300. https://doi.org/10.1016/j.ijpharm.2010.11.021

Cherukuvada, S., Babu, N.J., Nangia, A., 2011. Nitrofurantoin– p -aminobenzoic acid cocrystal: Hydration stability and dissolution rate studies. J. Pharm. Sci. 100, 3233–3244. https://doi.org/10.1002/jps.22546

Cherukuvada, S., Nangia, A., 2014. Eutectics as improved pharmaceutical materials: design, properties and characterization. Chem. Commun. 50, 906–923. https://doi.org/10.1039/C3CC47521B

Childs, S.L., Hardcastle, K.I., 2007. Cocrystals of Piroxicam with Carboxylic Acids. Cryst. Growth Des. 7, 1291–1304. https://doi.org/10.1021/cg060742p

Chuacharoen, T., Sabliov, C.M., 2016. Stability and controlled release of lutein loaded in zein nanoparticles with and without lecithin and pluronic F127 surfactants. Colloids Surfaces A Physicochem. Eng. Asp. 503, 11–18. https://doi.org/10.1016/j.colsurfa.2016.04.038

Clark, M.D., Kumar, S.K., Owen, J.S., Chan, E.M., 2011. Focusing Nanocrystal Size Distributions via Production Control. Nano Lett. 11, 1976–1980. https://doi.org/10.1021/nl200286j

Cogoni, G., Baratti, R., Romagnoli, J.A., 2013. On the influence of hydrogen bond interactions in isothermal and nonisothermal antisolvent crystallization processes. Ind. Eng. Chem. Res. 52, 9612–9619. https://doi.org/10.1021/ie303414b

Comuzzo, P., Battistutta, F., 2019. Acidification and pH Control in Red Wines, in: Red Wine Technology. Elsevier, pp. 17–34. https://doi.org/10.1016/B978-0-12-814399-5.00002-5

Cone, R.A., 2009. Barrier properties of mucus. Adv. Drug Deliv. Rev. 61, 75–85. https://doi.org/10.1016/j.addr.2008.09.008

Crowder, T.M., Rosati, J.A., Schroeter, J.D., Hickey, A.J., Martonen, T.B., 2002. Fundamental effects of particle morphology on lung delivery: Predictions of Stokes' law and the particular relevance to dry powder inhaler formulation and development. Pharm. Res. 19, 239–245. https://doi.org/https://doi.org/10.1023/A:1014426530935

Cruz-Cabeza, A.J., 2012. Acid–base crystalline complexes and the pKa rule. CrystEngComm 14, 6362. https://doi.org/10.1039/c2ce26055g

D'Addio, S.M., Prud'homme, R.K., 2011. Controlling drug nanoparticle formation by rapid precipitation. Adv. Drug Deliv. Rev. 63, 417–426. https://doi.org/10.1016/j.addr.2011.04.005

das Neves, J., Bahia, M.F., Amiji, M.M., Sarmento, B., 2011. Mucoadhesive nanomedicines: characterization and modulation of mucoadhesion at the nanoscale. Expert Opin.

Drug Deliv. 8, 1085–1104. https://doi.org/10.1517/17425247.2011.586334

de Jesús Valle, M.J., Maderuelo Martín, C., Zarzuelo Castañeda, A., Sánchez Navarro, A., 2017. Albumin micro/nanoparticles entrapping liposomes for itraconazole green formulation. Eur. J. Pharm. Sci. 106, 159–165. https://doi.org/10.1016/j.ejps.2017.05.066

De La Rosa, G.R., Champlin, R.E., Kontoyiannis, D.P., 2002. Risk factors for the development of invasive fungal infections in allogeneic blood and marrow transplant recipients. Transpl. Infect. Dis. 4, 3–9. https://doi.org/10.1034/j.1399-3062.2002.00010.x

De Rosa, F.G., Trecarichi, E.M., Montrucchio, C., Losito, A.R., Raviolo, S., Posteraro, B., Corcione, S., Di Giambenedetto, S., Fossati, L., Sanguinetti, M., Serra, R., Cauda, R., Di Perri, G., Tumbarello, M., 2013. Mortality in patients with early- or late-onset candidaemia. J. Antimicrob. Chemother. 68, 927–935. https://doi.org/10.1093/jac/dks480

De Smet, L., Saerens, L., De Beer, T., Carleer, R., Adriaensens, P., Van Bocxlaer, J., Vervaet, C., Remon, J.P., 2014. Formulation of itraconazole nanococrystals and evaluation of their bioavailability in dogs. Eur. J. Pharm. Biopharm. 87, 107–113. https://doi.org/10.1016/j.ejpb.2013.12.016

Deli, M.A., 2009. Potential use of tight junction modulators to reversibly open membranous barriers and improve drug delivery. Biochim. Biophys. Acta - Biomembr. 1788, 892–910. https://doi.org/10.1016/j.bbamem.2008.09.016

Delori, A., Friščić, T., Jones, W., 2012. The role of mechanochemistry and supramolecular design in the development of pharmaceutical materials. CrystEngComm 14, 2350. https://doi.org/10.1039/c2ce06582g

Denning, D.W., Hope, W.W., 2010. Therapy for fungal diseases: opportunities and priorities. Trends Microbiol. 18, 195–204. https://doi.org/10.1016/j.tim.2010.02.004

Descamps, M., Willart, J.F., 2016. Perspectives on the amorphisation/milling relationship in pharmaceutical materials. Adv. Drug Deliv. Rev. 100, 51–66. https://doi.org/10.1016/j.addr.2016.01.011

Desiraju, G.R., 1995. Supramolecular Synthons in Crystal Engineering—A New Organic Synthesis. Angew. Chemie Int. Ed. English 34, 2311–2327. https://doi.org/10.1002/anie.199523111

Dobry, D.E., Settell, D.M., Baumann, J.M., Ray, R.J., Graham, L.J., Beyerinck, R.A., 2009. A Model-Based Methodology for Spray-Drying Process Development. J. Pharm. Innov. 4, 133–142. https://doi.org/10.1007/s12247-009-9064-4

Douroumis, D., Fahr, A., 2013. Drug Delivery Strategies for Poorly Water-Soluble Drugs, Drug Delivery Strategies for Poorly Water-Soluble Drugs. John Wiley & Sons Ltd,

References

Oxford, UK. https://doi.org/10.1002/9781118444726

Douroumis, D., Ross, S.A., Nokhodchi, A., 2017. Advanced methodologies for cocrystal synthesis. Adv. Drug Deliv. Rev. 117, 178–195. https://doi.org/10.1016/j.addr.2017.07.008

Dressman, J.B., Amidon, G.L., Reppas, C., Shah, V.P., 1998. Dissolution Testing as a Prognostic Tool for Oral Drug Absorption: Imediate Release Dosage Forms. Pharm. Res. 15, 11. https://doi.org/10.1023/a:1011984216775

Duggirala, N.K., Perry, M.L., Almarsson, Ö., Zaworotko, M.J., 2016. Pharmaceutical cocrystals: along the path to improved medicines. Chem. Commun. 52, 640–655. https://doi.org/10.1039/C5CC08216A

Dünnhaupt, S., Kammona, O., Waldner, C., Kiparissides, C., Bernkop-Schnürch, A., 2015. Nano-carrier systems: Strategies to overcome the mucus gel barrier. Eur. J. Pharm. Biopharm. 96, 447–453. https://doi.org/10.1016/j.ejpb.2015.01.022

Duret, C., Merlos, R., Wauthoz, N., Sebti, T., Vanderbist, F., Amighi, K., 2014. Pharmacokinetic evaluation in mice of amorphous itraconazole-based dry powder formulations for inhalation with high bioavailability and extended lung retention. Eur. J. Pharm. Biopharm. 86, 46–54. https://doi.org/10.1016/j.ejpb.2013.03.005

Duret, C., Wauthoz, N., Sebti, T., Vanderbist, F., Amighi, K., 2012. Solid dispersions of itraconazole for inhalation with enhanced dissolution, solubility and dispersion properties. Int. J. Pharm. 428, 103–113. https://doi.org/10.1016/j.ijpharm.2012.03.002

Duret, C., Wauthoz, N., Sebti, T., Vanderbist, F., Amighi, K., Duret, Wauthoz, Sebti, Vanderbist, Amighi, 2012. New inhalation-optimized itraconazole nanoparticle-based dry powders for the treatment of invasive pulmonary aspergillosis. Int. J. Nanomedicine 7, 5475. https://doi.org/10.2147/IJN.S34091

Eedara, B.B., Tucker, I.G., Zujovic, Z.D., Rades, T., Price, J.R., Das, S.C., 2019. Crystalline adduct of moxifloxacin with trans-cinnamic acid to reduce the aqueous solubility and dissolution rate for improved residence time in the lungs. Eur. J. Pharm. Sci. 136, 104961. https://doi.org/10.1016/j.ejps.2019.104961

Elewski, B.E., 1993. Mechanisms of action of systemic antifungal agents. J. Am. Acad. Dermatol. 28, S28–S34. https://doi.org/10.1016/S0190-9622(09)80305-8

Elkin, I., Rabanel, J.-M., Hildgen, P., 2015. Influence of Hydrophobic Dendrimer Core Structure on the Itraconazole Encapsulation Efficiency. Macromol. Chem. Phys. 216, 2356–2367. https://doi.org/10.1002/macp.201500211

Ensign, L.M., Cone, R., Hanes, J., 2012. Oral drug delivery with polymeric nanoparticles: The gastrointestinal mucus barriers. Adv. Drug Deliv. Rev. 64, 557–570. https://doi.org/10.1016/j.addr.2011.12.009

Ensign, L.M., Hoen, T.E., Maisel, K., Cone, R.A., Hanes, J.S., 2013. Enhanced vaginal drug

delivery through the use of hypotonic formulations that induce fluid uptake. Biomaterials 34, 6922–6929. https://doi.org/10.1016/j.biomaterials.2013.05.039

Fakes, M.G., Dali, M. V, Haby, T.A., Morris, K.R., Varia, S.A., Serajuddin, A.T.M., 2000. Moisture Sorption Behavior of Selected Bulking Agents Used in Lyophilized Products. PDA J. Pharm. Sci. Technol. 54, 144–149.

Ferrari, M., 2005. Cancer nanotechnology: opportunities and challenges. Nat. Rev. Cancer 5, 161–171. https://doi.org/10.1038/nrc1566

Filipe, V., Hawe, A., Jiskoot, W., 2010. Critical Evaluation of Nanoparticle Tracking Analysis (NTA) by NanoSight for the Measurement of Nanoparticles and Protein Aggregates. Pharm. Res. 27, 796–810. https://doi.org/10.1007/s11095-010-0073-2

Fischer, F., Scholz, G., Benemann, S., Rademann, K., Emmerling, F., 2014. Evaluation of the formation pathways of cocrystal polymorphs in liquid-assisted syntheses. CrystEngComm 16, 8272–8278. https://doi.org/10.1039/C4CE00472H

Florence, A.T., Attwood, D., 2006. Physicochemical Principles of Pharmacy, 4th ed, Science.

Fontana, F., Figueiredo, P., Zhang, P., Hirvonen, J.T., Liu, D., Santos, H.A., 2018. Production of pure drug nanocrystals and nano co-crystals by confinement methods. Adv. Drug Deliv. Rev. 131, 3–21. https://doi.org/10.1016/j.addr.2018.05.002

Food and Drug Administration, 2017. Waiver of In Vivo Bioavailability and Bioequivalence Studies for Immediate-Release Solid Oral Dosage Forms Based on a Biopharmaceutics Classification System. Guid. Ind.

Freundlich, H., 1926. Colloid & capillary chemistry. Methuen & co. ltd.

Fuchs, N.A., 1959. Evaporation and Droplet Growth in Gaseous Media. Elsevier. https://doi.org/10.1016/C2013-0-08145-5

Gallego-Urrea, J.A., Tuoriniemi, J., Hassellöv, M., 2011. Applications of particle-tracking analysis to the determination of size distributions and concentrations of nanoparticles in environmental, biological and food samples. TrAC Trends Anal. Chem. 30, 473–483. https://doi.org/10.1016/j.trac.2011.01.005

Gao, L., Liu, G., Ma, J., Wang, X., Zhou, L., Li, X., 2012. Drug nanocrystals: In vivo performances. J. Control. Release 160, 418–430. https://doi.org/10.1016/j.jconrel.2012.03.013

Gao, Y., Zu, H., Zhang, J., 2011. Enhanced dissolution and stability of adefovir dipivoxil by cocrystal formation. J. Pharm. Pharmacol. 63, 483–490. https://doi.org/10.1111/j.2042-7158.2010.01246.x

García-Díaz, M., Birch, D., Wan, F., Nielsen, H.M., 2018. The role of mucus as an invisible cloak to transepithelial drug delivery by nanoparticles. Adv. Drug Deliv. Rev. 124, 107–124. https://doi.org/10.1016/j.addr.2017.11.002

Gavezzotti, A., Colombo, V., Lo Presti, L., 2016. Facts and Factors in the Formation and

Stability of Binary Crystals. Cryst. Growth Des. 16, 6095–6104. https://doi.org/10.1021/acs.cgd.6b01146

Ghannoum, M.A., Rice, L.B., 1999. Antifungal agents: mode of action, mechanisms of resistance, and correlation of these mechanisms with bacterial resistance. Clin. Microbiol. Rev. 12, 501–17. https://doi.org/10.1.1.322-6182

Gilis, P.M. V., Conde, V.F.V. De, Vandecruys, R.P.G., 1997. BEADS HAVING ACORE COATED WITH AN ANT FUNGALAND A POLYMER. US5633015A. https://doi.org/10.1016/j.scriptamat.2005.10.045

Glasmacher, A., Prentice, A., Gorschlüter, M., Engelhart, S., Hahn, C., Djulbegovic, B., Schmidt-Wolf, I.G.H., 2003. Itraconazole Prevents Invasive Fungal Infections in Neutropenic Patients Treated for Hematologic Malignancies: Evidence From a Meta-Analysis of 3,597 Patients. J. Clin. Oncol. 21, 4615–4626. https://doi.org/10.1200/JCO.2003.04.052

GODT, 2019. NEWSLETTER TRANSPLANT 2018 [WWW Document]. URL http://www.transplant-observatory.org/ (accessed 2.26.19).

Greenhalgh, D.J., Williams, A.C., Timmins, P., York, P., 1999. Solubility parameters as predictors of miscibility in solid dispersions. J. Pharm. Sci. 88, 1182–1190. https://doi.org/10.1021/js9900856

Grießinger, J., Dünnhaupt, S., Cattoz, B., Griffiths, P., Oh, S., Gómez, S.B. i, Wilcox, M., Pearson, J., Gumbleton, M., Abdulkarim, M., Pereira de Sousa, I., Bernkop-Schnürch, A., 2015. Methods to determine the interactions of micro- and nanoparticles with mucus. Eur. J. Pharm. Biopharm. 96, 464–476. https://doi.org/10.1016/j.ejpb.2015.01.005

Grohganz, H., Löbmann, K., Priemel, P., Tarp Jensen, K., Graeser, K., Strachan, C., Rades, T., 2013. Amorphous drugs and dosage forms. J. Drug Deliv. Sci. Technol. 23, 403–408. https://doi.org/10.1016/S1773-2247(13)50057-8

Grossjohann, C., Eccles, K.S., Maguire, A.R., Lawrence, S.E., Tajber, L., Corrigan, O.I., Healy, A.M., 2012. Characterisation, solubility and intrinsic dissolution behaviour of benzamide: dibenzyl sulfoxide cocrystal. Int. J. Pharm. 422, 24–32. https://doi.org/10.1016/j.ijpharm.2011.10.016

Guzmán, H.R., Tawa, M., Zhang, Z., Ratanabanangkoon, P., Shaw, P., Gardner, C.R., Chen, H., Moreau, J., Almarsson, Ö., Remenar, J.F., 2007. Combined Use of Crystalline Salt Forms and Precipitation Inhibitors to Improve Oral Absorption of Celecoxib from Solid Oral Formulations. J. Pharm. Sci. 96, 2686–2702. https://doi.org/10.1002/jps.20906

Hancock, B.C., Parks, M., 2000. What is the true solubility advantage for amorphous pharmaceuticals? Pharm. Res. 17, 397–404.

References

https://doi.org/https://doi.org/10.1023/A:1007516718048

Hansen, C., 2007. Hansen Solubility Parameters: A User's Handbook. CRC Press, Boca Raton, Florida. https://doi.org/10.1201/9781420006834

Hardin, T.C., Graybill, J.R., Fetchick, R., Woestenborghs, R., Rinaldi, M.G., Kuhn, J.G., 1988. Pharmacokinetics of itraconazole following oral administration to normal volunteers. Antimicrob. Agents Chemother. 32, 1310–1313. https://doi.org/10.1128/AAC.32.9.1310

Hoeben, B.J., Burgess, D.S., McConville, J.T., Najvar, L.K., Talbert, R.L., Peters, J.I., Wiederhold, N.P., Frei, B.L., Graybill, J.R., Bocanegra, R., Overhoff, K.A., Sinswat, P., Johnston, K.P., Williams, R.O., 2006. In Vivo Efficacy of Aerosolized Nanostructured Itraconazole Formulations for Prevention of Invasive Pulmonary Aspergillosis. Antimicrob. Agents Chemother. 50, 1552–1554. https://doi.org/10.1128/AAC.50.4.1552-1554.2006

Huang, Y., Li, J.-M., Lai, Z.-H., Wu, J., Lu, T.-B., Chen, J.-M., 2017. Phenazopyridine-phthalimide nano-cocrystal: Release rate and oral bioavailability enhancement. Eur. J. Pharm. Sci. 109, 581–586. https://doi.org/10.1016/j.ejps.2017.09.020

Huang, Z., Lin, L., McGoverin, C., Liu, H., Wang, L., Zhou, Q. (Tony), Lu, M., Wu, C., 2018. Dry powder inhaler formulations of poorly water-soluble itraconazole: A balance between in-vitro dissolution and in-vivo distribution is necessary. Int. J. Pharm. 551, 103–110. https://doi.org/10.1016/j.ijpharm.2018.09.018

Huckaby, J.T., Lai, S.K., 2018. PEGylation for enhancing nanoparticle diffusion in mucus. Adv. Drug Deliv. Rev. 124, 125–139. https://doi.org/10.1016/j.addr.2017.08.010

Jafarinejad, S., Gilani, K., Moazeni, E., Ghazi-Khansari, M., Najafabadi, A.R., Mohajel, N., 2012. Development of chitosan-based nanoparticles for pulmonary delivery of itraconazole as dry powder formulation. Powder Technol. 222, 65–70. https://doi.org/10.1016/j.powtec.2012.01.045

Janbon, G., Quintin, J., Lanternier, F., d'Enfert, C., 2019. Studying fungal pathogens of humans and fungal infections: fungal diversity and diversity of approaches. Genes Immun. 20, 403–414. https://doi.org/10.1038/s41435-019-0071-2

Jiang, Q., Yang, C.., Li, J.., 2002. Melting enthalpy depression of nanocrystals. Mater. Lett. 56, 1019–1021. https://doi.org/10.1016/S0167-577X(02)00667-5

Jog, R., Burgess, D.J., 2018. Nanoamorphous drug products – Design and development. Int. J. Pharm. 553, 238–260. https://doi.org/10.1016/j.ijpharm.2018.10.046

Johansson, M.E. V, Sjövall, H., Hansson, G.C., 2013. The gastrointestinal mucus system in health and disease. Nat. Rev. Gastroenterol. Hepatol. 10, 352–361. https://doi.org/10.1038/nrgastro.2013.35

Kalepu, S., Nekkanti, V., 2015. Insoluble drug delivery strategies: review of recent advances

and business prospects. Acta Pharm. Sin. B 5, 442–453. https://doi.org/10.1016/j.apsb.2015.07.003

Karagianni, A., Malamatari, M., Kachrimanis, K., 2018. Pharmaceutical Cocrystals: New Solid Phase Modification Approaches for the Formulation of APIs. Pharmaceutics 10, 18. https://doi.org/10.3390/pharmaceutics10010018

Karashima, M., Kimoto, K., Yamamoto, K., Kojima, T., Ikeda, Y., 2016. A novel solubilization technique for poorly soluble drugs through the integration of nanocrystal and cocrystal technologies. Eur. J. Pharm. Biopharm. 107, 142–150. https://doi.org/10.1016/j.ejpb.2016.07.006

Karashima, M., Sano, N., Yamamoto, S., Arai, Y., Yamamoto, K., Amano, N., Ikeda, Y., 2017. Enhanced pulmonary absorption of poorly soluble itraconazole by micronized cocrystal dry powder formulations. Eur. J. Pharm. Biopharm. 115, 65–72. https://doi.org/10.1016/j.ejpb.2017.02.013

Karimi-Jafari, M., Padrela, L., Walker, G.M., Croker, D.M., 2018. Creating Cocrystals: A Review of Pharmaceutical Cocrystal Preparation Routes and Applications. Cryst. Growth Des. 18, 6370–6387. https://doi.org/10.1021/acs.cgd.8b00933

Karthikeyan, N., Joseph Prince, J., Ramalingam, S., Periandy, S., 2015. Electronic [UV–Visible] and vibrational [FT-IR, FT-Raman] investigation and NMR–mass spectroscopic analysis of terephthalic acid using quantum Gaussian calculations. Spectrochim. Acta Part A Mol. Biomol. Spectrosc. 139, 229–242. https://doi.org/10.1016/j.saa.2014.11.112

Kato, K., Nagao, M., Nakano, S., Yunoki, T., Hotta, G., Yamamoto, M., Matsumura, Y., Ito, Y., Takakura, S., Chen, F., Bando, T., Matsuda, Y., Matsubara, K., Date, H., Ichiyama, S., 2014. Itraconazole prophylaxis for invasive Aspergillus infection in lung transplantation. Transpl. Infect. Dis. 16, 340–343. https://doi.org/10.1111/tid.12187

Kaur, G., Narang, R.K., Rath, G., Goyal, A.K., 2012. Advances in Pulmonary Delivery of Nanoparticles. Artif. Cells, Blood Substitutes, Biotechnol. 40, 75–96. https://doi.org/10.3109/10731199.2011.592494

Kawabata, Y., Wada, K., Nakatani, M., Yamada, S., Onoue, S., 2011. Formulation design for poorly water-soluble drugs based on biopharmaceutics classification system: Basic approaches and practical applications. Int. J. Pharm. 420, 1–10. https://doi.org/10.1016/j.ijpharm.2011.08.032

Khutoryanskiy, V. V. (Ed.), 2014. Mucoadhesive Materials and Drug Delivery Systems, 1st ed. John Wiley & Sons, Ltd, Chichester, United Kingdom. https://doi.org/10.1002/9781118794203

Knop, K., Hoogenboom, R., Fischer, D., Schubert, U.S., 2010. Poly(ethylene glycol) in Drug Delivery: Pros and Cons as Well as Potential Alternatives. Angew. Chemie Int. Ed.

References

49, 6288–6308. https://doi.org/10.1002/anie.200902672

Kolate, A., Baradia, D., Patil, S., Vhora, I., Kore, G., Misra, A., 2014. PEG — A versatile conjugating ligand for drugs and drug delivery systems. J. Control. Release 192, 67–81. https://doi.org/10.1016/j.jconrel.2014.06.046

Kozyra, A., Mugheirbi, N.A., Paluch, K.J., Garbacz, G., Tajber, L., 2018. Phase Diagrams of Polymer-Dispersed Liquid Crystal Systems of Itraconazole/Component Immiscibility Induced by Molecular Anisotropy. Mol. Pharm. 15, 5192–5206. https://doi.org/10.1021/acs.molpharmaceut.8b00724

Kumar, S., Shen, J., Burgess, D.J., 2014. Nano-amorphous spray dried powder to improve oral bioavailability of itraconazole. J. Control. Release 192, 95–102. https://doi.org/10.1016/j.jconrel.2014.06.059

Kumar, V., Wang, L., Riebe, M., Tung, H.-H., Prud'homme, R.K., 2009. Formulation and Stability of Itraconazole and Odanacatib Nanoparticles: Governing Physical Parameters. Mol. Pharm. 6, 1118–1124. https://doi.org/10.1021/mp900002t

Lai, S.K., O'Hanlon, D.E., Harrold, S., Man, S.T., Wang, Y.-Y., Cone, R., Hanes, J., 2007. Rapid transport of large polymeric nanoparticles in fresh undiluted human mucus. Proc. Natl. Acad. Sci. 104, 1482–1487. https://doi.org/10.1073/pnas.0608611104

Lai, S.K., Wang, Y.Y., Hanes, J., 2009. Mucus-penetrating nanoparticles for drug and gene delivery to mucosal tissues. Adv. Drug Deliv. Rev. 61, 158–171. https://doi.org/10.1016/j.addr.2008.11.002

Laitinen, R., Löbmann, K., Strachan, C.J., Grohganz, H., Rades, T., 2013. Emerging trends in the stabilization of amorphous drugs. Int. J. Pharm. 453, 65–79. https://doi.org/10.1016/j.ijpharm.2012.04.066

Lammert, A.M., Schmidt, S.J., Day, G.A., 1998. Water activity and solubility of trehalose. Food Chem. 61, 139–144. https://doi.org/10.1016/S0308-8146(97)00132-5

Lehto, T., Ezzat, K., Wood, M.J.A., EL Andaloussi, S., 2016. Peptides for nucleic acid delivery. Adv. Drug Deliv. Rev. 106, 172–182. https://doi.org/10.1016/j.addr.2016.06.008

Lele, B.., Hoffman, A.., 2000. Mucoadhesive drug carriers based on complexes of poly(acrylic acid) and PEGylated drugs having hydrolysable PEG–anhydride–drug linkages. J. Control. Release 69, 237–248. https://doi.org/10.1016/S0168-3659(00)00303-5

Lestner, J., Hope, W.W., 2013. Itraconazole: an update on pharmacology and clinical use for treatment of invasive and allergic fungal infections. [Review]. Expert Opin. Drug Metab. Toxicol. 9, 911–926. https://doi.org/10.1517/17425255.2013.794785

Lestner, J.M., Roberts, S.A., Moore, C.B., Howard, S.J., Denning, D.W., Hope, W.W., 2009. Toxicodynamics of itraconazole: implications for therapeutic drug monitoring. Clin. Infect. Dis. 49, 928–930. https://doi.org/10.1086/605499

References

Leuner, C., 2000. Improving drug solubility for oral delivery using solid dispersions. Eur. J. Pharm. Biopharm. 50, 47–60. https://doi.org/10.1016/S0939-6411(00)00076-X

Li, J., Wang, X., Zhang, T., Wang, C., Huang, Z., Luo, X., Deng, Y., 2015. A review on phospholipids and their main applications in drug delivery systems. Asian J. Pharm. Sci. 10, 81–98. https://doi.org/10.1016/j.ajps.2014.09.004

Lide, D.R. (Ed.), 1991. Handbook of Chemistry and Physics, 72nd ed. CRC Press.

Liechty, W. B., Kryscio, D.R., Slaughter, B. V. and Peppas, N.A., 2010. Polymers for drug delivery systems. Annu. Rev. Chem. Biomol. Eng. 1, 149–173. https://doi.org/10.1146/annurev-chembioeng-073009-100847.Polymers

Lieleg, O., Ribbeck, K., 2011. Biological hydrogels as selective diffusion barriers. Trends Cell Biol. 21, 543–551. https://doi.org/10.1016/j.tcb.2011.06.002

Limper, A.H., Adenis, A., Le, T., Harrison, T.S., 2017. Fungal infections in HIV/AIDS. Lancet Infect. Dis. 17, e334–e343. https://doi.org/10.1016/S1473-3099(17)30303-1

Ling, X., Huang, Z., Wang, J., Xie, J., Feng, M., Chen, Y., Abbas, F., Tu, J., Wu, J., Sun, C., 2016. Development of an itraconazole encapsulated polymeric nanoparticle platform for effective antifungal therapy. J. Mater. Chem. B 4, 1787–1796. https://doi.org/10.1039/C5TB02453F

Lipinski, C.A., Lombardo, F., Dominy, B.W., Feeney, P.J., 2012. Experimental and computational approaches to estimate solubility and permeability in drug discovery and development settings. Adv. Drug Deliv. Rev. 64, 4–17. https://doi.org/10.1016/j.addr.2012.09.019

Litsanov, B., Brocker, M., Oldiges, M., Bott, M., 2014. Succinic Acid, in: Bioprocessing of Renewable Resources to Commodity Bioproducts. John Wiley & Sons, Inc., Hoboken, NJ, USA, pp. 435–472. https://doi.org/10.1002/9781118845394.ch16

Loh, Z.H., Samanta, A.K., Sia Heng, P.W., 2015. Overview of milling techniques for improving the solubility of poorly water-soluble drugs. Asian J. Pharm. Sci. 10, 255–274. https://doi.org/10.1016/j.ajps.2014.12.006

Loira-Pastoriza, C., Todoroff, J., Vanbever, R., 2014. Delivery strategies for sustained drug release in the lungs. Adv. Drug Deliv. Rev. 75, 81–91. https://doi.org/10.1016/j.addr.2014.05.017

Maheshwari, C., André, V., Reddy, S., Roy, L., Duarte, T., Rodríguez-Hornedo, N., 2012. Tailoring aqueous solubility of a highly soluble compound via cocrystallization: effect of coformer ionization, pHmax and solute–solvent interactions. CrystEngComm 14, 4801. https://doi.org/10.1039/c2ce06615g

Maisel, K., Ensign, L., Reddy, M., Cone, R., Hanes, J., 2015. Effect of surface chemistry on nanoparticle interaction with gastrointestinal mucus and distribution in the gastrointestinal tract following oral and rectal administration in the mouse. J. Control.

Release 197, 48–57. https://doi.org/10.1016/j.jconrel.2014.10.026

Maisel, K., Reddy, M., Xu, Q., Chattopadhyay, S., Cone, R., Ensign, L.M., Hanes, J., 2016. Nanoparticles coated with high molecular weight PEG penetrate mucus and provide uniform vaginal and colorectal distribution in vivo. Nanomedicine 11, 1337–1343. https://doi.org/10.2217/nnm-2016-0047

Malamatari, M., Ross, S.A., Douroumis, D., Velaga, S.P., 2017. Experimental cocrystal screening and solution based scale-up cocrystallization methods. Adv. Drug Deliv. Rev. 117, 162–177. https://doi.org/10.1016/j.addr.2017.08.006

Malpani, V., Ganeshpure, P.A., Munshi, P., 2011. Determination of Solubility Parameters for the p -Xylene Oxidation Products. Ind. Eng. Chem. Res. 50, 2467–2472. https://doi.org/10.1021/ie101623c

Mansuri, S., Kesharwani, P., Jain, K., Tekade, R.K., Jain, N.K., 2016. Mucoadhesion: A promising approach in drug delivery system. React. Funct. Polym. 100, 151–172. https://doi.org/10.1016/j.reactfunctpolym.2016.01.011

Marr, K.A., Crippa, F., Leisenring, W., Hoyle, M., Boeckh, M., Balajee, S.A., Nichols, W.G., Musher, B., Corey, L., 2004. Itraconazole versus fluconazole for prevention of fungal infections in patients receiving allogeneic stem cell transplants. Blood 103, 1527–1533. https://doi.org/10.1182/blood-2003-08-2644

Marsac, P.J., Li, T., Taylor, L.S., 2009. Estimation of Drug–Polymer Miscibility and Solubility in Amorphous Solid Dispersions Using Experimentally Determined Interaction Parameters. Pharm. Res. 26, 139–151. https://doi.org/10.1007/s11095-008-9721-1

Matteucci, M.E., Hotze, M.A., Johnston, K.P., Williams, R.O., 2006. Drug Nanoparticles by Antisolvent Precipitation: Mixing Energy versus Surfactant Stabilization. Langmuir 22, 8951–8959. https://doi.org/10.1021/la061122t

McClurg, R.B., 2016. Taxonomy of Cocrystal Ternary Phase Diagrams. J. Chem. Eng. Data 61, 4313–4320. https://doi.org/10.1021/acs.jced.6b00791

McComiskey, K.P.M., Mugheirbi, N.A., Stapleton, J., Tajber, L., 2018. In situ monitoring of nanoparticle formation: Antisolvent precipitation of azole anti-fungal drugs. Int. J. Pharm. 543, 201–213. https://doi.org/10.1016/j.ijpharm.2018.03.054

McKee, J., Rabinow, B., Cook, C., Gass, J., 2010. Nanosuspension Formulation of Itraconazole Eliminates the Negative Inotropic Effect of SPORANOX® in Dogs. J. Med. Toxicol. 6, 331–336. https://doi.org/10.1007/s13181-010-0025-6

McKinsey, D.S., Wheat, L.J., Cloud, G.A., Pierce, M., Black, J.R., Bamberger, D.M., Goldman, M., Thomas, C.J., Gutsch, H.M., Moskovitz, B., Dismukes, W.E., Kauffman, C.A., Allergy, the N.I. of, 1999. Itraconazole Prophylaxis for Fungal Infections in Patients with Advanced Human Immunodeficiency Virus Infection: Randomized, Placebo-Controlled, Double-Blind Study. Clin. Infect. Dis. 28, 1049–1056. https://doi.org/10.1086/514744

References

Mellors, J.W., Rinaldo, C.R., Gupta, P., White, R.M., Todd, J.A., Kingsley, L.A., 1996. Prognosis in HIV-1 Infection Predicted by the Quantity of Virus in Plasma. Science (80-.). 272, 1167–1170. https://doi.org/10.1126/science.272.5265.1167

Merisko-Liversidge, E., Liversidge, G.G., 2011. Nanosizing for oral and parenteral drug delivery: A perspective on formulating poorly-water soluble compounds using wet media milling technology. Adv. Drug Deliv. Rev. 63, 427–440. https://doi.org/10.1016/j.addr.2010.12.007

Merlos, R., Wauthoz, N., Levet, V., Belhassan, L., Sebti, T., Vanderbist, F., Amighi, K., 2017. Optimization and scaling-up of ITZ-based dry powders for inhalation. J. Drug Deliv. Sci. Technol. 37, 147–157. https://doi.org/10.1016/j.jddst.2016.12.009

Mersmann, A., 1999. Crystallization and precipitation. Chem. Eng. Process. Process Intensif. 38, 345–353. https://doi.org/10.1016/S0255-2701(99)00025-2

Miroshnyk, I., Mirza, S., Sandler, N., 2009. Pharmaceutical co-crystals-an opportunity for drug product enhancement. Expert Opin. Drug Deliv. 6, 333–341. https://doi.org/10.1517/17425240902828304

Mirza, M.A., Panda, A.K., Asif, S., Verma, D., Talegaonkar, S., Manzoor, N., Khan, A., Ahmed, F.J., Dudeja, M., Iqbal, Z., 2016. A vaginal drug delivery model. Drug Deliv. 23, 3123–3134. https://doi.org/10.3109/10717544.2016.1153749

Moazeni, E., Gilani, K., Najafabadi, A.R., Reza Rouini, M., Mohajel, N., Amini, M., Barghi, M.A., 2012. Preparation and evaluation of inhalable itraconazole chitosan based polymeric micelles. DARU, J. Pharm. Sci. 20, 1–9. https://doi.org/10.1186/2008-2231-20-85

Moghimi, S.M., Hunter, A.C., Murray, J.C., 2001. Long-circulating and target-specific nanoparticles: theory to practice. Pharmacol. Rev. 53, 283–318.

Mohammad, M.A., Alhalaweh, A., Velaga, S.P., 2011. Hansen solubility parameter as a tool to predict cocrystal formation. Int. J. Pharm. 407, 63–71. https://doi.org/10.1016/j.ijpharm.2011.01.030

Mouton, J.W., van Peer, A., de Beule, K., Van Vliet, A., Donnelly, J.P., Soons, P.A., 2006. Pharmacokinetics of Itraconazole and Hydroxyitraconazole in Healthy Subjects after Single and Multiple Doses of a Novel Formulation. Antimicrob. Agents Chemother. 50, 4096–4102. https://doi.org/10.1128/AAC.00630-06

Mueller, C., Capelle, M.A.H., Arvinte, T., Seyrek, E., Borchard, G., 2011. Tryptophan-mPEGs: Novel excipients that stabilize salmon calcitonin against aggregation by non-covalent PEGylation. Eur. J. Pharm. Biopharm. 79, 646–657. https://doi.org/10.1016/j.ejpb.2011.06.003

Mugheirbi, N.A., Paluch, K.J., Tajber, L., 2014. Heat induced evaporative antisolvent nanoprecipitation (HIEAN) of itraconazole. Int. J. Pharm. 471, 400–411. https://doi.org/10.1016/j.ijpharm.2014.05.045

References

Mugheirbi, N.A., Tajber, L., 2015. Crystal Habits of Itraconazole Microcrystals: Unusual Isomorphic Intergrowths Induced via Tuning Recrystallization Conditions. Mol. Pharm. 12, 3468–3478. https://doi.org/10.1021/acs.molpharmaceut.5b00480

Mugheirbi, N.A., Tajber, L., 2015. Mesophase and size manipulation of itraconazole liquid crystalline nanoparticles produced via quasi nanoemulsion precipitation. Eur. J. Pharm. Biopharm. 96, 226–236. https://doi.org/10.1016/j.ejpb.2015.08.005

Müller, R.H., Gohla, S., Keck, C.M., 2011. State of the art of nanocrystals – Special features, production, nanotoxicology aspects and intracellular delivery. Eur. J. Pharm. Biopharm. 78, 1–9. https://doi.org/10.1016/j.ejpb.2011.01.007

Mullin, J., 2001. Crystallization, 4th ed. Butterworth-Heinemann.

Munoz, P., Rodriguez, C., Bouza, E., Palomo, J., Yanez, J.F., Dominguez, M.J., Desco, M., 2004. Risk Factors of Invasive Aspergillosis after Heart Transplantation: Protective Role of Oral Itraconazole Prophylaxis. Am. J. Transplant. 4, 636–643. https://doi.org/10.1111/j.1600-6143.2004.00390.x

Murgia, X., Loretz, B., Hartwig, O., Hittinger, M., Lehr, C.-M., 2018. The role of mucus on drug transport and its potential to affect therapeutic outcomes. Adv. Drug Deliv. Rev. 124, 82–97. https://doi.org/10.1016/j.addr.2017.10.009

Murnane, D., Marriott, C., Martin, G.P., 2008. Developing an environmentally benign process for the production of microparticles: Amphiphilic crystallization. Eur. J. Pharm. Biopharm. 69, 72–82. https://doi.org/10.1016/j.ejpb.2007.10.014

Musumeci, D., Hunter, C. a., Prohens, R., Scuderi, S., McCabe, J.F., 2011. Virtual cocrystal screening. Chem. Sci. 2, 883. https://doi.org/10.1039/C0SC00555J

Nagy, Z.K., Fujiwara, M., Braatz, R.D., 2008. Modelling and control of combined cooling and antisolvent crystallization processes. J. Process Control 18, 856–864. https://doi.org/10.1016/j.jprocont.2008.06.002

Netsomboon, K., Bernkop-Schnürch, A., 2016. Mucoadhesive vs. mucopenetrating particulate drug delivery. Eur. J. Pharm. Biopharm. 98, 76–89. https://doi.org/10.1016/j.ejpb.2015.11.003

Newby, J.M., Seim, I., Lysy, M., Ling, Y., Huckaby, J., Lai, S.K., Forest, M.G., 2018. Technological strategies to estimate and control diffusive passage times through the mucus barrier in mucosal drug delivery. Adv. Drug Deliv. Rev. 124, 64–81. https://doi.org/10.1016/j.addr.2017.12.002

Newman, S., 2014. Improving inhaler technique, adherence to therapy and the precision of dosing: major challenges for pulmonary drug delivery. Expert Opin. Drug Deliv. 11, 365–378. https://doi.org/10.1517/17425247.2014.873402

Newman, S.P., 2018. Delivering drugs to the lungs: The history of repurposing in the treatment of respiratory diseases. Adv. Drug Deliv. Rev. 133, 5–18. https://doi.org/10.1016/j.addr.2018.04.010

References

Nonappa, Lahtinen, M., Kolehmainen, E., Haarala, J., Shevchenko, A., 2013. Evidence of Weak Halogen Bonding: New Insights on Itraconazole and its Succinic Acid Cocrystal. Cryst. Growth Des. 13, 346–351. https://doi.org/10.1021/cg3015282

Norman, A.I., Ho, D.L., Greer, S.C., 2007. Partitioning, fractionation, and conformations of star polyethylene glycol in isobutyric acid and water. Macromolecules 40, 9628–9639. https://doi.org/10.1021/ma071568w

Noyes, A.A., Whitney, W.R., 1897. THE RATE OF SOLUTION OF SOLID SUBSTANCES IN THEIR OWN SOLUTIONS. J. Am. Chem. Soc. 19, 930–934. https://doi.org/10.1021/ja02086a003

Ober, C.A., Gupta, R.B., 2012. Formation of Itraconazole–Succinic Acid Cocrystals by Gas Antisolvent Cocrystallization. AAPS PharmSciTech 13, 1396–1406. https://doi.org/10.1208/s12249-012-9866-4

Ober, C.A., Montgomery, S.E., Gupta, R.B., 2013. Formation of itraconazole/L-malic acid cocrystals by gas antisolvent cocrystallization. Powder Technol. 236, 122–131. https://doi.org/10.1016/j.powtec.2012.04.058

Ógáin, O.N., Li, J., Tajber, L., Corrigan, O.I., Healy, A.M., 2011. Particle engineering of materials for oral inhalation by dry powder inhalers. I—Particles of sugar excipients (trehalose and raffinose) for protein delivery. Int. J. Pharm. 405, 23–35. https://doi.org/10.1016/j.ijpharm.2010.11.039

Oh, S., Wilcox, M., Pearson, J.P., Borrós, S., 2015. Optimal design for studying mucoadhesive polymers interaction with gastric mucin using a quartz crystal microbalance with dissipation (QCM-D): Comparison of two different mucin origins. Eur. J. Pharm. Biopharm. 96, 477–483. https://doi.org/10.1016/j.ejpb.2015.08.002

Onoue, S., Yamada, S., Chan, K., 2014. Nanodrugs: pharmacokinetics and safety. Int. J. Nanomedicine 9, 1025. https://doi.org/10.2147/IJN.S38378

Padrela, L., Rodrigues, M.A., Duarte, A., Dias, A.M.A., Braga, M.E.M., de Sousa, H.C., 2018. Supercritical carbon dioxide-based technologies for the production of drug nanoparticles/nanocrystals – A comprehensive review. Adv. Drug Deliv. Rev. 131, 22–78. https://doi.org/10.1016/j.addr.2018.07.010

Paluch, K.J., Tajber, L., McCabe, T., O'Brien, J.E., Corrigan, O.I., Healy, A.M., 2010. Preparation and solid state characterisation of chlorothiazide sodium intermolecular self-assembly suprastructure. Eur. J. Pharm. Sci. 41, 603–611. https://doi.org/10.1016/j.ejps.2010.08.013

Papadopoulou, V., Valsami, G., Dokoumetzidis, A., Macheras, P., 2008. Biopharmaceutics classification systems for new molecular entities (BCS-NMEs) and marketed drugs (BCS-MD): Theoretical basis and practical examples. Int. J. Pharm. 361, 70–77. https://doi.org/10.1016/j.ijpharm.2008.05.021

Papagianni, M., 2007. Advances in citric acid fermentation by Aspergillus niger: Biochemical

aspects, membrane transport and modeling. Biotechnol. Adv. 25, 244–263. https://doi.org/10.1016/J.BIOTECHADV.2007.01.002

Paranjpe, M., Müller-Goymann, C.C., 2014. Nanoparticle-mediated pulmonary drug delivery: A review. Int. J. Mol. Sci. 15, 5852–5873. https://doi.org/10.3390/ijms15045852

Pardeike, J., Weber, S., Haber, T., Wagner, J., Zarfl, H.P., Plank, H., Zimmer, A., 2011. Development of an Itraconazole-loaded nanostructured lipid carrier (NLC) formulation for pulmonary application. Int. J. Pharm. 419, 329–338. https://doi.org/10.1016/j.ijpharm.2011.07.040

Pardeike, J., Weber, S., Zarfl, H.P., Pagitz, M., Zimmer, A., 2016. Itraconazole-loaded nanostructured lipid carriers (NLC) for pulmonary treatment of aspergillosis in falcons. Eur. J. Pharm. Biopharm. 108, 269–276. https://doi.org/10.1016/j.ejpb.2016.07.018

Park, C.-M., Sheehan, R.J., 2000. Phthalic Acids and Other Benzenepolycarboxylic Acids, in: Kirk-Othmer Encyclopedia of Chemical Technology. John Wiley & Sons, Inc., Hoboken, NJ, USA. https://doi.org/10.1002/0471238961.1608200816011811.a01

Park, C.-W., Kim, J.-Y., Rhee, Y.-S., Oh, T.-O., Ha, J.-M., Choi, N.-Y., Chi, S.-C., Park, E.-S., 2012a. Preparation and valuation of a topical solution containing eutectic mixture of itraconazole and phenol. Arch. Pharm. Res. 35, 1935–1943. https://doi.org/10.1007/s12272-012-1110-y

Park, C.-W., Mansour, H.M., Oh, T.-O., Kim, J.-Y., Ha, J.-M., Lee, B.-J., Chi, S.-C., Rhee, Y.-S., Park, E.-S., 2012b. Phase behavior of itraconazole–phenol mixtures and its pharmaceutical applications. Int. J. Pharm. 436, 652–658. https://doi.org/10.1016/j.ijpharm.2012.07.054

Partenhauser, A., Bernkop-Schnürch, A., 2016. Mucoadhesive polymers in the treatment of dry X syndrome. Drug Discov. Today 21, 1051–1062. https://doi.org/10.1016/j.drudis.2016.02.013

Parveen, S., Misra, R., Sahoo, S.K., 2012. Nanoparticles: a boon to drug delivery, therapeutics, diagnostics and imaging. Nanomedicine 8, 147–66. https://doi.org/10.1016/j.nano.2011.05.016

Patil, S., Ujalambkar, V., Mahadik, A., 2017. Electrospray technology as a probe for cocrystal synthesis: Influence of solvent and coformer structure. J. Drug Deliv. Sci. Technol. 39, 217–222. https://doi.org/10.1016/j.jddst.2017.04.001

Patton, J.S., 2005. Unlocking the opportunity of tight glycaemic control. Innovative delivery of insulin via the lung. Diabetes, Obes. Metab. 7, S5–S8. https://doi.org/10.1111/j.1463-1326.2005.00530.x

Pawar, V.K., Singh, Y., Meher, J.G., Gupta, S., Chourasia, M.K., 2014. Engineered nanocrystal technology: In-vivo fate, targeting and applications in drug delivery. J. Control. Release 183, 51–66. https://doi.org/10.1016/j.jconrel.2014.03.030

References

Pearce, E.M., 1978. Kirk-Othmer encyclopedia of chemical technology, 3rd ed., Vol. I, Wiley-Interscience, New York, 1978. J. Polym. Sci. Polym. Lett. Ed. 16, 248–248. https://doi.org/10.1002/pol.1978.130160508

Peña, M.A., Reíllo, A., Escalera, B., Bustamante, P., 2006. Solubility parameter of drugs for predicting the solubility profile type within a wide polarity range in solvent mixtures. Int. J. Pharm. 321, 155–161. https://doi.org/10.1016/j.ijpharm.2006.05.014

Peppas, N.A., Huang, Y., 2004. Nanoscale technology of mucoadhesive interactions. Adv. Drug Deliv. Rev. 56, 1675–1687. https://doi.org/10.1016/j.addr.2004.03.001

Peppas, N.A., Sahlin, J.J., 1996. Hydrogels as mucoadhesive and bioadhesive materials: a review. Biomaterials 17, 1553–1561. https://doi.org/10.1016/0142-9612(95)00307-X

Pinto Reis, C., Neufeld, R.J., Ribeiro, A.J., Veiga, F., 2006. Nanoencapsulation I. Methods for preparation of drug-loaded polymeric nanoparticles. Nanomedicine Nanotechnology, Biol. Med. 2, 8–21. https://doi.org/10.1016/j.nano.2005.12.003

Ponchel, G., Touchard, F., Duchêne, D., Peppas, N.A., 1987. Bioadhesive analysis of controlled-release systems. I. Fracture and interpenetration analysis in poly(acrylic acid)-containing systems. J. Control. Release 5, 129–141. https://doi.org/10.1016/0168-3659(87)90004-6

Prozorov, T., Prozorov, R., Suslick, K.S., 2004. High Velocity Interparticle Collisions Driven by Ultrasound. J. Am. Chem. Soc. 126, 13890–13891. https://doi.org/10.1021/ja049493o

Qiao, N., Li, M., Schlindwein, W., Malek, N., Davies, A., Trappitt, G., 2011. Pharmaceutical cocrystals: An overview. Int. J. Pharm. 419, 1–11. https://doi.org/10.1016/j.ijpharm.2011.07.037

Rabanel, J.-M., Hildgen, P., Banquy, X., 2014. Assessment of PEG on polymeric particles surface, a key step in drug carrier translation. J. Control. Release 185, 71–87. https://doi.org/10.1016/j.jconrel.2014.04.017

Rabinow, B.E., 2004. Nanosuspensions in drug delivery. Nat. Rev. Drug Discov. 3, 785–796. https://doi.org/10.1038/nrd1494

Rajasingham, R., Smith, R.M., Park, B.J., Jarvis, J.N., Govender, N.P., Chiller, T.M., Denning, D.W., Loyse, A., Boulware, D.R., 2017. Global burden of disease of HIV-associated cryptococcal meningitis: an updated analysis. Lancet Infect. Dis. 17, 873–881. https://doi.org/10.1016/S1473-3099(17)30243-8

Ranjan, S., Devarapalli, R., Kundu, S., Vangala, V.R., Ghosh, A., Reddy, C.M., 2017. Three new hydrochlorothiazide cocrystals: Structural analyses and solubility studies. J. Mol. Struct. 1133, 405–410. https://doi.org/10.1016/j.molstruc.2016.12.019

Remenar, J.F., Morissette, S.L., Peterson, M.L., Moulton, B., MacPhee, J.M., Guzmán,

References

H.R., Almarsson, Ö., 2003. Crystal engineering of novel cocrystals of a triazole drug with 1,4-dicarboxylic acids. J. Am. Chem. Soc. 125, 8456–8457. https://doi.org/10.1021/ja035776p

Rex, J.H., Pfaller, M.A., Galgiani, J.N., Bartlett, M.S., Espinel-Ingroff, A., Ghannoum, M.A., Lancaster, M., Odds, F.C., Rinaldi, M.G., Walsh, T.J., Barry, A.L., 1997. Development of Interpretive Breakpoints for Antifungal Susceptibility Testing: Conceptual Framework and Analysis of In Vitro-In Vivo Correlation Data for Fluconazole, Itraconazole, and Candida Infections. Clin. Infect. Dis. 24, 235–247. https://doi.org/10.1093/clinids/24.2.235

Richardson, M., Lass-Flörl, C., 2008. Changing epidemiology of systemic fungal infections. Clin. Microbiol. Infect. 14, 5–24. https://doi.org/10.1111/j.1469-0691.2008.01978.x

Rodahl, M., Kasemo, B., 1995. On The Measurement Of Thin Liquid Overlayers With The Quartz-crystal Microbalance, in: Proceedings of the International Solid-State Sensors and Actuators Conference - TRANSDUCERS '95. IEEE, pp. 743–746. https://doi.org/10.1109/SENSOR.1995.721939

Rowe, R., Sheskey, P., Cook, W., Quinn, M. (Eds.), 2012. Handbook of Pharmaceutical Excipients, 7th ed. Pharmaceutical Press, London.

Saag, M.S., Dismukes, W.E., 1988. Azole antifungal agents: emphasis on new triazoles. Antimicrob. Agents Chemother. 32, 1–8. https://doi.org/10.1128/AAC.32.1.1

Sanchez, A., Larsen, R., 2007. Fungal infections in solid organ transplantation. Curr. Opin. Organ Transplant. 12, 579–584. https://doi.org/10.1097/MOT.0b013e3282f1fc12

Sander, J.R.G., Bučar, D.-K., Henry, R.F., Zhang, G.G.Z., MacGillivray, L.R., 2010. Pharmaceutical Nano-Cocrystals: Sonochemical Synthesis by Solvent Selection and Use of a Surfactant. Angew. Chemie Int. Ed. 49, 7284–7288. https://doi.org/10.1002/anie.201002588

Sander, J.R.G., Zeiger, B.W., Suslick, K.S., 2014. Sonocrystallization and sonofragmentation. Ultrason. Sonochem. 21, 1908–1915. https://doi.org/10.1016/j.ultsonch.2014.02.005

Sauerbrey, G., 1959. Verwendung von Schwingquarzen zur Wägung dünner Schichten und zur Mikrowägung. Zeitschrift für Phys. 155, 206–222. https://doi.org/10.1007/BF01337937

Schafroth, N., Arpagaus, C., Jadhav, U.Y., Makne, S., Douroumis, D., 2012. Nano and microparticle engineering of water insoluble drugs using a novel spray-drying process. Colloids Surfaces B Biointerfaces 90, 8–15. https://doi.org/10.1016/j.colsurfb.2011.09.038

Schultheiss, N., Newman, A., 2009. Pharmaceutical Cocrystals and Their Physicochemical Properties. Cryst. Growth Des. 9, 2950–2967. https://doi.org/10.1021/cg900129f

Scorzoni, L., de Paula e Silva, A.C.A., Marcos, C.M., Assato, P.A., de Melo, W.C.M.A., de

References

Oliveira, H.C., Costa-Orlandi, C.B., Mendes-Giannini, M.J.S., Fusco-Almeida, A.M., 2017. Antifungal Therapy: New Advances in the Understanding and Treatment of Mycosis. Front. Microbiol. 08, 1–23. https://doi.org/10.3389/fmicb.2017.00036

Serra, L., Doménech, J., Peppas, N.A., 2009. Engineering design and molecular dynamics of mucoadhesive drug delivery systems as targeting agents. Eur. J. Pharm. Biopharm. 71, 519–528. https://doi.org/10.1016/j.ejpb.2008.09.022

Shah, D.A., Murdande, S.B., Dave, R.H., 2016. A Review: Pharmaceutical and Pharmacokinetic Aspect of Nanocrystalline Suspensions. J. Pharm. Sci. 105, 10–24. https://doi.org/10.1002/jps.24694

Shaikh, R., Singh, R., Walker, G.M., Croker, D.M., 2018. Pharmaceutical Cocrystal Drug Products: An Outlook on Product Development. Trends Pharmacol. Sci. 39, 1033–1048. https://doi.org/10.1016/j.tips.2018.10.006

Shalaev, E., Wu, K., Shamblin, S., Krzyzaniak, J.F., Descamps, M., 2016. Crystalline mesophases: Structure, mobility, and pharmaceutical properties. Adv. Drug Deliv. Rev. 100, 194–211. https://doi.org/10.1016/j.addr.2016.04.002

Shan, N., Toda, F., Jones, W., 2002. Mechanochemistry and co-crystal formation: effect of solvent on reaction kinetics. Chem. Commun. 1, 2372–2373. https://doi.org/10.1039/b207369m

Shete, A., Murthy, S., Korpale, S., Yadav, A., Sajane, S., Sakhare, S., Doijad, R., 2015. Cocrystals of itraconazole with amino acids: Screening, synthesis, solid state characterization, in vitro drug release and antifungal activity. J. Drug Deliv. Sci. Technol. 28, 46–55. https://doi.org/10.1016/j.jddst.2015.05.006

Shevchenko, A., Bimbo, L.M., Miroshnyk, I., Haarala, J., Jelínková, K., Syrjänen, K., van Veen, B., Kiesvaara, J., Santos, H.A., Yliruusi, J., 2012. A new cocrystal and salts of itraconazole: Comparison of solid-state properties, stability and dissolution behavior. Int. J. Pharm. 436, 403–409. https://doi.org/10.1016/j.ijpharm.2012.06.045

Shevchenko, A., Miroshnyk, I., Pietilä, L.-O., Haarala, J., Salmia, J., Sinervo, K., Mirza, S., van Veen, B., Kolehmainen, E., Nonappa, Yliruusi, J., 2013. Diversity in Itraconazole Cocrystals with Aliphatic Dicarboxylic Acids of Varying Chain Length. Cryst. Growth Des. 13, 4877–4884. https://doi.org/10.1021/cg401061t

Sigurdsson, H.H., Kirch, J., Lehr, C.-M., 2013. Mucus as a barrier to lipophilic drugs. Int. J. Pharm. 453, 56–64. https://doi.org/10.1016/j.ijpharm.2013.05.040

Simon, A., Amaro, M.I., Cabral, L.M., Healy, A.M., de Sousa, V.P., 2016. Development of a novel dry powder inhalation formulation for the delivery of rivastigmine hydrogen tartrate. Int. J. Pharm. 501, 124–138. https://doi.org/10.1016/j.ijpharm.2016.01.066

Sinha, B., Müller, R.H., Möschwitzer, J.P., 2013. Bottom-up approaches for preparing drug nanocrystals: Formulations and factors affecting particle size. Int. J. Pharm. 453, 126–141. https://doi.org/10.1016/j.ijpharm.2013.01.019

References

Slain, D., Rogers, P.D., Cleary, J.D., Chapman, S.W., 2001. Intravenous itraconazole. Ann. Pharmacother. 35, 720–729.

Smart, J., 2005. The basics and underlying mechanisms of mucoadhesion. Adv. Drug Deliv. Rev. 57, 1556–1568. https://doi.org/10.1016/j.addr.2005.07.001

Sosnik, A., das Neves, J., Sarmento, B., 2014. Mucoadhesive polymers in the design of nano-drug delivery systems for administration by non-parenteral routes: A review. Prog. Polym. Sci. 39, 2030–2075. https://doi.org/10.1016/j.progpolymsci.2014.07.010

Sosnowski, T.R., 2015. Nanosized and Nanostructured Particles in Pulmonary Drug Delivery. J. Nanosci. Nanotechnol. 15, 3476–3487. https://doi.org/10.1166/jnn.2015.9863

Speight, D.J.G., 2017. Lange's Handbook of Chemistry, Seventeenth Edition, 17th editi. ed. McGraw-Hill Education, New York.

Spitzer, D., Risse, B., Schnell, F., Pichot, V., Klaumünzer, M., Schaefer, M.R., 2015. Continuous engineering of nano-cocrystals for medical and energetic applications. Sci. Rep. 4, 6575. https://doi.org/10.1038/srep06575

Sriamornsak, P., Burapapadh, K., 2015. Characterization of recrystallized itraconazole prepared by cooling and anti-solvent crystallization. Asian J. Pharm. Sci. 10, 230–238. https://doi.org/10.1016/j.ajps.2015.01.003

Stevens, D. a, 1999. Itraconazole in Cyclodextrin Solution. Pharmacotherapy 19, 603–611. https://doi.org/10.1592/phco.19.8.603.31529

Stoler, E., Warner, J., 2015. Non-Covalent Derivatives: Cocrystals and Eutectics. Molecules 20, 14833–14848. https://doi.org/10.3390/molecules200814833

Suk, J.S., Xu, Q., Kim, N., Hanes, J., Ensign, L.M., 2016. PEGylation as a strategy for improving nanoparticle-based drug and gene delivery. Adv. Drug Deliv. Rev. 99, 28–51. https://doi.org/10.1016/j.addr.2015.09.012

Suksiriworapong, J., Mingkwan, T., Chantasart, D., 2017. Enhanced transmucosal delivery of itraconazole by thiolated d -α-tocopheryl poly(ethylene glycol) 1000 succinate micelles for the treatment of Candida albicans. Eur. J. Pharm. Biopharm. 120, 107–115. https://doi.org/10.1016/j.ejpb.2017.08.012

Svensson, O., Arnebrant, T., 2010. Mucin layers and multilayers — Physicochemical properties and applications. Curr. Opin. Colloid Interface Sci. 15, 395–405. https://doi.org/10.1016/j.cocis.2010.05.015

Teli, M.K., Mutalik, S., Rajanikant, G.K., 2010. Nanotechnology and nanomedicine: going small means aiming big. Curr. Pharm. Des. 16, 1882–92.

Teófilo, R.F., Ferreira, M.M.C., 2006. Quimiometria II: planilhas eletrônicas para cálculos de planejamentos experimentais, um tutorial. Quim. Nova 29, 338–350. https://doi.org/10.1590/S0100-40422006000200026

References

Tewes, F., Paluch, K.J., Tajber, L., Gulati, K., Kalantri, D., Ehrhardt, C., Healy, A.M., 2013. Steroid/mucokinetic hybrid nanoporous microparticles for pulmonary drug delivery. Eur. J. Pharm. Biopharm. 85, 604–613. https://doi.org/10.1016/j.ejpb.2013.03.020

Thakkar, H.P., Khunt, A., Dhande, R.D., Patel, A.A., 2015. Formulation and evaluation of Itraconazole nanoemulsion for enhanced oral bioavailability. J. Microencapsul. 32, 559–569. https://doi.org/10.3109/02652048.2015.1065917

Thakuria, R., Delori, A., Jones, W., Lipert, M.P., Roy, L., Rodríguez-Hornedo, N., 2013. Pharmaceutical cocrystals and poorly soluble drugs. Int. J. Pharm. 453, 101–125. https://doi.org/10.1016/j.ijpharm.2012.10.043

The Merck Index, 2013. . The Royal Society of Chemistry.

Thiry, J., Lebrun, P., Vinassa, C., Adam, M., Netchacovitch, L., Ziemons, E., Hubert, P., Krier, F., Evrard, B., 2016. Continuous production of itraconazole-based solid dispersions by hot melt extrusion: Preformulation, optimization and design space determination. Int. J. Pharm. 515, 114–124. https://doi.org/10.1016/j.ijpharm.2016.10.003

Thorat, A.A., Dalvi, S. V., 2012. Liquid antisolvent precipitation and stabilization of nanoparticles of poorly water soluble drugs in aqueous suspensions: Recent developments and future perspective. Chem. Eng. J. 181–182, 1–34. https://doi.org/10.1016/j.cej.2011.12.044

Tolman, J.A., Williams, R.O., 2010. Advances in the pulmonary delivery of poorly water-soluble drugs: influence of solubilization on pharmacokinetic properties. Drug Dev. Ind. Pharm. 36, 1–30. https://doi.org/10.3109/03639040903092319

Trask, A. V, Motherwell, W.D.S., Jones, W., 2004. Solvent-drop grinding: green polymorph control of cocrystallisationElectronic supplementary information (ESI) available: additional powder XRD patterns. See http://www.rsc.org/suppdata/cc/b4/b400978a/. Chem. Commun. 890. https://doi.org/10.1039/b400978a

Trask, A. V., 2007. An Overview of Pharmaceutical Cocrystals as Intellectual Property †. Mol. Pharm. 4, 301–309. https://doi.org/10.1021/mp070001z

Tsapis, N., Bennett, D., Jackson, B., Weitz, D.A., Edwards, D.A., 2002. Trojan particles: Large porous carriers of nanoparticles for drug delivery. Proc. Natl. Acad. Sci. 99, 12001–12005. https://doi.org/10.1073/pnas.182233999

Tucker, R.M., Denning, D.W., Arathoon, E.G., Rinaldi, M.G., Stevens, D.A., 1990. Itraconazole therapy for nonmeningeal coccidioidomycosis: Clinical and laboratory observations. J. Am. Acad. Dermatol. 23, 593–601. https://doi.org/10.1016/0190-9622(90)70261-F

Tung, H., 2013. Industrial Perspectives of Pharmaceutical Crystallization. Org. Process Res. Dev. 17, 445–454. https://doi.org/10.1021/op3002323

References

Tyner, T., Francis, J., 2018. Oxalic Acid Dihydrate, in: ACS Reagent Chemicals. American Chemical Society, Washington, DC. https://doi.org/10.1021/acsreagents.4251.20160601

Unaids, 2018. Fact sheet - Worl Aids day 2018 [WWW Document]. URL http://www.unaids.org/sites/default/files/media_asset/UNAIDS_FactSheet_en.pdf (accessed 2.26.19).

Van Eerdenbrugh, B., Froyen, L., Van Humbeeck, J., Martens, J.A., Augustijns, P., Van den Mooter, G., 2008a. Drying of crystalline drug nanosuspensions-The importance of surface hydrophobicity on dissolution behavior upon redispersion. Eur. J. Pharm. Sci. 35, 127–135. https://doi.org/10.1016/j.ejps.2008.06.009

Van Eerdenbrugh, B., Van den Mooter, G., Augustijns, P., 2008. Top-down production of drug nanocrystals: Nanosuspension stabilization, miniaturization and transformation into solid products. Int. J. Pharm. 364, 64–75. https://doi.org/10.1016/j.ijpharm.2008.07.023

Vanić, Ž., Škalko-Basnet, N., 2013. Nanopharmaceuticals for improved topical vaginal therapy: Can they deliver? Eur. J. Pharm. Sci. 50, 29–41. https://doi.org/10.1016/j.ejps.2013.04.035

Vekilov, P.G., 2010. The two-step mechanism of nucleation of crystals in solution. Nanoscale 2, 2346. https://doi.org/10.1039/c0nr00628a

Velaga, S.P., Djuris, J., Cvijic, S., Rozou, S., Russo, P., Colombo, G., Rossi, A., 2018. Dry powder inhalers: An overview of the in vitro dissolution methodologies and their correlation with the biopharmaceutical aspects of the drug products. Eur. J. Pharm. Sci. 113, 18–28. https://doi.org/10.1016/j.ejps.2017.09.002

Venkatesan, P., Perfect, J.R., Myers, S.A., 2005. Evaluation and management of Fungal infections in Immunocompromised patients. Dermatol. Ther. 18, 44–57. https://doi.org/10.1111/j.1529-8019.2005.05001.x

Verma, S., Gokhale, R., Burgess, D.J., 2009. A comparative study of top-down and bottom-up approaches for the preparation of micro/nanosuspensions. Int. J. Pharm. 380, 216–222. https://doi.org/10.1016/j.ijpharm.2009.07.005

Voinova, M. V., Rodahl, M., Jonson, M., Kasemo, B., 1999. Viscoelastic Acoustic Response of Layered Polymer Films at Fluid-Solid Interfaces: Continuum Mechanics Approach. Phys. Scr. 59, 391–396. https://doi.org/10.1238/Physica.Regular.059a00391

Vojta, D., Vrankić, M., Bertmer, M., Schaumann, G.E., 2016. Dehydration of α-oxalic acid dihydrate: Structural, spectroscopic and thermal study with implications on the disruption of water molecular bridges in soil organic matter. Thermochim. Acta 643, 73–82. https://doi.org/10.1016/J.TCA.2016.09.019

Wang, Y., Zheng, Y., Zhang, L., Wang, Q., Zhang, D., 2013. Stability of nanosuspensions in drug delivery. J. Control. Release 172, 1126–1141.

References

https://doi.org/10.1016/j.jconrel.2013.08.006

Wang, Y.-Y., Lai, S.K., Suk, J.S., Pace, A., Cone, R., Hanes, J., 2008. Addressing the PEG Mucoadhesivity Paradox to Engineer Nanoparticles that "Slip" through the Human Mucus Barrier. Angew. Chemie Int. Ed. 47, 9726–9729. https://doi.org/10.1002/anie.200803526

Wauthoz, N., Amighi, K., 2014. Phospholipids in pulmonary drug delivery. Eur. J. Lipid Sci. Technol. 116, 1114–1128. https://doi.org/10.1002/ejlt.201300368

Weng, J., Wong, S.N., Xu, X., Xuan, B., Wang, C., Chen, R., Sun, C.C., Lakerveld, R., Kwok, P.C.L., Chow, S.F., 2019. Cocrystal Engineering of Itraconazole with Suberic Acid via Rotary Evaporation and Spray Drying. Cryst. Growth Des. 19, 2736–2745. https://doi.org/10.1021/acs.cgd.8b01873

Weyna, D.R., Shattock, T., Vishweshwar, P., Zaworotko, M.J., 2009. Synthesis and Structural Characterization of Cocrystals and Pharmaceutical Cocrystals: Mechanochemistry vs Slow Evaporation from Solution. Cryst. Growth Des. 9, 1106–1123. https://doi.org/10.1021/cg800936d

Wiecinski, P.N., Metz, K.M., Mangham, A.N., Jacobson, K.H., Hamers, R.J., Pedersen, J.A., 2009. Gastrointestinal biodurability of engineered nanoparticles: Development of an in vitro assay. Nanotoxicology 3, 202–214. https://doi.org/10.1080/17435390902859556

Willems, L., van der Geest, R., de Beule, K., 2001. Itraconazole oral solution and intravenous formulations: a review of pharmacokinetics and pharmacodynamics. J. Clin. Pharm. Ther. 26, 159–169. https://doi.org/10.1046/j.1365-2710.2001.00338.x

Williams, D.H., Fleming, I., 1995. Spectroscopic Methods in Organic Chemistry, 5th ed. McGraw-Hill.

Wu, L., Zhang, J., Watanabe, W., 2011. Physical and chemical stability of drug nanoparticles. Adv. Drug Deliv. Rev. 63, 456–469. https://doi.org/10.1016/j.addr.2011.02.001

Xu, Q., Ensign, L.M., Boylan, N.J., Schön, A., Gong, X., Yang, J.C., Lamb, N.W., Cai, S., Yu, T., Freire, E., Hanes, J., 2015. Impact of Surface Polyethylene Glycol (PEG) Density on Biodegradable Nanoparticle Transport in Mucus ex Vivo and Distribution in Vivo. ACS Nano 9, 9217–9227. https://doi.org/10.1021/acsnano.5b03876

Yamasaki, K., Kwok, P.C.L., Fukushige, K., Prud'homme, R.K., Chan, H.-K., 2011. Enhanced dissolution of inhalable cyclosporine nano-matrix particles with mannitol as matrix former. Int. J. Pharm. 420, 34–42. https://doi.org/10.1016/j.ijpharm.2011.08.010

Yang, Q., Jones, S.W., Parker, C.L., Zamboni, W.C., Bear, J.E., Lai, S.K., 2014. Evading immune cell uptake and clearance requires PEG grafting at densities substantially

References

exceeding the minimum for brush conformation. Mol. Pharm. 11, 1250–1258. https://doi.org/10.1021/mp400703d

Yang, W., Chow, K.T., Lang, B., Wiederhold, N.P., Johnston, K.P., Williams, R.O., 2010. In vitro characterization and pharmacokinetics in mice following pulmonary delivery of itraconazole as cyclodextrin solubilized solution. Eur. J. Pharm. Sci. 39, 336–347. https://doi.org/10.1016/j.ejps.2010.01.001

Yang, W., Tam, J., Miller, D.A., Zhou, J., McConville, J.T., Johnston, K.P., Williams, R.O., 2008. High bioavailability from nebulized itraconazole nanoparticle dispersions with biocompatible stabilizers. Int. J. Pharm. 361, 177–188. https://doi.org/10.1016/j.ijpharm.2008.05.003

Yoncheva, K., Gómez, S., Campanero, M.A., Gamazo, C., Irache, J.M., 2005. Bioadhesive properties of pegylated nanoparticles. Expert Opin. Drug Deliv. 2, 205–18. https://doi.org/10.1517/17425247.2.2.205

Yoshida, Y., Aoyama, Y., 1990. Stereoselective interaction of an azole antifungal agent with its target, lanosterol 14?-demethylase (cytochromep-45014dm): A model study with stereoisomers of triadimenol and purified cytochromep-45014dm from yeast. Chirality 2, 10–15. https://doi.org/10.1002/chir.530020103

Yoshida, Y., Aoyama, Y., 1991. Sterol 14α-demethylase and its inhibition: structural considerations on interaction of azole antifungal agents with lanosterol 14α-demethylase (P -450 14DM) of yeast. Biochem. Soc. Trans. 19, 778–782. https://doi.org/10.1042/bst0190778

Yu, L., 2001. Amorphous pharmaceutical solids: preparation, characterization and stabilization. Adv. Drug Deliv. Rev. 48, 27–42. https://doi.org/10.1016/S0169-409X(01)00098-9

Zhang, G.G.Z., Henry, R.F., Borchardt, T.B., Lou, X., 2007. Efficient Co-crystal Screening Using Solution-Mediated Phase Transformation. J. Pharm. Sci. 96, 990–995. https://doi.org/10.1002/jps.20949

Zhang, H.-X., Wang, J.-X., Zhang, Z.-B., Le, Y., Shen, Z.-G., Chen, J.-F., 2009. Micronization of atorvastatin calcium by antisolvent precipitation process. Int. J. Pharm. 374, 106–113. https://doi.org/10.1016/j.ijpharm.2009.02.015

Zhang, S., Lee, T.W.Y., Chow, A.H.L., 2016. Crystallization of Itraconazole Polymorphs from Melt. Cryst. Growth Des. 16, 3791–3801. https://doi.org/10.1021/acs.cgd.6b00342

Zhao, H., Wang, J., Zhang, H., Shen, Z., Yun, J., Chen, J., 2009. Facile Preparation of Danazol Nanoparticles by High-Gravity Anti-solvent Precipitation (HGAP) Method. Chinese J. Chem. Eng. 17, 318–323. https://doi.org/10.1016/S1004-9541(08)60210-4

Zhao, Z., Huang, Z., Zhang, X., Huang, Y., Cui, Y., Ma, C., Wang, G., Freeman, T., Lu, X.,

References

Pan, X., Wu, C., 2018. Low density, good flowability cyclodextrin-raffinose binary carrier for dry powder inhaler: anti-hygroscopicity and aerosolization performance enhancement. Expert Opin. Drug Deliv. 15, 443–457. https://doi.org/10.1080/17425247.2018.1450865

Zhou, L., Dodd, S., Capacci-Daniel, C., Garad, S., Panicucci, R., Sethuraman, V., 2016. Co-crystal formation based on structural matching. Eur. J. Pharm. Sci. 88, 191–201. https://doi.org/10.1016/j.ejps.2016.02.017

Zuorro, A., Iannone, A., Lavecchia, R., 2019. Water–Organic Solvent Extraction of Phenolic Antioxidants from Brewers' Spent Grain. Processes 7, 126. https://doi.org/10.3390/pr7030126

Appendices

Appendix 1
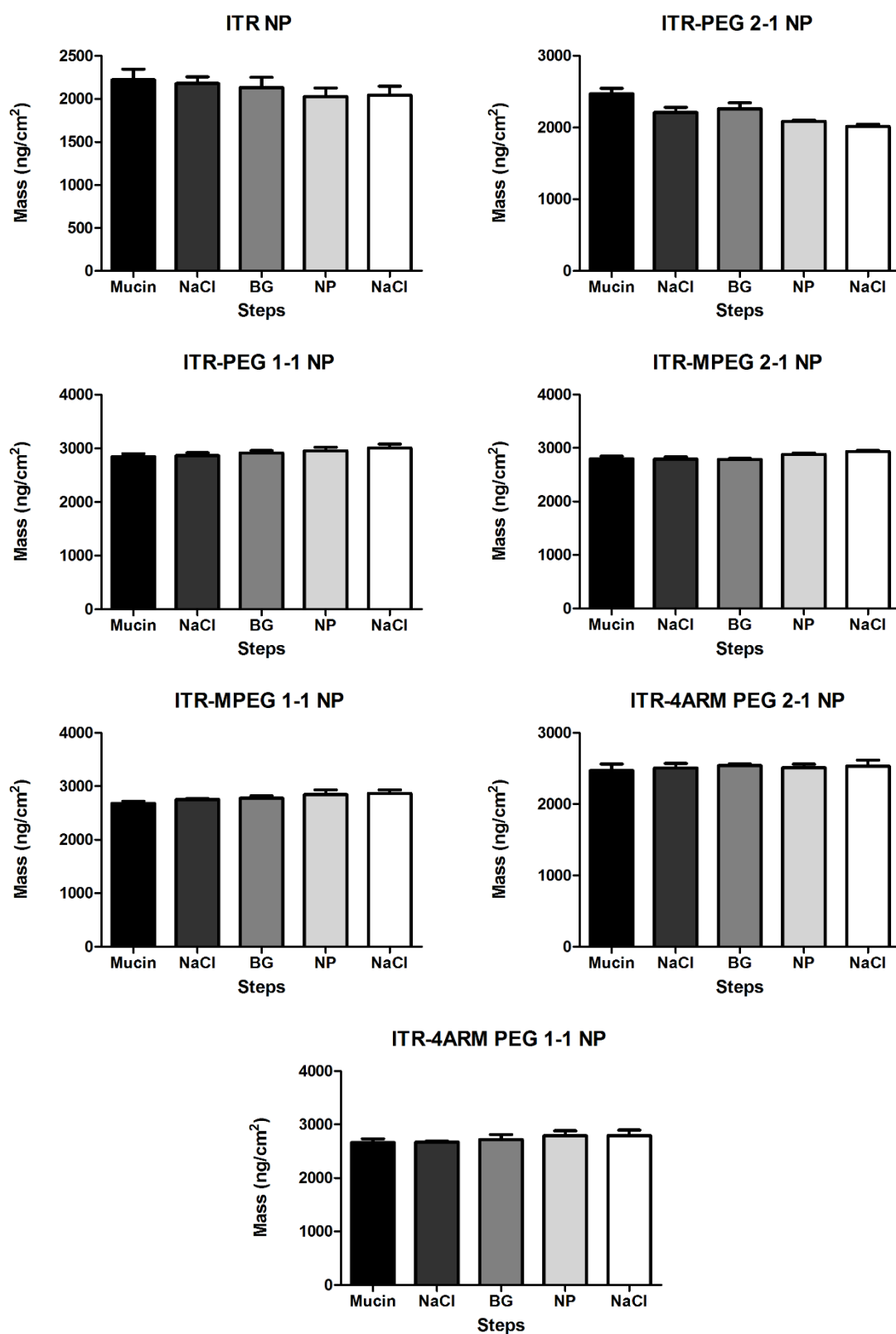
Fig A.1.1: Statistical analysis of the mass of adsorbed layers after each step during QCM-D experimental procedure. Data is expressed as mean ± SD. BG: background solution. NPs: nanoparticles.

Appendix 2

Table A.2.1: FT-IR spectrum of ITR-TER

Wavenumber (cm⁻¹)	Vibration assignments
1705	ν(C=O)
1587	aromatic ring ν(C=C)
1552	aromatic ring ν(C=C)
1510	aromatic ring ν(C=C)
1452	ν(C-N) or δ(C-H)
1381	ν(C-N) or δ(C-H)
1325	ν(C-N) or δ(C-H)
1270	carboxylic carbon ν(C-C) or aromatic amine ν(C-N)
1254	carboxylic carbon ν(C-C) or aromatic amine ν(C-N)
1226	alkyl aryl ether ν(C-O)
1158	aromatic ring δ(C-H)
1123	carboxylic acid ν(C-O)
1104	ν(C-Cl)
1044	ether ν(C-O)
1010	δ(C-H)
976	ether ν(C-O)
900	1,2,4 trisubstituted ring γ(C-H)
864	γ(C-H)
824	triazole or 1,4 disubstituted ring γ(C-H)
796	triazole or 1,4 disubstituted ring γ(C-H)
764	aromatic ring γ(C-H)
736	aromatic ring γ(C-H)

ν = stretching; δ = in plane bending; γ = out plane bending
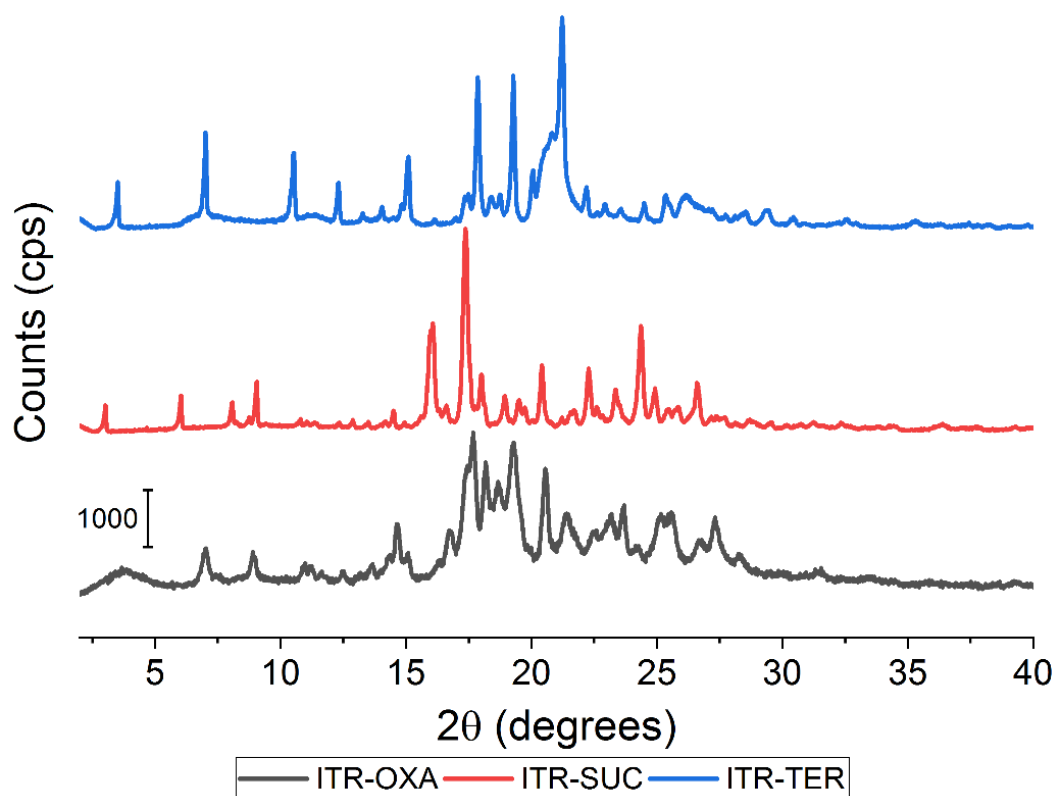
Fig. A.2.1: PXRD diffractograms of cocrystals: ITR-OXA, ITR-SUC and ITR-TER cocrystals prepared in the scale-up studies.
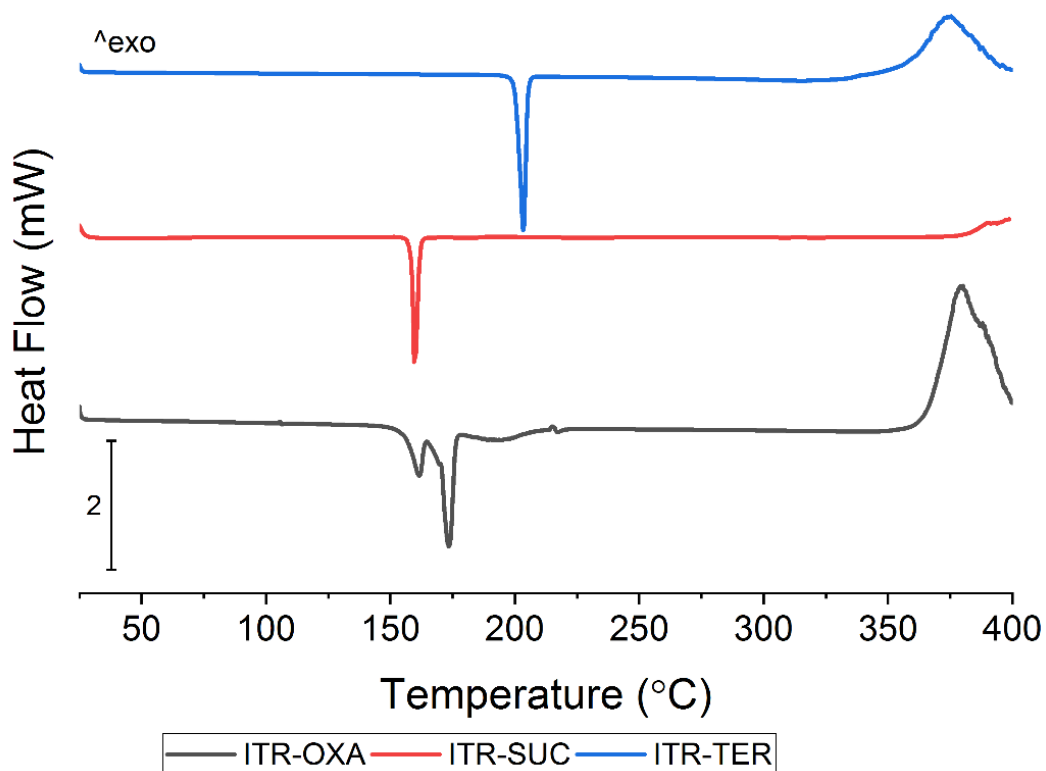

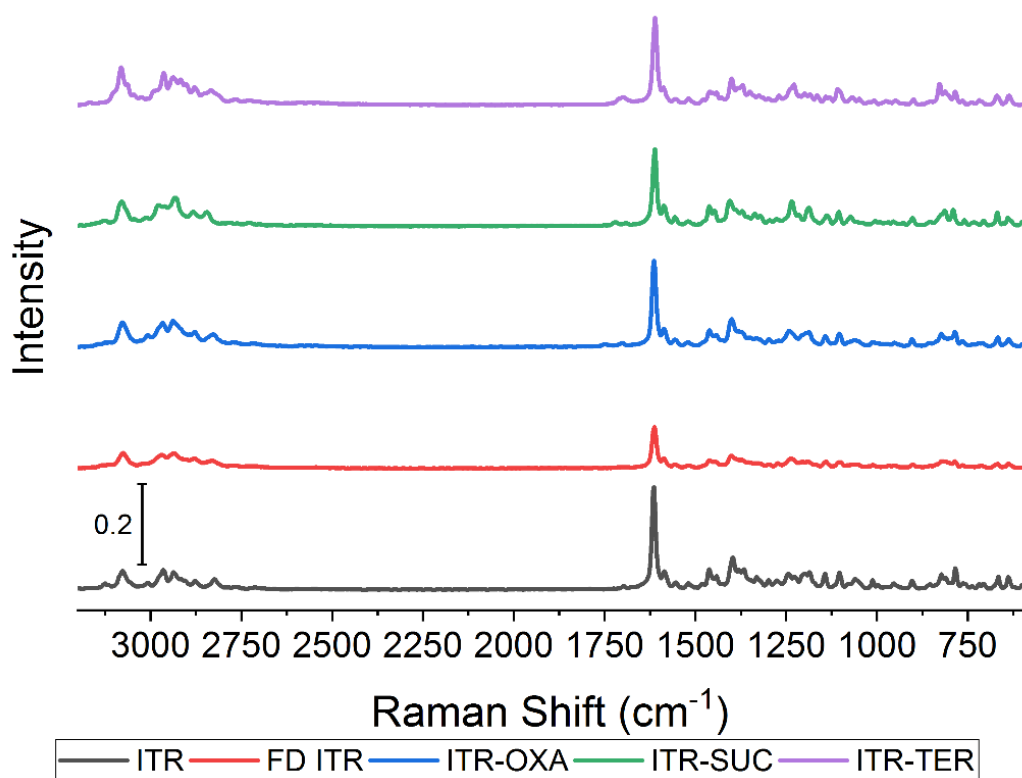**Fig. A.2.2:** DSC thermograms of cocrystals: ITR-OXA, ITR-SUC and ITR-TER cocrystals prepared in the scale-up studies.
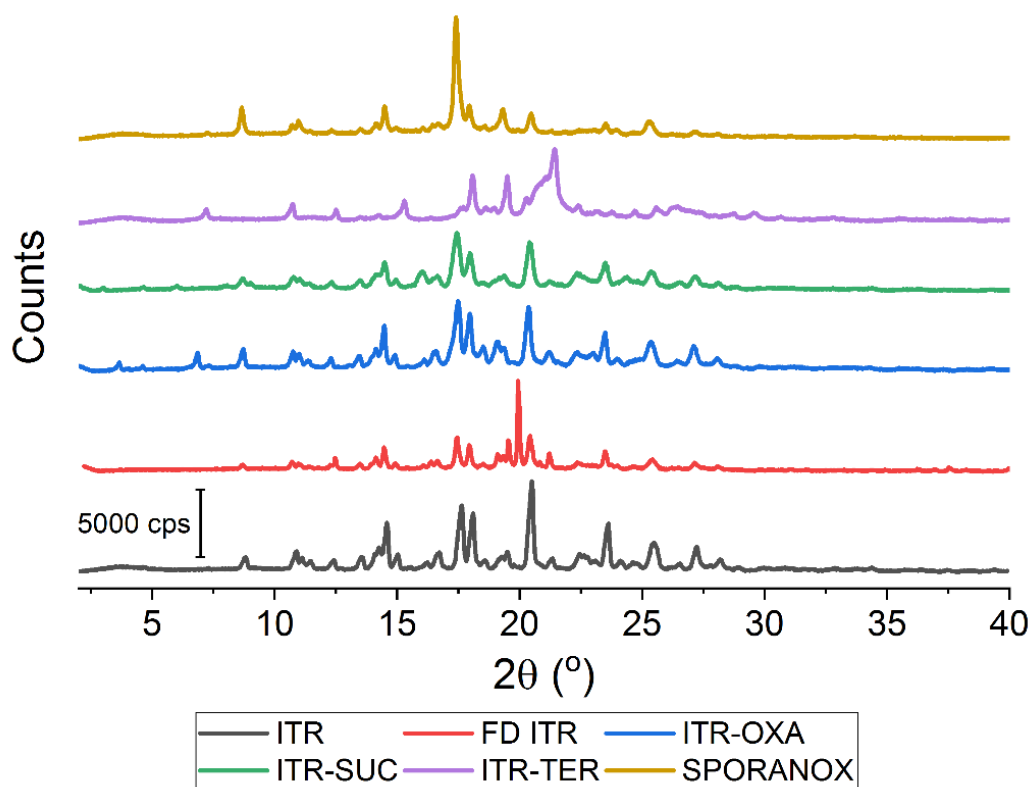
Fig. A.2.3: Raman analysis of disks after IDR.

Fig. A.2.4: PXRD diffractograms of undissolved material in powder dissolution experiment of Sporanox® and the crystalline ITR, freeze dried ITR (FD ITR) and the cocrystals ITR-OXA, ITR-SUC and ITR-TER mixed with lactose.
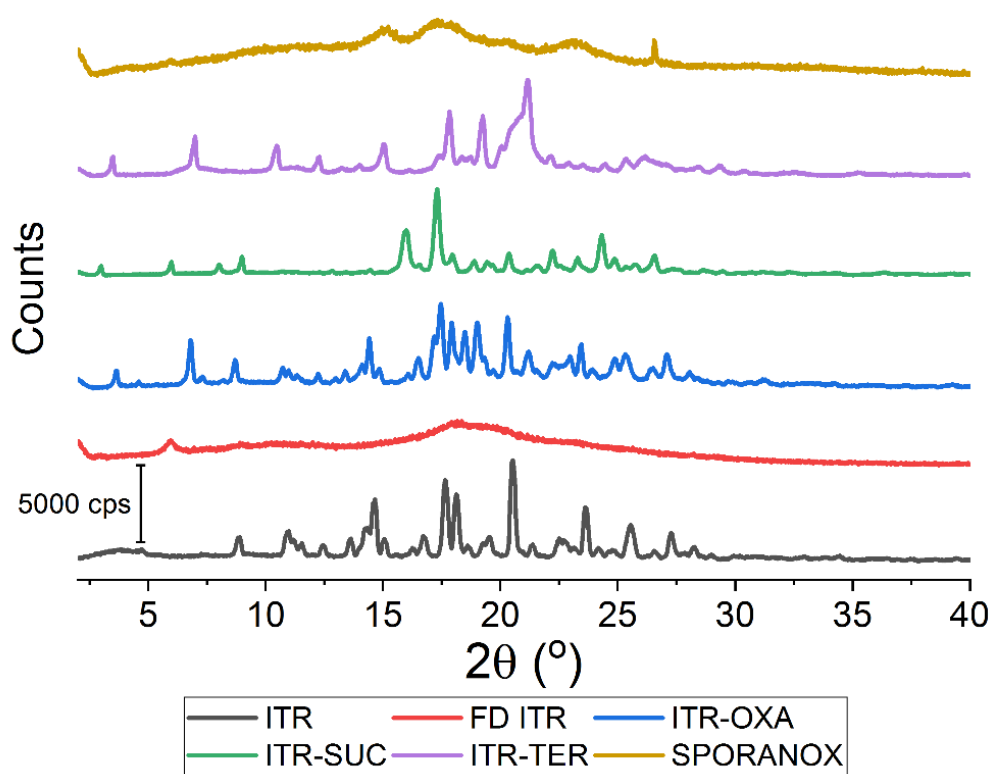
Fig. A.2.5: PXRD diffractograms of undissolved material in powder dissolution experiment of Sporanox® and the crystalline ITR, freeze dried ITR (FD ITR) and the cocrystals ITR-OXA, ITR-SUC and ITR-TER mixed with excipients from the Sporanox® formulation.